Abstract

The first measurement of bottom quark production in the forward detector at CDF is presented in this thesis. Events from the 1988/89 Fermilab collider run were selected with forward muons with nearby jets to form a bottom quark tag. The efficiency and acceptance of the detector are then taken into account and the number of events is turned into a cross section: $\sigma(p_t^b > 20 \text{ GeV}, 1.9 < |\eta^b| < 2.5) = (124. \pm 35. \pm 76.)$ nb. The contribution from direct bottom quarks is $\sigma(p_t^b > 20 \text{ GeV}, p_t^{\bar{b}} > 15 \text{ GeV}, 1.9 < |\eta^b| < 2.5) = (100. \pm 30.^{+30.}_{-31.})$ nb.

Acknowledgements

As my graduate career draws to a close, my thoughts are drawn in retrospect to those without whom this thesis would not have been produced. My deepest thanks go to those who struggled with me through the creation of this document.

From the FMU group, I am indebted to my advisor, Professor Duncan Carlsmith for his continued support. Both Duncan and Professor Lee Pondrom evaluated my work critically and their insight has been invaluable. I am grateful to Chris Wendt for his original ideas many of which are presented here and also for working through the details of this analysis with me. I am also grateful to Karen Byrum for her collaborative work on the Inclusive FMU Spectrum. I would like to thank Jesse, George, Bob, Jim, and Hugh for their technical support. Thanks also go to Joe, Les, and Theresa who proofread parts of this thesis. Finally, I would like to thank literally hundreds of my collaborators who have contributed in one way or another to the data collection and computer codes used in this analysis.

In addition to technical support, I am grateful to many of my collaborators

for their emotional support. Personally, I would like to thank the CDF party gang for making the experiment worthwhile. Specifically, I give the credit to Vic, Phil, Hovhannes - the famous Illinois boys, as well as Leigh, John, Les, Paul, Brian, Peter, Tiny, Tom, Dave, William (sorry about embarrassing you) Steve, and Dee. I would also like to thank the CDF band -Steve, Vic, Andrew, Randy, Brian, John, Gary, Jim, Rick and Owen for being hip in more recent years.

There are many friends who supported me during my graduate school years. Early on Kavoose introduced me to my advisor, John cooked dinner regularly, Janet explained why physics was worthwhile and Dan helped when there were tears. I would like to extend many thanks to Marie for an outside ear, Hassan for his love, and Robin for her friendship and hospitality. I'd also like to thank the Chesebros for adopting me into their family on many occasions. Finally, thank you Karen, Erik, Chris and more recently Theresa and Paul for your friendship, advise and many interesting experiences. I have a million memories which I will keep forever.

My deepest thanks go to my parents who have always believed in me and provided a safety net to catch me should I fail. I would also like to thank my siblings, Rhea, Burt, John, and Connie for keeping strong family ties even over long distances. Thanks to Tegers and Marina who have suffered for this thesis even though they can't understand a word of it. To my Grandma Charlotte, thank you for sharing so much with me. To my aunts, Nancy and Irene, thank you for being examples of women in careers and to Pat Ellerington, thank you for

inspiring my mind and bolstering my self confidence in high school. My thanks go also to Raymond who always let me choose the channel. Thank you for being a big inspiration in my life Grandma Lelia even though you never saw me start graduate school and also Grandpa Lamoureux who isn't here to see me complete it. Finally, I would like to dedicate this thesis to those who can't remember when I wasn't a graduate student: Karl, Emily, Lelia, and the one still waiting for a name. Truly there is more wonderous development in the growth of a child than in the greatest masterpiece of man.

This work was supported by the United States Department of Energy Contract DE-AC02-76ER00881.

Contents

Abstract ii

Acknowledgements iii

List of Tables x

List of Figures xiv

1 Introduction 1

1.1 Direction and overview 4

2 Theory and Background 6

2.1 Calculation of QCD cross sections at leading order 7

2.2 Extension of QCD cross sections to next-to-leading order 13

2.3 Status of bottom quark cross sections 15

2.4 Motivation for the measurement of direct bottom at forward η . . 18

3 Forward Muon Measurement 20

3.1 Overview of the experimental facilities and the Collider Detector at Fermilab(CDF) 21

3.2 Forward Muon Detector components 25

3.3 Luminosity for the FMU trigger 34

3.4 Forward Muon Detector efficiency 36

3.5 Forward muon momentum resolution 38

3.6 Forward muon direction resolution 40

3.7 Trigger acceptance and efficiency 47

3.8 Tracking algorithm efficiency 51

3.9 Fake muon rate estimate 53

4 Jet Measurement **55**

4.1 The CDF calorimeters 55

4.2 Energy scale in the central calorimeter 57

4.3 Energy resolution in the central calorimeters 66

4.4 Energy scale in the forward calorimeters 77

4.5 Energy resolution in the forward calorimeters 82

4.6 Position resolution in the forward calorimeters 86

4.7 Acceptance in the plug/forward boundary region 87

4.8 Summary 90

5 Muons in Jets Data Selection **93**

5.1 Inclusive muon selection 94

5.2 Inclusive muon spectra 98

5.3 Muons in jets selection 106

5.4 Muons in jets spectra 119

5.5 p_t^{rel} 119

6 Bottom Content in FMU and Jets Data **125**

6.1 Simulation 126

6.2 Total b quark cross section from fit using p_t^{rel} 133

6.3 Direct b quark cross section from fit using η_{opp} 146

6.3.1 Simple fits 149

6.3.2 Global fits 155

6.3.3 Connection between global fits and the simpler fits 157

6.3.4 Extraction of direct bottom cross section 172

6.4 Systematic effects 173

6.4.1 Jet energy scale 175

6.4.2 Jet resolution 178

6.4.3 Forward muon momentum resolution 178

6.4.4 Angular resolution 179

6.4.5 Modelling 180

6.5 Summary of the total and direct bottom quark cross section . . . 181

6.6 Dilepton check of the direct bottom content 182

6.7 Interpretation 185

A FMU 88/89 Detector Efficiency **190**

A.1 Single channel contribution to the trigger efficiency 191

A.1.1 Drift chamber 194

A.1.2 Scintillator 195

A.2 Group failures 198

A.3 Single chamber losses 205

A.4 Level 1 trigger electronics efficiency 206

A.5 Combined results 208

A.6 Comparisons to track distributions 209

B Simulating Decay-in-Flight Muons **213**

C Single Heavy Quark Differential Distributions **216**

C.1 Comparison of NDE, MNR and ISAJET heavy quark production 217

C.2 Comparison of MNR and ISAJET at forward η 222

D Heavy Quark Double Differential Distributions **225**

D.1 Energy distribution in bottom events 225

D.2 Kinematics of bottom events 229

E Glossary of Abreviations **237**

Bibliography **240**

List of Tables

2.1 *Lowest order heavy quark production matrix elements.* 13

3.1 *FMU trigger configurations and associated luminosity for the 1988/89 CDF run.* 35

3.2 *Sources contributing to the momentum resolution.* 43

4.1 *Jet energy scale from Feynman-Field and Peterson Fragmentation.* 63

4.2 *Resolution,* $\sigma(k_{t\|}^{norm})$, *of jets in different detector regions.* 84

4.3 *Uncertainty in the resolution,* $\sigma(k_{t\|}^{norm})$, *of jets in different detector regions.* 86

5.1 *Efficiency of quality cuts.* 97

6.1 *The number of events generated with ISAJET and those which survive the simulated efficiency and acceptance of the detector, trigger and analysis cuts. Included are the generation cuts for each physics process simulated and the integrated luminosity for the simulation.* 130

6.2 *The p_t^{rel} fractions for the simulations and data.* 136

6.3 *The fit results for various simulated signal and background shapes.* 136

6.4 *The bottom quark cross sections for various signal and background assumptions. The uncertainty in the measured cross section is only statistical.* 143

6.5 *The results of the fit to the η_{opp} distribution in the bottom enhanced region, $p_t^{rel} > 2$ GeV.* 150

6.6 *The results of the fit to the mean of the η_{opp} distribution in the bottom enhanced region, $p_t^{rel} > 2$ GeV.* 154

6.7 *The variation in the number of events in the data sample which are attributed to direct bottom decays for a range of global fits. The fits constrain the ratio of gluon splitting charm and bottom in the background simulations as well as the ratio of light quark contributions.* 156

6.8 *One of the global fits. The ratio of direct charm and π decay in flight are fixed. Also held fixed is the ratio of gluon splitting bottom and charm. The χ^2 of this fit over 4 bins with 5 distributions and 2 constraints is .81. There is one degree of freedom in the fit and the uncertainty in the fit values are the statistical uncertainties extracted from the diagonal covariance matrix elements.* 158

6.9 *Systematic uncertainties for the jet energy measurement which affect the direct bottom quark measurement.* 175

6.10 *Fluctuations in the bottom content of the data sample with systematic shifts in the jet energy scale.* 177

6.11 *The global fit used to determine the cross section with the jet cuts adjusted according to the uncertainty in the jet energy scale. The ratio of the direct charm and π/K decay in flight are fixed. Also held fixed is the ratio of gluon splitting bottom and charm.* 177

6.12 *Fluctuations in the bottom content of the data sample with fits over $\delta\phi$ instead of p_t^{rel}.* 180

6.13 *The global fit used to determine the cross section with the η_{opp} distribution weighted. The ratio of the direct charm and π/K decay in flight are fixed. Also held fixed is the ratio of gluon splitting bottom and charm.* 181

6.14 *Summary of the total and direct measured bottom quark cross sections compared to theory. In all cases, the first uncertainty is statistical and the second is systematic. The cross sections are calculated using equations 6.6 to 6.9.* 183

A.1 *Number of volunteer tracks with 5 and 6 hits available for the fit.* 196

A.2 *The chamber efficiency and probability for finding 5 and 6 hit tracks.* 196

A.3 *The scintillator contribution to the trigger efficiency.* 197

A.4 *The group fraction for four sections of the 1988/89 run.* 205

A.5 *The single chamber failures for four sections of the CDF 1988/89 run.* 206

A.6 *Efficiencies of triggers and volunteer tracks.* 210

A.7 *The prediction of data yields on the east compared to the west.* . 211

List of Figures

1.1 *Schematic representation of dijet events where one of the jets has a muon nearby.* 5

2.1 *Leading and next-to-leading order bottom production diagrams.* . 8

2.2 *In proton-antiproton collisions, the partons (quarks and gluons) inside the parent particles interact. All leftover partons interact minimally and are thus called spectators to the interaction. The parton subprocess is one of the interactions from the previous figure.* 9

2.3 *The distribution functions, $f(x)$, represent the probability of finding a quark with momentum fraction $x = p/P_{proton}$ between x and $x + dx$. The distribution functions are shown for the up, down and sea quarks with the gluon. For this plot, EHLQ1 structure functions were used.* 11

2.4 *The b quark production cross sections measured using electrons as well as other CDF measurements and the QCD prediction by NDE.* 16

2.5 *The b quark production cross sections measured at UA1 with the QCD prediction by NDE.* 17

3.1 *Overhead view of the Fermilab accelerator complex.* 22

3.2 *Side view of the CDF detector.* 24

3.3 *Side view of the Forward Muon Detector. The detector is symmetric about the vertex.* 26

3.4 *Each plane consists of 24 chambers each of which spans 15° in azimuth.* 27

3.5 *Schematic of the various chamber parts in the forward muon detector.* 30

3.6 *Schematic of the forward muon detector readout electronics.* . . . 31

3.7 *Efficiency as a function of gain for the FMU drift chambers.* . . . 37

3.8 *Residuals for FMU + Jet with Jet $E_t > 10$ GeV. For each hit on a track, the residual is the radial distance from the measured hit to the fitted track position.* 41

3.9 *Residuals for Z_0 candidates.* 42

3.10 *Uncertainty in Theta* 44

3.11 *Pad pulse height distributions. (a.) 1×1 tower centered on the muon. (b.) 1×1 tower centered on azimuth opposite the muon. (c.) 1×3 tower centered on the muon (d.) 1×3 tower centered on azimuth opposite the muon.* 46

3.12 *Geometric trigger acceptance for the NUPU 50% road.* 48

3.13 *Vertex distribution in data.* 49

3.14 *Simulated vertex distribution for negatively charged muons* 50

4.1 *Average single particle response* (E/p) *measured for hadrons in the central calorimeter as a function of momentum.* 60

4.2 *Average electron response* (E/p) *measured in the central calorimeter as a function of momentum.* 61

4.3 *Systematic uncertainty in the jet energy scale associated with the uncertainty in single particle responses of pions and electrons, light quark and gluon fragmentation, and the underlying event.* 65

4.4 *The observed and correct missing* E_t *parallel to the primary electron direction in conversion events as a function of the* E_t *of the primary electron.* 67

4.5 *Photon - Jet balancing using events collected with the photon trigger,* $E_t^\gamma > 10$ *GeV.* 68

4.6 *Photon - Jet balancing using events collected with the photon trigger,* $E_t^\gamma > 23$ *GeV.* 69

4.7 *Dijet balancing coordinate system in the plane transverse to the beam direction.* 72

4.8 *Dijet balancing with central jets; longitudinal and perpendicular* k_t *fractions.* 72

4.9 *Jet resolution as a function of jet energy.* 74

4.10 *Momentum spectrum for particles in 10 to 12 GeV jets compared to that of 30 to 35 GeV jets.* 75

4.11 *Electron - jet balancing. The resolution from events simulated with SETPRT+QFL agree well with the data.* 76

4.12 *Missing E_t projection fraction as a function of η_d measured with dijet data in the ranges a) 50 GeV/c $< \sum P_t <$ 100 GeV/c and b) 100 GeV/c $< \sum P_t <$ 130 GeV/c.* 80

4.13 *Missing E_t projection fraction as a function of η_d after correction for dijet data in the ranges a) 50 GeV/c $< \sum P_t <$ 100 GeV/c and b) 100 GeV/c $< \sum P_t <$ 130 GeV/c.* 81

4.14 *The MPF distribution for simulated jets.* 82

4.15 *The correction factor β as a function of jet E_t for selected values of η_d.* 83

4.16 *Perpendicular P_t fraction for different η_d regions.* 85

4.17 *The separation in η between the simulated jet direction and the vector sum of particle tracks which contribute to the jet. Low, medium and high jet E_t are between 10 GeV and 20 GeV, 20 GeV and 50GeV, and above 50 GeV respectively.* 88

4.18 *The azimuthal separation between the simulated jet direction and the vector sum of particle tracks which contribute to the jet. Low, medium and high jet E_t are between 10 GeV and 20 GeV, 20 GeV and 50GeV, and above 50 GeV respectively.* 89

4.19 *Jet finding inefficiency limit (3rd jet< 5 GeV).* 91

5.1 *Distributions of energy deposited in a 3×3 array of calorimeter towers centered on the tower through which the forward muon was thought to pass.* 99

5.2 *Ratio of positively charged muons to negatively charged muons as a function of momentum.* 100

5.3 *East versus West muon yield. The distributions are shown before and after correcting for the detector efficiency on each end.* 101

5.4 *Muon spectrum from W bosons, bottom and charm quarks and decay-in-flight prior to detector simulation.* 103

5.5 *Momentum spectrum for inclusive forward muons compared to simulated processes.* 104

5.6 *Rapidity distribution for inclusive forward muons compared to simulated processes.* 105

5.7 *Momentum spectrum for inclusive forward muons compared to the predicted contributions from physics processes. The band shows the upper and lower theoretical estimates.* 107

5.8 *Rapidity distribution for inclusive forward muons compared to the predicted contributions from physics processes. The band shows the upper and lower theoretical estimates.* 108

5.9 *Charged particle spectrum at CDF.* 109

5.10 *Ratio of positively charged muons to negatively charged muons as a function of momentum in the muons in jets data sample.* 112

5.11 *Vertex distribution of the muons in jets data sample.* 113

5.12 *The probability of χ^2 distribution for the muons in jets data sample.* 114

5.13 *Number of wire hits in the octant containing the track.* 116

5.14 *Pulse height distributions for pads in units of ADC counts.* 117

5.15 *Plug electromagnetic and hadronic energy in the 3×3 array of towers centered on the tower through which the forward muon passed.* 118

5.16 *Transverse energy and rapidity distributions of both jets in the muons in jets sample.* 120

5.17 *(A) Muon momentum and (B) pseudorapidity distributions of the muons in jets sample. (C) P_t^{rel} (D) δR.* 121

5.18 *(A) Opening azimuthal angle between the muon and the opposite jet. (B) Opening azimuthal angle between the muon and the near by jet. (C) Difference in pseudorapidity between the muon and the near by jet. (D) $\delta R_{\mu-jet}$ between the muon and the near by jet.* 122

6.1 *Distributions of p_t^{rel} normalized to unit area for the different processes which contribute to the muons in jets data sample. Notice that bottom quark processes have a different shape than light quark processes.* 135

6.2 *Simulated bottom quark p_t and η distributions for events which passed all analysis cuts.* 138

6.3 *Measured bottom production with the assumption that direct b production represents the entire sample.* 141

6.4 *Measured bottom production with the assumption that gluon splitting b production represents the entire sample.* 142

6.5 *Comparison of the measured and predicted cross sections for bottom production. The extreme modelling assumptions bound the result on the horizontal axis. The real result lies somewhere between the two. The measured result is higher than predicted for all values of p_t^{min}.* 145

6.6 *Distributions of η_{opp} normalized to unit area for the different processes which contribute to the muons in jets data sample. Notice that quark processes have a different shape than gluon processes.* 148

6.7 *The distribution of η_{opp} in the bottom enhanced region, $p_t^{rel} > 2$ GeV, for the muons in jets data sample.* 151

6.8 *Momentum distribution for forward muons in CDF data displayed with the result of the global fit in Table 6.8.* 159

6.9 *Pseudorapidity distribution for forward muons in CDF data displayed with the result of the global fit in Table 6.8.* 160

6.10 *Corrected E_t distribution for the jet near the muon in CDF data displayed with the result of the global fit in Table 6.8.* 161

6.11 *Corrected E_t distribution for the opposite jet in CDF data displayed with the result of the global fit in Table 6.8.* 162

6.12 *The pseudorapidity distribution for the jet near the muon in CDF data displayed with the result of the global fit in Table 6.8.* 163

6.13 *The pseudorapidity distribution for the opposite jet in CDF data displayed with the result of the global fit in Table 6.8.* 164

6.14 *The p_t^{rel} distribution for CDF data displayed with the result of the global fit in Table 6.8.* 165

6.15 *The azimuthal distance between the muon and the opposite jet for CDF data compared to the result of the global fit in Table 6.8.* . . 166

6.16 *The vertex distribution for CDF data compared to the result of the global fit in Table 6.8.* 167

6.17 *The probability of χ^2 distribution for CDF data compared to the result of the global fit in Table 6.8.* 168

6.18 *The distribution of δR between the forward muon and the nearby jet for CDF data displayed with the result of the global fit in Table 6.8.* 169

6.19 *The distribution of $\delta\phi$ between the forward muon and the nearby jet for CDF data displayed with the result of the global fit in Table 6.8.* 170

6.20 *The distribution of $\delta\eta$ between the forward muon and the nearby jet for CDF data displayed with the result of the global fit in Table 6.8.* 171

6.21 *Transverse momentum spectrum of $\bar{b}$ in simulated direct bottom quark events which passed all analysis cuts.* 174

6.22 *The measured η dependence of the cross section compared to the theoretical prediction normalized to the central measurement.* . . 187

6.23 *The μ scale dependence of the predicted cross section.* 188

A.1 *Front, middle and rear plane chamber hit rates.* 200

A.2 *The rates for the first 420 nb^{-1} of the run compared to the average rate.* 202

A.3 *Average wire hit rates for each run and octant.* 203

A.4 *Average wire hit rates for each run and octant.* 204

A.5 *The efficiency calculation compared to data yield as a function of octant.* 212

C.1 *Comparison of the MNR and ISAJET cross section calculations to the published NDE cross section.* 219

C.2 *Transverse momentum distribution for central bottom quarks.* . . 220

C.3 *Gluon splitting production bottom quark momentum correction function.* 221

C.4 *Comparison of the MNR and ISAJET cross section calculations for* $p_t^b > 20$ *GeV.* 223

C.5 *Comparison of the MNR and ISAJET transverse momentum distributions for* $1.9 < |\eta^b| < 2.4$. 224

D.1 *The azimuthal difference between the b quark and both the* $\bar{b}$ *quark and the gluon.* 227

D.2 *The transverse momentum distribution for three partons in bottom events.* 228

D.3 *Distribution of* η_{opp} *for either the* $\bar{b}$ *or the gluon.* 231

D.4 *The azimuthal difference between the b quark and both the* $\bar{b}$ *quark and the gluon for* $1.9 < |\eta^b| < 2.5$. 233

D.5 *The transverse momentum distribution for three partons in bottom events with* $1.9 < |\eta^b| < 2.5$. 234

D.6 *The weighting function applied to the ISAJET simulation so it models the NLO calculation more closely.* 235

Chapter 1

Introduction

The Collider Detector at Fermilab (CDF) is used to examine particle interactions produced at the largest center of mass energy currently generated in any laboratory. These interactions are described by the mathematical theory known as the Standard Model. Testing the predictions of this model is currently the primary task of the CDF collaboration. To this end, this thesis measures bottom quark production in proton - antiproton collisions and compares it to the prediction from the Standard Model. This is the first measurement of bottom quark production in the forward region of the detector and therefore the first comparison with theory in this region.

Bottom quarks decay via the electroweak interaction into a charm quark and a W boson. The W boson can decay to either a pair of quarks or leptons. The charm and any other light quarks usually decay hadronically into a jet of particles

which are detected by the calorimeter. When the W boson decays to a pair of leptons, one is a neutrino which goes undetected. The semileptonic decay mode contains a jet from the decay of the charm quark and a lepton which can be identified by the detector. In semileptonic bottom decays the lepton and jet are usually within a few degrees of each other, therefore the lepton is surrounded by some jet activity. This provides a way to distinguish bottom decays from the decay products of gluons, which are the primary source of jets at CDF.

The central muon and electromagnetic detectors at CDF have a limited acceptance for this signal since they require isolation for good lepton identification. In the case of electrons, isolation is essential to distinguish between the jet energy and the electron energy deposited in the calorimeter. For muons, isolation is necessary due to the large "punch through" background from jets which are not fully contained in the calorimeters and leak into the muon detector. These central lepton tags have been used in other analyses.[1] The isolation requirement is unnecessary in the forward muon detector (FMU) because the two meters of steel in the toroidal magnets of this detector make the punch through background negligible. The primary background to prompt muons observed with the FMU detector results from pion and kaon decay-in-flight between the interaction point and the calorimeter face.

The FMU subsystem of the CDF detector is located in the pseudorapidity region from $1.9 < |\eta_d| < 3.0$. Detector pseudorapidity is defined as:

$$\eta_d = -ln(tan(\theta/2)) \tag{1.1}$$

The bulk of FMU events contain muons with momenta transverse to the beamline between our trigger threshold of 5 GeV and about 40 GeV. The inclusive muon spectrum in this momentum region is difficult to analyze due to copious quantities of isolated pions and kaons which decay-in-flight. This spectrum is described by known physics processes, but not conducive to a good measurement of bottom quarks. To enhance the bottom content relative to the background, the presence of a jet near the muon is required.

The data sample consisting of events with muons which are accompanied by a nearby jet with corrected energy, $E_t^{cor} > 10$ GeV, has a smaller background fraction than the inclusive FMU event sample. A schematic representation of dijet events where one of the jets contains a muon is shown in Figure 1.1. The additional requirement of a substantial amount of energy in the calorimeter ensures that events are the result of a harder scattering process than the muon alone can assure. Even though the primary constituents of jets are pions and kaons, the signal and background can be separated by kinematic features related to the large mass of the bottom quark. The large mass tends to broaden the spatial distribution of the decay products, therefore jets from bottom quarks are, on average, broader than those from lighter quarks. Some ambiguity results, however, when a gluon splits into a quark-antiquark pair and the two partons remain near each other in the detector. Since there may be some shared energy between the two jets, the exact position of the quark, which decayed into a lepton, can't be reconstructed. These, "gluon splitting" events can be distinguished from the "di-

rect" bottom events by their topology. When two quarks are produced directly, they tend to be correlated in η, whereas those from gluon splitting tend to be uncorrelated in η. Using these kinematical features of lepton and jet events, this analysis will measure the fraction of events attributed to bottom quark decays and then the fraction of events attributed to direct bottom quark decays. The measured number of events in the data sample attributed to all or direct bottom quark decays will then be turned into the measured cross section by accounting for the efficiency and acceptance of the detector, trigger and analysis cuts.

1.1 Direction and overview

This analysis depends on both the calculation of the theoretical bottom cross section and the complete understanding of the experimental apparatus. Therefore, chapter 2, will describe the theoretical framework for calculating bottom quark cross sections followed in chapters 3 and 4 by the features of the forward muon detector and calorimeters. The data selection and checks on the performance of the forward muon trigger and efficiency are presented in chapter 5. Finally, the extraction of the measured bottom quark cross section will be presented in chapter 6 followed by a discussion of the systematic effects which affect the result.

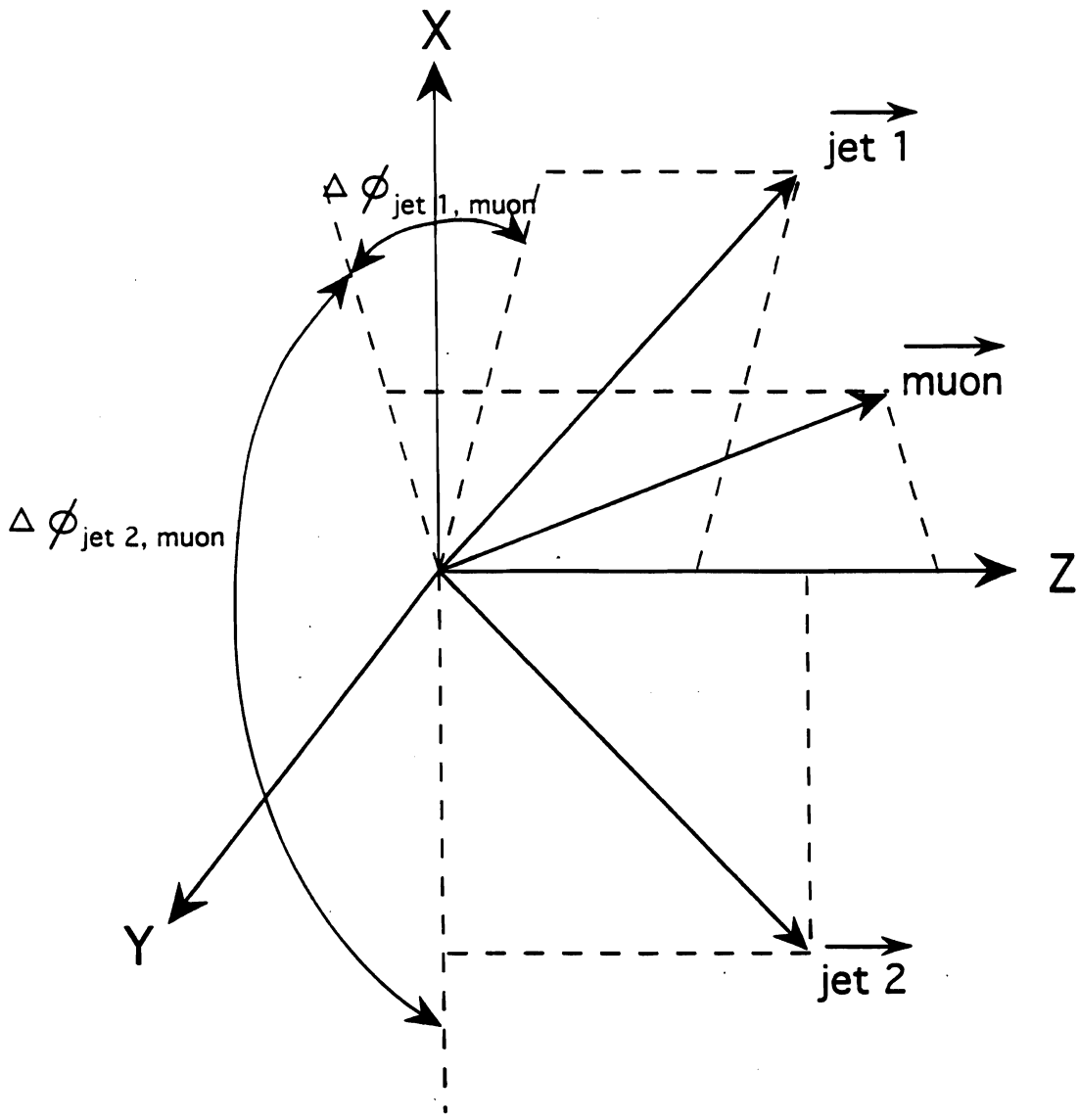

Figure 1.1: ***Schematic representation of dijet events where one of the jets has a muon nearby.***

Chapter 2

Theory and Background

The production of bottom quarks from collisions between protons and anti-protons is described by Quantum Chromodynamics (QCD). The exact solutions of QCD are complicated and have not yet been found. Only perturbative solutions exist and these are usually expressed as the sum of a series of terms. For most purposes, these series solutions are truncated after the leading or next-to-leading order terms. Recently, the next-to-leading order (NLO) calculation of the heavy quark cross section has been worked through completely and compared to measurements at CERN and Fermilab. The following sections describe the leading order calculation and issues involved in extending the calculation to next-to-leading order. The results of previous measurements and their implications are also discussed.

2.1 Calculation of QCD cross sections at leading order

There are a limited number of topological ways at each order of α_s to connect two incoming partons to make bottom quarks. Feynman diagrams of the leading and next-to-leading order interactions are shown in Figure 2.1. Each vertex carries a factor of $\sqrt{\alpha_s}$, the coupling constant of the strong force. Since the leading-order diagrams contain two vertices, and the square of the number of vertices enters the cross section, these interactions are of order $O(\alpha_s^2)$. The next-to-leading order interactions with three vertices are of order $O(\alpha_s^3)$. Since α_s is smaller than one, higher order terms may be neglected. Unfortunately, we have learned that α_s is not sufficiently small to make the series converge at just leading order. Even at next-to-leading order there is evidence that the series is not fully convergent, but a higher order calculation is not yet available. At each order of α_s one can write down the predicted cross section, $\hat{\sigma}$, which is called the parton cross section.

It should be noted that the next-to-leading order diagrams in Figure 2.1 contain either three or four vertices. It has already been mentioned that $\sqrt{\alpha_s}$ contributes to the cross section as the square of the number of vertices. There are, however, interference terms between diagrams at different orders which also contribute. The product of a lowest order diagram with a next-to-leading order diagram contributes at $O(\alpha_s^{5/2})$ or $O(\alpha_s^3)$. These interference terms are clearly not of the same order, but the calculation retains all terms at $O(\alpha_s^3)$.

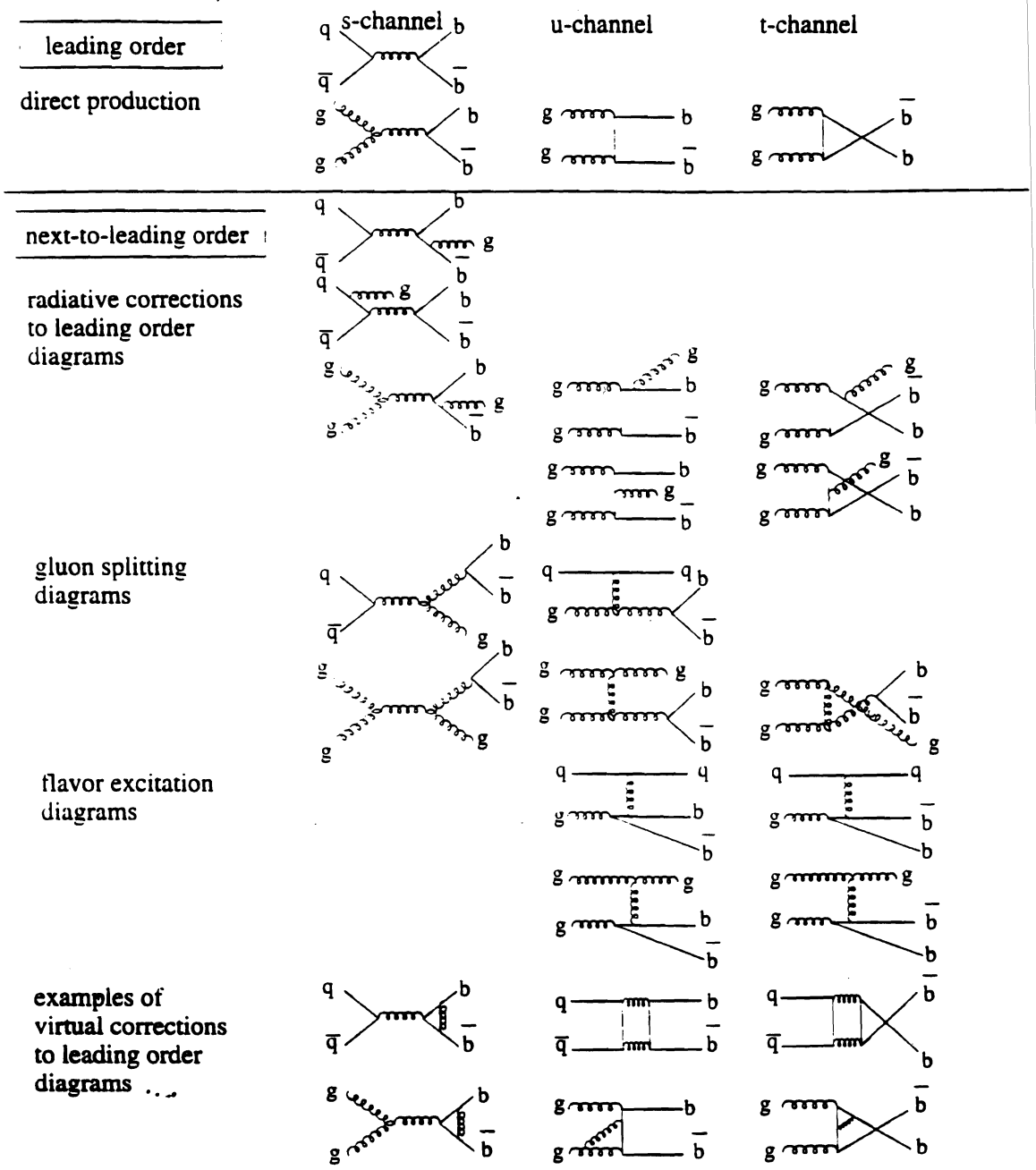

Figure 2.1: ***Leading and next-to-leading order bottom production diagrams.***

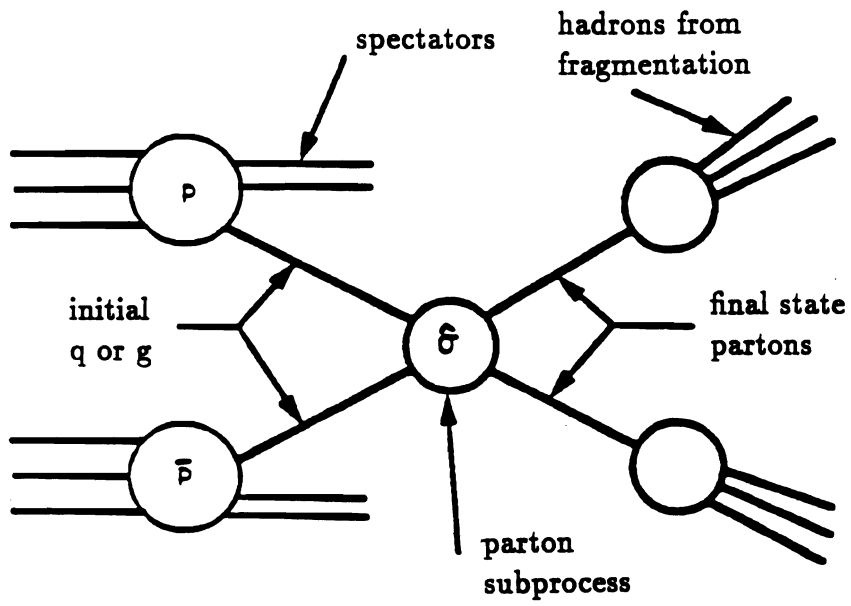

Figure 2.2: *In proton-antiproton collisions, the partons (quarks and gluons) inside the parent particles interact. All leftover partons interact minimally and are thus called spectators to the interaction. The parton subprocess is one of the interactions from the previous figure.*

Since the initial state is composed of quarks and gluons which are part of the proton or antiproton, they are not truly independent as the diagrams in Figure 2.1 assume. Figure 2.2 demonstrates the concept of proton-antiproton interactions in the spectator model. Here, we assume that the partons in the proton and antiproton interact independently. This approximation becomes more realistic as the collision energy is increased.

In order to calculate the cross section for $\bar{b}b$ quark production in proton-

antiproton collisions, the parton cross sections, $\hat{\sigma}$, must be convolved with the momentum spectrum of the initial state partons and summed over all possible initial states. The parton momentum distributions in the proton and antiproton are described by structure functions which are found empirically. EHLQ1 structure functions are shown as an example in Figure 2.3, where x is the fraction of the proton momentum carried by a particular parton. The cross section is then calculated as:

$$\sigma_{tot}(P\bar{P} \longrightarrow b\bar{b} + X) = \sum_{i,j} \int_0^1 \int_0^1 dx_i dx_j f(x_j) f(x_i) \hat{\sigma}(p_i p_j \longrightarrow b\bar{b} + X) \quad (2.1)$$

where $P(\bar{P})$ are proton (antiproton) momenta, $b(\bar{b})$ are bottom (antibottom) quark momenta, p are parton momenta, $\hat{\sigma}(p_i p_j \longrightarrow b\bar{b} + X)$ is the parton level cross section and the sum over i and j represent the sum over all possible partons in the proton. By inserting the parton cross sections for the diagrams in Figure 2.1 into this integral, we can predict the expected yield of bottom quarks measured by the experiment.

The cross sections, $\hat{\sigma}$, are crucial to the total cross section, and are found from the QCD theory. The leading order calculation is easy to summarize. Strong interactions are described by the group, SU(3).[2] This is a non-abelian gauge group which defines the QCD Lagrangian:

$$\text{Ł} = -\frac{1}{4} F_a^{\mu\nu} F_{a\mu\nu} + \bar{\psi}_j (i\gamma_\mu D^\mu_{jk} - M_{jk}) \psi_k \quad (2.2)$$

where the indices a, j and k refer to color. The color couplets range from $a = 1, ..., 8$ and there are three color charges in the theory; $j, k = 1, 2, 3$. The covariant

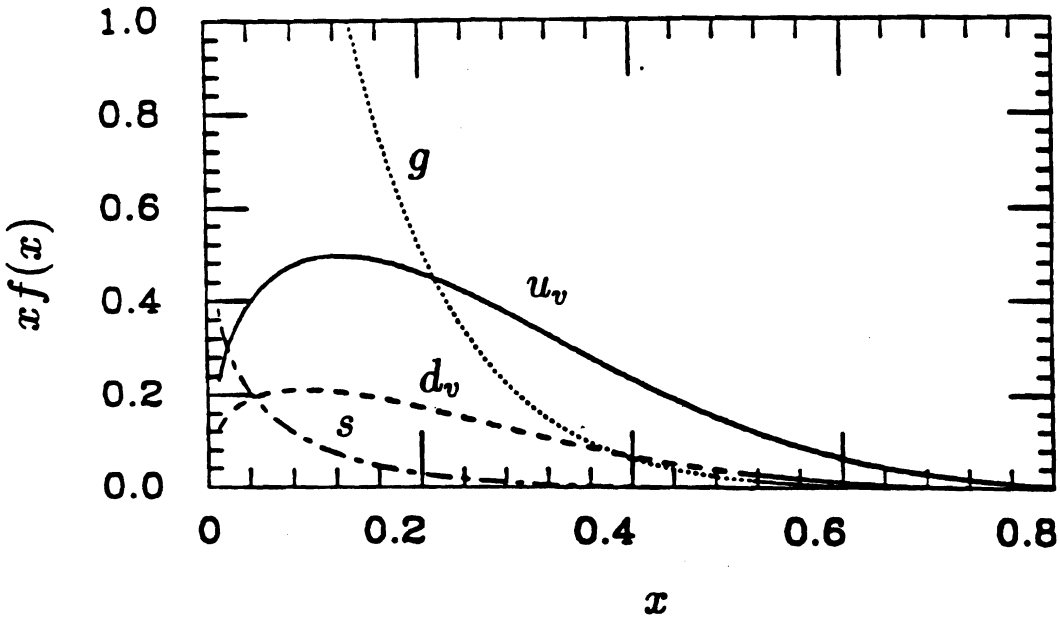

Figure 2.3: *The distribution functions, $f(x)$, represent the probability of finding a quark with momentum fraction $x = p/P_{proton}$ between x and $x + dx$. The distribution functions are shown for the up, down and sea quarks with the gluon. For this plot, EHLQ1 structure functions were used.*

derivative D is defined to maintain local gauge invariance.

$$D^{\mu}_{jk} = \delta_{jk}\partial^{\mu} + ig(T_a)_{jk}G^{\mu}_a \tag{2.3}$$

where G^{μ}_a are the gluon fields, T_a are the SU(3) generators, and g is the strong coupling. M_{jk} is the quark mass matrix. The gluon field tensor is

$$F^{\mu\nu}_a = \partial^{\mu}G^{\nu}_a - \partial^{\nu}G^{\mu}_a - gf_{abc}G^{\mu}_b G^{\nu}_c \tag{2.4}$$

where f_{abc} are the constants defined by the commutation of the SU(3) generators. The SU(3) commutation relation is:

$$[T_a, T_b] = if_{abc}T_c \tag{2.5}$$

The Lagrangian contains quark-gluon and gluon-gluon self interactions. The diagrams in Figure 2.1 contain such interactions. At first order, all the diagrams are tree level, and the calculation of the cross sections is straight forward. For the process $\hat{\sigma}(ab \longrightarrow cd)$, it is customary to define the Mandelstaam variables:[2, 3]

$$\hat{s} = (p_a + p_b)^2 \tag{2.6}$$

$$\hat{t} = (p_a - p_c)^2 \tag{2.7}$$

$$\hat{u} = (p_a - p_d)^2 \tag{2.8}$$

where the four vector of each particle is denoted by p_{μ}. Then the cross section is:

$$d\hat{\sigma}/d\hat{t}(ab \longrightarrow cd) = |M|^2/(16\pi\hat{s}^2). \tag{2.9}$$

Table 2.1 lists all the matrix elements, $|M|^2$ for the first order heavy quark and gluon production processes.[2]

parton subprocess	$\lvert M\rvert^2/g_s^4$
$q\bar{q} \longrightarrow Q\bar{Q}$	$\frac{4}{9}\frac{\hat{t}^2+\hat{u}^2}{\hat{s}^2}$
$gg \longrightarrow Q\bar{Q}$	$\frac{1}{6}\frac{\hat{u}^2+\hat{t}^2}{\hat{u}\hat{t}} - \frac{3}{8}\frac{\hat{u}^2+\hat{t}^2}{\hat{s}^2}$
$q\bar{q} \longrightarrow gg$	$\frac{32}{27}\frac{\hat{u}^2+\hat{t}^2}{\hat{u}\hat{t}} - \frac{8}{3}\frac{\hat{u}^2+\hat{t}^2}{\hat{s}^2}$
$gg \longrightarrow gg$	$\frac{9}{4}(\frac{\hat{s}^2+\hat{u}^2}{\hat{t}^2} + \frac{\hat{s}^2+\hat{t}^2}{\hat{u}^2} + \frac{\hat{u}^2+\hat{t}^2}{\hat{s}^2} + 3)$
$qg \longrightarrow qg$	$\frac{\hat{s}^2+\hat{u}^2}{\hat{t}^2} - \frac{4}{9}\frac{\hat{s}^2+\hat{u}^2}{\hat{u}\hat{s}}$

Table 2.1: *Lowest order heavy quark production matrix elements.*

2.2 Extension of QCD cross sections to next-to-leading order

There are two complications which must be handled carefully when extending the leading order calculation to higher orders. First, one must adopt a regularization procedure that renormalizes any integrals that are infinite. To first order, the $1/\hat{u}$ and $1/\hat{t}$ terms are infinite only when the final state has no observable p_t. Since these limits are not observable, the calculation can be cut off to eliminate these regions of phase space without affecting the observed cross section. At the next order, the divergences occur when the energy of the emitted gluons is zero or the opening angle of a vertex in the event is zero. With three final state partons, the first two can be produced with observable rapidity and momentum at the same time that gluons with diverging probability are produced. Thus, for three final state partons, the divergences affect the cross section for observable events.

Divergences from soft radiation, when properly regulated cancel between real and virtual graphs. Collinear divergences must be factorized later. A fractional space-time dimension ($D = 4 - 2\epsilon$) is introduced to express the matrix element as a finite quantity. The matrix element is then expanded into a series which is valid for small ϵ and the series is terminated at $O(\epsilon)$.

The second complication to a NLO theory is in defining which partons are part of the proton and which are the result of hard interactions. Perhaps a better question is: exactly what distinguishes a hard scattering from the proton internal interactions? There are two schemes which are appropriate to next-to-leading order calculations, DIS and $\bar{MS}$. Both of these distribute the radiative corrections between the structure functions and parton cross section in a consistent way. Although the two schemes are not interchangeable, conversions from one to the other exist. In this analysis, the $\bar{MS}$ scheme was used. Next-to-leading order structure function definitions lead to "scheme" dependent definitions of α_s, and $\hat{\sigma}$. Specifically, α_s becomes a function of μ^2 where μ is a scale factor on order of the energy exchanged in the interaction. Since $\hat{u}, \hat{t}$, and $\hat{s}$ diagrams contribute to a single cross section, the definition of μ is not exact, but the calculation is expected to remain constant over a large range of μ values.

There are two main sources for the NLO calculations. Nason, Dawson, and Ellis (NDE) have published the single particle inclusive cross section and differential cross sections with respect to momentum and rapidity for heavy quark production.[4] Mangano, Nason, and Ridolfi (MNR) realized the need for fully

differential cross sections and have made a computer code available to the CDF collaboration which calculates these.[5] The first is sufficient to compare to inclusive bottom cross section measurements. The second allows for the study of correlations between the three final state partons.

2.3 Status of bottom quark cross sections

The inclusive cross section for bottom quark production at central rapidities has been measured and compared to the NDE theory. Figure 2.4 shows the comparison of all CDF measurements, ($\sqrt{s}$ = 1.8 TeV) , with the NDE prediction.[6] Clearly the measured points lie above the theoretical band. Note that the measured cross section at UA1, shown in Figure 2.5 where the center of mass collisional energy is smaller ($\sqrt{s}$ = 0.63 TeV) agrees well with the theoretical prediction.[7] The publication of the CDF measurements has caused doubts about the NLO calculation. Ellis claims that the NLO theory is flawed.[6] The NLO calculation turns out to be a strong function of μ, the scale factor. The dependence of the cross section on μ is a large part of the uncertainty in the theoretical prediction. However, the μ scale dependence is a symptom, not the real effect. The reason for the discrepancy is due to the fact that $\sqrt{s} >> m >> \Lambda$ at CDF. In this particular limit, the perturbation series is no longer an expansion in α_s, but rather $\alpha_s ln(s/m^2)$ and therefore does not converge. As yet, an improved theory in this particular kinematic region has not been worked out.

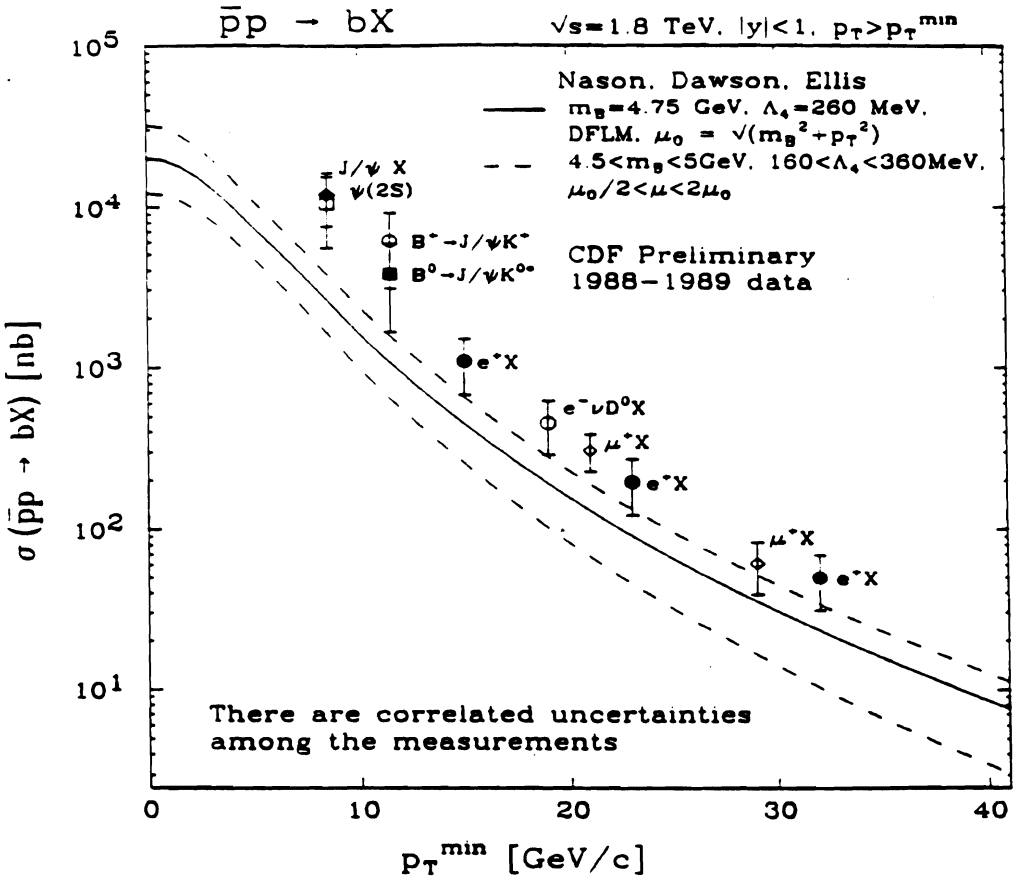

Figure 2.4: *The b quark production cross sections measured using electrons as well as other CDF measurements and the QCD prediction by NDE.*

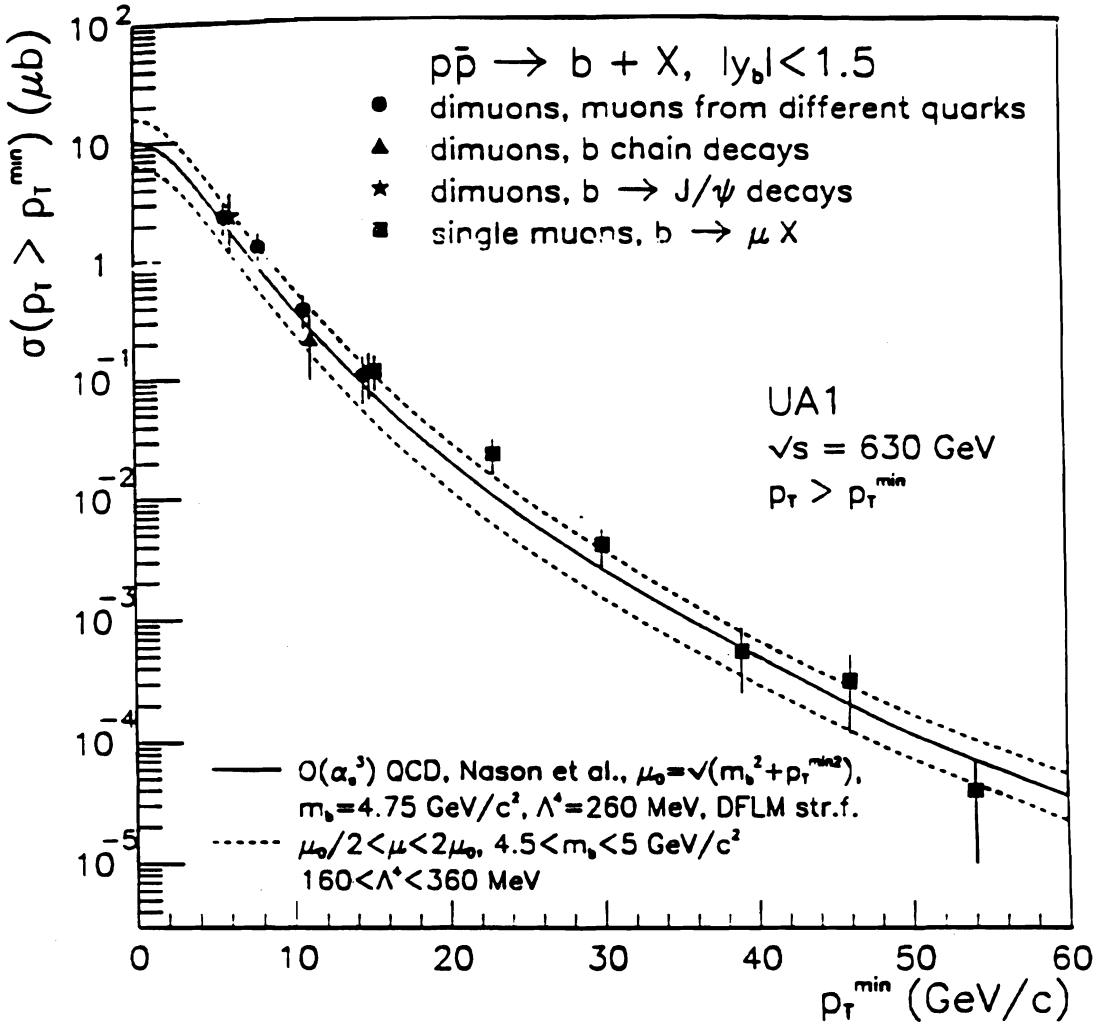

Figure 2.5: *The b quark production cross sections measured at UA1 with the QCD prediction by NDE.*

There are other possible explanations that are being investigated to account for the discrepancy. Since the gluon distribution was measured at lower energies and extrapolated to CDF energies, it is possible to modify the shape of this distribution while maintaining consistency with available measurements of structure functions in such a way that it increases the predicted cross section at CDF.[8] While this may account for part of the discrepancy, it has already been shown that the structure function cannot be modified enough to account for all of it.

Finally, all the measurements at CDF are correlated. The Peterson fragmentation model is used to evolve the bottom quark into a bottom meson with the appropriate momentum spectrum. This model has a free parameter which was measured by CLEO [9] and is used in all the CDF measurements. If there are any uncertainties in this model, they feed into all the measurements identically. So, there could conceivably be a shift in all the CDF bottom quark cross section measurements due to the dependence on a single fragmentation model.

2.4 Motivation for the measurement of direct bottom at forward η

The forward muon bottom tag is unique in that it will give information about the η dependence of the cross section. Theory predicts that the cross section drops off at high η, but the exact shape of this drop has not been measured. The magnitude of the drop off is related to the mix of LO and NLO diagrams. Hence,

the forward region is of particular interest.

Another feature of the forward measurement is that it specifically requires jets in the events and therefore the correlations between different partons can be compared. In particular, the mix of diagrams that look topologically more or less like LO and those that are NLO may be compared. Since the LO calculation with small radiated gluons is far more stable with respect to the μ scale, it is possible to see whether the discrepancy between theory and measurement persists without the calculational source of uncertainty from the perturbation theory.

Chapter 3

Forward Muon Measurement

The Collider Detector at Fermilab (CDF) is designed to measure the momentum and energy of electrons, photons, muons, hadrons and jets. The forward muon (FMU) detector is one component of the CDF detector. In this chapter, I will describe the experimental facilities at Fermilab, and the detector components used in the identification and momentum measurement of forward muons. In addition, I will present the FMU detector efficiency, resolution, luminosity, and trigger efficiency which defines the quantity and quality of observed muons.

3.1 Overview of the experimental facilities and the Collider Detector at Fermilab(CDF)

The accelerator at Fermilab consists of several stages of particle acceleration to reach the final collision energy of 900 GeV in each beam. Figure 3.1 shows the general layout of the accelerator. First, H^- ions are produced in a Cockroft-Walton Generator. The ions are injected into a linear accelerator where they reach an energy of .5 GeV. In a booster ring the electrons are stripped off the ions which become bare protons and are then accelerated to 8 GeV. Next the protons are injected into the Fermilab Main Ring which is a proton synchrotron with radius 1 Km. Here they are accelerated to 150 GeV. To obtain proton-antiproton collisions, the first protons are used to make antiprotons. Antiprotons are created when protons from the main ring are smashed into a tungsten target. The antiprotons are stored and stochastically cooled in an accumulator ring until there is a stack of sufficient size to make a high luminosity beam. Then six bunches of protons and another six bunches of antiprotons are injected into the Tevatron where they are accelerated in opposite directions to 900 GeV. As viewed from an airplane, the protons travel clockwise around they ring, and the antiprotons travel counterclockwise. The bunches meet each other 6 times as they travel once around the Tevatron.

The Collider Detector at Fermilab (CDF) resides at B0, which is one of the six points where the Tevatron Beams collide. It uses a combination of tracking

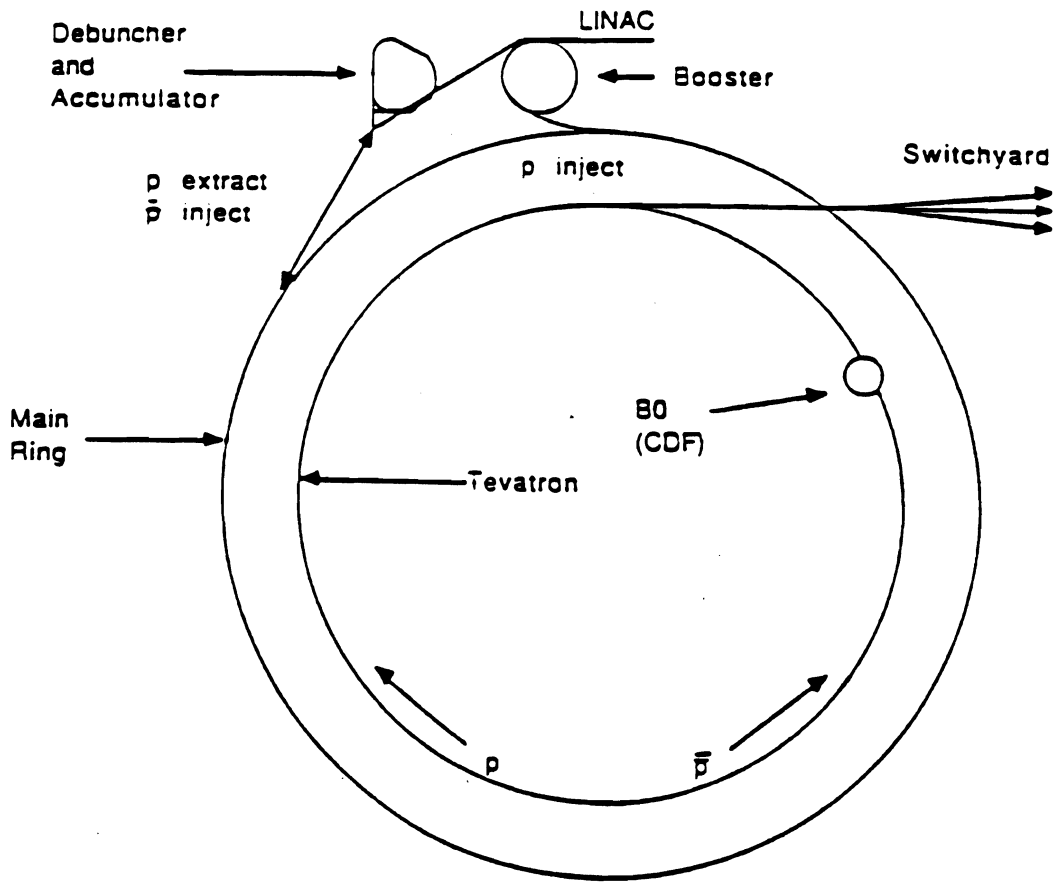

Figure 3.1: *Overhead view of the Fermilab accelerator complex.*

chambers and calorimeters to measure the momentum and energy of particles created in proton-antiproton collisions. It is designed to give the four-momenta of all possible leptons and jets, which are the general features of high energy events. Figure 3.2 shows the layout of the detector. It has a cylindrical symmetry surrounding the Tevatron beam pipe. Coordinates for the collider are defined such that the Z axis is aligned along the proton direction at the interaction point. The X axis points away from the center of the Tevatron Ring, which leaves the Y axis pointing up out of the ground. X_0, Y_0, Z_0 is defined to be the center point of the detector. This convention will hence forth be referred to as CDF coordinates. In the central region the detectors are layered like an onion, with the Vertex Detector adjacent to the beam pipe followed by the Central Tracking Chamber. The 1.5 Tesla superconducting solenoidal magnet surrounds this to provide the bend of charged particle tracks necessary for the momentum measurement. Next, an electromagnetic (EM) calorimeter and a hadronic (HAD) calorimeter measure the electron and jet energies. Finally, muon chambers are mounted on the exterior of the detector.

In the forward region, from about $\theta < 30°$, the endcaps of the solenoid are layered away from the vertex with the Plug Calorimeters (EM and then HAD). For the far forward region which is not covered by the Plug Calorimeters, the Forward Calorimeters are used. Finally, behind this resides the Forward Muon Detector (FMU).

The detector components used in this analysis are the Forward Muon Detec-

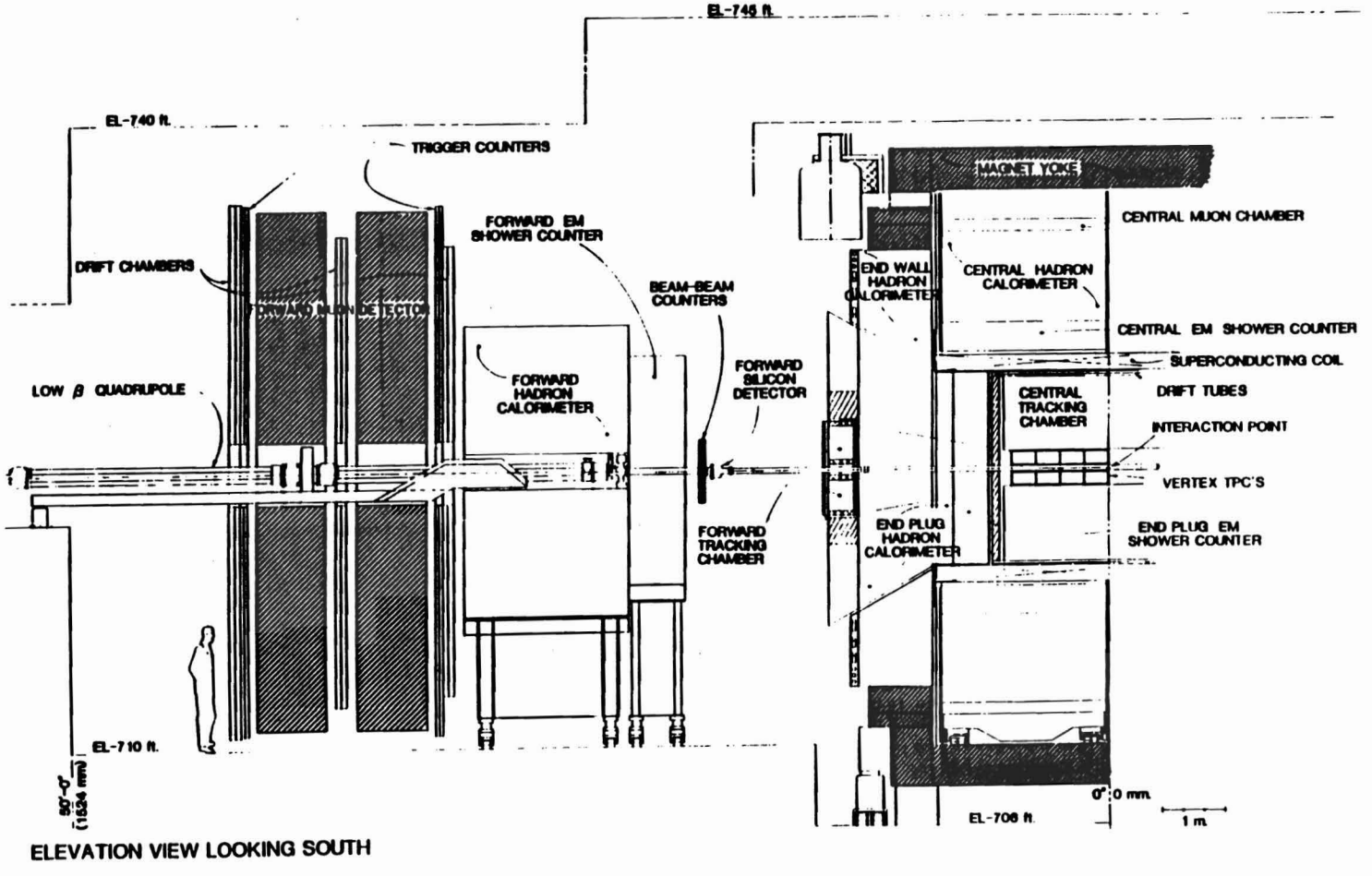

Figure 3.2: *Side view of the CDF detector.*

tor, the Central, Plug and Forward Calorimeters, and the Vertex Detector. These devices provide us with enough information in each event to measure the vertex, forward muon momenta, and jet energies. The rest of this chapter details the measurement of muons in the forward detector. The next chapter describes the measurement of jets.

3.2 Forward Muon Detector components

The Forward Muon (FMU) Detector is a muon spectrometer in the small angle region at CDF as shown in the cutaway schematic of Figure 3.3. At each end of CDF there are a set of toroidal magnets (1.6 to 2.0 Tesla field strength) with planes of drift chambers in front, between, and behind. In the front and rear planes a scintillator plane is sandwiched between the drift chamber and the toroid. Each plane consists of 24 chamber wedges as shown in Figure 3.4. The scintillator chambers were abutted into position whereas the drift chambers were mounted so they overlapped. Thus, the active volume of the scintillators contained small gaps near the wedge boundaries whereas the drift chambers had no gaps. The specific design parameters for the chambers as well as the survey procedure may be found elsewhere. [10, 11] Instead of concentrating on previously documented dimensions and construction materials, I will describe the general detector design schematically. With this approach it is easier to understand the diagnostic checks for the system which were used during the run and later offline with data.

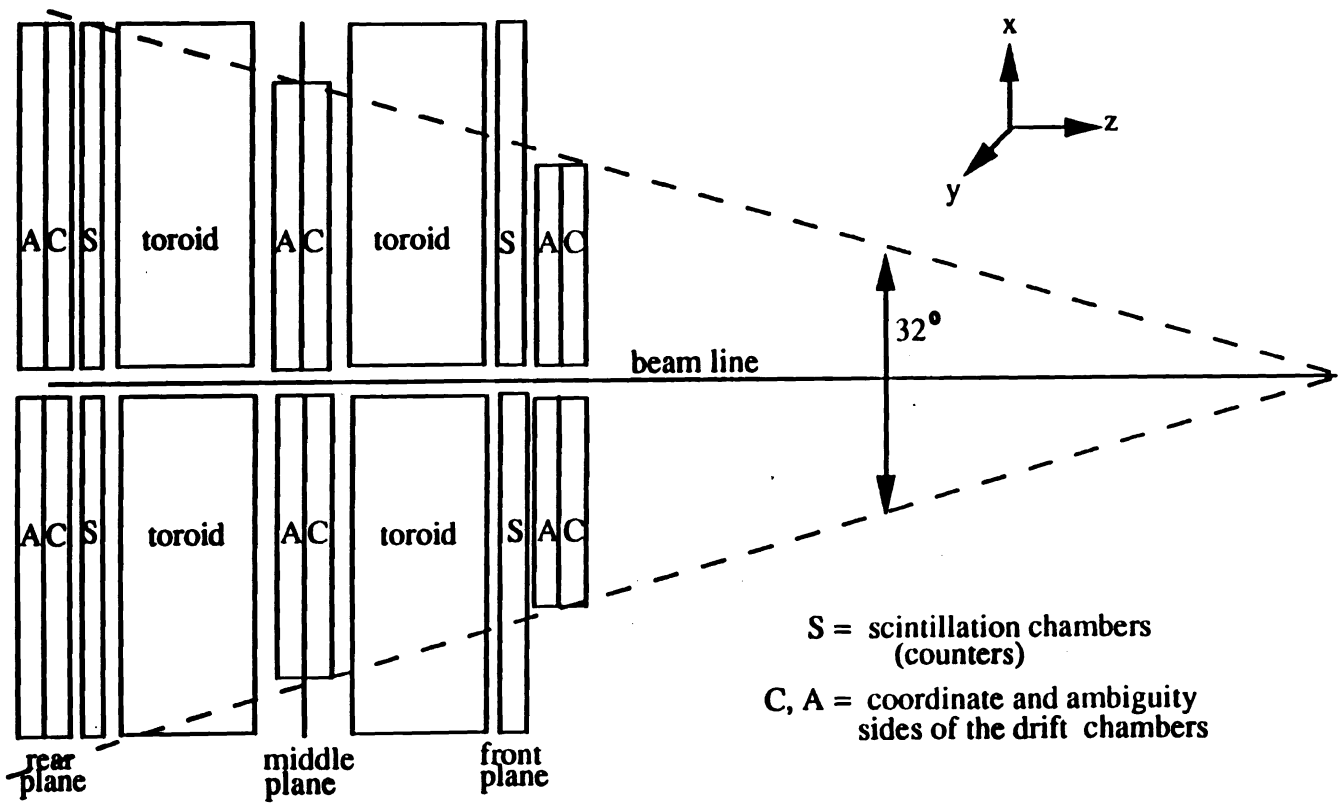

Figure 3.3: *Side view of the Forward Muon Detector. The detector is symmetric about the vertex.*

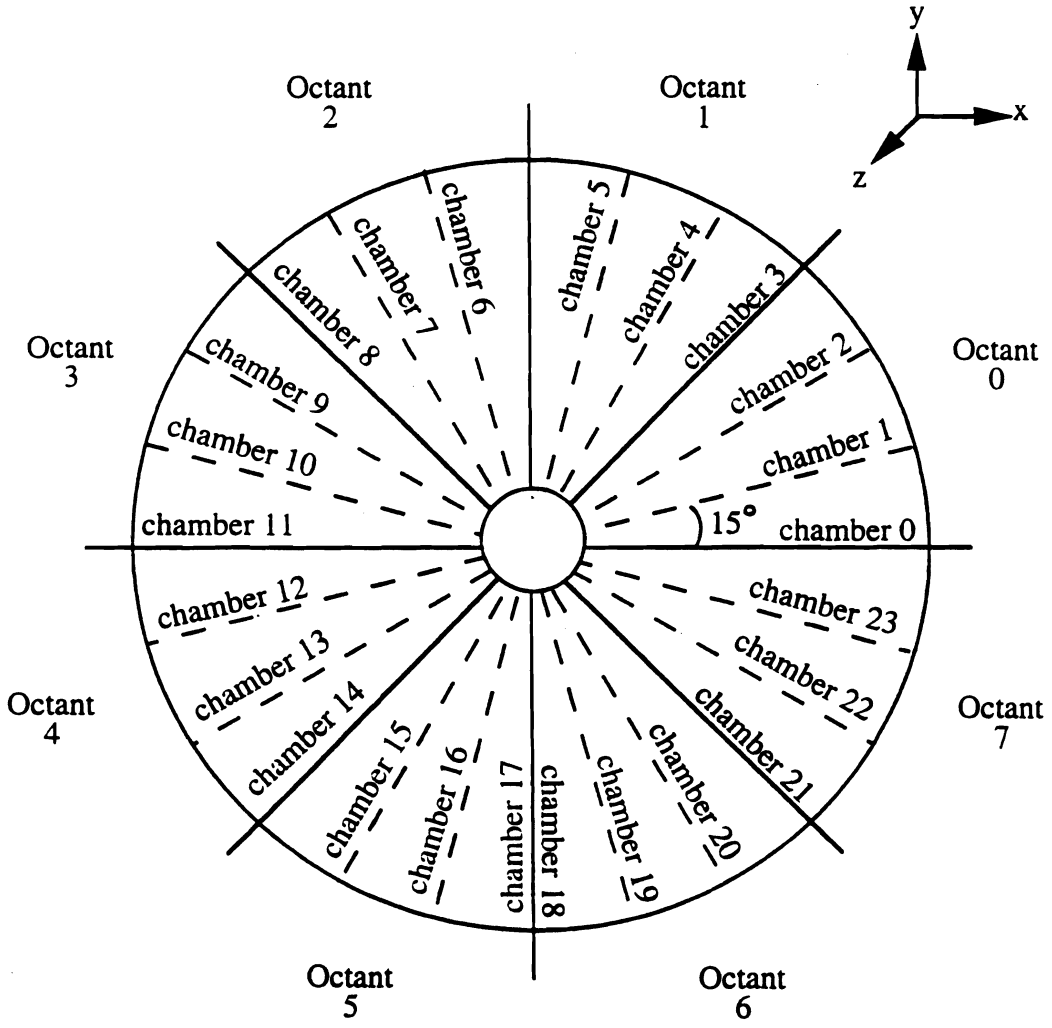

Figure 3.4: ***Each plane consists of 24 chambers each of which spans 15° in azimuth.***

As mentioned, there were two chamber types, scintillator and drift. The important features of these are pictured in Figure 3.5. The drift chamber contains a coordinate plane of 56 wire cells and an ambiguity plane of 40 wire cells. For angles greater than 7°, the coordinate and ambiguity wires are half cell staggered to resolve the left right ambiguity. The wires and pads are arranged to form projective towers. The cell size increases with radius such that tracks contained within a projective wire tower correspond to a constant p_t threshold. The wires were held at high voltage and the pads formed the ground plane between the two sides. Figure 3.6 shows a schematic of the readout system. The pulse height (volts) on each wire was amplified on the chamber with a preamplifier. Since the number of time to digital convertor (TDC) channels was limited, the signals from corresponding wires on the three chambers in each octant were OR'ed together at the input to the amplifier/discriminator board. If the pulse height of any chamber wire in the octant was over threshold, then a square pulse was sent through 200 feet of cable to the TDCs in the counting room where they were read out through Fastbus. The TDCs recorded chamber hits for a full octant. The pad signals were also amplified on the chamber before being sent through 50 feet of cable to the Rabbit Cards. The Rabbit Cards measure integrated current, or charge. Any signal above the pedestal value of 200 ADC counts was read out through a Fermilab multiplexer module (MX) into Fastbus. The pad data are used during track reconstruction to provide the azimuth of the track to within 5°. The scintillator segmentation is 15° in azimuth. Each scintillator is observed by

four phototubes, whose outputs are OR'd together to improve the light detection efficiency.

Diagnostics for many parts of the system were included in the design. On each scintillator was mounted an LED which could be pulsed through Fastbus and read out through the normal data path. In addition, by turning off the voltage to all of the phototubes except one in a chamber, each phototube could be tested individually, thus fully verifying its operation. The diagnostic for the wire chamber consisted of a wire which ran the length of the chamber and coupled capacitively to the sense wires in the chamber. When the long wire was pulsed, the signals would follow the normal data path and be recorded in the TDCs. To check that the chamber gain was high enough, Fe55 sources were mounted in four chambers in each plane. Each chamber contained a variety of cell sizes, each necessitating a different voltage. One cell of each size was monitored with the Fe55 source. The gas-gain system used the signal from the Fe55 source to diagnose overall gain problems.

The FMU trigger used the projective tower geometry of the drift chambers to search for patterns of wire hits likely to be high p_t tracks. The front chambers were smaller than the middle chambers which were smaller than the rear chambers. In principle, a straight line connecting the same cell number in all three chambers also included the vertex. The actual chamber positions during data taking were not perfectly placed in Z and therefore only approximated the ideal configuration. Tracks that emanated from the event vertex and traversed

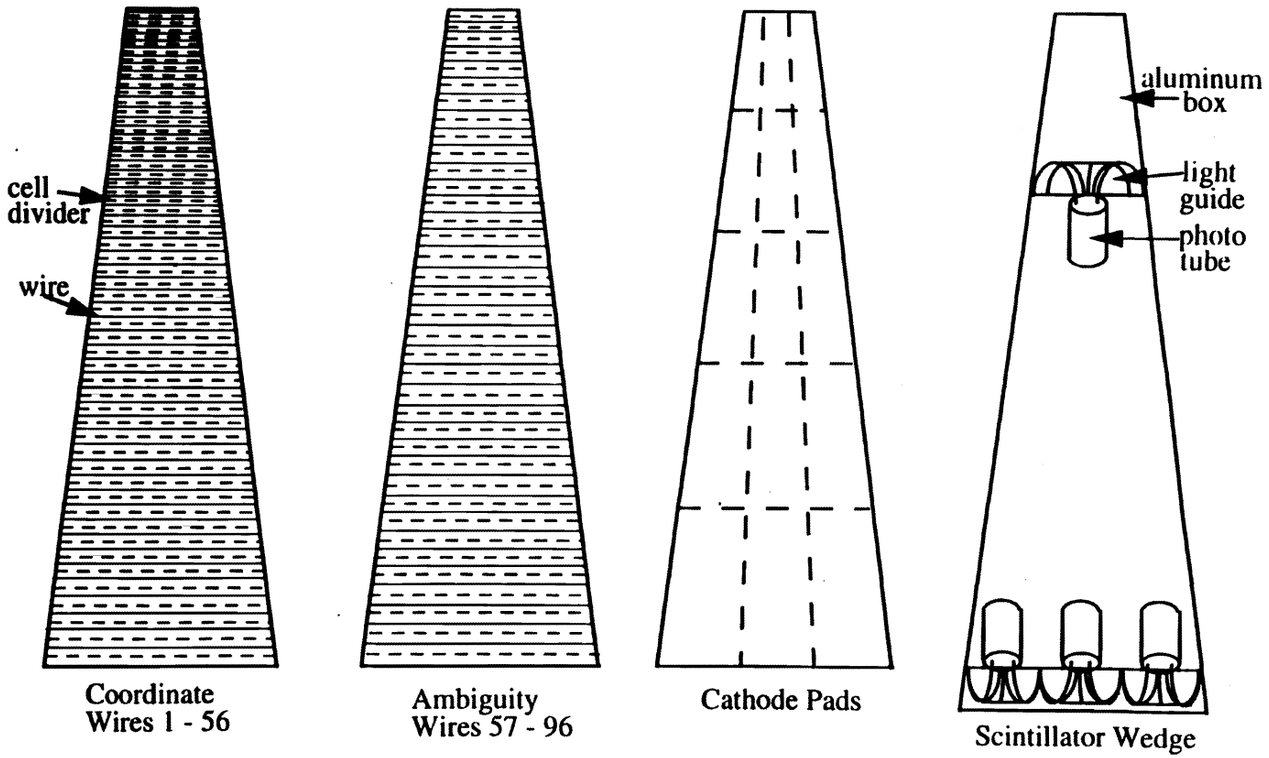

Figure 3.5: *Schematic of the various chamber parts in the forward muon detector.*

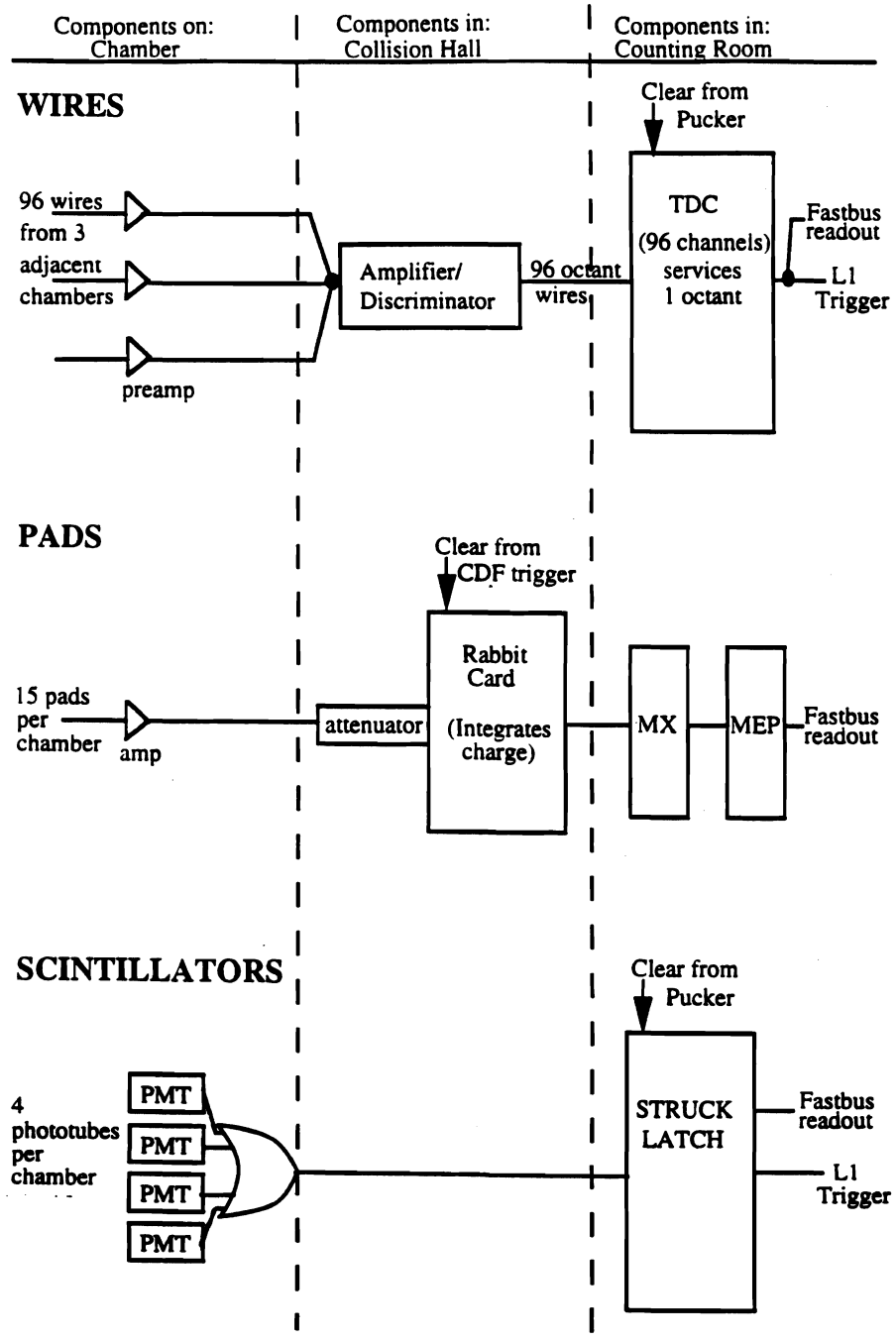

Figure 3.6: *Schematic of the forward muon detector readout electronics.*

all three chamber planes without deviating by more than a chamber cell were deemed to have large p_t. The wire hits were sent to the trigger boards through the TDC auxiliary fastbus connector which is located on the back plane of the Fastbus crate. Although test programs were written to test the different modules in the trigger itself, the back plane jumpers between the TDCs and the trigger boards were not tested after they were installed. A sample of these jumpers were tested in place after the run and found to contain $(2.9 \pm 1.1)\%$ broken connections which accounts for the Level 1 trigger electronics efficiency. The trigger resided in the counting room Fastbus crates which made it easy to set trigger inputs and read back the expected triggers. .

A complication of analysis with the FMU trigger is that both the trigger and chamber configuration changed during the run. Two different Level 1 trigger boards were used. The first FMU trigger used Half-Octant Pattern Units or HOPU boards. Each HOPU contained the logic to analyze the wire hit information from an octant in ϕ and 7° to 16° in θ to determine whether a muon had passed one of three p_t thresholds defined by the hit pattern. The p_t threshold used to select the data was satisfied by a simple coincidence of hits in the same coordinate-wire cell number in each of the three chamber planes. In other FMU documentation, this is referred to as the 100% trigger.

The original HOPU trigger, consisting of a coincidence between 3 coordinate wires, yielded an unacceptably large rate. To solve this problem, a temporary DIHOPU trigger was installed covering the range 7° to 16°. Two HOPUs were

used for each octant wedge with one HOPU searching the coordinate plane wires and the other HOPU searching the ambiguity plane wires. A valid DIHOPU trigger required a 3-wire coincidence among coordinate hits and also a 3-wire coincidence among ambiguity hits. The two coincidences were not required to be satisfied in the same octant, however. Again, all HOPU thresholds were set at the 100% level in FMU terminology.

In the final trigger, the 3 coordinate wires were required to line up both in η and $\phi(45°)$ with the 3 ambiguity wires. This was achieved with a new trigger board that searched for a 6 wire coincidence within one octant. One New Octant Pattern Unit, called a NUPU, replaced both the coordinate and ambiguity HOPUs covering the angular range 7° to 16°. The main difference between the DIHOPU and NUPU triggers was that the latter was more efficient at selecting real muons, thus reducing the trigger rate. The NUPU p_t threshold chosen required stiffer tracks than the other thresholds available and is referred to as the 50% threshold in the FMU documentation.

The other detector change was the result of an HV accident which occurred during December 1988. Since many channels were disabled, Fermilab allowed the Wisconsin group access to remove a large fraction of the chambers with their associated electronics and fix them. The chambers and electronics were arranged differently in the system when reinstalled. Therefore, the luminosity and efficiency calculations require separate treatment for the data taking periods separated by these changes in FMU configuration.

Events passing the hardware trigger were passed to an event processor (Level 3) which ran the event reconstruction algorithm on the events. If a reconstructed muon could be found with either 5 or 6 hits, the event was written to a data tape.

3.3 Luminosity for the FMU trigger

The luminosity that CDF was able to write to tape during the 88/89 run was $(4.4 \pm .32)$ pb^{-1}. The CDF luminosity on the data tapes used in this analysis was $(3.63 \pm .25)$ pb^{-1} which is lower because some tapes were unreadable and there was a period where the FMU voltage was turned off around the time of the Christmas repair.[12, 13, 14] These numbers have been calculated tape by tape and reflect multiple interaction corrections. The FMU trigger was limited to a constant rate of .1 Hz, therefore any trigger which came in closer than 10 seconds after the previous accepted trigger was automatically rejected. Since trigger rates scaled with the luminosity delivered by the accelerator, each run had a characteristic rate and the amount rejected due to the rate limit varied. For each data taking run, the CDF shift crew recorded trigger statistics with a monitor program called LUMMON. The monitor summaries included the Level 1 cross section before and after the rate limit. The ratio of these numbers is the average FMU prescale. The FMU luminosity is calculated by multiplying the CDF luminosity by the FMU trigger prescale factor on a run by run basis. The

RUNS	TRIG	CDFLUM(nb^{-1})	FMULUM(nb^{-1})
R15880-R16566	HOPU	102.1 ± 6.9	4.9 ± 1.9
R16567-R18199	DIHOPU	1345.2 ± 91.5	668.4 ± 63.2
Christmas Repair			
R18685-R18847	DIHOPU	139.0 ± 9.5	92.1 ± 6.7
R18848-End	NUPU	2047.1 ± 139.2	1037.1 ± 70.7
Total		3633.4 ± 247.1	1802.5 ± 142.5

Table 3.1: *FMU trigger configurations and associated luminosity for the 1988/89 CDF run.*

FMU effective luminosity corresponding to 3.63 pb^{-1} corrected for deadtime in the 88/89 run is $(1.80 \pm .14)$ pb^{-1}. The error bar includes a 6.8% uncertainty in the CDF luminosity, statistical errors from the Level 1 and Level 2 trigger scaler values recorded in the LUMMON end of run summaries, and 5% uncertainty in the rates assigned to a small number of runs missing LUMMON summaries. As mentioned before, there were changes in the FMU configuration which require separate treatment. Table 3.1 lists the luminosity for CDF and the FMU trigger for time segments corresponding to different trigger conditions.

3.4 Forward Muon Detector efficiency

The overall efficiency may be divided into two parts. The design efficiency for the FMU system was very high. The actual efficiency, including occasional hardware failures, was somewhat lower. In general it can be shown that the system performed at the design efficiency and that a small fraction of component failures account for the degradation of this to the measured efficiency.

The gas gain system used Fe55 sources to monitor the gain of the chambers. The signals from the Fe55 sources were read out through an emitter follower attached to an alternative output on the preamplifier. As these signals were produced on the chamber and monitored 200 feet away, a significant amount of attenuation occurred in the cable. The chamber HV was adjusted so as to maintain an Fe55 pulse height of (200 ± 85) mV at the monitoring station, corresponding to 460 mV to 1140 mV as measured at the chamber output. For comparison, a test setup was used to measure the chamber efficiency as a function of the size of the source signals. Figure 3.7 shows how the chamber efficiency depends on the source signals. From this I conclude that the gas gain was high enough to collect data with $(99.6 \pm .5)\%$ efficiency, for channels in good working order. [13, 15]

Component failures consisted of broken electronic channels which affected either a single chamber wire or the set of three chamber wires which were read out together in a single TDC channel. These were estimated with the ratio of 5 hit to 6 hit tracks in the system. Since the chamber efficiency of the gas was

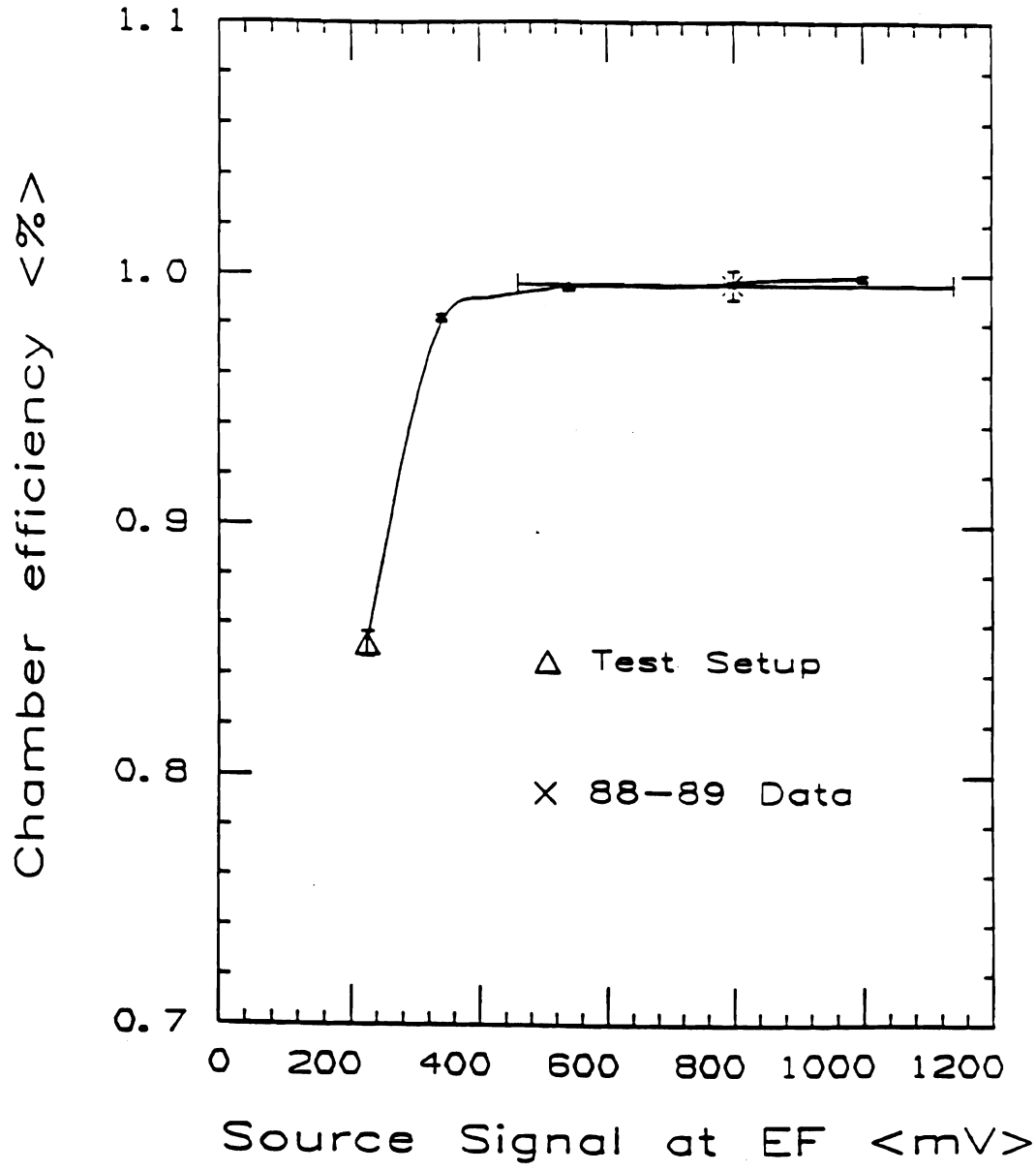

Figure 3.7: ***Efficiency as a function of gain for the FMU drift chambers.***

shown to be excellent, the missing hits in the 5 hit tracks were assumed to be broken readout channels or wires in the chambers. Correlated failures, which take out 2 or more hits on a track, were not accounted for with this technique. Failures of groups of wires in both the coordinate and ambiguity plane occurred due to broken HV connections, gas impurities (due to leaks in the wire chambers) or problems with the power for preamps. A similar effect occasionally resulted from TDCs which were temporarily disabled to mask "hot" trigger octants. These failures were identified by occupancy observations, and were tabulated run by run to account for inefficiencies. The detector efficiency has contributions from the six hit chamber efficiency, $\epsilon_{ce}(6)$, the group failures, ϵ_{group}, and single non-functioning wire chambers, ϵ_{sc}.

$$\epsilon_{6\ \mathrm{hit}} = \epsilon_{ce}(6) \times \epsilon_{group} \times \epsilon_{sc}. \tag{3.1}$$

The product of these efficiencies is calculated separately for the west, $\eta < 0$, and east, $\eta > 0$, ends of the detector. The efficiency of finding 6 hit tracks as described in appendix A is $(.570 \pm .028)$ on the west and $(.452 \pm .023)$ on the east. The average over east and west is $(.511 \pm .026)$. These efficiencies include all types of component failure.

3.5 Forward muon momentum resolution

A detailed description of the tracking algorithm may be found elsewhere.[10, 16] A least squares fit was performed using the vertex and 3 hit positions at each

chamber plane. First a simple parabolic fit was made. Using the parameters found in the parabolic fit as an input, the more complicated fit including multiple scattering and chamber resolution was performed iteratively. The square root of the diagonal covariance matrix elements for least squares fits are the uncertainties of the fitted parameters.

The momentum resolution of the FMU system has three components. First, there is a momentum uncertainty due to the fact that muons scatter in the forward calorimeters and the toroids, thus hits are distributed about the ideal track direction. This contribution is described by random walk statistics.[10] Since high momentum tracks are scattered less than low momentum tracks, this contribution is momentum independent, namely

$$\Delta P/P = .166 \pm .004. \tag{3.2}$$

The second contribution comes from the chamber resolution. When the electrons shower in the gas to make a hit on the wire, there is an intrinsic resolution to the pulse and readout electronics. The resolution of the hit positions was measured in the data using the distance between coordinate and ambiguity hit positions, corrected for the slope of the track. These distributions are shown in Figures 3.8 and 3.9 for FMU + jet and Z events. The resolution of the chamber is related to this distribution by

$$\sigma_{ch} = \frac{\sigma_{R_c - R_a}}{\sqrt{2}}. \tag{3.3}$$

The resolution was therefore (672±61) μm in the Z events and (631±15) μm in the

FMU + jet events. Since the momentum resolution does not depend critically on the exact value of the position resolution and there could be systematic differences between different data samples, a round number of 650 μm was used. A test setup was used to study the chamber resolution and it was found that the chambers by themselves have (450±50) μm resolution. The difference between this number and the resolution measured in the CDF data has been accounted for by chamber to chamber variations in wire spacing, t_0, drift velocity and gain variations coupled with gain dependent time slewing in the amp/disc cards.[13] Simulated tracks with hits smeared by a gaussian of width 650 μm were found to have a momentum resolution of

$$\Delta P/P = (.0015 \pm .0003) \times P \tag{3.4}$$

The third contribution comes from uncertainties in the chamber positions from the survey. [13] Table 3.2 lists the contribution from each of these sources and in closed form, the momentum resolution is given by:

$$\Delta P/P = \sqrt{(.166)^2 + (.0019P/\text{ GeV})^2}. \tag{3.5}$$

3.6 Forward muon direction resolution

Since this analysis involves the direction of the muon relative to the direction of nearby jets, the direction resolution of both the muon and the jet affect the shape

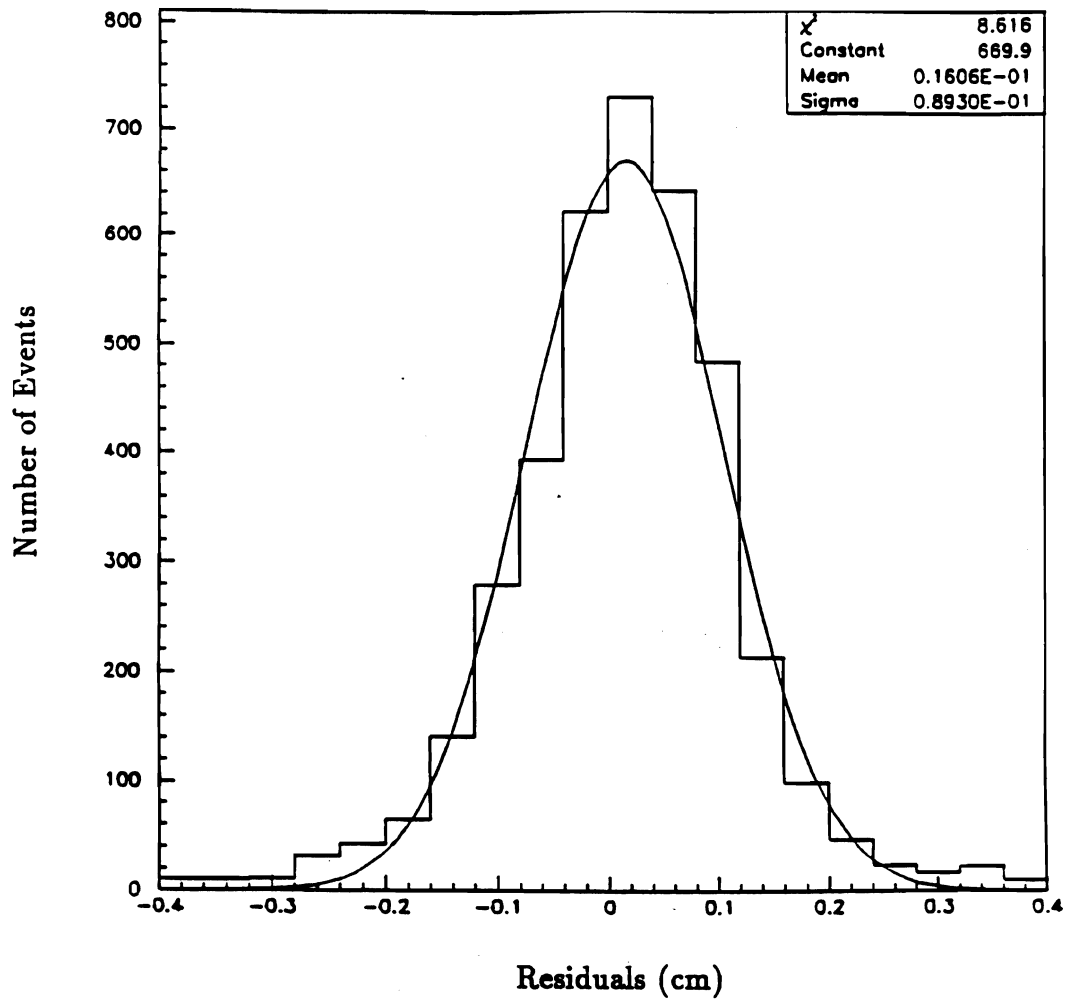

Figure 3.8: ***Residuals for FMU + Jet with Jet $E_t > 10$ GeV. For each hit on a track, the residual is the radial distance from the measured hit to the fitted track position.***

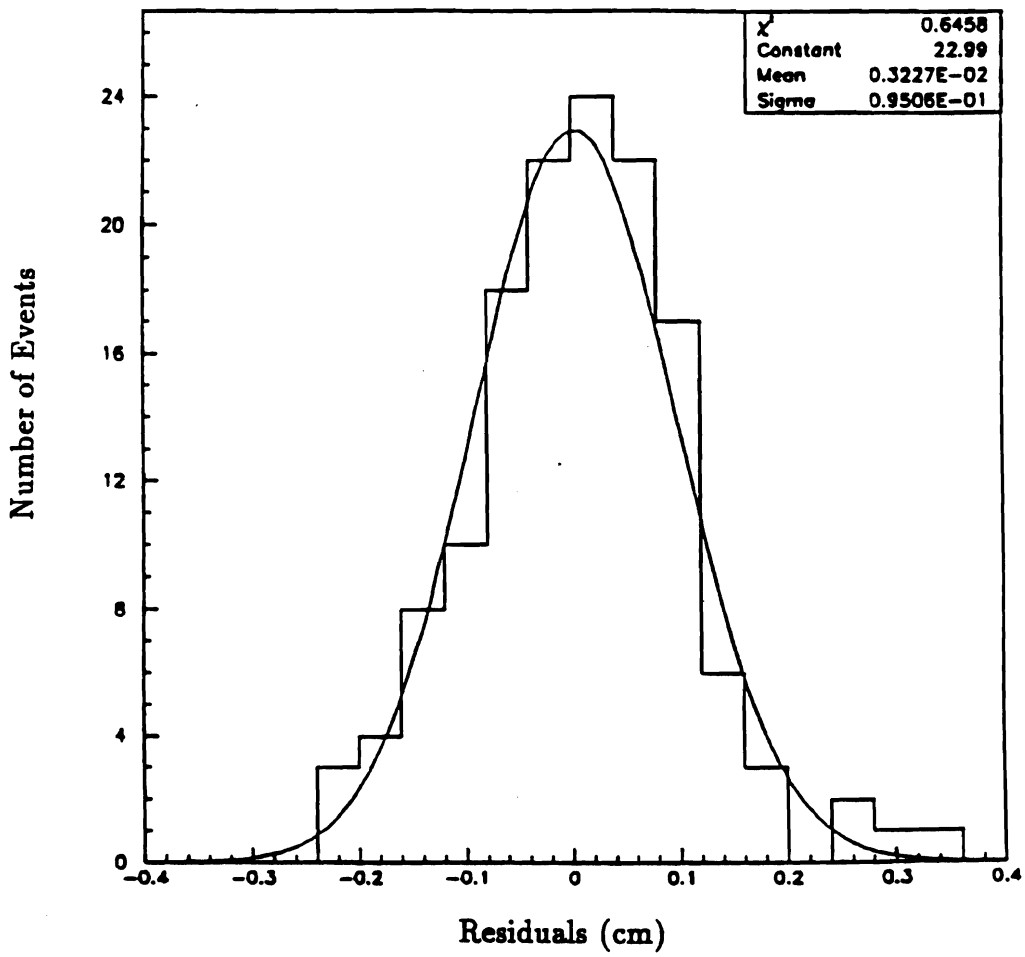

Figure 3.9: *Residuals for Z_0 candidates.*

Momentum Resolution Factors	$\Delta P/P$
Multiple Scattering	$.166 \pm .004$
Chamber Resolution (650 microns)	$(.0015 \pm .0003) \times P$
Survey Uncertainties	$(.0012 \pm .0003) \times P$

Table 3.2: *Sources contributing to the momentum resolution.*

of distributions used in the measurement. The track θ is determined from the fit of the track to the hits. Figure 3.10 shows the uncertainty in theta, $\sigma_\mu(\theta)$, for the events in my data sample. The uncertainty in theta is just the square root of the covariance matrix element determined by the fit for theta. The mean of the distribution is $\sigma_\mu(\theta) = .4154°$.

The azimuth of forward muons was determined within the 5° segmentation of the cathode pads by finding a sequence of pad hits (front, middle, rear) consistent in both ϕ and η with the passage of a muon through the detector. Since muons can multiple scatter several centimeters in the toroids, the allowed coincidence patterns included those with hits in neighboring 5° wedges, but the ϕ of the first pad was used for the muon azimuth. Pad hits could be lost due to the inefficiency of the electronics and extra pad hits were observed accompanying delta rays and also from electronic noise. When a pad coincidence was not found, a scintillator coincidence was used to determine the azimuth to within a 15° range. In the absence of either a scintillator or a pad coincidence the 45° segmentation of the

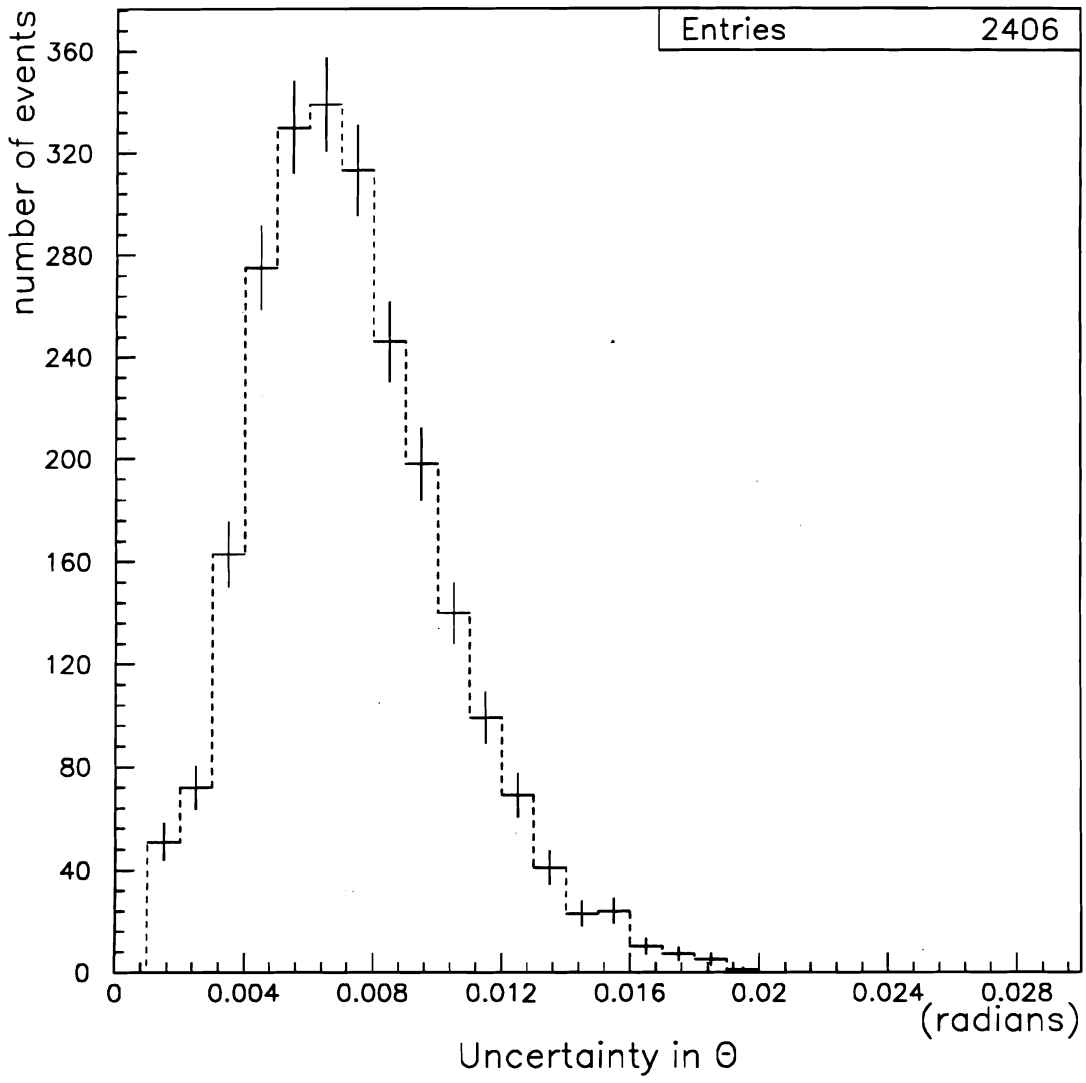

Figure 3.10: ***Uncertainty in Theta***

anode wire readout was used to determine the azimuth.

Errors in the azimuthal assignment can result from missing pad hits, from noise hits, and from multiple scattering. Figure 3.11a shows the pulse height distribution for pads which are associated with a track in the inclusive muon sample. A typical muon will show a pad pulse height signal of greater than 2000 ADC counts. Figure 3.11b shows the pulse height distribution for the tower opposite in ϕ from the track to show the background rate of a random pad contributing to a track. Since multiple scattering can bend a track from one pad to the adjacent one, it is better to compare the sum of pulse heights in the 3 pads closest to the track road. Figure 3.11c shows this pulse height distribution and Figure 3.11d shows the background from three pads which are opposite the track in ϕ. Of the tracks in Figure 3.11c, 99.7% are observed to have good pad hits in two or more planes, a good hit being defined as a pulse height of 1000 ADC counts or higher. This sets the efficiency of the pad coincidence technique for measuring ϕ.

The small number of events without a pad in two or more planes can be explained by measuring the inefficiency of the pads. All pad signals over the pedestal were histogrammed for the entire run, and it was found that $(2.62 \pm .46)\%$ of all pad channels were not operational. The probability that three pads will have two or more dead channels is $(.20 \pm .08)\%$ which accounts for the small number of events missing two or more pad signals.

The probability that the wrong pad assignment is made due to an accidental

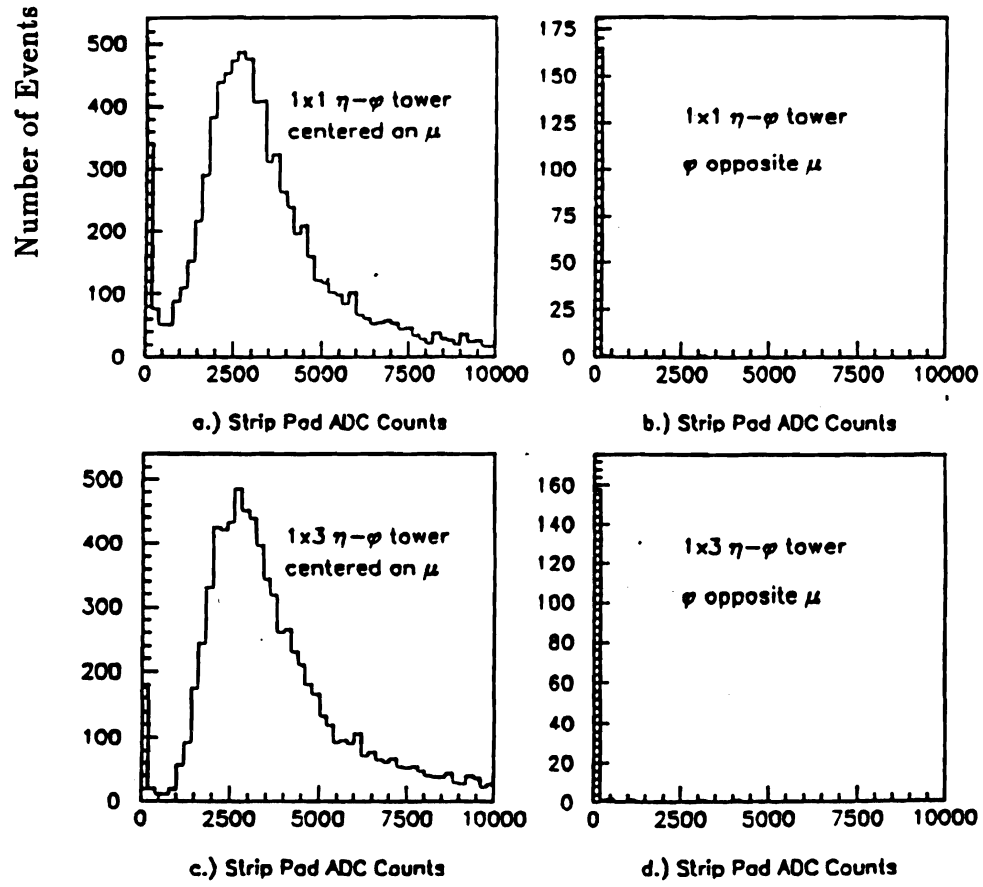

Figure 3.11: *Pad pulse height distributions. (a.)* 1×1 *tower centered on the muon. (b.)* 1×1 *tower centered on azimuth opposite the muon. (c.)* 1×3 *tower centered on the muon (d.)* 1×3 *tower centered on azimuth opposite the muon.*

pad signal is also small. The total pad occupancy per event is on the order of 1%.[17] If the proper pad hit is missing, then an adjacent pad hit may be used. The probability that this happens is two times the product of the pad inefficiency and the occupancy per event. The factor of two comes from the possibility that the pad on either side of the one missing a signal is hit. Clearly this is a small effect happening only .05% of the time..

The third source of ϕ misassignment is multiple scattering. The amount of ϕ smearing depends on the track momentum. For typical muons in the present analysis ($p_t = 8$ GeV), the smearing is about .15°. This is negligible compared to that which is intrinsic to the 5° pad segmentation, namely $5°/\sqrt{12} = 1.4°$.

3.7 Trigger acceptance and efficiency

The trigger acceptance is determined by the chamber construction and placement. First, there is a charge bias due to the opposite sign of the curvature in the toroids. The trigger road required that tracks passing through the FMU magnets remain fairly straight. Negatively charged tracks satisfied the trigger road more easily than positively charged tracks, so there was a geometric trigger bias which preferentially selected negatively charged tracks.[13] Figure 3.12 shows the trigger acceptance for positive and negative charged muons determined by Monte-Carlo simulation. This effect was the same for the NUPU and DIHOPU triggers. The efficiency was somewhat higher for the original HOPU trigger, but

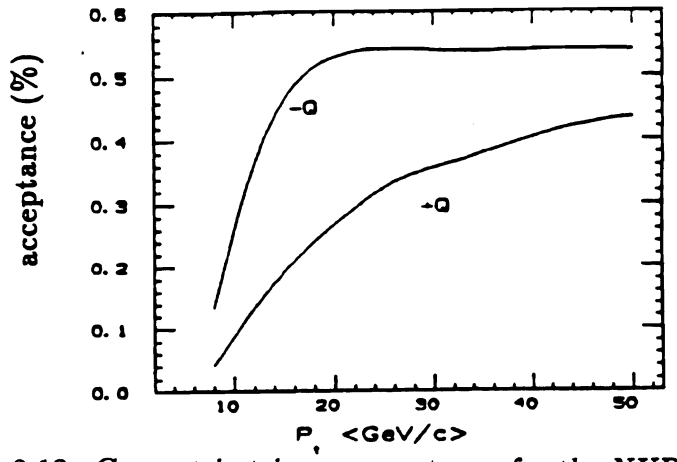

Figure 3.12: *Geometric trigger acceptance for the NUPU 50% road.*

the backgrounds for this trigger were so great that it contributes a negligible amount to the final data sample.

Second, the acceptance depends on the event vertex position. Figure 3.13 shows the vertex distribution for a sample of muons and jets. Figure 3.14 shows the vertex distribution for a simulated sample of negatively charge muons and jets with positive rapidity only. The sample was created with a gaussian vertex distribution centered on zero with a width of 30 cm. Notice that the FMU trigger preferentially accepts displaced vertices. To account for the vertex distribution in the data, this distribution may be added to a reflection of itself multiplied by the east-west efficiency factor. The resulting distribution has a mean of -2.97 cm and a sigma of 37.40 cm, in good agreement with the data.

The trigger efficiency includes the efficiency due to component failures mentioned in section 3.4 as well as the trigger electronics, $\epsilon_{DIHOPU/NUPU}$, and scintillator efficiency, ϵ_{scint}. The calculation of these efficiencies are described in

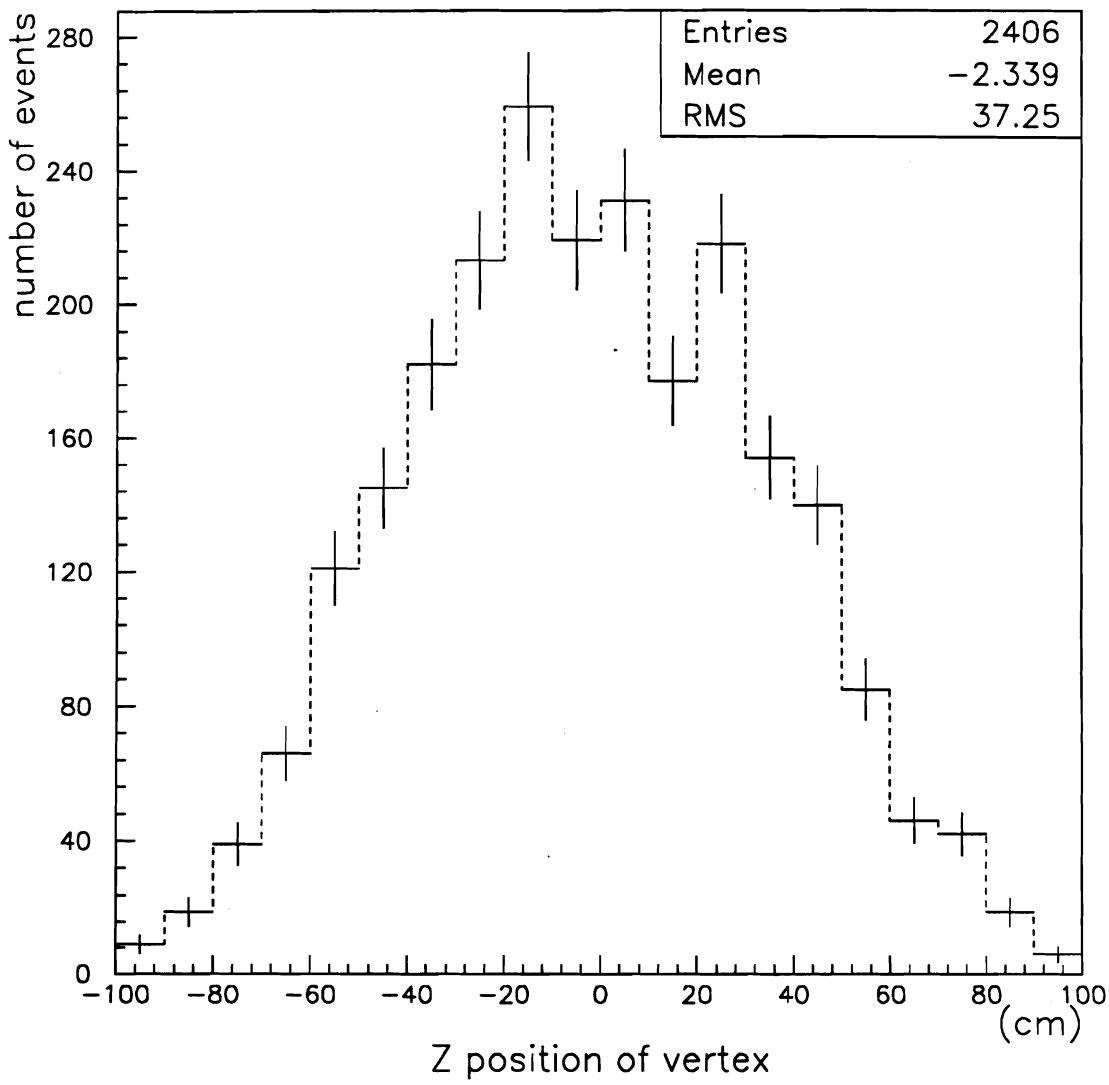

Figure 3.13: ***Vertex distribution in data.***

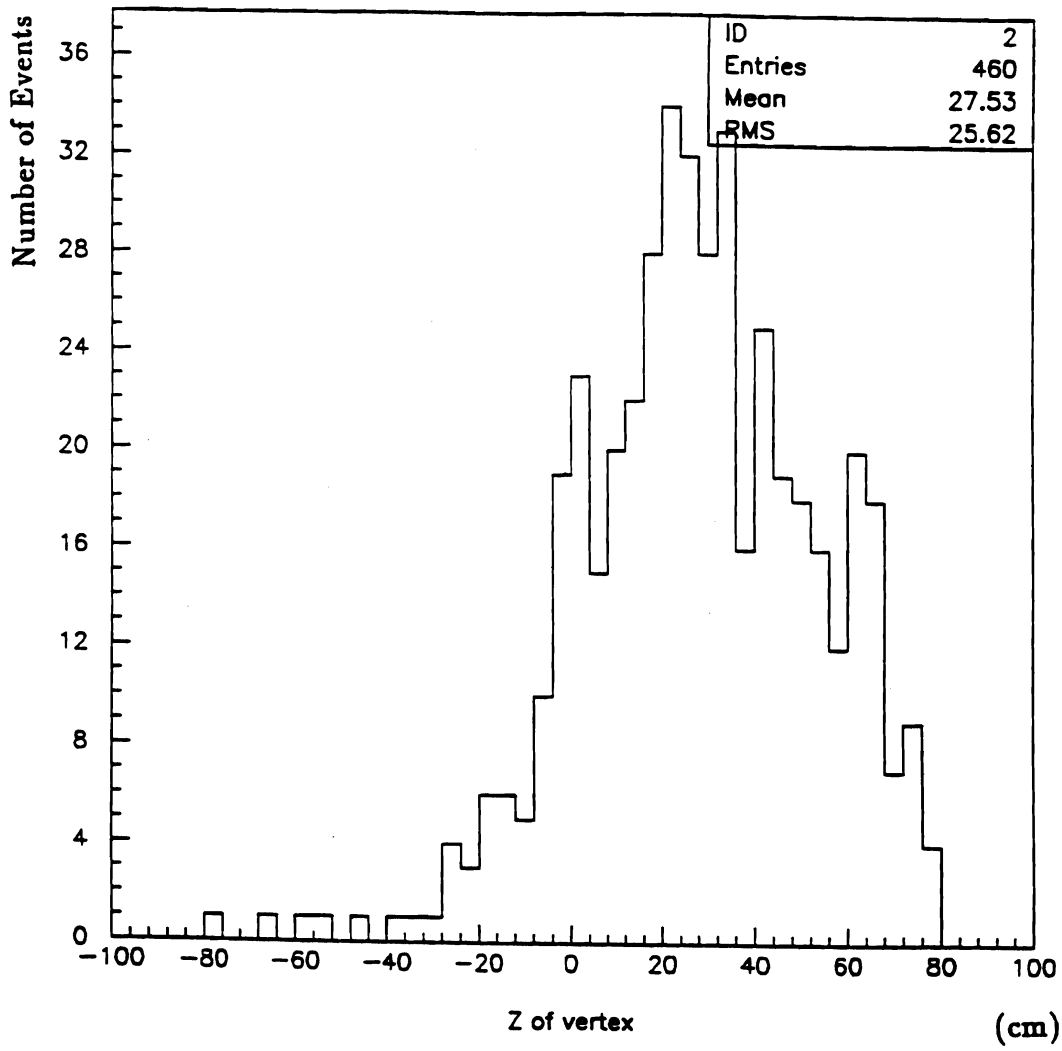

Figure 3.14: *Simulated vertex distribution for negatively charged muons*

Appendix A. The trigger efficiency,

$$\epsilon_{trigger} = \epsilon_{6\ \mathrm{hit}} \times \epsilon_{scint} \times \epsilon_{DIHOPU/NUPU} \tag{3.6}$$

is $(435 \pm .022)$ on the west and $(.355 \pm .018)$ on the east. The average trigger efficiency for the FMU system is $(.395 \pm .014)$.

3.8 Tracking algorithm efficiency

The requirements for reconstruction of a muon track are fairly simple, and therefore the probability of failures in the reconstruction can be estimated straightforwardly. The reconstruction begins by finding any sets of six hits, one per chamber plane, which are in cells that line up with the detector origin. For this purpose the cells are taken to line up if the track would shift by no more than one cell as it passes from the front plane to the middle and rear planes. Working from sets of six hits, two additional cuts are made; first, at each chamber station the coordinate and ambiguity hits are required to match to within 0.5 cm in the radial direction, after correcting for the slope of the track and second, if there are cathode pad hits associated to the wire hits then these are required to lie within a 10° azimuthal wedge.

The first effect to consider is the probability that the hits from a muon will line up well enough with the detector origin. It turns out that any set of six hits which satisfies the forward muon trigger (section 3.2) always satisfies this requirement.

Therefore any loss of tracks from this requirement will be accounted for already in the trigger acceptance, and it does not have to be considered separately here.

The requirement of six hits which pass the 0.5 cm matching cut is also already taken into account in the calculation of the trigger efficiency. There, the single-hit efficiency is taken to the sixth power, where the single-hit efficiency is computed from the number of tracks which are missing a hit (Appendix A.1). In that computation, if there really are six hits on a track but one pair fails the 0.5 cm matching cut, then the track is counted as missing one hit. Therefore, the single-hit efficiency automatically includes the loss of hits due to the matching cut.

The final source of reconstruction failures is the requirement that the cathode pad hits lie within a 10° wedge. The algorithm does not require that a pad hit is present in each plane, only that if there are pad hits then they must be consistent in azimuth with each other. Therefore in order to lose a track, not only must a hit be lost, but also a noise hit must must be present in the same plane, in the same rapidity range and at a different azimuth. The probability that this happens is the product of the probability that a hit is missing on one of three planes ($3 \times 2.6\%$) with the pad occupancy (1%), and a factor of six which comes from the six pads where a noise hit can confuse the algorithm. This is a rare occurrence, happening only .5% of the time.

Since all the significant contributions to loss of tracks are included in the trigger efficiency, a separate number for track reconstruction efficiency need not

be quoted.

Other effects on the track reconstruction may be considered, but they result only in a small change in reconstructed p_t or χ^2, and not in a loss of tracks. For example, the event vertex is used in the fit, and in a small fraction of events the event vertex is not reconstructed (then the detector origin is used in its place) or it is confused with a second event vertex in the same beam crossing. The probability to miss the event vertex is less than 1% in a crossing without a second vertex [18], and the probability to confuse it with a second vertex is estimated as less than 2%. This latter estimate follows from the fraction of events with a second vertex (about 10%), the probability of reconstructing the second vertex (80%) [18], and the probability that the second vertex has more tracks than the primary vertex so that it is chosen in place of the primary vertex (less than 20%). In the small fraction of events where the wrong vertex is chosen, the effect on the track p_t amounts to an additional smearing of about 4%. This when taken in quadrature with the momentum resolution from other sources ($> 16.6\%$) is negligible.

3.9 Fake muon rate estimate

A fake muon is one which is composed of hits not coming from a muon traversing the chambers. As these hits are not expected to be correlated like those coming from a real muon track, it is expected that the χ^2 of the track fit will in general be much worse for fakes. The characteristic shape of the χ^2 distribution for fakes can

be used to estimate the purity of the data sample. A simulation which presented the tracking algorithm with hits chosen randomly within an 8 cm window in the radial direction reconstructed 1841 tracks. Of these, 1660 had a probability of χ^2 less than .02. Over 90% of the fake tracks have poor χ^2. This will be used in section 5.3 to estimate the fake rate in the muons in jets sample.

Chapter 4

Jet Measurement

Jet energy scale and resolution in the central as well as the plug and forward detectors have been extensively studied in previous CDF measurements. These include measurements of the inclusive jet E_t spectrum [19, 20], the dijet angular distribution[21], the dijet differential cross section [22, 23], the jet fragmentation properties [24], the topology of three jet events [25] and the γ, W and Z p_t spectra [26, 27, 28, 29] I will summarize the most recent results which determine the jet energy scale and resolution. Since the jet energy scale can not be known exactly, there is a systematic error associated with its value.

4.1 The CDF calorimeters

The calorimetry at CDF is divided into three rapidity segments. The central calorimeter covers the region from $|\eta_d| \leq 1.3$, the plug $1.3 \leq |\eta_d| \leq 2.4$ and the

forward $2.3 \leq |\eta_d| \leq 4.2$. The physical features of the detectors are described elsewhere. [30] The placement of the calorimeters in the detector can be seen in the diagram of the CDF detector in the previous chapter. Briefly, the central detector is a modular device consisting of 31 layers of scintillator (polystyrene, .5 cm thick) and absorber (lead, .32 cm thick) in the electromagnetic section and 32 layers of scintillator (acrylic, 1.0 cm thick) and absorber (iron, 2.5 cm thick) in the hadronic section. Each calorimeter in the detector is segmented into projective towers of size $.1 \times 15°$ ($\Delta\eta \times \Delta\phi$). The plug calorimeter caps the end of the central detector with a hole of 10° for the beam pipe and associated electronics. It consists of 34 layers of proportional tube chambers (50/50 Argon-Ethane gas) and absorber (lead, .27 cm thick) in the electromagnetic section and 20 layers of proportional tube chambers and absorber (iron, 5.1 cm thick) in the hadronic section. The Endwall calorimeter covers the gap between the central and plug hadron calorimeters ($0.7 \leq |\eta_d| \leq 1.3$). It consists of 15 layers of scintillator (acrylic, 1.0 cm thick) and absorber (iron, 5.1 cm thick). The forward calorimeter covers the 10° hole in the plug with circular plate chambers. The forward calorimeter consists of 30 layers of proportional tube chambers and absorber (94% lead and 6% Sb, .48 cm thick) in the electromagnetic section and 27 layers of proportional tube chambers and absorber (iron, 5.1 cm thick) in the hadronic section. The tower size in the plug is $.09 \times 5°$ and in the forward is $.1 \times 5°$. Additional proportional chambers are imbedded near the shower maximum in the central and plug electromagnetic calorimeters to measure the shower shape and

position more accurately.

4.2 Energy scale in the central calorimeter

The jet energy in CDF is defined as the sum of energy from all particles within a spatial cone, ($\Delta R = \sqrt{\Delta\eta^2 + \Delta\phi^2} = 0.7$), around the nominal jet direction, excluding those from the soft underlying event. For several reasons, this "true" energy differs from the measured energy calculated from calorimeter pulse heights. The conversion from pulse height to nominal jet energy assumes a fixed proportionality constant, which is set from test beam measurements of single particle response. In fact the calorimeter response is nonlinear, and therefore the response to a jet involves different proportionality constants for each particle in the jet. As a result there is a shift in the mean jet energy scale. In addition, the calorimeter response varies across the gaps between individual cells. These effects lead to an average measured jet energy which increases from 75% to 90% of the true jet energy as the latter rises from 10 GeV to 100 GeV. In the gaps between the different CDF calorimeters, the response can degrade to as little as 20%.

The jet energy may be corrected for these known effects in an average way, which is done in a standardized FORTRAN subroutine (QDJSCO).[31, 32] However the accurate reconstruction of a true jet energy spectrum requires a full simulation of energy smearing due to single particle energy resolution, jet fragmentation, calorimeter nonlinearities, and geometrical response variations. All of

these must be correctly modelled in order to avoid bias in the reconstructed jet energy spectrum, and therefore may be said to set the jet energy scale in CDF. In this sense, the jet energy scale is not a single number, but a set of parameters put into the simulation. The full simulation of events has three parts. There is an event generator which makes partons according to their QCD cross section, a fragmentation routine (SETPRT) which decays the parton into a list of hadrons and leptons, and finally, a detector simulation which models the response of the detector to the hadrons and leptons (QFL). In this section I will describe the measurements which are used to set parameters in these routines and the resulting uncertainties in the jet energy scale. In addition, I will describe checks of the jet energy scale, which involve studies of transverse energy balancing and comparisons between simulation and data.

The single particle response of the central calorimeter has been measured with charged pions at the test beam and with low pt isolated tracks in minimum bias data from the collider. [33, 34, 35] For the minimum bias sample, the momentum, p, of isolated charged pions is measured with the central tracking chamber, and this is compared with the central calorimeter energy, E. Figure 4.1 shows the ratio E/p as a function of momentum. The errors shown by the band in Figure 4.1 are larger than the statistical errors in the data because of systematic uncertainties. The dominant uncertainty in the minimum bias data comes from the uncertainty in subtracting the neutral pion contamination from the sample (5%). Isolated tracks are used to ensure that the measured energy really came

from a single particle. Since neutral pions leave no tracks, there is an uncertainty in the isolation of the track. Adjacent tower energy deposition was used to estimate the neutral pion contamination, but a residual uncertainty is still present. At higher momenta, E/p is measured from test beam pions where the dominant uncertainties are the variation in response across the face of the calorimeter (5%) and energy depositions in ϕ cracks between calorimeter cells (2.5%). In addition, the test beam E/p values are uncertain due to statistical errors in the calibration of the PMT gains (3%).

Jets also have a photon component, and the electron response has been measured to calibrate this component of the jet energy measurement. Figure 4.2 shows the electron response map at the center of a calorimeter tower. For 5 and 10 GeV electrons, E/p is $(92 \pm 4)\%$. When the response is measured as a function of position in the calorimeter, it drops to 20% in the ϕ cracks. At low photon energy, it is expected that the response decreases. However, this has not been explicitly observed in low momentum electron samples. Therefore the expected drop in response is taken as a systematic error between .5 and 3.5 GeV, depending on photon energy.

As mentioned above, in correcting the nominal measured jet energy to true energy one must account for the jet fragmentation, and how it couples with the variations in single particle response. The mean correction is obtained from the simulation, and is included in the standard jet correction routine QDJSCO. The fragmentation model used in the simulation, SETPRT, has been tuned to real

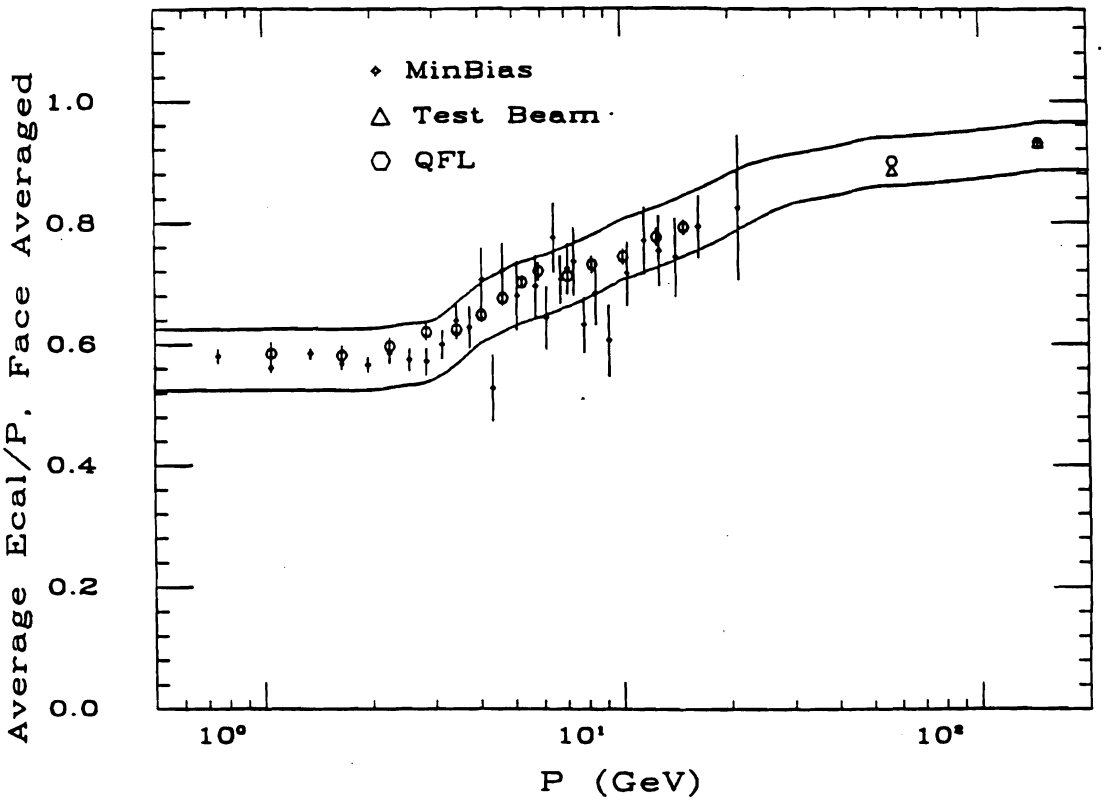

Figure 4.1: *Average single particle response (E/p) measured for hadrons in the central calorimeter as a function of momentum.*

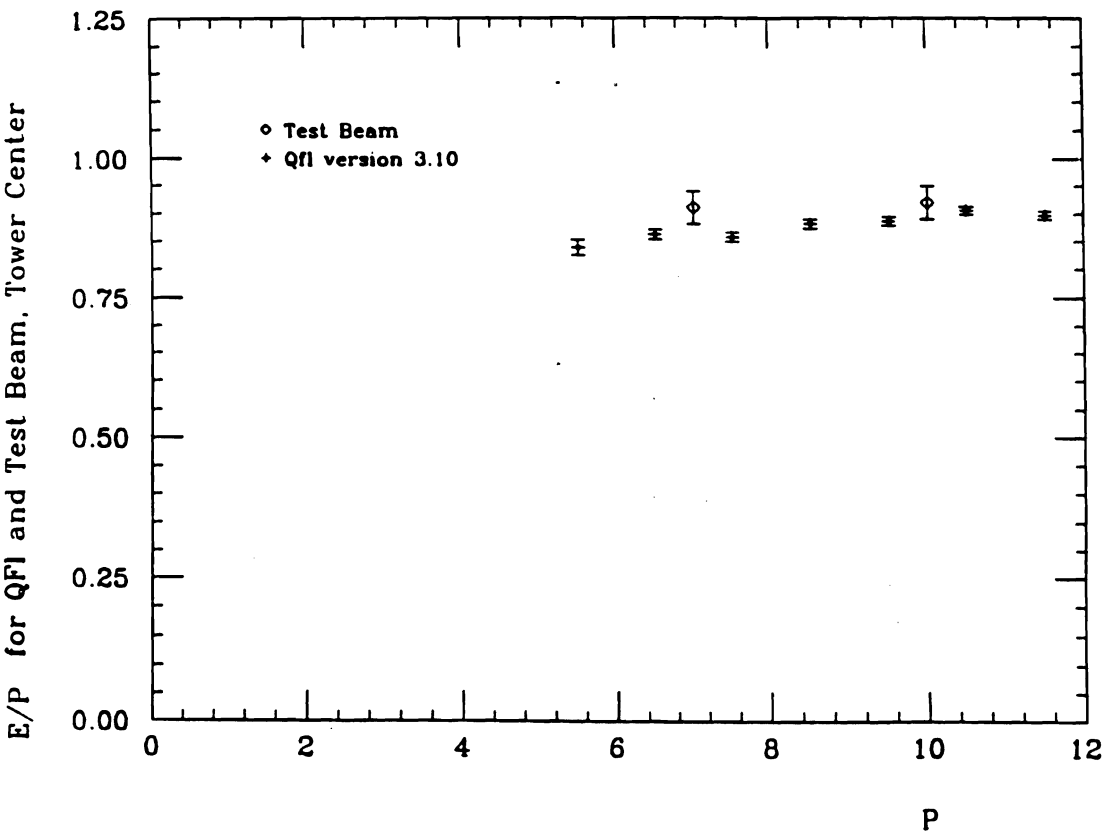

Figure 4.2: *Average electron response (E/p) measured in the central calorimeter as a function of momentum.*

data using tracks pointing at jets in the calorimeter. SETPRT uses a Feynman-Field fragmentation model [36] The dominant source of uncertainty in checking that the tuning is correct comes from inefficiencies in track finding, when the tracks are in the high-density environment of a jet. The uncertainty in the track finding efficiency was estimated as $\pm 7\%$. This was determined by inserting Monte-Carlo tracks into the real jet data and measuring the performance of the track reconstruction for those tracks. [37] The resulting uncertainty on the jet energy scale is 1.8% at $E_t^{corr} = 20$ GeV. As an additional test of possible systematic shifts due to uncertainty in the fragmentation model, the fragmentation model used in the HERWIG Monte-Carlo program was substituted for SETPRT. This is a parton shower model which is inspired by QCD theory. The two fragmentation models were found to give energy scales matching to within 1.5% at all E_t. [38]

For the present analysis, the ISAJET Monte-Carlo simulation program was used [39] to establish the relationship between the true b-quark spectrum and the observed spectrum. This simulation includes a parton shower model followed by a phenomenological fragmentation scheme which is different for light and heavy quarks. Light quarks and gluons are fragmented according to the Feynman-Field ansatz, whereas heavy quark (c and b) fragmentation follows the Peterson parametrization.[40] Within the simulation, I have compared the responses predicted for gluon or light quark jets with b-quark jets. The fragmentation of these two types of jets is predicted to be significantly different, however, the effect on the energy scale is found to be less than 10%. Table 4.1 shows the comparison

		$E_t(jet)/E_t(true)$ light quark fragmentation (Feynman-Field)	$E_t(jet)/E_t(true)$ bottom quark fragmentation (Peterson)
CENTRAL $\lvert\eta_d\rvert < 1$	$10 \leq E_t(true) \leq 12$	$.753 \pm .001$	$.748 \pm .001$
	$15 \leq E_t(true) \leq 17$	$.713 \pm .001$	$.678 \pm .002$
	$20 \leq E_t(true) \leq 24$	$.735 \pm .002$	$.676 \pm .002$
	$30 \leq E_t(true) \leq 36$	$.763 \pm .003$	$.693 \pm .004$
PLUG/FORW $\lvert\eta_d\rvert > 2$	$10 \leq E_t(true) \leq 12$	$.761 \pm .001$	$.743 \pm .002$
	$15 \leq E_t(true) \leq 17$	$.707 \pm .002$	$.658 \pm .004$
	$20 \leq E_t(true) \leq 24$	$.729 \pm .004$	$.648 \pm .007$
	$30 \leq E_t(true) \leq 36$	$.727 \pm .010$	$.678 \pm .015$

Table 4.1: *Jet energy scale from Feynman-Field and Peterson Fragmentation.*

between the true and measured jet energy for the light and heavy quark fragmentation. In particular, the bin 20 GeV$< E_t^{true} < 24$ corresponds to the central E_t^{corr} cut of 15 GeV and has a +9% effect. Since this estimates the total effect, we will take the systematic uncertainty due to this to be +5%.

Another correction to the jet energy scale is necessitated by soft particles associated with the underlying event, which deposit energy in the jet cone. The average underlying event energy is assumed to be uniformly distributed throughout the detector (η, ϕ), and has been measured using dijet events in the data. In

the dijet sample, which was selected by requiring the absence of a third cluster with $E_t > 15$ GeV, the amount of energy deposited in a 20° band around 90° from the thrust axis was found to be $(.99 \pm .34)$ GeV/rad^2. [41] The error is primarily systematic and was estimated by varying the cut on the third cluster ($\Delta E_t^{und} = .3$ GeV), and by considering run to run variations in calorimeter calibrations (.1 GeV). Additional statistical uncertainty is present in the measurement of average energy in the 20° band (.08 GeV) and in the measurement of energy dependence (.1 GeV). There is also a theoretical uncertainty on how much of the underlying event E_t is actually uncorrelated to the jets. HERWIG for example predicts that half of the observable energy distributed in the 20° band is of jet origin. [38]. Therefore a systematic error in the underlying event energy of $^{+30}_{-50}\%$ is used to be consistent with other CDF analyses.

The effect of each of these systematic effects has been translated into an equivalent uncertainty in the jet energy scale. The results of all but the bottom quark fragmentation uncertainty are shown in Figure 4.3. These uncertainties are added in quadrature for the total systematic uncertainty in the jet energy.[42, 38] The total uncertainty varies from $^{+7.5\%}_{-6.5\%}$ at $E_t = 15$ GeV to $^{+3.2\%}_{-2.6\%}$ at $E_t = 100$ GeV. At low E_t, the largest contribution comes from the underlying event. In addition, for bottom tagged jets there is a +5% uncertainty due to the heavy quark fragmentation.

Various checks have been made to verify the jet energy corrections. The first check was the momentum balance in electron-plus-jet events where the electron

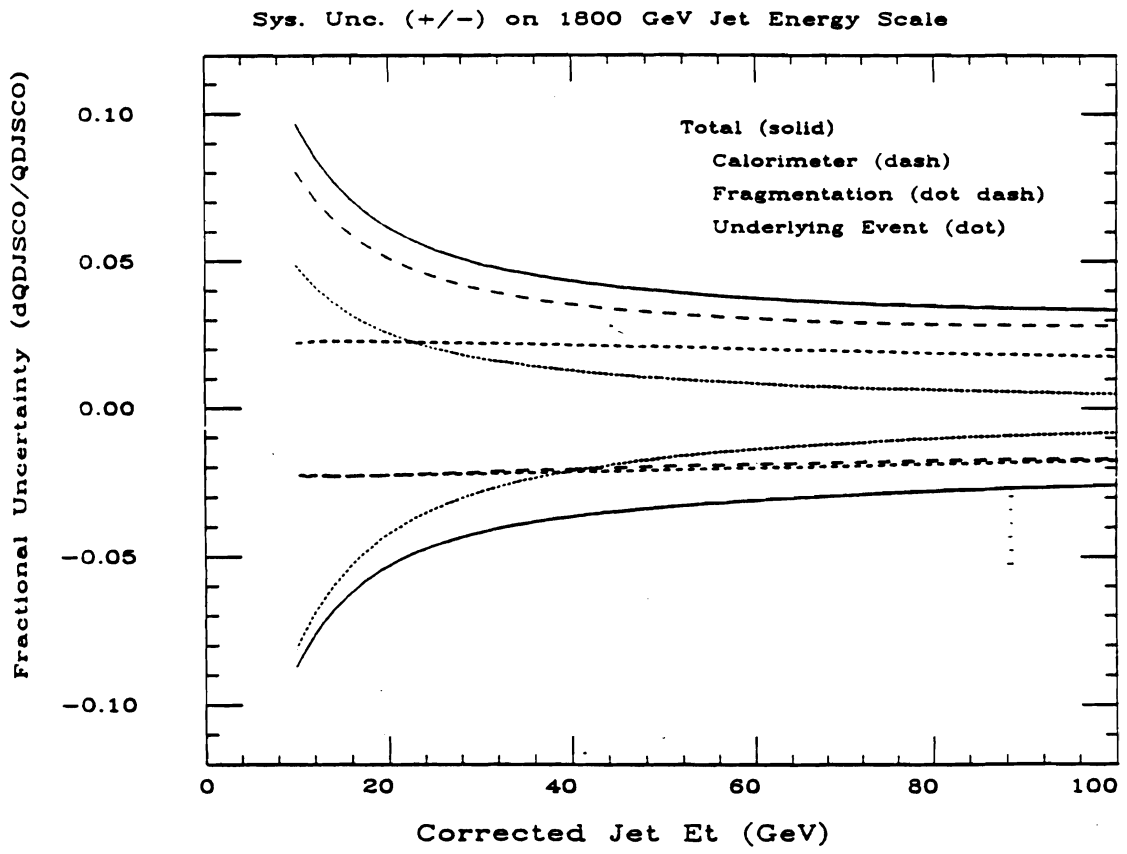

Figure 4.3: *Systematic uncertainty in the jet energy scale associated with the uncertainty in single particle responses of pions and electrons, light quark and gluon fragmentation, and the underlying event.*

is believed to be one leg of an asymmetric conversion pair. [38, 43] The electron E_t interval is 20 GeV to 60 GeV. After correcting for the known shifts in the jet energy scale, Et balance is maintained at the level of 1% to 2% (Figure 4.4). A similar check of the energy scale was conducted using gamma + jet events. [38, 44] Figures 4.5 and 4.6 compare E_t balance in photon-plus-jet events with photon trigger thresholds of $E_t > 10$ GeV and 23 GeV. The quantity plotted is the difference of the photon E_t and the projection of the jet E_t along the photon direction. Simulated data was made for comparison. The simulation includes trigger effects and QCD radiation, which gives the photon-jet system a non-zero transverse momentum (k_t kick). Agreement between data and simulation is good at both energies. Finally, a similar balancing study has been carried out for Z-plus-jet events, where the transverse component of the Z is well measured. [46]

4.3 Energy resolution in the central calorimeter

The true jet spectrum falls steeply as a function of jet E_t. Due to the limited jet energy resolution, however, the slope of the measured spectrum is smaller. Since there are more low E_t jets, they tend to slide up in energy more often than high E_t jets slide down. The amount of smearing depends on the resolution of the jet energy. The resolution is measured at CDF using a dijet balancing technique, as

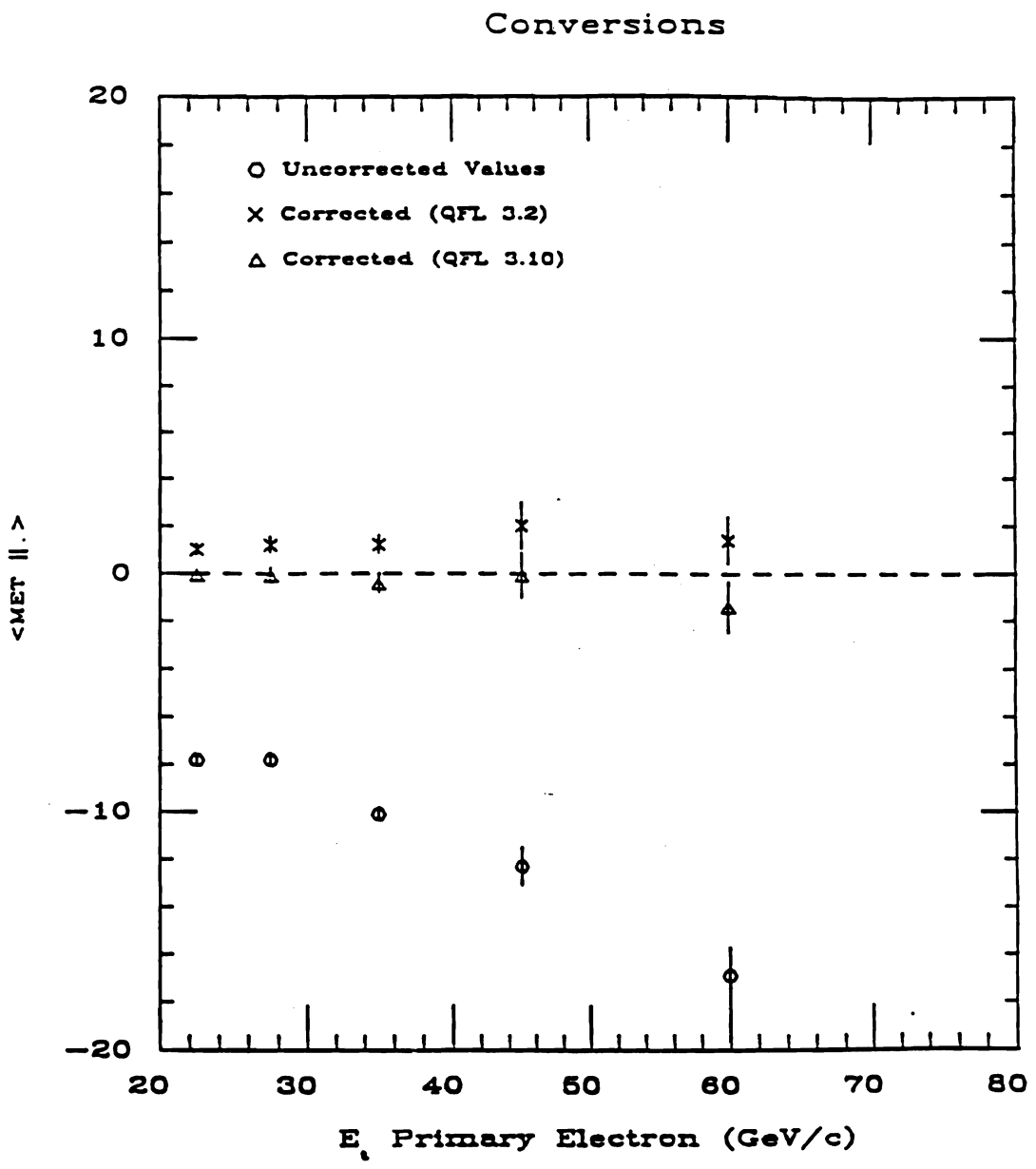

Figure 4.4: *The observed and correct missing E_t parallel to the primary electron direction in conversion events as a function of the E_t of the primary electron.*

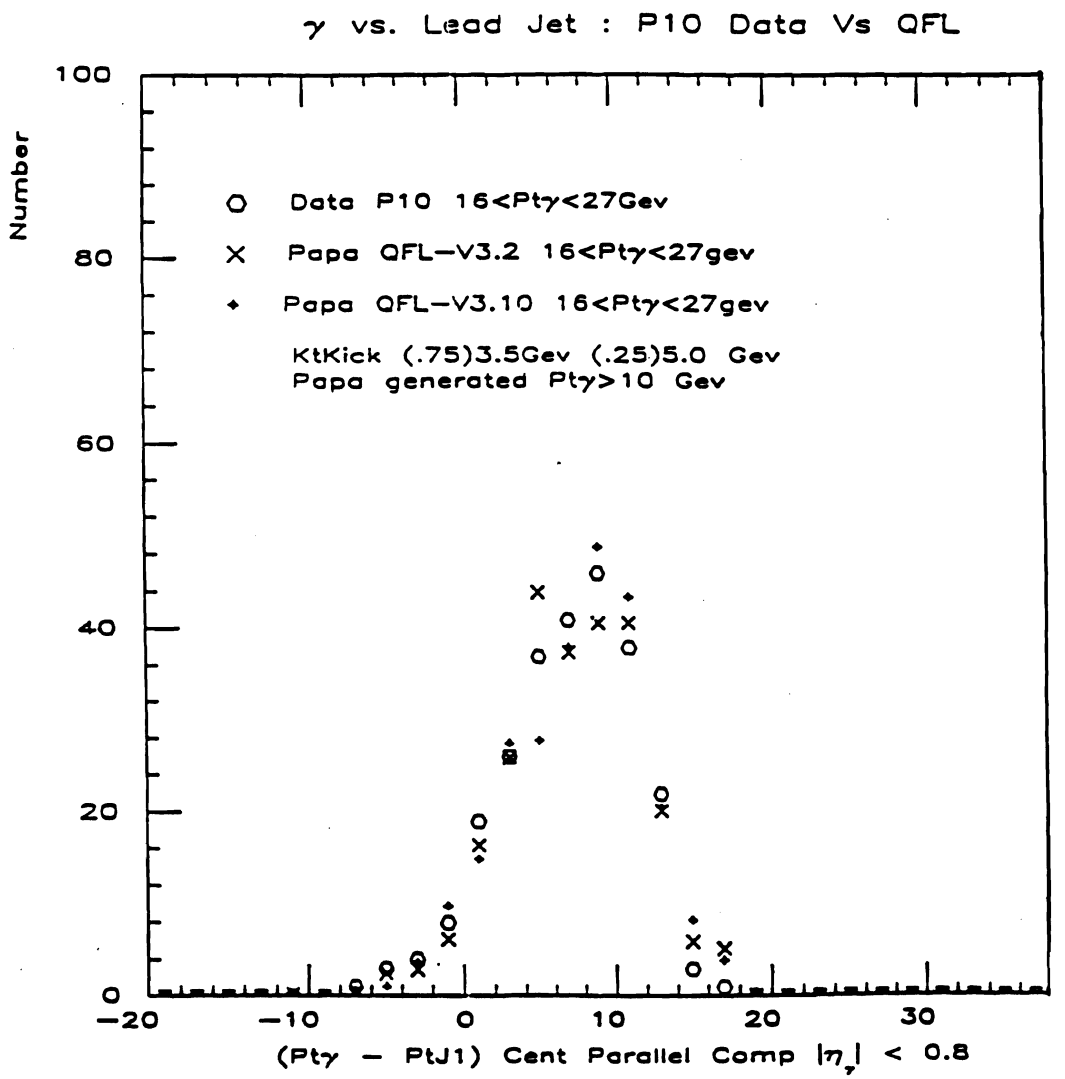

Figure 4.5: *Photon - Jet balancing using events collected with the photon trigger,* $E_t^\gamma > 10$ *GeV.*

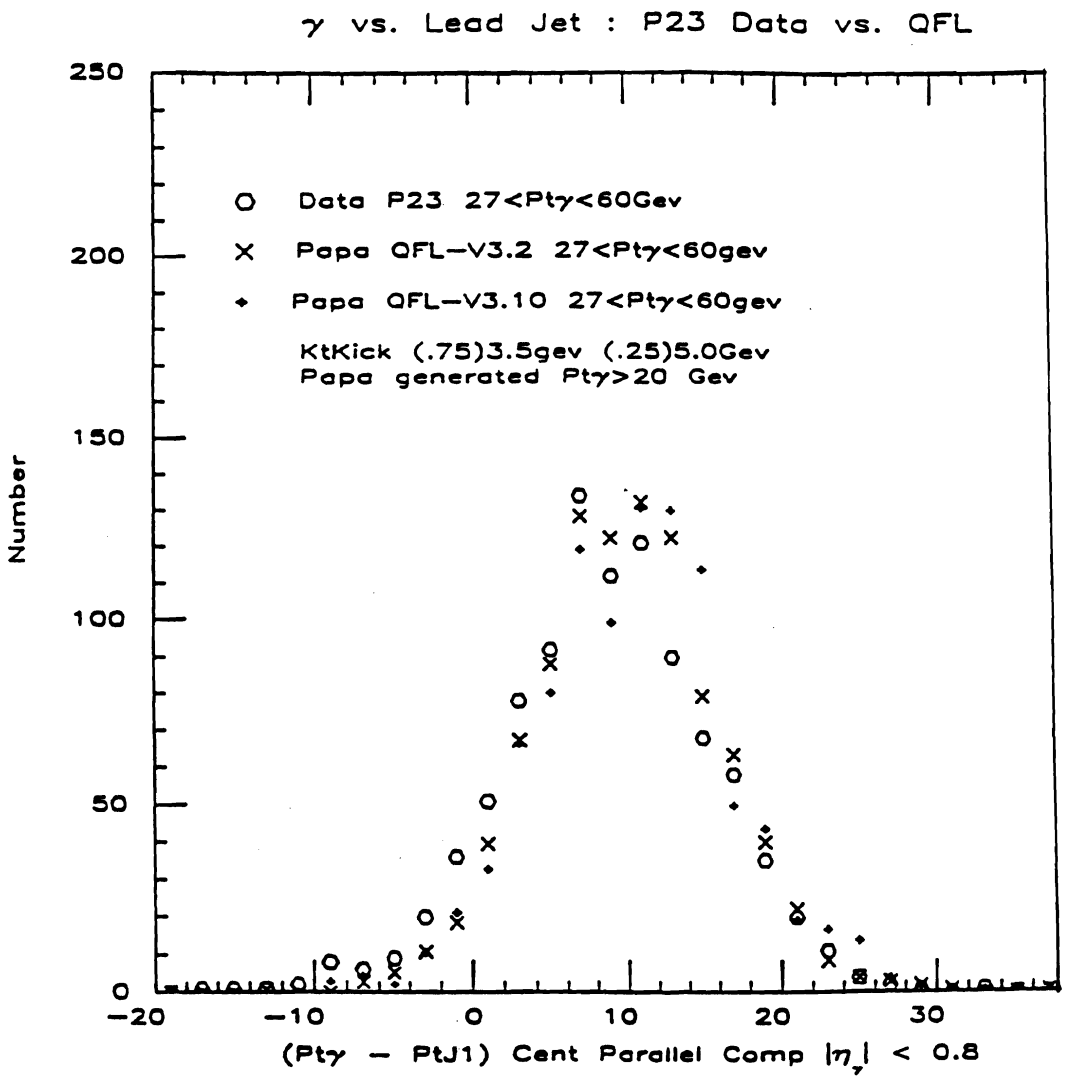

Figure 4.6: *Photon - Jet balancing using events collected with the photon trigger,* $E_t^\gamma > 23$ *GeV.*

first done by UA2. [47]

Dijet balancing is applied to events with two and only two identifiable jets. Events are selected which have two and only two jets above $E_t = 15$ GeV and the sum of the jet E_t's must be over 50 GeV. In addition, the jets are required to be central ($0.2 < |\eta| < 0.7$) and back to back in phi ($|\Delta\phi| > 2.5$). In the plane perpendicular to the beam direction, the vector sum of the two jet momenta is $\vec{k}_t$. In an ideal world, conservation of momentum would ensure that $\vec{k}_t$ was uniformly zero. However, in the real world, contributions to the imbalance of the jets comes from the detector resolution and additional radiation from soft physics processes.

The coordinate system of the dijet events in the plane transverse to the beam (shown in Figure 4.7) is defined so that the perpendicular bisector of the two jet directions is $\perp$ and the direction orthogonal to this is $||$. Defining this coordinate system then implies that

$$k_{t\perp} = (p_{t1} + p_{t2})\cos(\frac{\Delta\phi_{12}}{2}) \tag{4.1}$$

$$k_{t||} = (p_{t1} - p_{t2})\sin(\frac{\Delta\phi_{12}}{2}). \tag{4.2}$$

Here $\Delta\phi_{12}$ is the azimuthal angle between the two jets and p_{t1} and p_{t2} are the jet momenta in the transverse plane. Figure 4.8 shows the distributions of these quantities normalized to the jet energy for both data and simulation:

$$k_{t\perp}^{norm} = \frac{k_{t\perp}}{(p_{t1} + p_{t2})} \tag{4.3}$$

$$k_{t||}^{norm} = \frac{k_{t||}}{(p_{t1} + p_{t2})}. \tag{4.4}$$

The simulation starts with ISAJET 2-jet events and then uses the QFL detector model, which simulates the sum of single particle responses and smearing as determined from the testbeam measurements. The distributions agree in shape well. The widths of both $k_{t\perp}^{norm}$ and $k_{t||}^{norm}$ distributions have contributions from soft radiation and jet resolution, but there is a fundamental kinematic difference between the two. The soft radiation is produced more or less symmetrically in azimuth and therefore contributes equally to $k_{t\perp}^{norm}$ and $k_{t||}^{norm}$. However, the jet resolution affects primarily the magnitude of the jet vectors, and therefore its effect is almost entirely contained in the width of the $k_{t||}^{norm}$ distribution. Taking the difference between the widths of the distributions thus yields the jet resolution. The jet resolution can be expressed as:

$$\frac{\sigma(p_t)}{p_t} = \frac{1}{\sqrt{2}}\sqrt{\sigma^2(k_{t\perp}^{norm}) - \sigma^2(k_{t||}^{norm})} \tag{4.5}$$

The measured jet resolution from the data is thus $(7.5 \pm 0.4)\%$ of the corrected jet momentum. This may be compared with the analogous calculation using the simulated data from QFL, which yields $(6.3 \pm 0.4)\%$. This corresponds to a difference of $(1.2 \pm 0.4)\%$.

The distribution of

$$\sigma(P_t) = \frac{1}{\sqrt{2}}\sqrt{\sigma^2(k_{t\perp}) - \sigma^2(k_{t||})} \tag{4.6}$$

as a function of p_t is shown in Figure 4.9. This confirms that as a function of p_t the resolution is well understood. The calculation above corresponds to jet energies 30 GeV $< E_t^{corr} <$ 40 GeV and has been added as the first point on

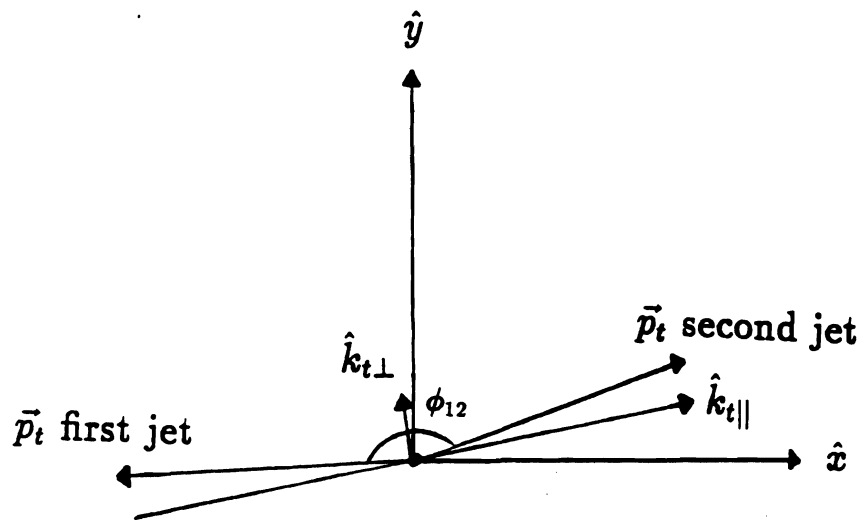

Figure 4.7: *Dijet balancing coordinate system in the plane transverse to the beam direction.*

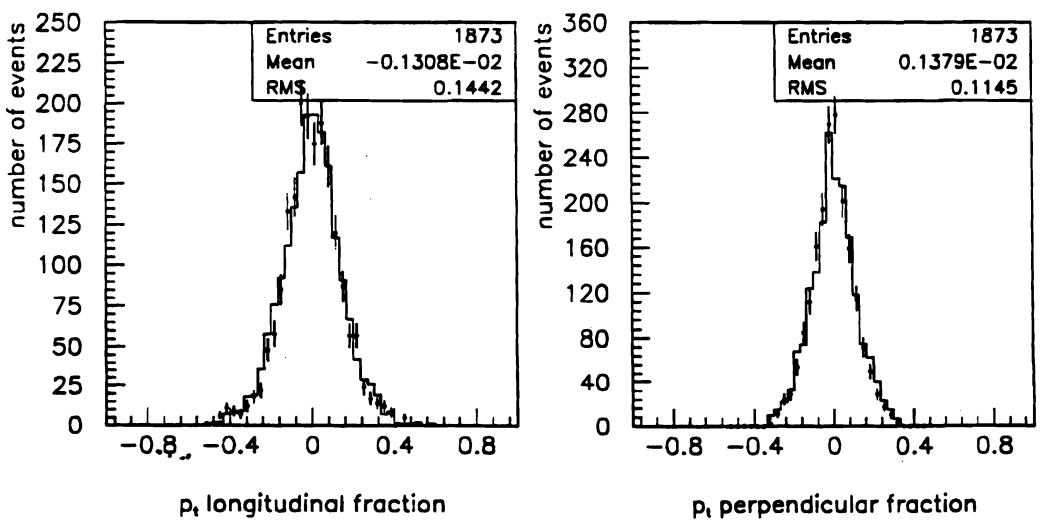

Figure 4.8: *Dijet balancing with central jets; longitudinal and perpendicular k_t fractions.*

the plot. The only problem with this plot is that we still must extrapolate the resolution to low E_t.

Figure 4.10 shows the spectrum of particles in 10 GeV and 30 GeV simulated jets. Notice that the energy spectrum of particles contributing to jets is very similar between the two. Only the high momentum tail, where a single particle carries most of the energy in the jet differs. Thus, the difference in resolution between low and high energy jets must depend for the most part on statistical issues involving the number of particles in the jet. Since we think that these fluctuations are well understood, it is reasonable to trust the extrapolation of the simulated energy resolution to low energy.

The electron plus jets sample confirms that the jet resolution in QFL is well understood at high energy. Figure 4.11 shows the electron - jet balance for sum 200 GeV $< E_t <$ 220 GeV. For low E_t jet balance, Figures 4.5 and 4.6 are relevant. The γ plus jet sample provides the basis for the claim that the resolution is understood to within 10% of itself at 10 GeV. [48] For these plots, the simulation is based on the PAPAGENO Monte-Carlo program, and also includes a model of the k_t kick as well as trigger efficiencies, the usual SETPRT fragmentation scheme, and QFL detector modelling. In the photon plus jet case, the k_t kick modelling is tuned so that it reproduces the observed distribution of $k_{t\perp}$, in analogy with the subtraction of the $k_{t\perp}$ width in the dijet case just described. Therefore the agreement seen in Figures 4.5 and 4.6, which depends on both the k_t kick and the jet resolution, indicates that the jet resolution is modelled correctly by QFL.[44]

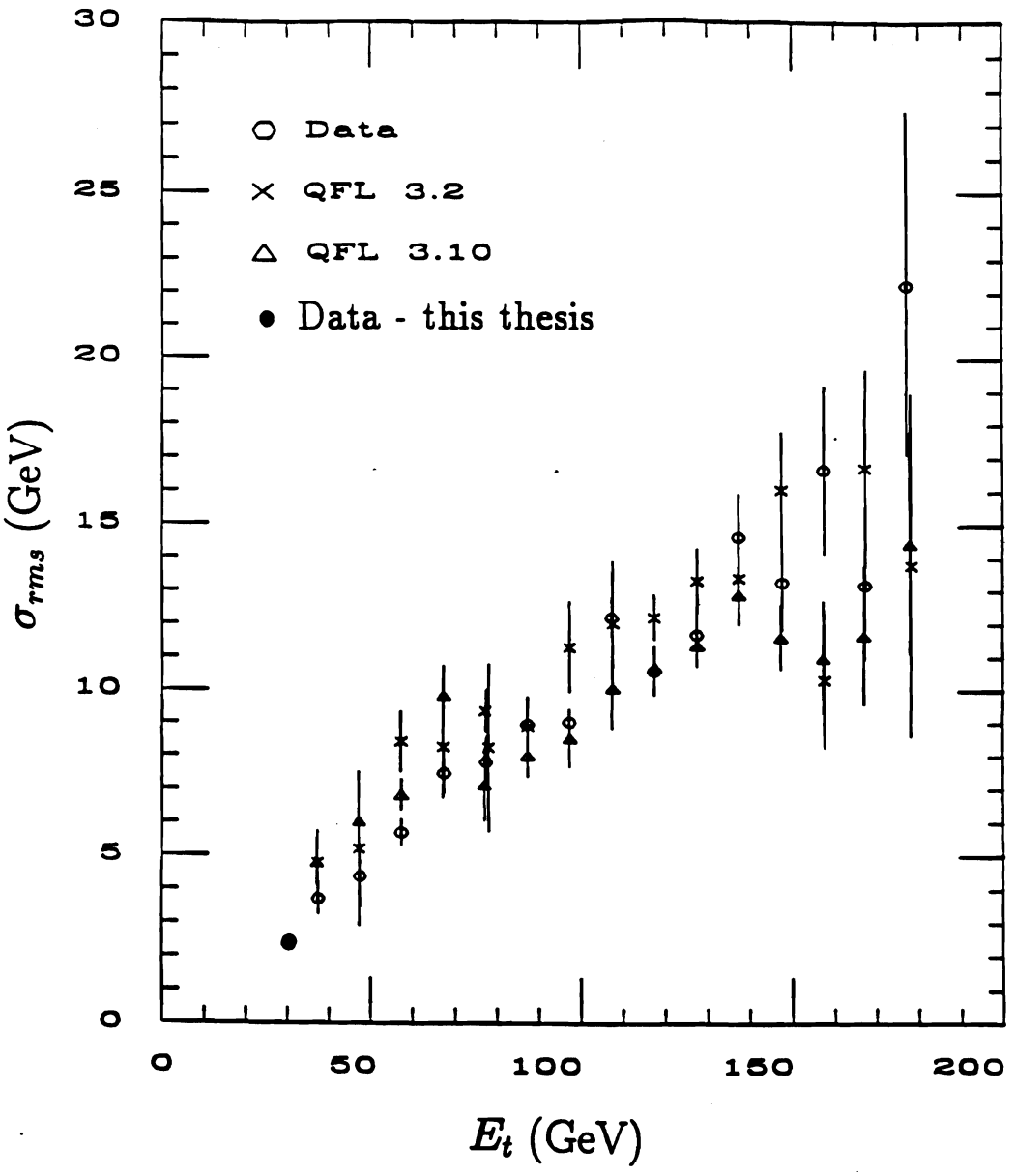

Figure 4.9: *Jet resolution as a function of jet energy.*

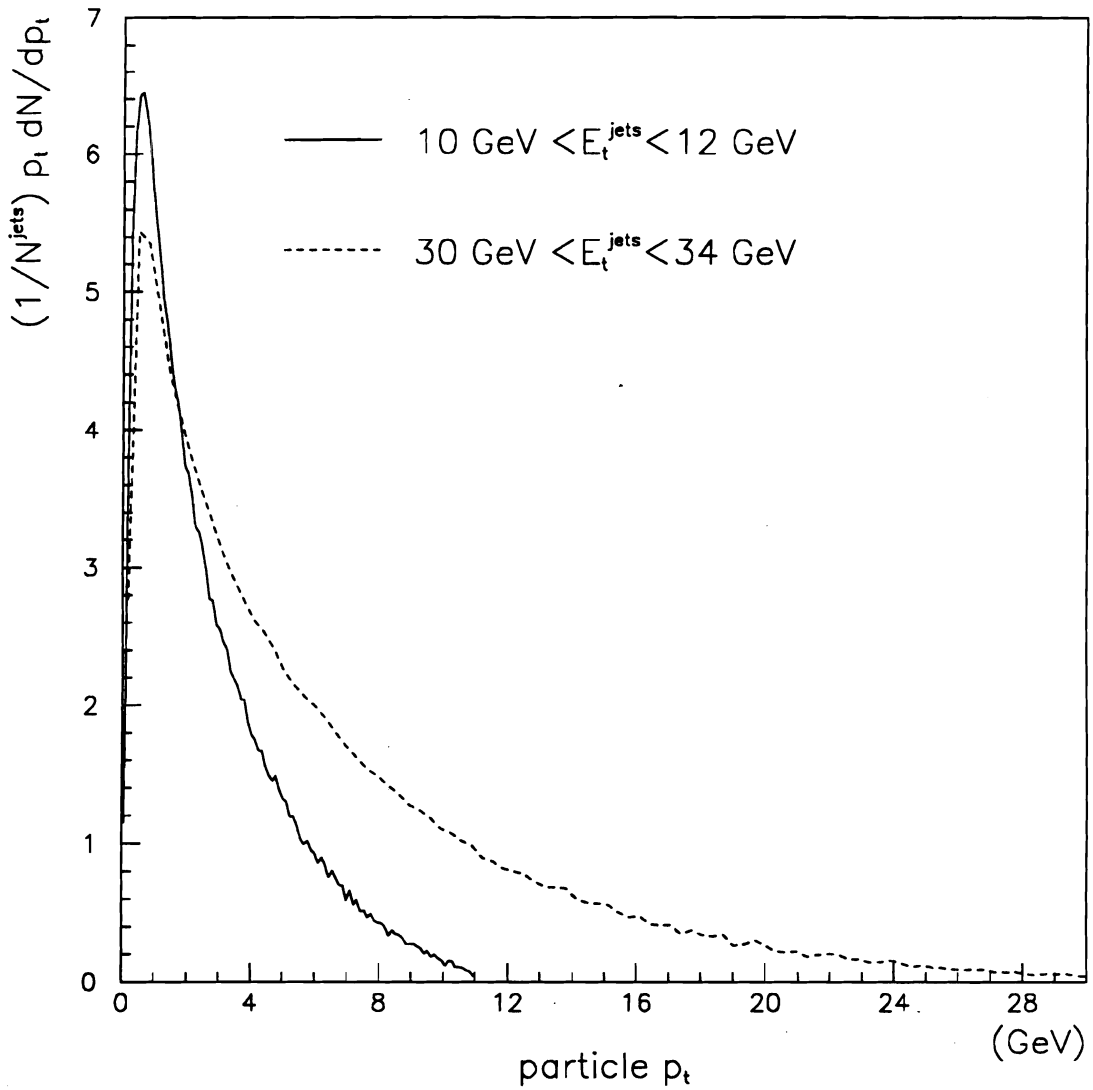

Figure 4.10: ***Momentum spectrum for particles in 10 to 12 GeV jets compared to that of 30 to 35 GeV jets.***

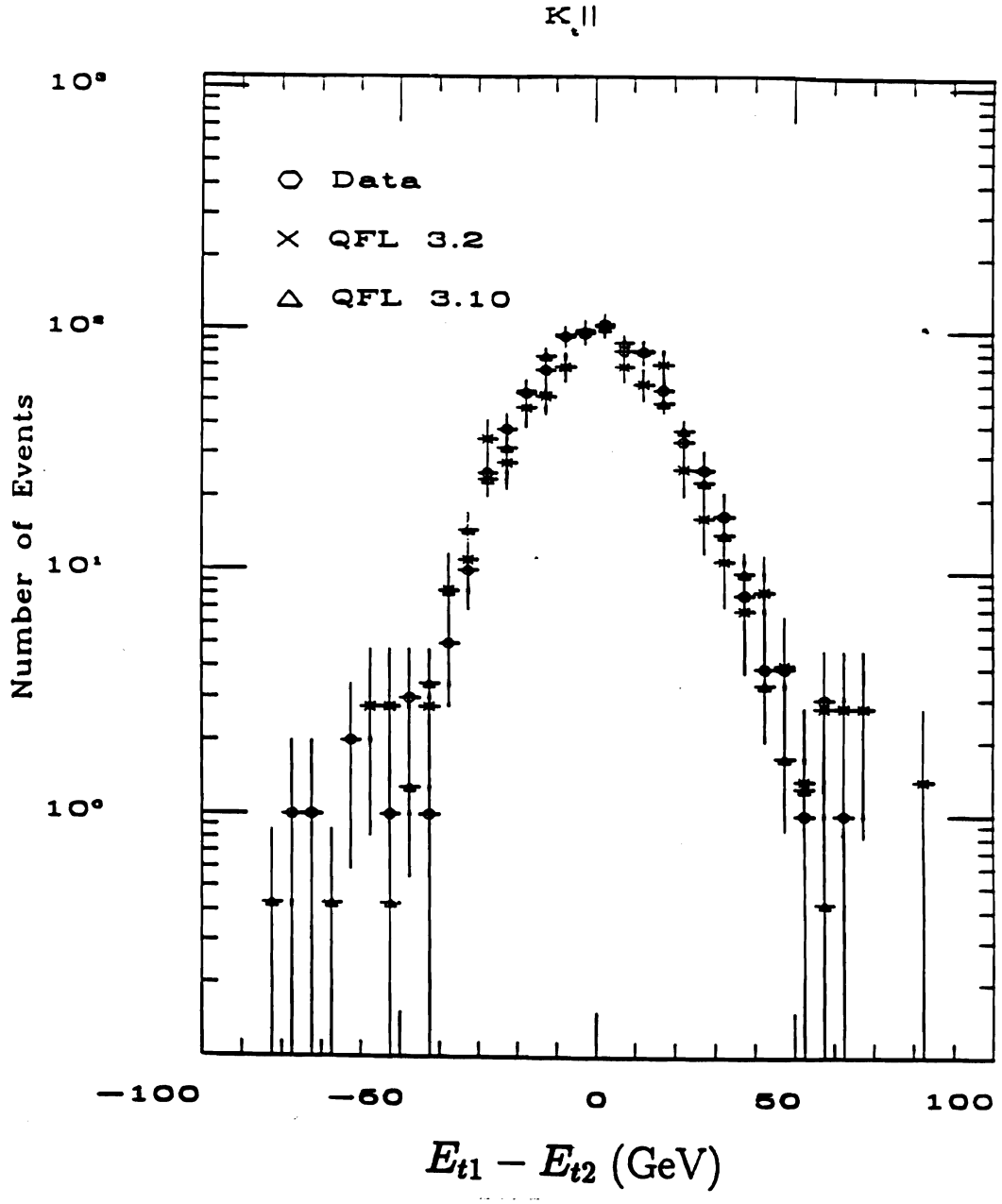

Figure 4.11: *Electron - jet balancing. The resolution from events simulated with SETPRT+QFL agree well with the data.*

4.4 Energy scale in the forward calorimeters

The energy scale determination in the forward detectors and crack regions is somewhat simpler than the absolute energy scale in the central detector. Since the energy scale is already set in the central detector, all we need is to establish the energy scale relative to this. In events with one jet in the central detector and one jet elsewhere, the missing E_t projection fraction (MPF) is used to find the optimal energy correction for the non-central jet. Such a technique is essential for cracks where a large fraction of particles in the jet may miss the detector entirely. The MPF is defined to be: [31, 45]

$$MPF = \frac{2\vec{\not{E}}_t \cdot \hat{p}_t^{probe}}{p_{t||}^{trigger} + p_t^{probe}} \tag{4.7}$$

where $\vec{\not{E}}_t$ is the missing transverse energy in the event, the trigger jet is a central jet and the probe jet has a detector rapidity elsewhere in the detector. If both jets are central, then a random choice is made to define the trigger and probe jet. Events were again selected which have two and only two jets $E_t > 15$ GeV and $\Delta\phi > 2.5$. This selection is designed to ensure that the dominant physics process contributing is that of dijet events. The cuts also tend to limit the missing transverse energy in the event. However, as we will see, it is the mean energy correction which is important here, so as long as the mean of the MPF distribution is preserved, the cuts are satisfactory. In effect, we can define the

momenta in the problem as:

$$\vec{\not{E}}_t = -\vec{p}_t^{\,trigger} - \vec{p}_t^{\,probe} - \vec{p}_t^{\,other} \tag{4.8}$$

where $-\vec{p}_t^{\,other}$ is the momentum from all other sources of energy in the event. Now let us define the projections of these momenta along the "probe" direction:

$$p_{t||}^{trigger} = -\vec{p}_t^{\,trigger} \cdot \vec{p}_t^{\,probe} \tag{4.9}$$

$$p_{t||}^{other} = -\vec{p}_t^{\,other} \cdot \vec{p}_t^{\,probe} \tag{4.10}$$

Then the missing E_t projection fraction may be rewritten as:

$$MPF = 2\frac{p_{t||}^{trigger} + p_{t||}^{other} - p_t^{probe}}{p_{t||}^{trigger} + p_t^{probe}} \tag{4.11}$$

Since $\vec{p}_t^{\,other}$ is not biased toward or away from the probe jet, the average value of MPF is:

$$\langle MPF \rangle = 2\left\langle \frac{p_{t||}^{trigger} - p_t^{probe}}{p_{t||}^{trigger} + p_t^{probe}} \right\rangle . \tag{4.12}$$

The correction factor, β, for the probe jet is defined to give an average value of the corrected MPF equal to zero,

$$0 = \langle MPF^{corr} \rangle = 2\left\langle \frac{p_{t||}^{trigger} - \beta p_t^{probe}}{p_{t||}^{trigger} + p_t^{probe}} \right\rangle . \tag{4.13}$$

Using the last two equations and the fact that

$$1 = \left\langle \frac{p_{t||}^{trigger} + p_t^{probe}}{p_{t||}^{trigger} + p_t^{probe}} \right\rangle , \tag{4.14}$$

the solution for β can be easily obtained:

$$\beta = \frac{2 + \langle MPF \rangle}{2 - \langle MPF \rangle} \tag{4.15}$$

Figure 4.12 shows the $\langle MPF \rangle$ and β distributions for uncorrected jets in the detector. QDJSCO uses spline fits to interpolate between these points in both energy and rapidity when correcting the jet energy for any given jet in the detector. After correcting all the jets with QDJSCO, Figure 4.13 shows that the $\langle MPF \rangle$ distribution is very flat as expected. Notice, however that the statistical errors are still very large in the far forward region. Since the full simulation using Isajet plus QFL is supposed to take all the detector effects into account, we can see how well it does by checking the output after correcting all the jets with QDJSCO. Figure 4.14 shows the $\langle MPF \rangle$ distribution for simulated jets. There is an overall 5% shift in the forward region. The systematic uncertainty in the forward jet energy scale above that from the absolute energy scale in the central is $\pm 5\%$. The breakdown of the dijet balancing for forward jets, $|\eta_d| > 2.4$, is due to limited statistics in the dijet balancing procedure. The statistical uncertainty in Figure 4.12 increases at the same point that the modeling of QFL drifts. The energy scale beyond $\eta_d = 2.4$ is not well determined and therefore only jets with $\eta_d < 2.4$ will be used for the current analysis.

The correction function, $\beta(E_t, \eta)$ extends down to jet energies of 30 GeV beyond which, the result is extrapolated. The energy spectrum of particles in 30 GeV and 10 GeV jets has already been shown in Figure 4.10. The energy spectrum of particles contributing to jets is very similar between the two. Only the high momentum tail, where a single particle carries most of the energy in the jet differs. Thus, the difference in the measured jet energy between low and

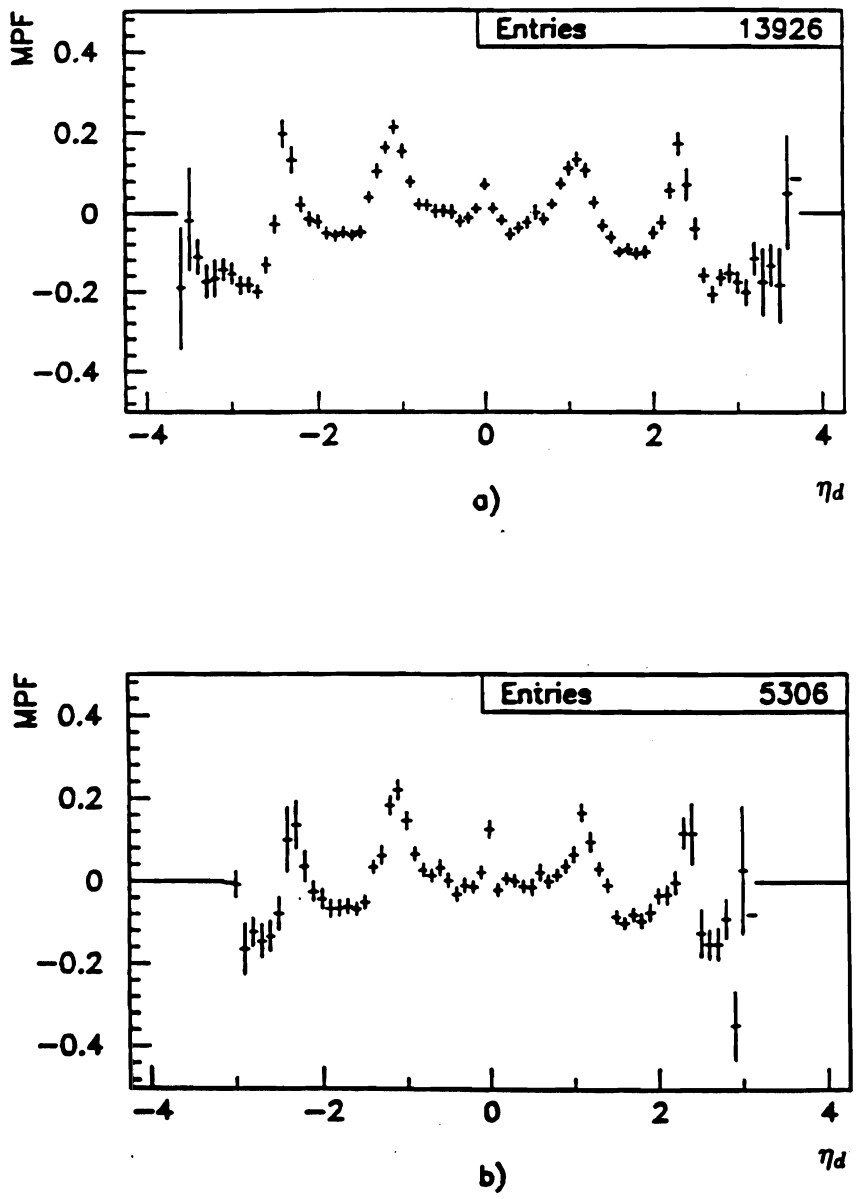

Figure 4.12: *Missing E_t projection fraction as a function of η_d measured with dijet data in the ranges a) 50 GeV/c $< \sum P_t <$ 100 GeV/c and b) 100 GeV/c $< \sum P_t <$ 130 GeV/c.*

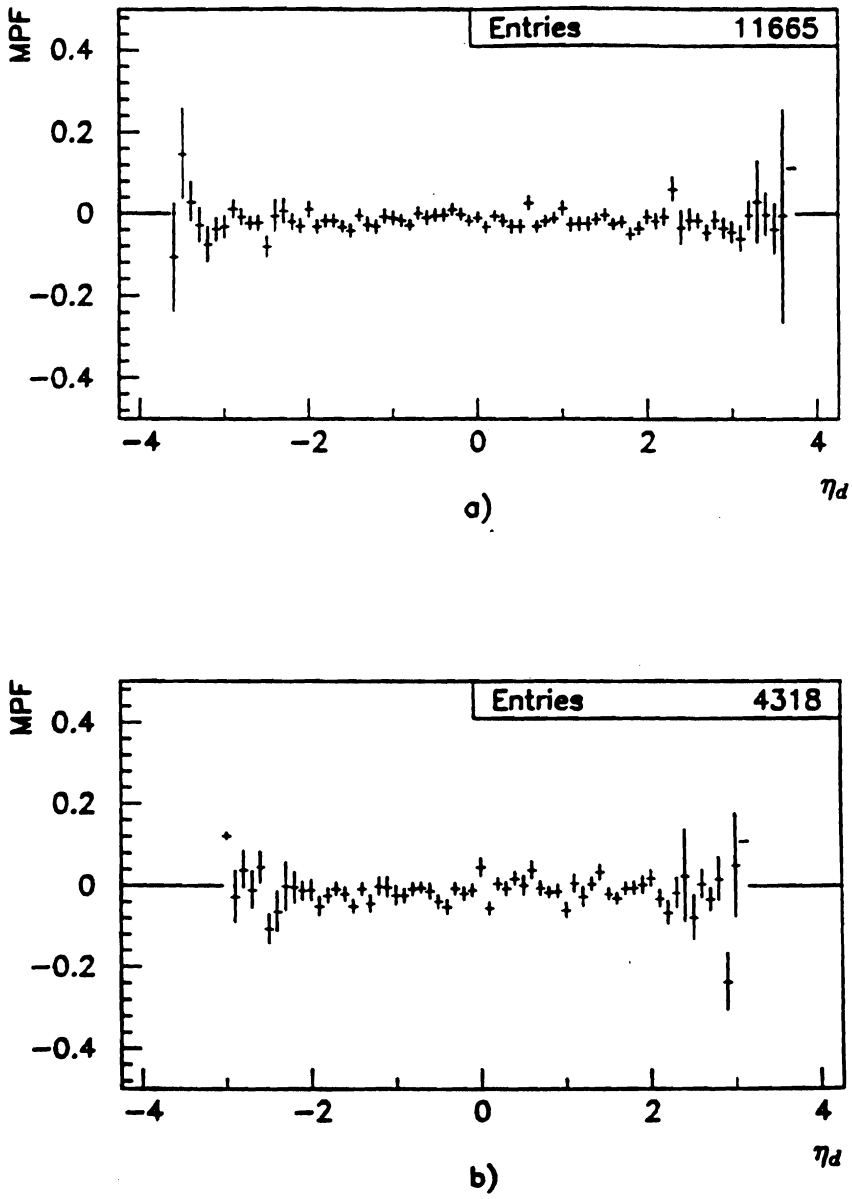

Figure 4.13: *Missing E_t projection fraction as a function of η_d after correction for dijet data in the ranges a) 50 GeV/c $< \sum P_t <$ 100 GeV/c and b) 100 GeV/c $< \sum P_t <$ 130 GeV/c.*

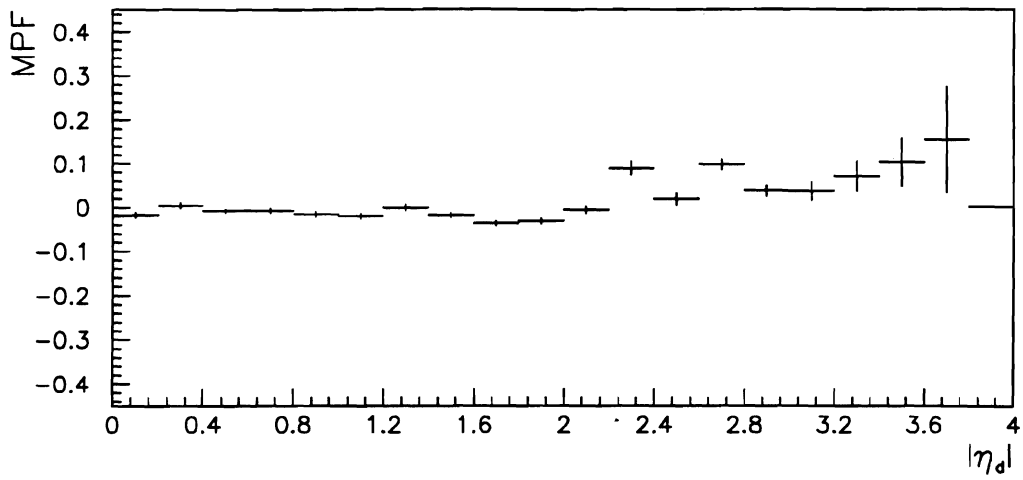

Figure 4.14: *The MPF distribution for simulated jets.*

high energy jets must depend for the most part on statistical issues involving the number of particles in the jet. Since these fluctuations are well understood, it is reasonable to trust the extrapolation of the energy scale to low energy. The β function for selected η_d are shown in Figure 4.15.

4.5 Energy resolution in the forward calorimeters

The dijet balancing technique was described earlier. Here it will be used to find the uncertainty in the jet resolution for jets which are not central. The trigger jet in all cases is a central jet, and the probe jet is not a central jet. Since we think

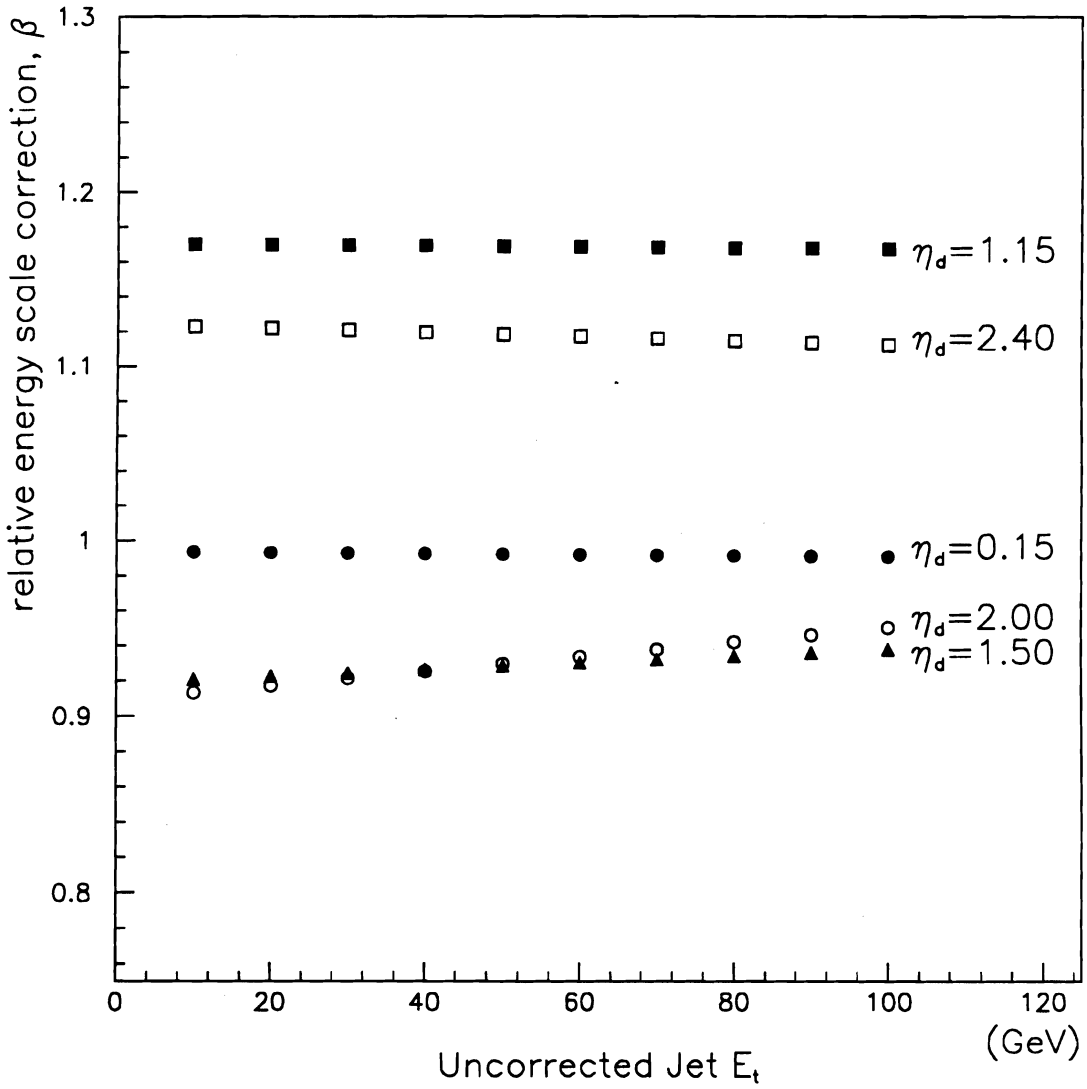

Figure 4.15: ***The correction factor β as a function of jet E_t for selected values of η_d.***

	Data	Sim
90° crack	$.150 \pm .006$	$.144 \pm .005$
central	$.143 \pm .003$	$.144 \pm .003$
30° crack	$.146 \pm .004$	$.149 \pm .004$
plug	$.154 \pm .003$	$.148 \pm .003$
10° crack	$.162 \pm .010$	$.169 \pm .011$
forward	$.150 \pm .007$	$.157 \pm .008$

Table 4.2: *Resolution, $\sigma(k_{t\|\|}^{norm})$, of jets in different detector regions.*

that we have some understanding of the central jet, any discrepancies between the data and the simulation will be attributed to the probe jet. The RMS of the $k_{t\|\|}^{norm}$ distribution is the sum of the central jet resolution and the forward jet resolution. Figure 4.16 shows the distributions for the different regions of the detector and Table 4.2 summarizes the distribution widths. The consistency between Isajet plus QFL and the data is remarkable. However, we will try to estimate the uncertainty in the resolution from the statistical uncertainty on σ in Table 4.3. The resolution of each detector region can be extracted from the distribution by subtracting off the central calorimeter resolution,

$$\sigma(k_{t\|\|}^{norm}) = \sqrt{\left(\frac{\sigma(P_t^{trigger})}{2P_t^{trigger}}\right)^2 + \left(\frac{\sigma(P_t^{probe})}{2P_t^{probe}}\right)^2}, \tag{4.16}$$

which can be solved for the resolution of the probe region. The systematic uncertainty can be overestimated by assuming that all of the difference between

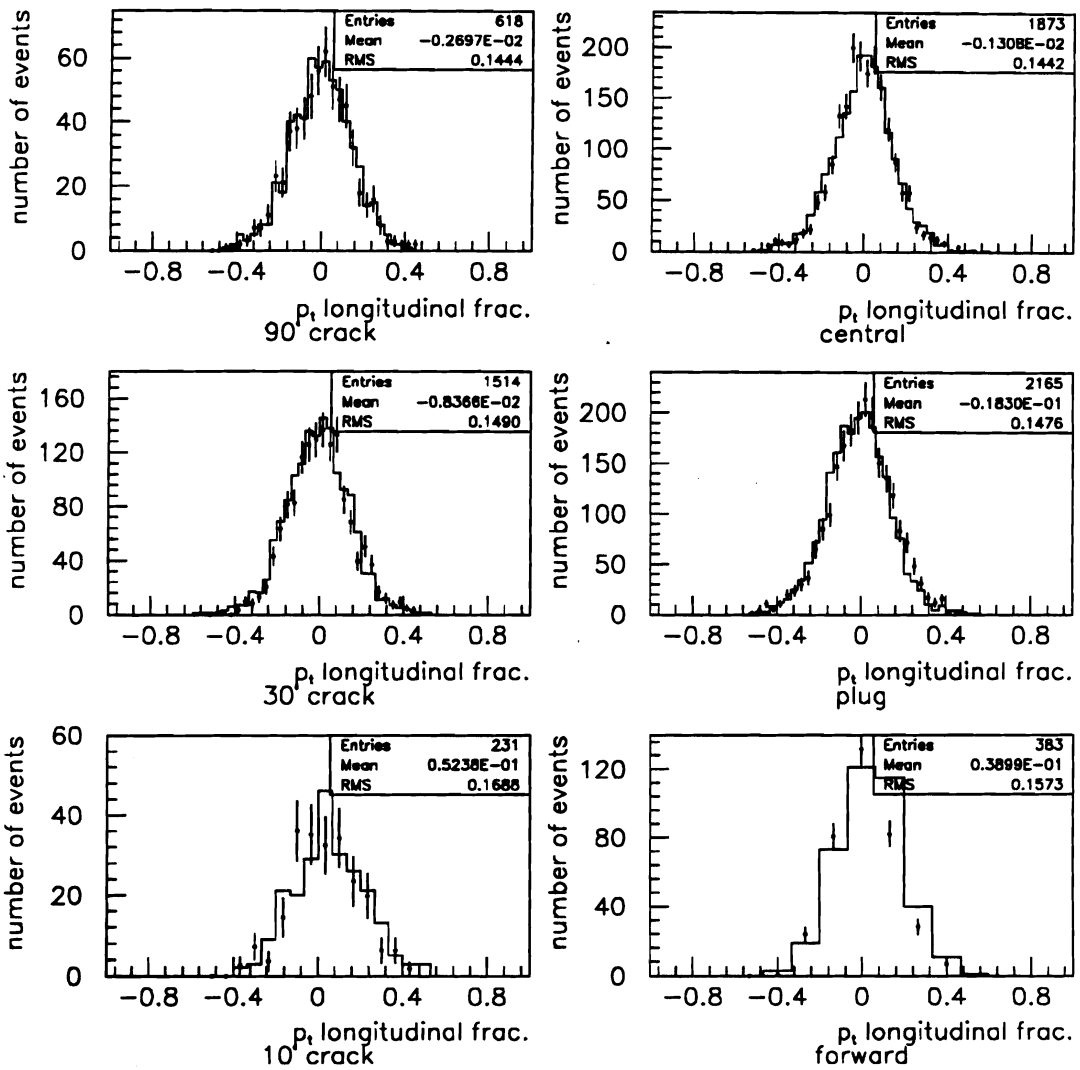

Figure 4.16: ***Perpendicular P_t fraction for different η_d regions.***

	90° crack	central	30° crack	Plug	10° crack	Forward
Relative Unc. in $\sigma(P_t)/P_t$	±7.6%	±4.2%	±6.8%	±8.4%	±12.%	±10.%

Table 4.3: *Uncertainty in the resolution, $\sigma(k_{t\|\|}^{norm})$, of jets in different detector regions.*

the data and the simulation is due to the resolution of the probe jet. These uncertainties are summarized in Table 4.4. Notice that the uncertainty in the resolution is within 10% of the resolution itself.

4.6 Position resolution in the forward calorimeters

To measure the p_t of forward muons relative to the jet axis, it's important to understand the position resolution of the plug and forward calorimeters. Figures 4.17 and 4.18 show the distance between the vector sum of particle momenta within a jet cone and the centroid of the energy cluster in simulated jets. Energy clusters are calculated with the jet clustering algorithm used on the data. The RMS of the distribution distance in η is less than .053 which translates into $\pm 0.5°$ in θ in the forward region. The RMS of the distribution in ϕ is less than .04 radians which is about $\pm 2.5°$. This resolution corresponds to the size of

a tower in the plug and forward calorimeters. Since the major contribution to shifts in the centroid are due to the segmentation of the calorimeter, it is simple to see that QFL, which contains the detector geometry, simulates well the centroid direction resolution.

4.7 Acceptance in the plug/forward boundary region

The acceptance of the calorimeters is modelled with QFL where the geometry of each calorimeter is meticulously accounted for. In addition, the vertex distribution for central jets changes the event's view of the calorimeters. The vertex distribution is gaussian with $\sigma = 30$ cm for central jets. The vertex distribution for the jets in my data sample, described in chapter 3, is distorted by the forward muon trigger bias.

As a general check on the jet finding efficiency, a γ plus jets study suggests that the jet inefficiency can be determined by looking opposite a photon and counting how many times the jet is missing. [44] The inefficiency distribution plotted in Figure 4.19 is $(20 \pm 4)\%$ at 12 GeV and drops linearly to 1% at 23 GeV for all detected Jet η. This technique underestimates the jet efficiency for a number of reasons. First, it is impossible to find a truly clean sample of photons, so many of the "photons" in the events are π^0s. Since pions don't necessarily come from the hard scattering in the event, they may not be balanced by a jet. Second,

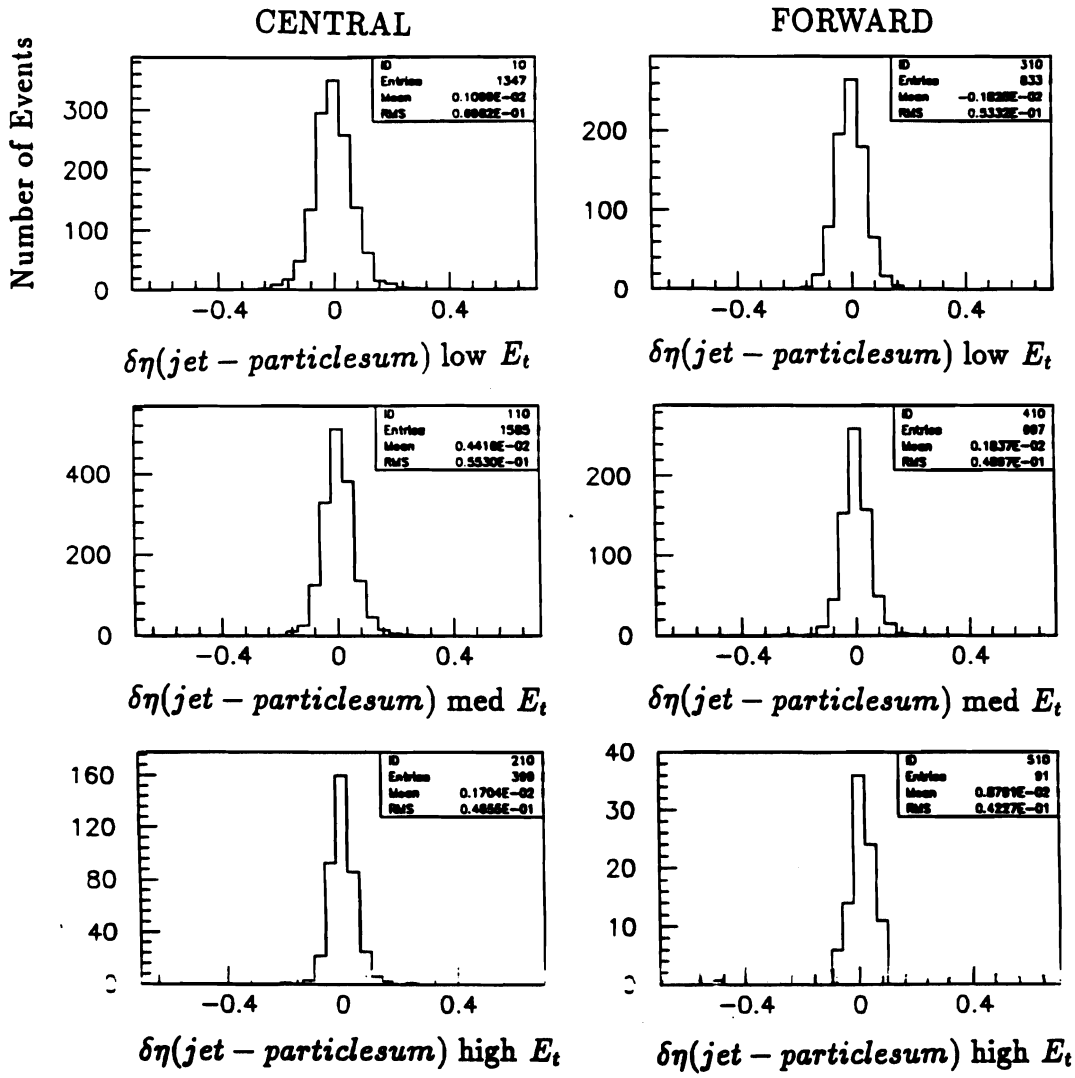

Figure 4.17: *The separation in η between the simulated jet direction and the vector sum of particle tracks which contribute to the jet. Low, medium and high jet E_t are between 10 GeV and 20 GeV, 20 GeV and 50GeV, and above 50 GeV respectively.*

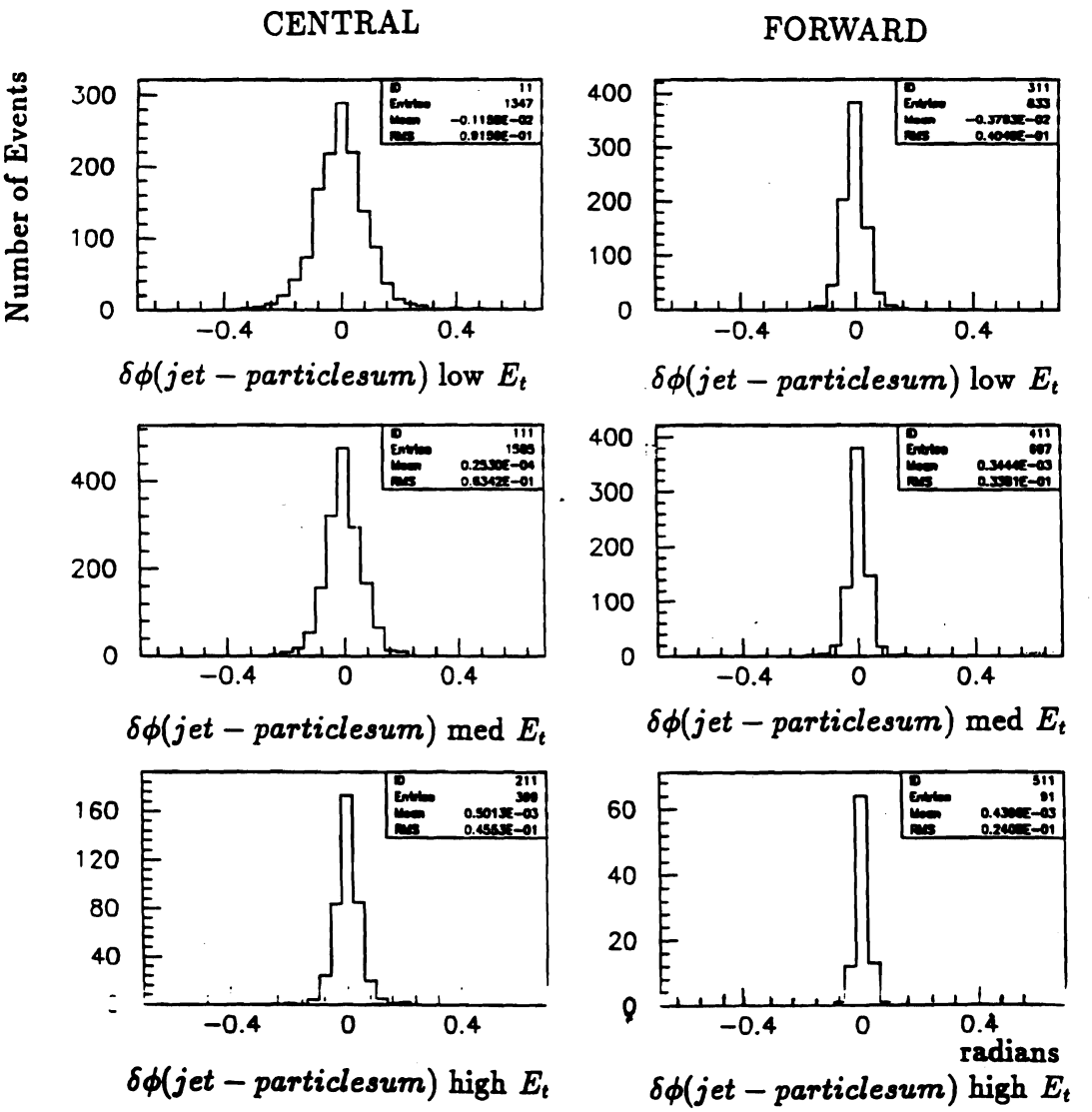

Figure 4.18: *The azimuthal separation between the simulated jet direction and the vector sum of particle tracks which contribute to the jet. Low, medium and high jet E_t are between 10 GeV and 20 GeV, 20 GeV and 50GeV, and above 50 GeV respectively.*

even though this analysis used all the calorimeters at CDF, there are still some losses in cracks between detector components. These holes are modelled explicitly in QFL and are part of the acceptance already discussed. Finally, the explicit requirement that all third jets be less than 5 GeV may not really be satisfactory. In a crack, it is possible that a 5 GeV jet is a miss-measured 10 GeV jet, so that it underestimates the efficiency especially for the lower energy bins. For another estimate of the jet finding inefficiency, I have taken Isajet plus QFL and looked for jets which match in η and ϕ with clusters of generator level tracks. For comparison, the inefficiency is $(4.13 \pm .4)\%$ at 12 GeV and drops to 1% at 20 GeV. This estimate includes the detector acceptance modelled in QFL, but does not suffer from the inability to identify photons or explicit jet cuts which make the sample more back to back in ϕ.

4.8 Summary

For the analysis to follow, I will use the Isajet event generator and fragmentation models of Field and Feynman as well as Peterson to model the production of particles. QFL will be used to simulate the detector response and the standard CDF jet clustering routines will be used to identify energy clusters. I will use QDJSCO to correct the jet energy of both simulated and real data back to the "true" jet energy. These routines embody the central and forward jet energy scales and resolution. Since the integrated cross section is to be measured, and

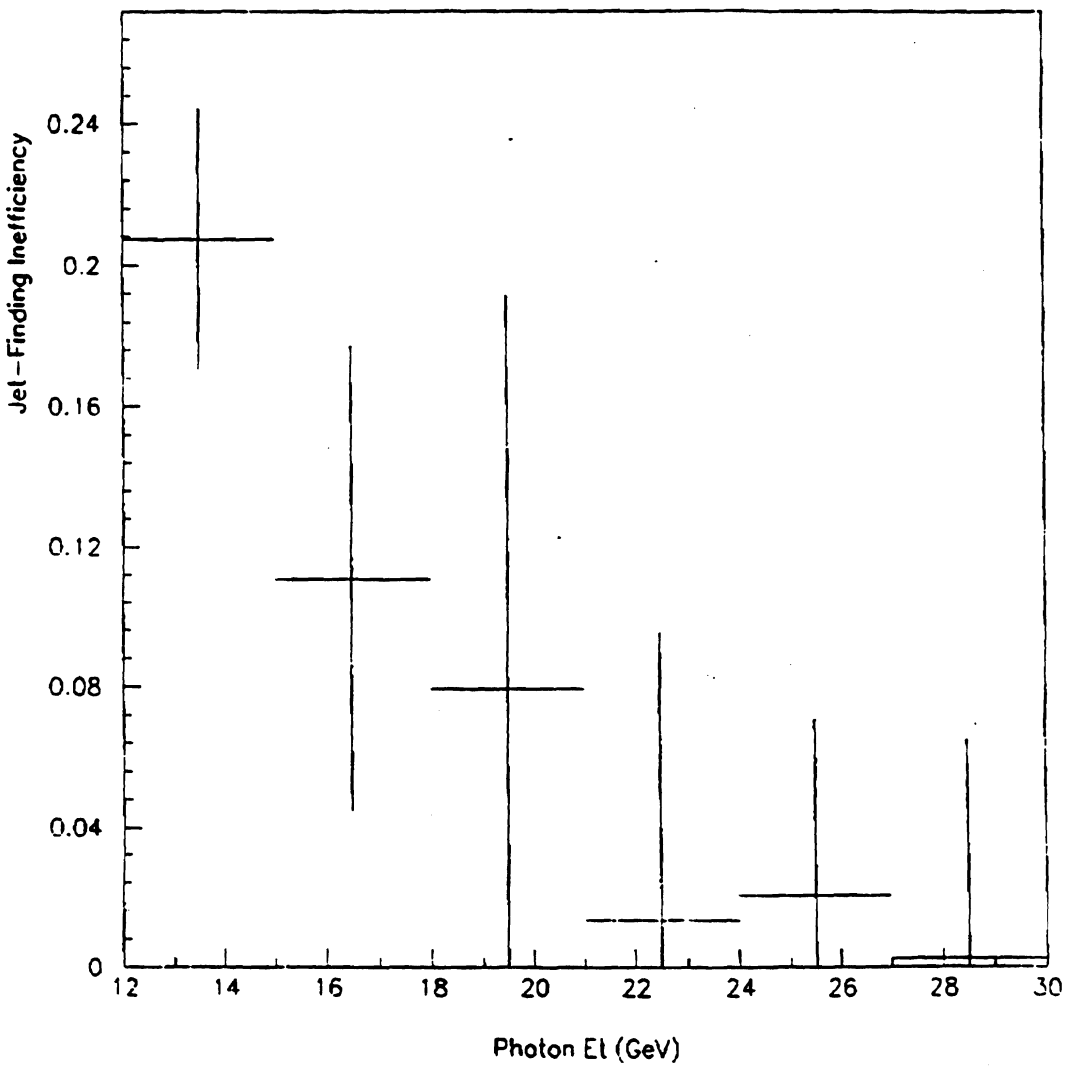

Figure 4.19: *Jet finding inefficiency limit (3rd jet< 5 GeV).*

not the jet energy spectrum, the systematic uncertainty on the cross section due to the jet cuts is simply the number of events which drift into or out of the sample as the jet cut is varied from its nominal value to the max and min values dictated by the systematic uncertainty. The systematic uncertainty of the jet energy scale in the central detector is $^{+7.5\%}_{-6.5\%}$ for 15 GeV jets. In the plug, $1 < |\eta_d| < 2.4$, this is increased slightly to $^{+7.6}_{-6.6}\%$. For 10 GeV plug jets, the systematic uncertainty is $^{+9.7}_{-8.8}$. In addition, the energy scale for simulated bottom jets has a fragmentation uncertainty of +5%. Finally, the uncertainty in the resolution of the calorimeters is ±10% of the resolution. The jet cuts in my final data sample will be varied by these uncertainties to find the uncertainty in the data yield from these sources.

Chapter 5

Muons in Jets Data Selection

Events containing b quarks in the forward region are selected by requiring a forward muon with a nearby jet, and a second jet somewhere else in the detector. The muon and near jet form a b tag while the other jet in the events balances the energy of the b decay. As a starting point, the jet requirements are dropped in order to study the inclusive forward muon spectrum. The inclusive distributions are compared to the sum of simulated physics processes which is used to show that the forward muon data is quantitatively understood. The detector performance is also evaluated with this data sample because it has better statistics than the muons in jets sample. After establishing the quality and efficiency of forward muon data, the remainder of the chapter describes the muons in jets data selection and distributions.

5.1 Inclusive muon selection

The data used in this analysis were selected with the FMU trigger as described in section 3.2. The FMU integrated luminosity for this trigger is $(1.80 \pm .14)$ nb^{-1}. The first level selection included events with reconstructed forward muon tracks containing 5 or 6 chamber hits and the vertex. Coordinate and ambiguity wire hits were associated into pairs if they matched to within 0.5 cm in the radial direction. The fits used a hit resolution of 500 microns in calculating the momentum error matrix and a cathode pulse height of 500 ADC counts. There were 79,731 events selected by these requirements.

Events passing the first level selection were retracked with improved parameters. The tracking parameters that differed were the chamber resolution, now 650 microns and the minimum cathode pulse height which was raised to 800 ADC counts. In the case of the chamber resolution, the change affected the track χ^2 and made it more consistent with the expected shape of the χ^2 distribution. Although retracking the events with the correct resolution causes shifts in the muon momentum and χ^2 of the track, there were no cuts on either momentum or χ^2, so no tracks were lost due to these changes. The cathode pulse height threshold was raised to reduce confusion between noise hits and signals from real muons. The cut of 800 ADC counts is very efficient for real muons, so the effect of raising the threshold was that noise hits were not confused with real pad signals and accidentally used to determine the track ϕ. Since events had not been cut based

on pad ϕ determination, the data yield was not affected.

The inclusive forward muon data sample was selected from retracked events using a standard set of FMU cuts. These cuts are described in detail elsewhere[13] and consist of:

- $p_t^\mu > 6$ GeV
- Trigger cut: all 6 possible hits were found in the muon reconstruction and these hits form a valid trigger pattern which actually fired the FMU trigger.
- No more than 17 chamber hits in the octant with the muon ($3° < \theta < 16°$).
- Track fit must have a $P(\chi^2) > .02$.
- Muon track passes through cell numbers 33 to 55 in the first plane of drift chambers ($1.9 < |\eta_d| < 2.7$).
- An event vertex was reconstructed with 0 cm $< |z_{vtx}| <$ 100 cm
- Calorimeter cut: A minimum ionizing calorimeter energy was required in either the plug or forward calorimeters depending on which calorimeter the track traversed.
  1. Plug electromagnetic energy (PEM) > 0.1 GeV
  2. Plug hadronic energy (PHA) > 0.9 GeV
  3. Forward electromagnetic energy (FEM) > 0.2 GeV
  4. Forward hadronic energy (FHA) > 1.5 GeV

The main cuts which define the acceptance for muon events are the p_t cut and the restriction to cell numbers 33 to 55. Both of these cuts as well as the additional requirements on the reconstructed muon hits restrict the selected sample to muons for which the trigger efficiency is well understood. The trigger and detector efficiencies were discussed in chapter 3. Note that the cell number requirement excludes only one triggered wire which had a different efficiency from the rest. The event vertex is used in the momentum determination and so is required to be in the acceptance region of the VTPC which is the CDF detector component relevant for measuring the vertex position. The motivation for the other cuts is to improve the rejection of fake muon events.

This data set contains 2822 events. This is more than an order of magnitude fewer events than before. Roughly, the rejection may be accounted for as a factor of 2 from requiring only six hit tracks, then another factor of 3 or 4 from requiring these to satisfy the FMU trigger. The cut on the number of hits in the octant with the muon and $P(\chi^2)$ reject another factor of 3. The requirement that the track pass through cell numbers 33 to 55 rejects about 20% of the events. The p_t cut on the muon is not a large factor because the trigger road requirement is strongly momentum dependent and the calorimetry requirement is also not a very large effect for muons passing the other cuts. Thus, the expected rejection factor is roughly 25.

The efficiency of these cuts is listed in Table 5.1. [13, 49, 50] Monte-carlo simulations of decay-in-flight muons were used to determine the $P(\chi^2)$ cut ef-

Cut	Efficiency
$P(\chi^2)$	$.887 \pm .010$
extra hits	$.86 \pm .01$
calorimetry	$.974 \pm .005$
combined	$.743 \pm .015$

Table 5.1: *Efficiency of quality cuts.*

ficiency. These showed consistency also with the data sample. The extra hits distribution as a function of ϕ was used to determine the efficiency of the extra hits cut since the main ring was the major contributor and it was located at the top of the detector. The calorimetry cut efficiency was determined by looking at the minimum ionizing signals associated with the muons in the data. The cut efficiencies were checked with a sample of muons from Z decays and also a sample of muons in jets.

Distributions characterizing the detector's response to the inclusive muon sample are shown in Figures 3.11 and 5.1 to 5.3 The distribution of pad pulse heights (Figure 3.11) clearly show a peak attributed to the energy deposited in the FMU gas volume by minimum ionizing particles. The calorimeter energy associated with the tracks, shown in Figure 5.1, is also consistent with minimum ionizing particles. Together these observations assure us that the sample is largely real muons. Fake muons, namely sets of six noise hits which could coincide to look like a muon track, would not display peaks in these distributions. The lack

of a peak in the PEM is not so much a reflection on the muon as a reflection on the response of the PEM calorimeter to minimum ionizing signals.

The understanding of the charge bias in the trigger is displayed in Figure 5.2 which shows the ratio of positively charged tracks to negatively charged tracks. The bias is due to the geometric trigger road as described in chapter 3. Here we see that there is good agreement between data and simulation.

Finally, as described in chapter 3, the east end of the detector was less efficient than the west. Mainly due to disabled detector components, the efficiency on the east was $.452 \pm .023$ and on the west it was $.570 \pm .028$. Figure 5.3 shows the raw yield on the two ends in both p_t and η and then the same corrected for the E/W efficiency. This shows that our understanding of the trigger efficiency is consistent with the data sample.

5.2 Inclusive muon spectra

The inclusive forward muon sample is expected to result from bottom and charm semileptonic decays, leptonic decays of W bosons, and decay-in-flight pions and kaons. In order to compare the data to expectations, the ISAJET program was used to simulate the bottom and charm contributions, where the results were rescaled by K factors in order to be consistent with the next-to-leading order calculations of NDE.[13, 51] The W boson spectrum was also simulated with ISAJET. The decay-in-flight spectrum was derived from the inclusive charged

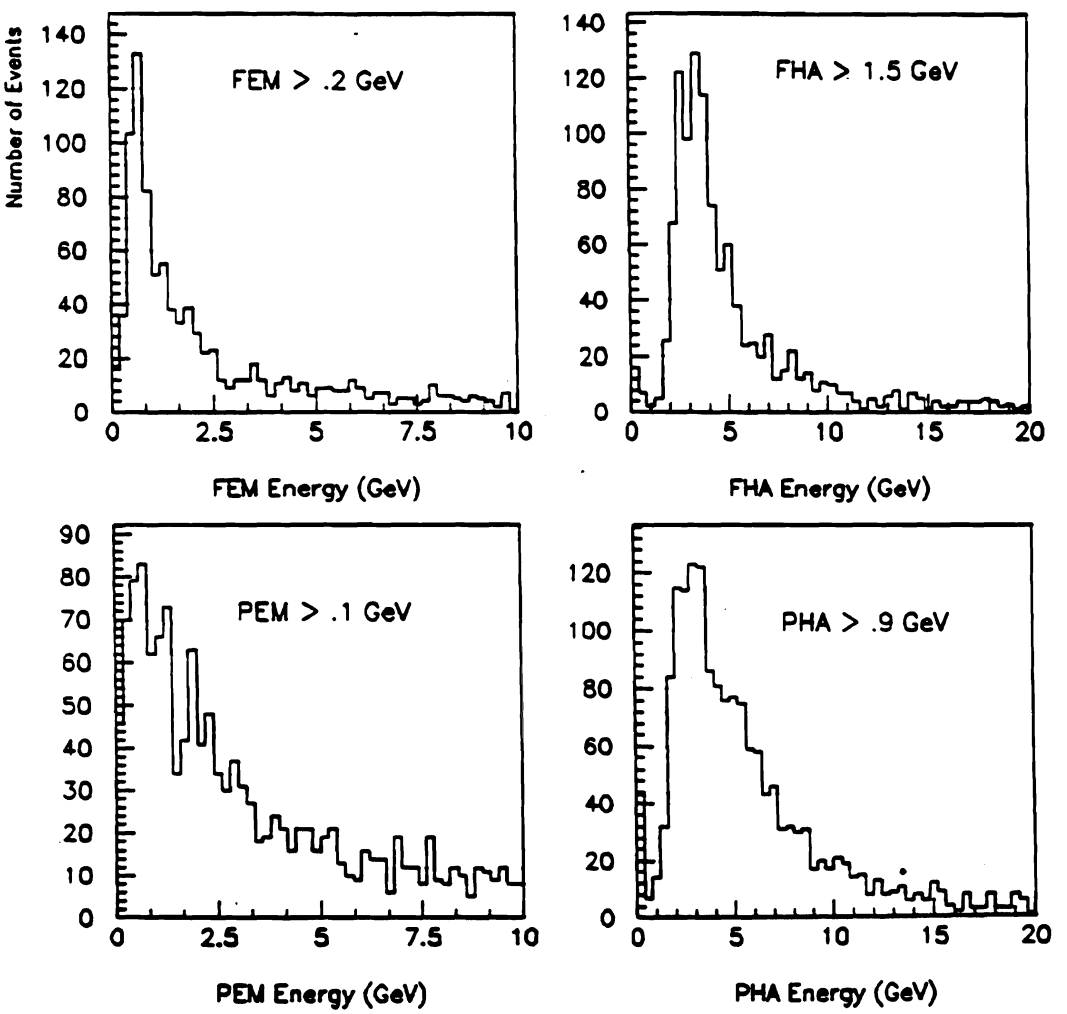

Figure 5.1: *Distributions of energy deposited in a 3×3 array of calorimeter towers centered on the tower through which the forward muon was thought to pass.*

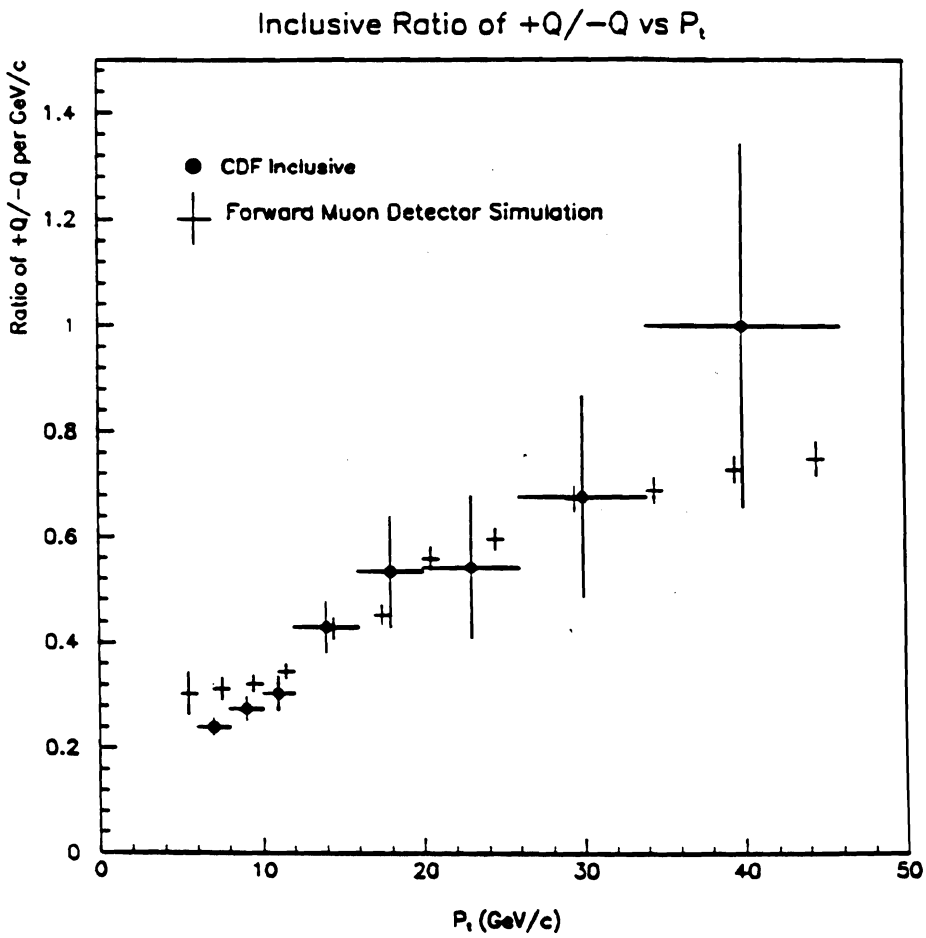

Figure 5.2: *Ratio of positively charged muons to negatively charged muons as a function of momentum.*

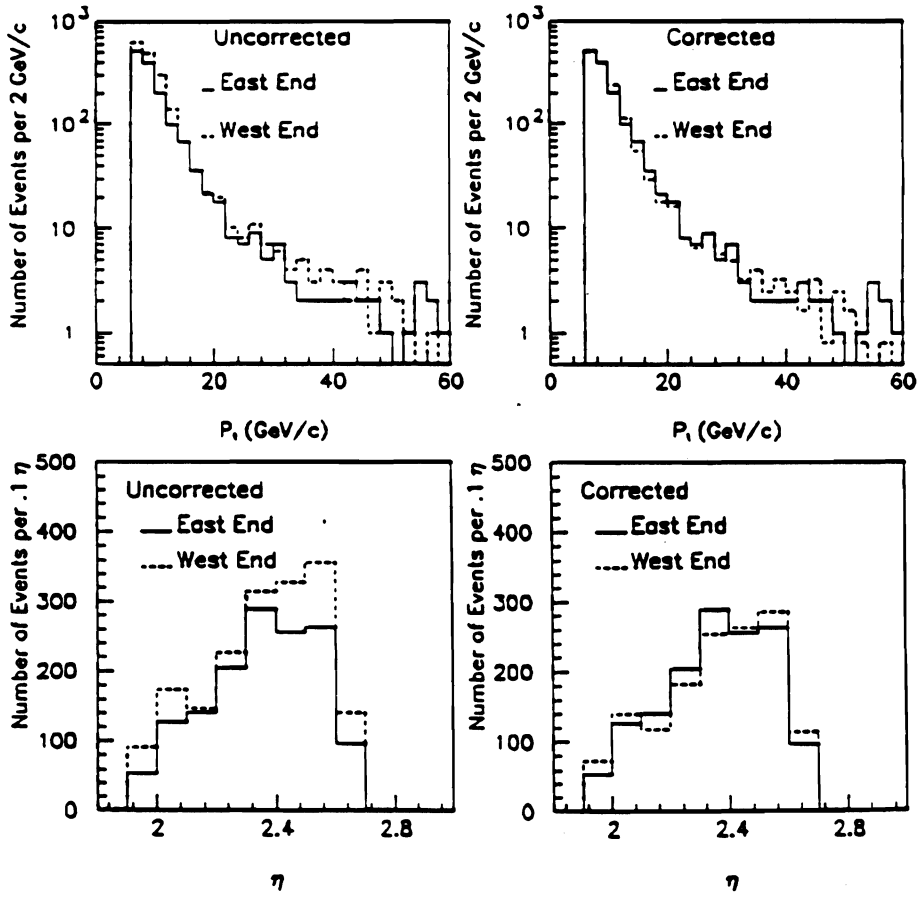

Figure 5.3: *East versus West muon yield. The distributions are shown before and after correcting for the detector efficiency on each end.*

particle spectrum measured by CDF using minimum bias events and two special triggers. The expected muon spectra in the region $1.9 < |\eta| < 2.7$ from these sources are shown in Figure 5.4 before accounting for detector effects. The fully simulated p_t and η distributions of muons - after detector simulation - are shown in Figures 5.5 and 5.6 with the CDF inclusive FMU data. After accounting for momentum smearing, the decay-in-flight process is expected to give a large contribution even at high p_t. The decay-in-flight contamination is especially large for muons with the longer path length to the forward calorimeter. The additional flight path contributes approximately a factor of 3 to the decay-in-flight contribution for the forward calorimeter region ($2.4 < |\eta_d|$) as compared with the plug ($1.9 < |\eta_d| < 2.4$). This is visible in the η distribution.

The data are compared to the sum of the expected contributions in Figures 5.7 and 5.8. The upper and lower bound of the calculated spectra are shown with the data superimposed. The error estimate includes a factor of 2 uncertainty in the bottom and charm cross sections. The measured bottom cross section at CDF in the central detector is about a factor of 2 higher than NDE, and the factor of 2 in the charm cross section is consistent with other CDF analyses.[52, 53] The uncertainty in the decay-in-flight contribution comes from the uncertainty in the shape of the momentum spectrum for isolated π/K measured at CDF. Figure 5.9 shows fits to the charged particle spectrum for all tracks and then also for isolated tracks. The different fits contribute to the uncertainty in the muon yield from this source. Not shown is the uncertainty coming from the π/K ratio. In

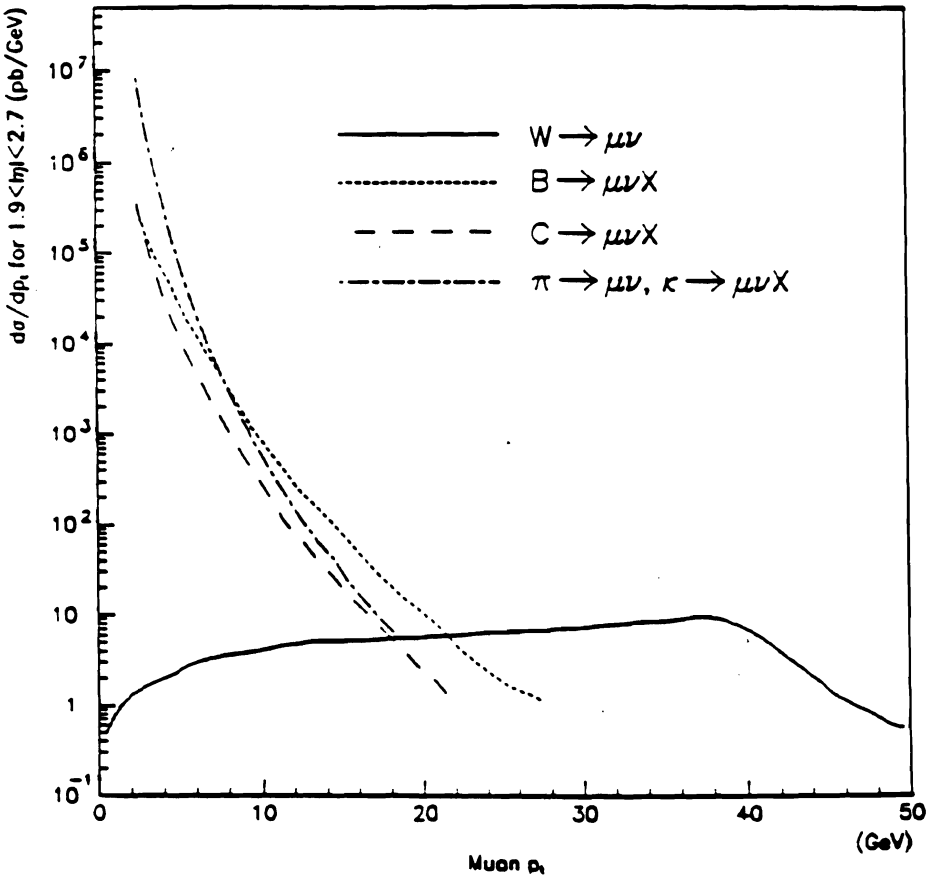

Figure 5.4: *Muon spectrum from W bosons, bottom and charm quarks and decay-in-flight prior to detector simulation.*

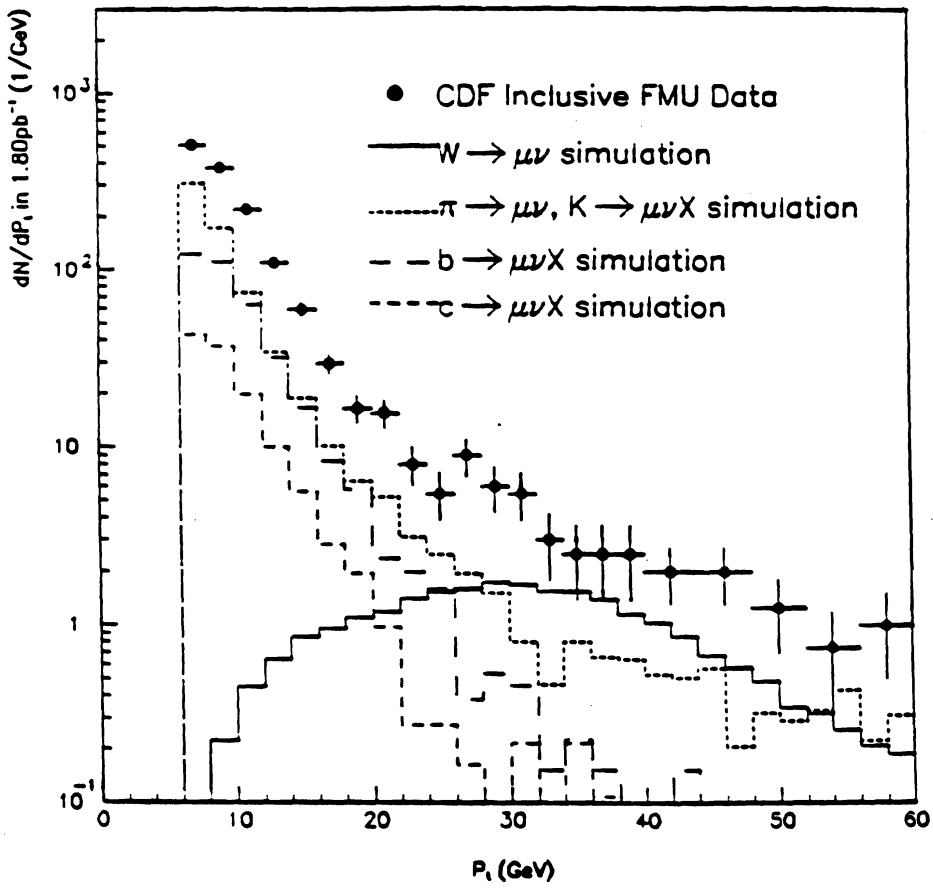

Figure 5.5: *Momentum spectrum for inclusive forward muons compared to simulated processes.*

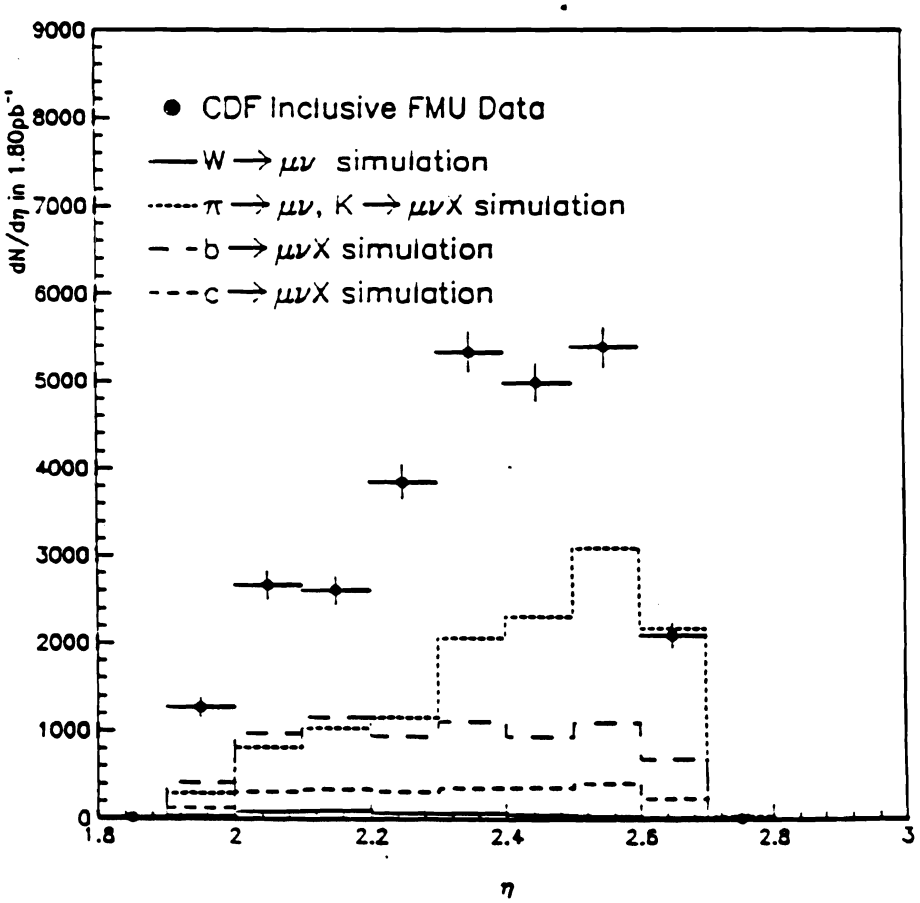

Figure 5.6: *Rapidity distribution for inclusive forward muons compared to simulated processes.*

addition, the tails in the multiple scattering distribution are not well measured and contribute an uncertainty at high p_t which is not shown. Hence, within the uncertainty of the predictions, we have demonstrated that the inclusive sample is consistent with known sources of muons.

5.3 Muons in jets selection

For the muons in jets sample, some of the standard forward muon cuts are relaxed and additional jet cuts are imposed. The bottom quark tag is formed from a muon, $p_t > 5$ GeV, and a nearby jet, corrected $E_t > 10$ GeV. An opposing jet, $E_t > 15$ GeV is chosen which is as far from the muon in azimuth as possible. Finally, a few of the standard forward muon cuts are used to ensure that the muon was of sufficient quality to satisfy the trigger and have a reliably measured momentum. The cuts which define the muons in jets sample are listed below under headings which indicate the purpose for each cut. Also listed are the parameters used in the tracking.

- bottom quark tag

    1. 5 GeV $< p_t^{\mu} <$ 100 GeV
    2. Jet $E_t^{corr} > 10$ GeV
    3. find the closest jet by minimizing $\delta R_{\mu-jet}$
    4. required $\delta R_{\mu-jet} < 1$

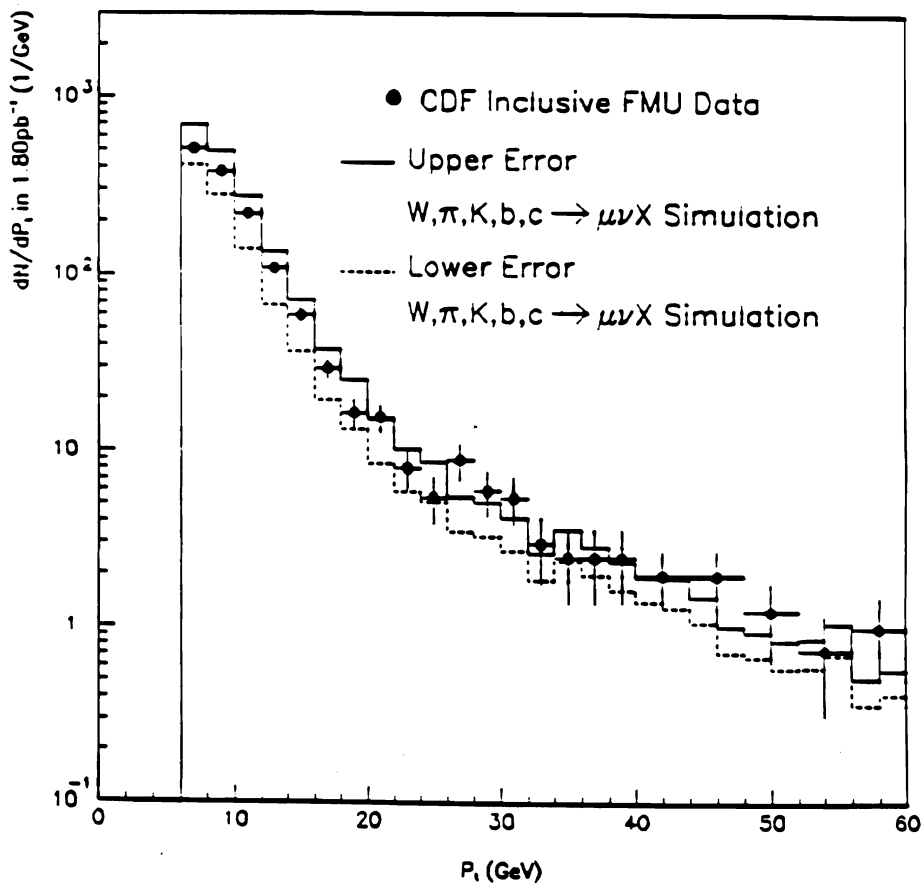

Figure 5.7: ***Momentum spectrum for inclusive forward muons compared to the predicted contributions from physics processes. The band shows the upper and lower theoretical estimates.***

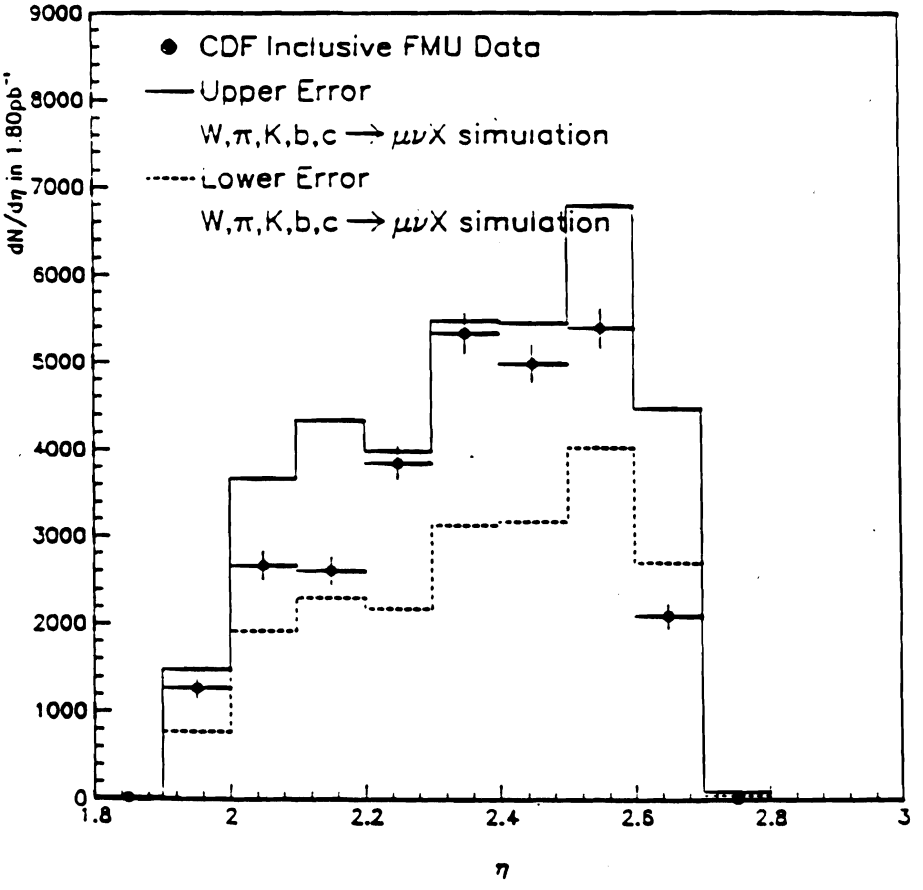

Figure 5.8: ***Rapidity distribution for inclusive forward muons compared to the predicted contributions from physics processes. The band shows the upper and lower theoretical estimates.***

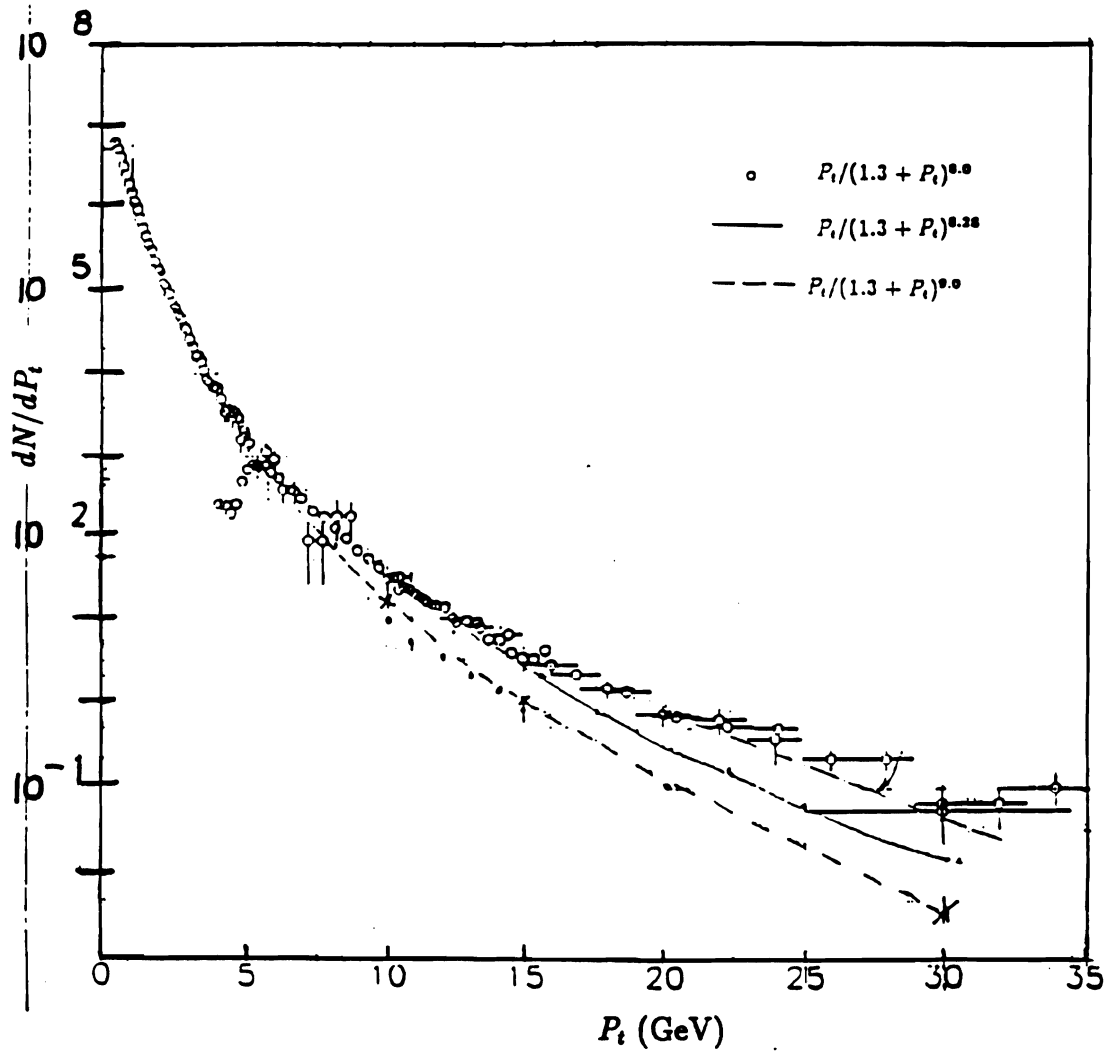

Figure 5.9: *Charged particle spectrum at CDF.*

5. Jet $|\eta_D| < 2.4$

- opposite jet

  1. Jet $E_t^{corr} > 15$ GeV
  2. choose the jet with the largest azimuthal opening angle
  3. $|\eta_D^{oppjet}| < 2.4$

- FMU trigger and quality requirements

  1. all 6 possible hits were found the muon reconstruction and these hits form a valid NUPU 50% trigger pattern which actually fired the FMU trigger
  2. Muon track passes through cell numbers 33 to 55 in the first plane of drift chambers ($1.9 < |\eta_d| < 2.7$)
  3. Track fit must have $P(\chi^2) > .02$

- FMU tracking parameters

  1. 650 micron chamber resolution
  2. pad threshold = 800 ADC counts

The bottom tag requires that there is a muon which is very near a jet. The distance in $\eta - \phi$ space is measured using the quantity $\delta R = \sqrt{\delta\eta^2 + \delta\phi^2}$. The jet passing the E_t cut with the smallest δR is selected. The opposite jet is chosen

as that which passes the E_t cut and is closest to 180° away in ϕ from the muon. This jet is expected to maintain energy balance in the events.

There are 326 events in the forward muons in jets sample. 158 events were in the East detector and 168 were in the west. This gives an E/W ratio of $.94 \pm .10$ which is consistent with expectations. The charge bias of the trigger as a function of p_t is shown in Figure 5.10. This is in agreement with that of the inclusive sample from the previous section (figure 5.2.

There are a number of additional checks that we have on the data to ensure that the particles have a satisfactory muon signature. These will be discussed in detail for the rest of this section.

The vertex Z distribution is shown in Figure 5.11. The distribution has a slightly displaced mean and a wider RMS than the beam spot, which was explained in chapter 3.

The quality of the FMU track fit is shown by the probability of χ^2 distribution (Figure 5.12). This distribution is very flat which indicates that the tracking algorithm works correctly and that the resolution of the detector is correctly modeled.

Sometimes a low momentum track will fake a higher momentum track when hits contaminate the reconstruction. Extra hits can arise from muon bremstrahlung and delta rays, or they may come from other sources independent of the muon. The problem of reconstruction errors goes up as the number of extra hits gets large. The distribution of the number of hits in the octant with

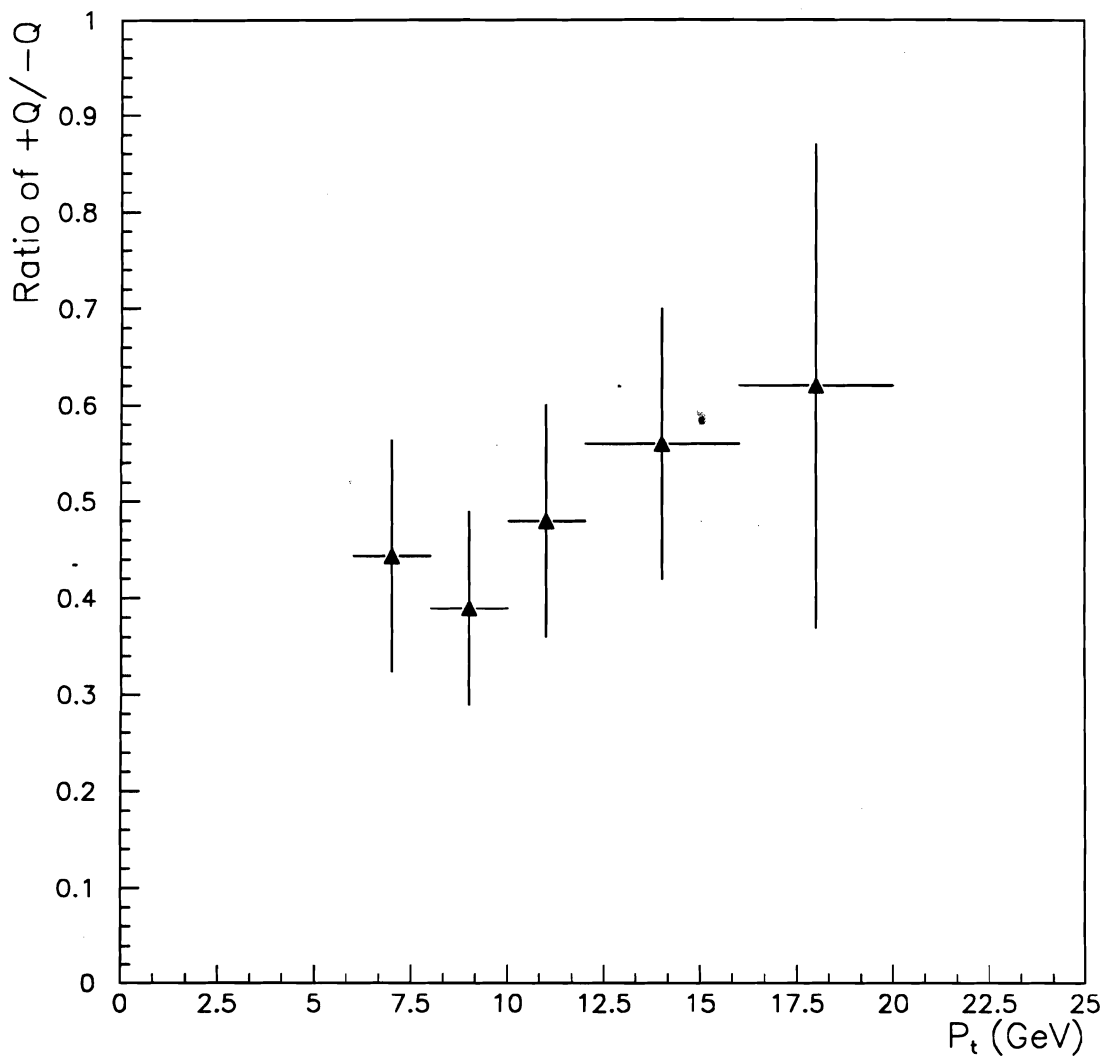

Figure 5.10: ***Ratio of positively charged muons to negatively charged muons as a function of momentum in the muons in jets data sample.***

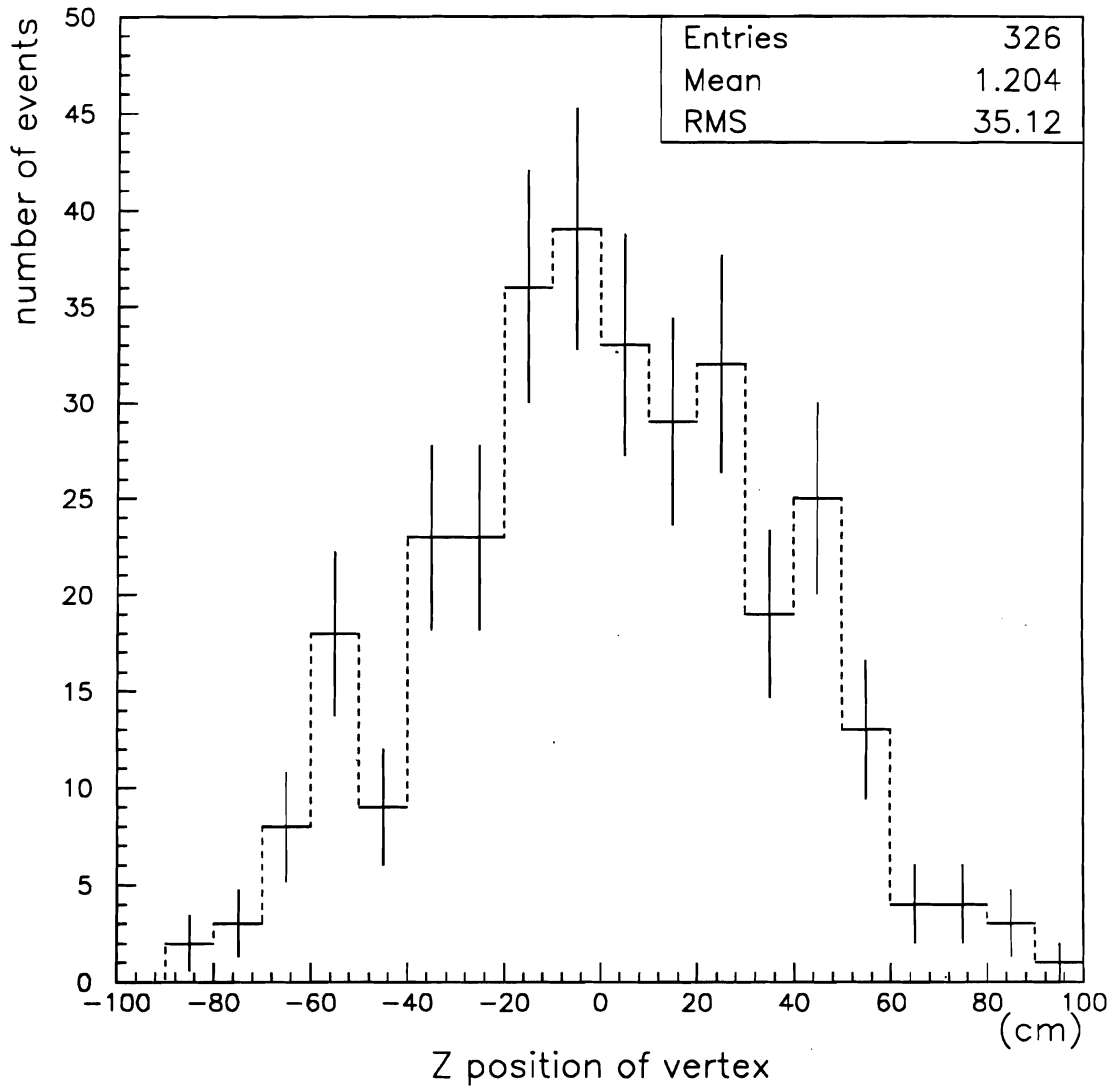

Figure 5.11: ***Vertex distribution of the muons in jets data sample.***

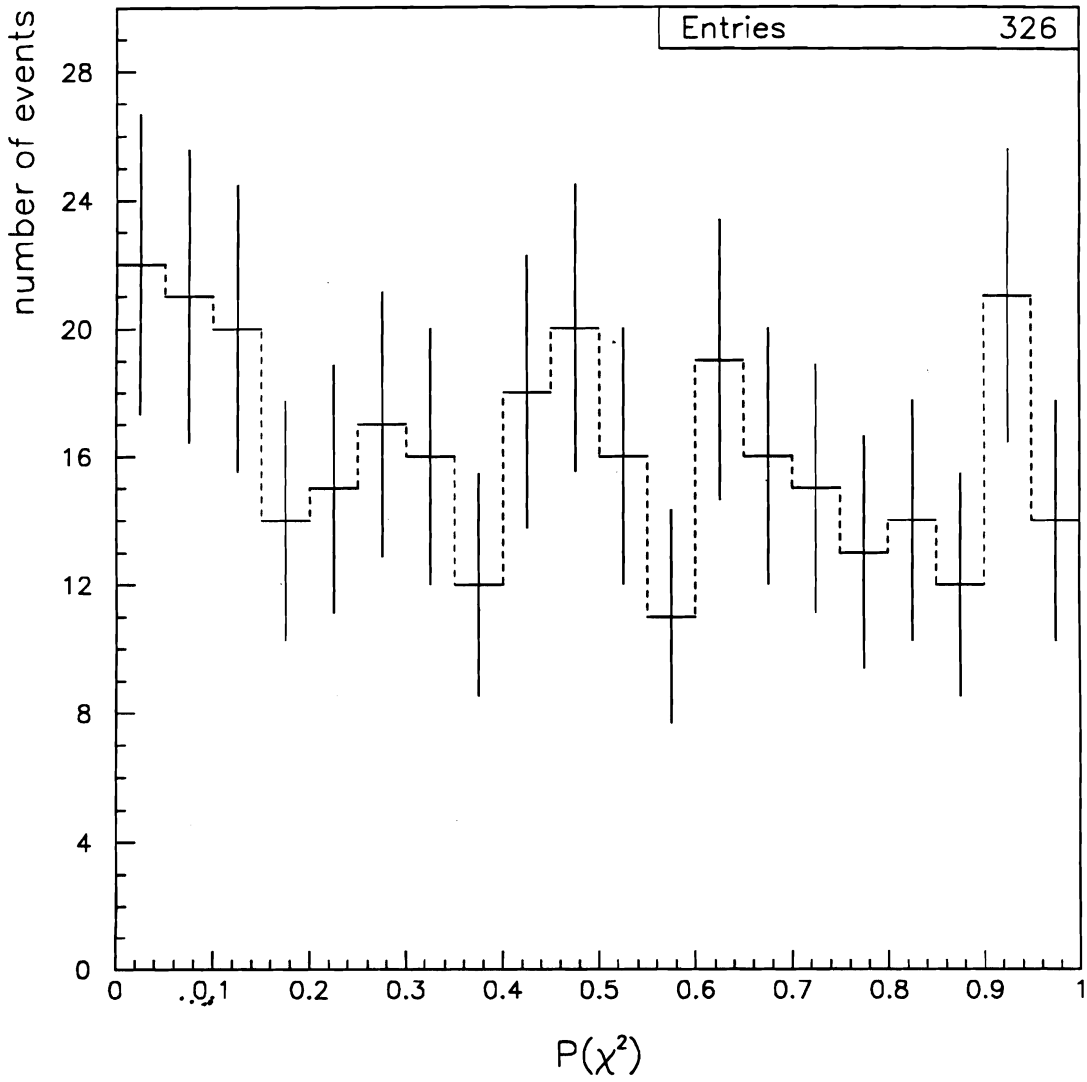

Figure 5.12: ***The probability of χ^2 distribution for the muons in jets data sample.***

the track is shown in Figure 5.13. The track itself should give 6 hits, so all hits above this may be considered "extra." The distribution is consistent with other FMU data samples, for example $Z \longrightarrow \mu\mu$.[13]

The distribution of pulse heights read out from the pads clearly show a minimum ionizing peak in Figure 5.14. Only seven events in the sample have more than one pad with pulse height below 1000 ADC counts. This is $(2.1 \pm .8)\%$ which may be compared to the inefficiency in Figure 3.11a of 4.8%. Since the momentum spectrum is stiffer for the muons in jets data, it is expected that the multiple scattering is a smaller effect than in the inclusive sample. The plug calorimeter signals for the muons in jets sample are shown in Figure 5.15. These have a higher energy spectrum than the inclusive spectrum due to the requirement of a jet in the vicinity of the muon.

A limit for the fake muons in the sample comes from the χ^2 distribution. Not shown in the $P(\chi^2)$ distribution (Figure 5.12) are the 78 events which fail the cut on this variable but otherwise would have entered the muons in jets sample. Random hits which fake muon tracks were discussed in section 3.9. Over 90% of fake muon tracks have a $P(\chi^2)$ which fails the cut. If all the low $P(\chi^2)$ events are fakes then the data sample contains 8.5 ± 1.2 fakes which is $(2.6 \pm .4)\%$ of the data sample. Since not all low $P(\chi^2)$ tracks are fakes, this constitutes an upper bound.

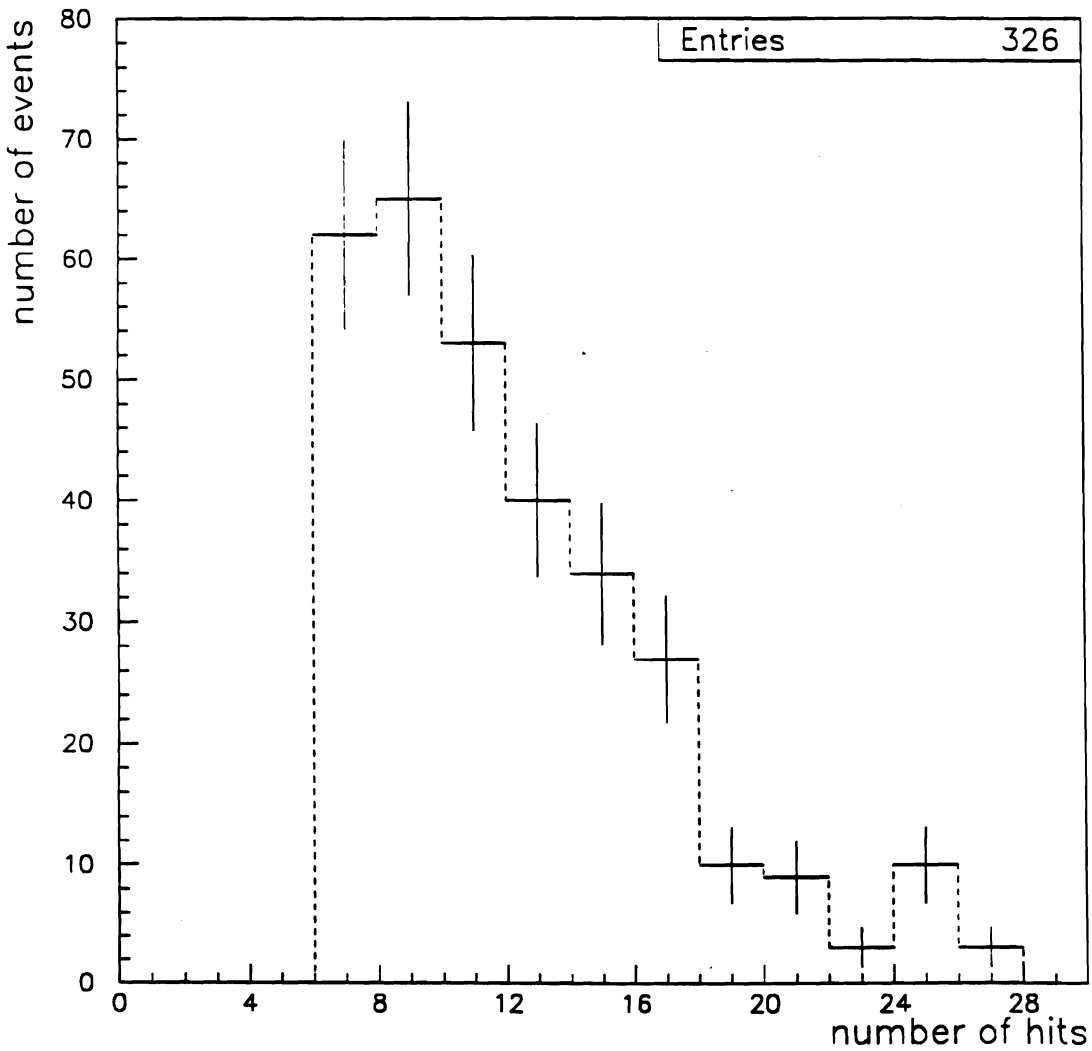

Figure 5.13: ***Number of wire hits in the octant containing the track.***

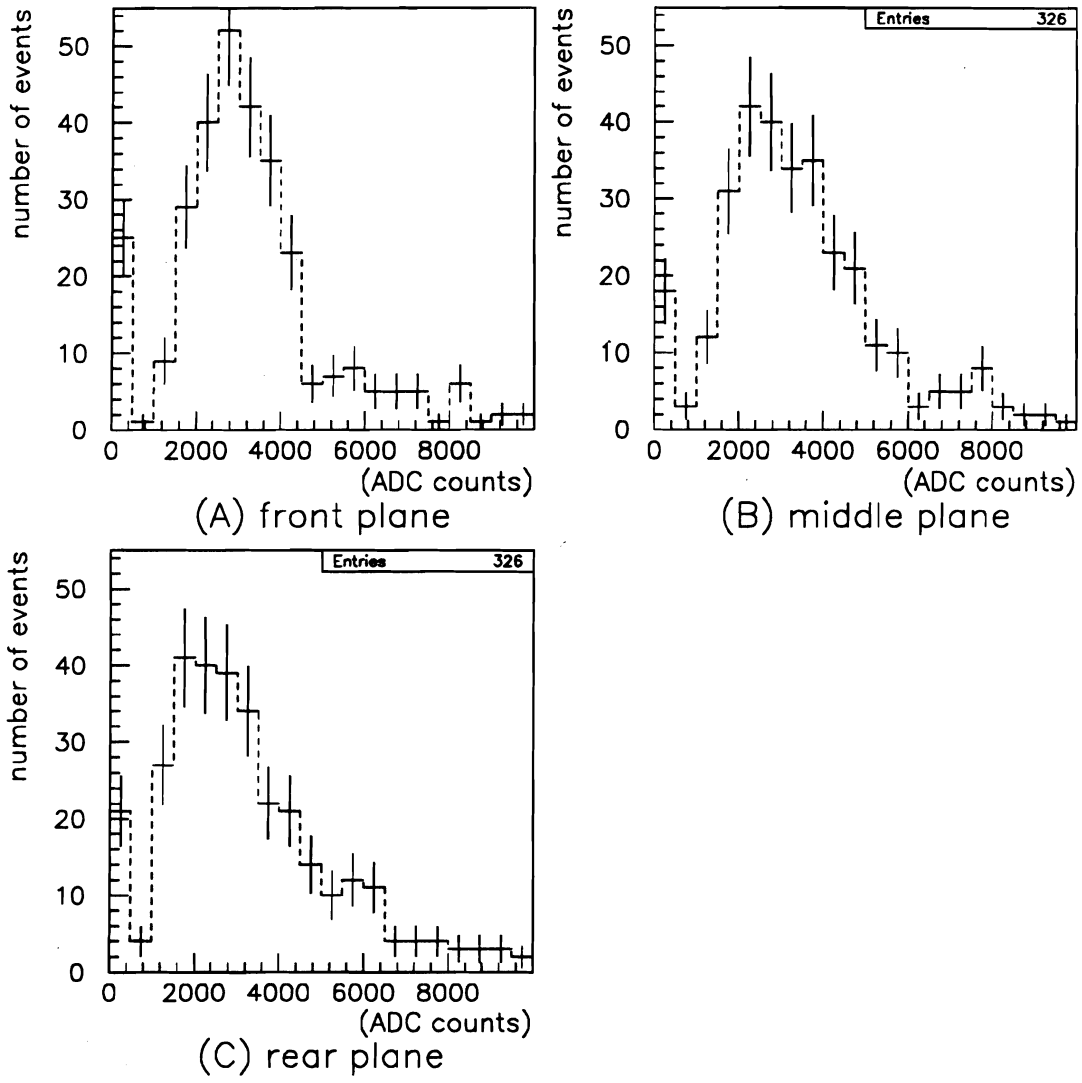

Figure 5.14: ***Pulse height distributions for pads in units of ADC counts.***

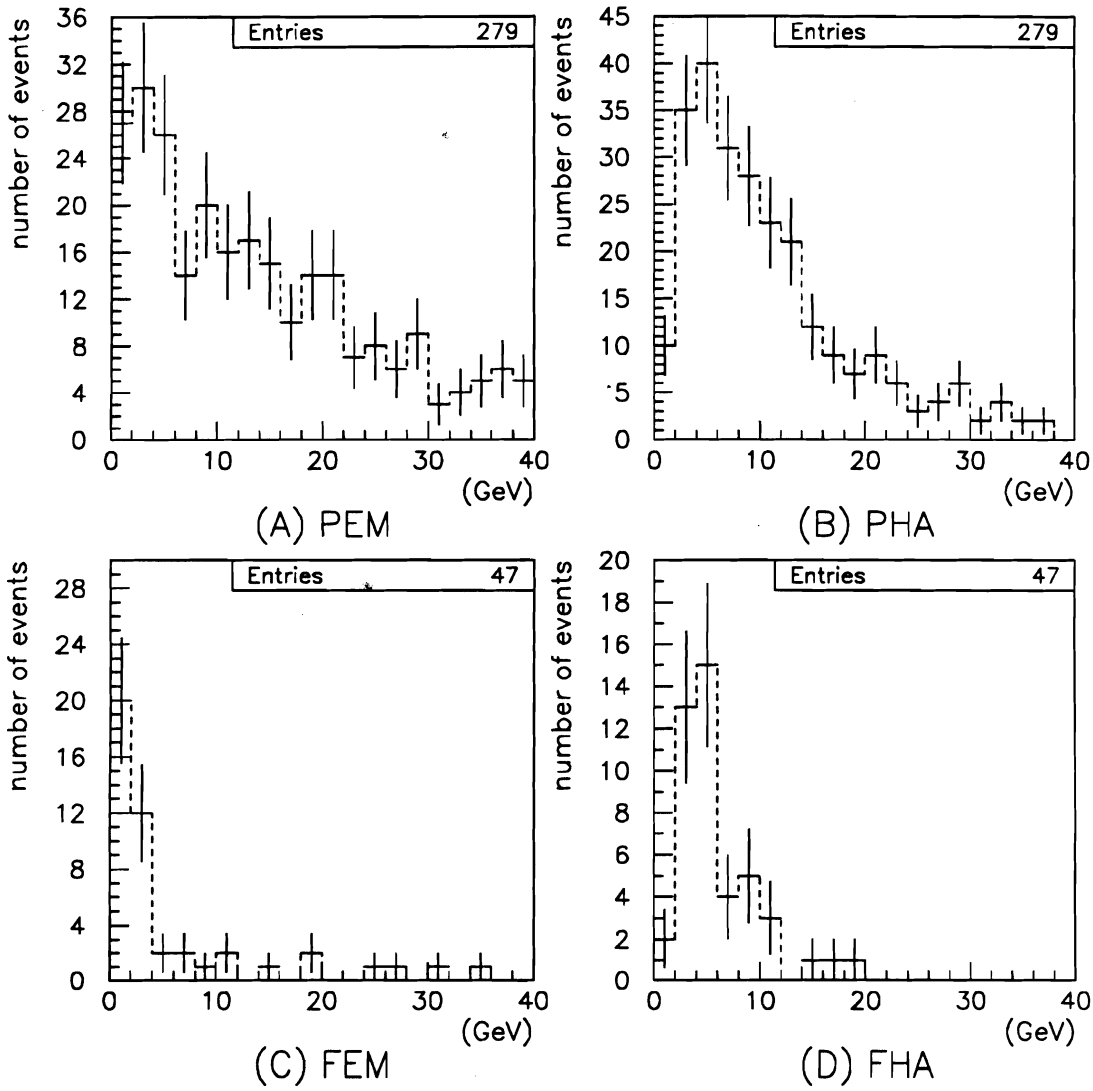

Figure 5.15: ***Plug electromagnetic and hadronic energy in the 3×3 array of towers centered on the tower through which the forward muon passed.***

5.4 Muons in jets spectra

Each event in the muons in jets sample contains one muon and two jets. Each of these objects is described by a four vector which can be analysed separately or in relation to each of the other vectors. Since there are too many relationships between the jet and muon objects to explore them all, a sensible set is chosen here. The corrected transverse energy and rapidity distributions for the jets are shown in Figure 5.16 Muon distributions of p_t and η are shown in Figures 5.17A and 5.17B. The angular distance between the muon and closest jet is shown in Figure 5.17D and the p_t of the muon relative to this jet axis, p_t^{rel} is shown in Figure 5.17C. Figure 5.18A shows the azimuthal opening angle between the muon and the opposite jet as well as the opening angle in ϕ and η between the muon and the near by jet.

5.5 p_t^{rel}

The most intriguing distribution in this sample is the p_t of the muon relative to the jet axis which is defined as:

$$p_t^{rel} = p^{\mu} \sin \alpha \tag{5.1}$$

where p^{μ} is the muon momentum and α is the space angle between the jet and the muon. The p_t^{rel} distribution is broader for heavy objects. Therefore, since different quarks have different masses, this variable can be used to distinguish

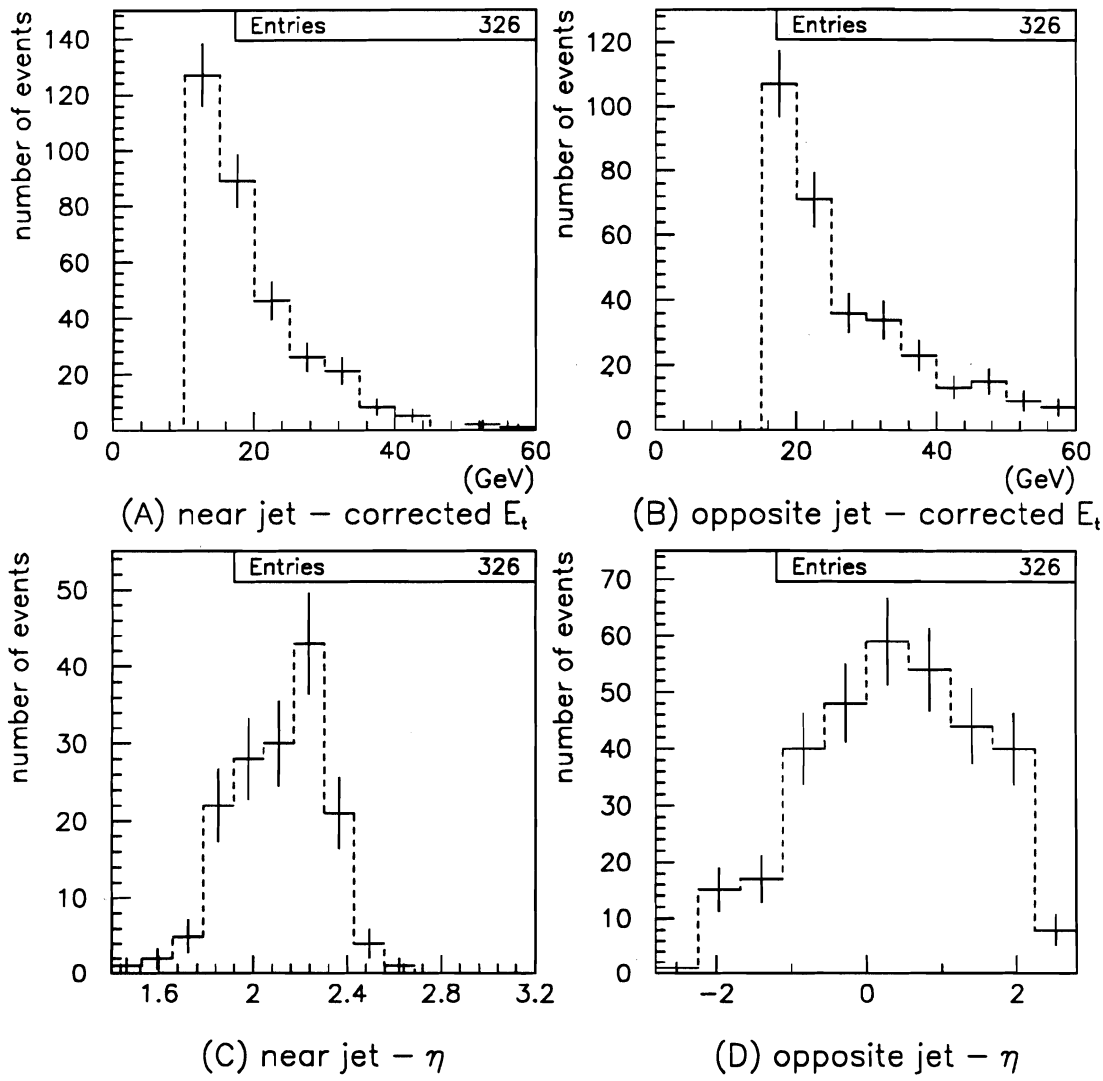

Figure 5.16: ***Transverse energy and rapidity distributions of both jets in the muons in jets sample.***

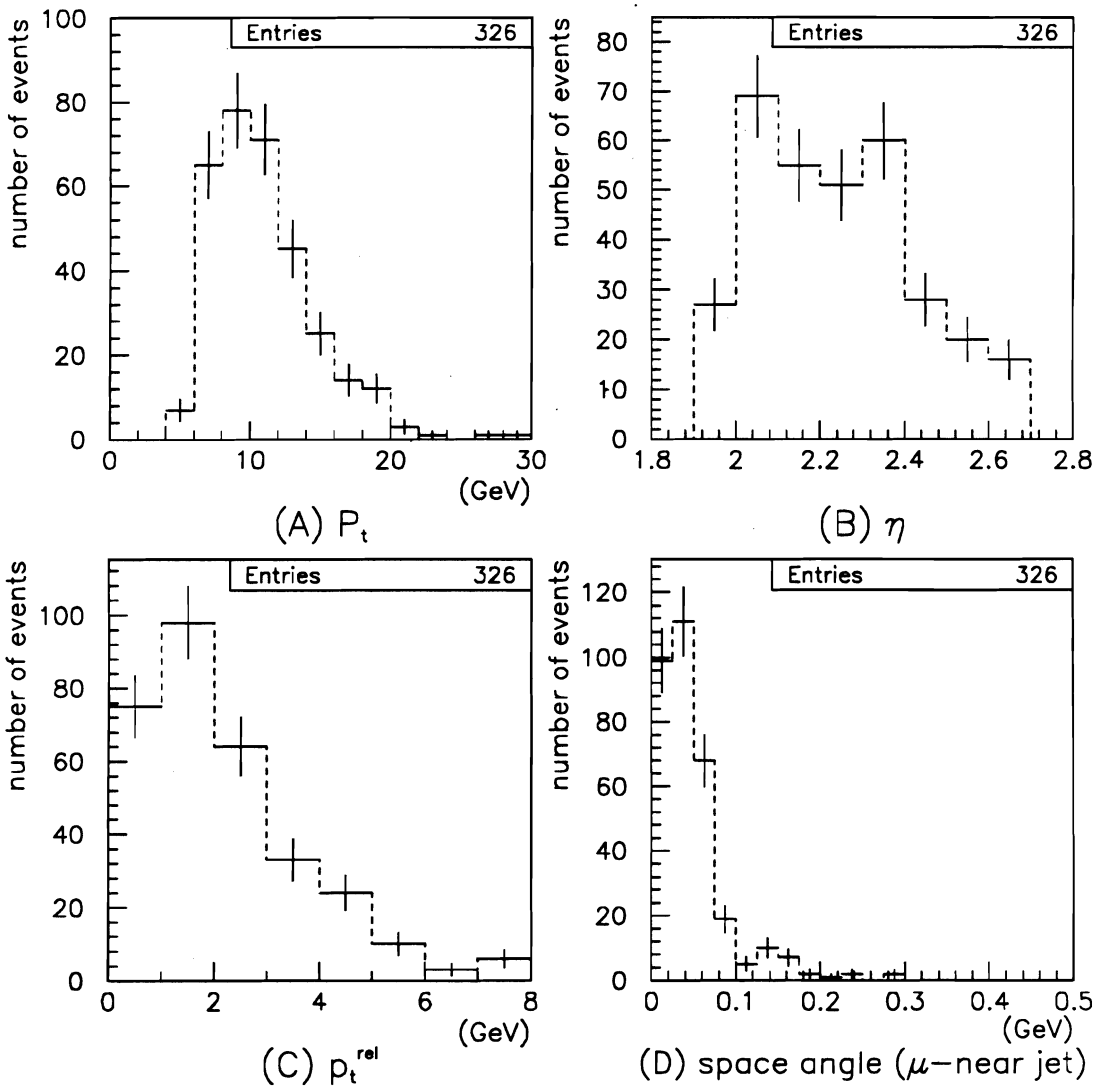

Figure 5.17: ***(A) Muon momentum and (B) pseudorapidity distributions of the muons in jets sample. (C) P_t^{rel} (D) δR.***

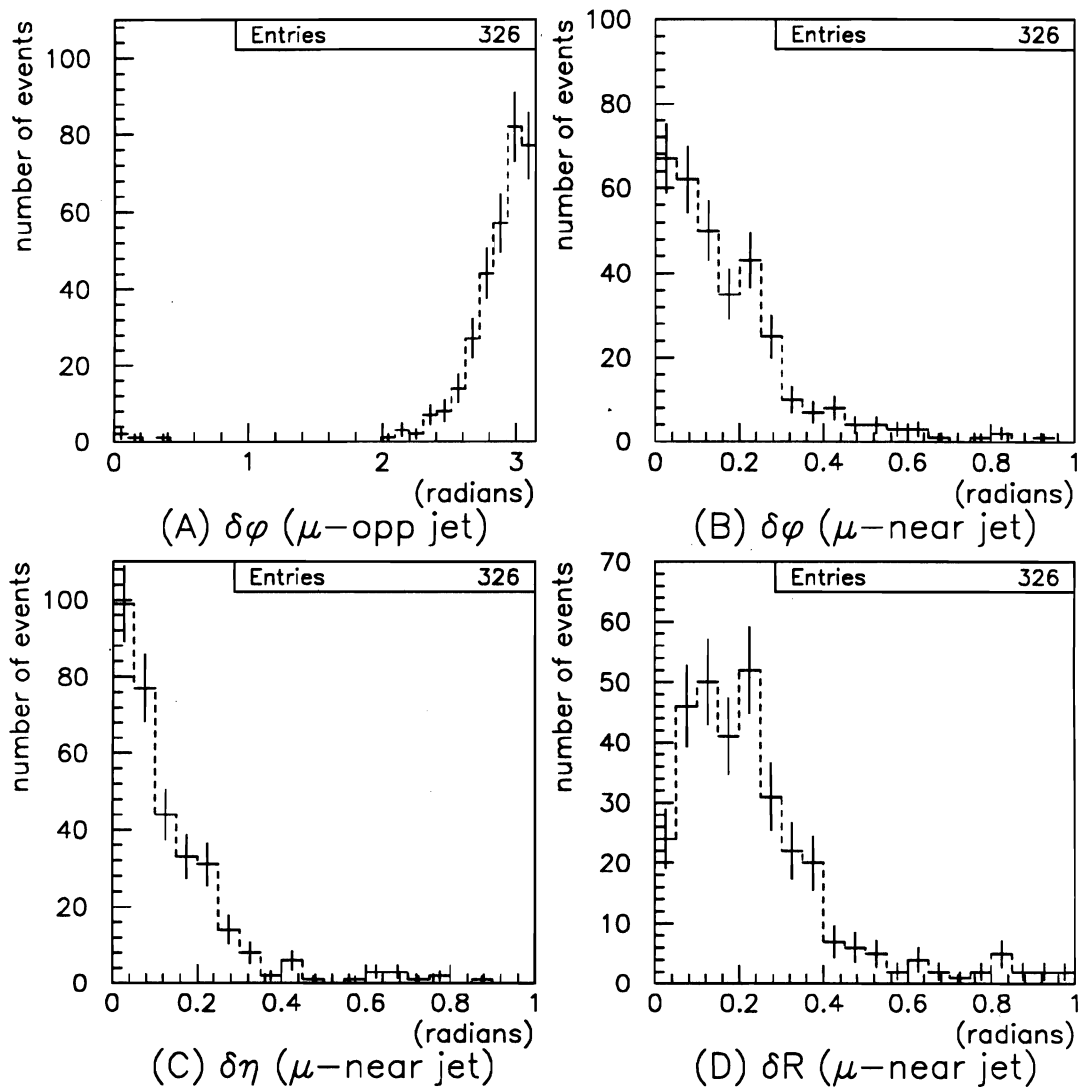

Figure 5.18: ***(A) Opening azimuthal angle between the muon and the opposite jet. (B) Opening azimuthal angle between the muon and the near by jet. (C) Difference in pseudorapidity between the muon and the near by jet. (D) $\delta R_{\mu-jet}$ between the muon and the near by jet.***

quark flavor.

When a jet is accompanied by a lepton, we know that there was a semi-leptonic decay of a hadron somewhere in the group of particles which make up the jet. The p_t of the lepton with respect to the original hadron direction is an invariant under boosts in that direction. A boost to the rest frame of the hadron which decayed is given by the Lorentz transformation:

$$E' = \gamma(E - \beta p_{||}) \tag{5.2}$$

$$p'_{||} = \gamma(p_{||} - \beta E) \tag{5.3}$$

$$p'_t = p_t. \tag{5.4}$$

where $\gamma = E_{had}/P_{had}$. Now we define $p_t^{rel'}$ to be the component of the lepton momentum along the boost direction;

$$p_t^{rel'} = p^{lep} \sin \alpha' \tag{5.5}$$

where α' is the angle between the lepton and boost direction. Since the hadron decay is isotropic in its rest frame, the average value of $\sin \alpha'$ is $2/\pi$. The average momentum of the decay product is proportional to the mass of the hadron. Hence, the average value of $p_t^{rel'}$ is proportional to the mass of the decaying hadron and since this quantity is invariant under boosts, we can use it to tag hadron masses.

In the data, p_t^{rel} is calculated using the jet direction instead of the original hadron direction. Since cuts on the lepton p_t and jet E_t bias the sample toward neutrinos of small momenta, it is approximately true that the p_t^{rel} defined this

way is twice the value it would be if it were defined along the boost axis. It is preferable for data analysis to use α to minimize the dependence of p_t^{rel} on the energy of the jet. With this definition, only the direction of the jet is used, whereas for α', the sum of the jet and muon four-vectors must be used. The systematics of α are minimal, and the quark flavors are still separable.

Here we have shown that the mean of the p_t^{rel} distribution is broader for heavier quarks. The full distribution, however, is smeared about the average result by decay kinematics and detector resolution. Simulated distributions will be used in the following chapter to show that the broadening with increased mass is still observable in the data.

Chapter 6

Bottom Content in FMU and Jets Data

The purpose of this chapter is to extract the number of events in the data which are due to bottom quark decays. The method is to compare the data to simulated distributions of muons from all the known physics processes which contribute to the muons in jets sample. The number of events attributed to bottom quark decays can then be turned into a cross section by accounting for acceptances, efficiency and modelling. There are several ways to determine the fraction of observed events due to bottom quarks. The simplest method uses p_t^{rel}, the component of the muon momentum perpendicular to the nearest jet direction. Additional information on the contribution of "direct" b production is then obtained from the opposite jet. Lending support to these results are distributions which

reproduce many features of the observed data as a sum of contributions from the calculated signal and backgrounds. Finally, the systematic uncertainties associated with modelling and the detection of muons and jets are calculated.

6.1 Simulation

Simulated events are generated with the ISAJET program which models the fundamental physics interactions at the parton level and subsequently models the formation and decay of real particles from the simulated partons. The detector simulation of muons and jets is performed separately. The passage of muons through the detector is simulated using a special purpose fast subroutine (FSIM).[13] The calorimeter response is simulated using QFL, a standard CDF routine, which includes resolution, nonlinearities and detector nonuniformity effects in the jet energy measurement. The output of the detector simulations is filtered with the same analysis code as my data.

Five physics processes are simulated. Events with only a pair of bottom quarks at the parton level, "direct" bottom, are generated with bottom quarks in the kinematic region: 7 GeV $< p_t^b <$ 100 GeV and $.5 < \eta^b < 3$. Bottom mesons are formed using the Peterson fragmentation model. The fraction of these mesons which decay in the muon channel is taken as $B(B \longrightarrow \mu + X) = .11$. Direct charm events are generated in the same way with 8 GeV $< p_t^c <$ 100 GeV and $B(C \longrightarrow \mu + X) = .16$. The Feynman-Field fragmentation scheme is used for

charm events.

In practice, the simulation of "direct" quarks proceeds in two separate simulations. First, the quark pairs are generated where only the negatively charged quarks are forced to decay to μ^-. Then another sample of quark pairs are generated where only the positively charged quarks are forced to decay to μ^+. The events in the two final samples are then added together as one sample. As long as the same number of bottom quark events are generated in the two samples, they have the same luminosity and may represent the semileptonic decay of either quark or anti-quark. The occasional event where both quarks decay semileptonically is simulated by allowing the natural branching ratio to act on the other quark in the simulated events. Since the trigger road acceptance for muons has a charge bias, the simulation of both charges is necessary. The requirement of a jet opposite in azimuth from the muon makes it necessary to allow the other partons in the event to decay naturally.

Bottom or charm quarks can also be produced in pairs from gluon splitting in events where the initial state partons collide and produce one or more gluons. To simulate these processes, events with two final state gluons are generated in the kinematic region (8 GeV $< p_t^{gl} <$ 100 GeV). In some fraction of these events, bottom or charm quark pairs are found in the shower of particles stemming from a gluon, and then the negatively charged quark is forced to decay to a μ^-. Again, the simulation of both positive and negatively charge muons is necessary. To save computational time, however, each muon is simulated twice, once with the

correct charge and once with the sign of the charge flipped. In addition, since the acceptance and efficiency of detecting low momentum muons are so low, each muon is simulated ten times so that fewer events need to be generated. Finally, the decay-in-flight background is simulated by generating two-jet events of all kinds, finding final state pions and kaons, and allowing these to decay to muons (see Appendix B). In this sample, muons of both charges were simulated simultaneously and each muon was simulated ten times. The simulated luminosity has been adjusted to reflect the additional factor of ten.

All muons, $p_t^\mu > 2$ GeV, were simulated with the fast simulation monte-carlo module. The fast simulation module contains the geometry of the iron in the plug and forward calorimeters and the two toroids. It accesses the geometry data base to find surveyed chamber and wire positions and calculates the toroidal magnetic field. As the muons traverse the iron in the detector, they lose small amounts of energy due to ionization. dE/dx energy losses are simulated including Landau fluctuations. Chamber hits are displaced from the perfect track position by multiple scattering which is included as a gaussian distribution about the mean direction. The width, σ, is given by

$$\sigma = \frac{1}{\sqrt{3}} x\theta_0 \tag{6.1}$$

where x is the length of material traversed by a straight track and θ_0 is given by

$$\theta_0 = \frac{13.6MeV}{\beta cp}\sqrt{\frac{x}{X_0}}[1 + 0.038ln(\frac{x}{X_0})]. \tag{6.2}$$

Here p is the muon momentum, βc its velocity and X_0 is the radiation length

of the material. The survey uncertainty and chamber resolution contribute to the measured chamber resolution of 650 microns. Chamber hits are smeared by a gaussian of width 650 microns to account for this contribution. Finally, as muons pass through detector, they produce extra particles like delta rays and bremsstrahlung photons. Particles that are produced in the last centimeter of steel before the chambers can be energetic enough to escape the toroid steel and produce extra hits in the chambers. These hits have been modelled with GEANT and the resulting distributions are added to the simulation. The extra hits provide a realistic challenge to the tracking algorithm which makes decisions on which hits belong to a particular track or not. The extra hits were also used to model the two hit resolution from the Amplifier/Discriminator. If two hits are produced in the chamber simulation which would be recorded by the TDCs within 100 ns of each other, then the second hit is dropped. Other effects such as the non-gaussian tails of multiple scattering and additional survey errors were not simulated and are treated as systematic effects on the measurement.

The energy deposition in the calorimeter from the final state particles created by ISAJET were simulated with the QFL module. It simulates the calorimeter cracks in ϕ and η as well as the single particle response to pions and electrons. The sum of the calorimeter energy in each tower is then written into the element banks where the clustering and jet finding codes are then run on it. Jet banks are then analysed by the same analysis module used on the data to identify jets which are associated with muons.

physics process	generation cuts	N^{gen} (million)	N^{sim} (events)	$\int_{sim} Ldt$ (pb^{-1})
direct b	7 GeV $< p_t^b <$ 100 GeV $.5 < \|\eta^b\| < 3.$	2.8	829	27.9
direct c	8 GeV $< p_t^c <$ 100 GeV $.5 < \|\eta^c\| < 3.$	1.4	206	9.89
gluon split b	8 GeV $< p_t^{gl} <$ 100 GeV	49.7	415	4.81
gluon split c			307	3.77
decay-in-flight π	8 GeV $< p_t^{parton} <$ 100 GeV	.7	289	4.81
decay-in-flight K			149	1.13

Table 6.1: *The number of events generated with ISAJET and those which survive the simulated efficiency and acceptance of the detector, trigger and analysis cuts. Included are the generation cuts for each physics process simulated and the integrated luminosity for the simulation.*

A large number of events is generated, N^{gen}, for each physics process simulated. After simulating the efficiency, ϵ_{sim}, and acceptance, A, of the detector, trigger and analysis cuts, the number of events still in the sample is N^{sim}. This number of events left in the simulated sample corresponds to a simulated integrated luminosity, $\int_{sim} Ldt$. Table 6.1 lists the number of generated and simulated events as well as the generation cuts and luminosity that these events correspond to.

There are several factors which contribute to $\int_{sim} Ldt$. The integrated luminosity for each ISAJET simulation run is given at the end of the computer job. This luminosity has to be corrected by hand for simulation cuts and weighting factors. The only simulation cut was applied to the direct bottom and charm simulations. For these, only quarks produced at positive rapidity were simulated, therefore, a factor of $\epsilon_{cut} = 2$ is necessary to correct the luminosity for the measurement in the backward detector. The ISAJET luminosity must also be corrected for the branching ratio of all decays which were produced with the FORCE command. Bottom and charm quarks have their own branching ratio, (.11 for bottom and .16 for charm), and the decay-in-flight events are each weighted by the probability that the muon actually decayed. The average probability that a pion in the sample decayed to a muon is .0013. The average probability that a kaon in the sample decayed to a muon is .0047. These are the equivalent branching ratios for the decay-in-flight spectrum. There is one final correction factor for the simulated luminosity for simulations which were later corrected with a weighting function, $f(p_t, \eta)$. Where the quark production cross section is corrected with a QCD correction factor, K, or a function in p_t and η, the equivalent luminosity is modified. The definition of the simulated luminosity is,

$$\int_{sim} Ldt = \frac{\int_{ISAJET} Ldt}{\epsilon_{cut} \times B(quark \longrightarrow \mu) \times K \times f(p_t, \eta)} \tag{6.3}$$

Most of these correction factors do not apply to all the simulations. Where a particular term is irrelevant, it is replaced by 1.

Naively, one may wish to divide the last two columns in Table 6.1 and multiply by the FMU integrated luminosity to predict the number of events in the sample coming from various physics processes. This, however, leads one to the conclusion that the number of events in the data sample is far smaller than the predicted number of events. The answer to this dilema is that the normalizations for the backgrounds in ISAJET are known to be untrustworthy. The charm cross section is not known accurately at $\sqrt{s} = 1.8$ TeV and this contributes two background processes. Other analyses at CDF have normalized this distribution to the NLO NDE predictions and then added an arbitrary uncertainty of a factor of two. Since the other analyses are not highly affected by the rate, this is considered conservative. In this analysis, the charm contribution is determined by fits of the simulated distribution to data. Similarly, the ISAJET simulation of particles in jets is not perfectly tuned to match real jets. The π/K ratio for all particles in the simulated events is modified to match the inclusive measurements, but the uncertainty in this ratio is not included. In addition, the particle spectrum in the ISAJET events is not perfectly tuned. Therefore, this analysis does not rely on the simulated number of events for anything other than the statistical uncertainty in the simulation. Instead, the shapes of simulated distributions will be used. The distributions chosen for the fits rely on specific kinematic features of the events which are believed to be reliably simulated.

6.2 Total b quark cross section from fit using p_t^{rel}

The simulated p_t^{rel} distributions are shown in Figure 6.1. Each of the simulated distributions is normalized to unit area. Notice that the light quark processes are concentrated at small p_t^{rel}. Table 6.2 shows the fraction of events with p_t^{rel} in two bins, one above and one below 2 GeV for each simulated process and for the observed data. The signal to be measured is the sum of direct bottom and gluon splitting bottom events and the background is a mix of charm events and decay-in-flight. Since both signal and background are composed of several pieces with relative weights unknown, it is not possible to solve directly for the signal fraction using only the numbers in Table 6.2. However, it is possible to set upper and lower bounds on the signal fraction. First, a fit involving one choice of signal process and one choice of background process is easily produced. The linear combination of a signal process, S, and background process, B, are used to match the number of events in the data, D, in two bins, the $p_t^{rel} > 2$ bin is labelled by $>$ and the other by $<$. Specifically,

$$D^{>} = \alpha B^{>} + \beta S^{>} \tag{6.4}$$

$$D^{<} = \alpha B^{<} + \beta S^{<} \tag{6.5}$$

where α and β are the parameters to be found. Since D is the number of events in the data and B and S are the fraction of events in the simulations, the pa-

rameters α and β are the number of background and signal events measured in the sample. Six fits for all combinations of signal and background processes can be made with this method. The bounds of the fit, however, come from the direct and gluon splitting charm background processes. The fit results assuming a background with the decay-in-flight shape are between those for the charm simulations. Therefore, the results are bounded by the signal and background choices listed in Table 6.3. The signal events account for somewhere between 67% and 83% of the data sample. The background composition contributes an uncertainty of 19 to 26 events and the signal composition contributes an uncertainty of 29 to 36 events which are somewhat smaller than the statistical uncertainties in the fits.

The bottom quarks which contribute to the muons in jets sample are primarily those produced at high rapidity with p_t^b above 15 GeV. Figure 6.2 shows the p_t and η distributions of the bottom quarks in simulated events which are selected by the analysis cuts. The p_t spectra are cut off on the low end by the selection cuts in the data sample. At large p_t, the spectra fall due to the cross section. The η distribution drops off on one side due to the acceptance of the forward muon detector and on the other due to the acceptance of the plug calorimeter. The acceptance region $1.9 < |\eta^b| < 2.5$ and $p_t^b > 20$ GeV contains 90% of the direct bottom quarks. The acceptance region $1.8 < |\eta^b| < 2.5$ and $p_t^b > 14$ GeV contains 90% of the gluon splitting events. The difference in acceptance is attributed to the jet energy sharing in the gluon splitting simulation of bottom decays and jet

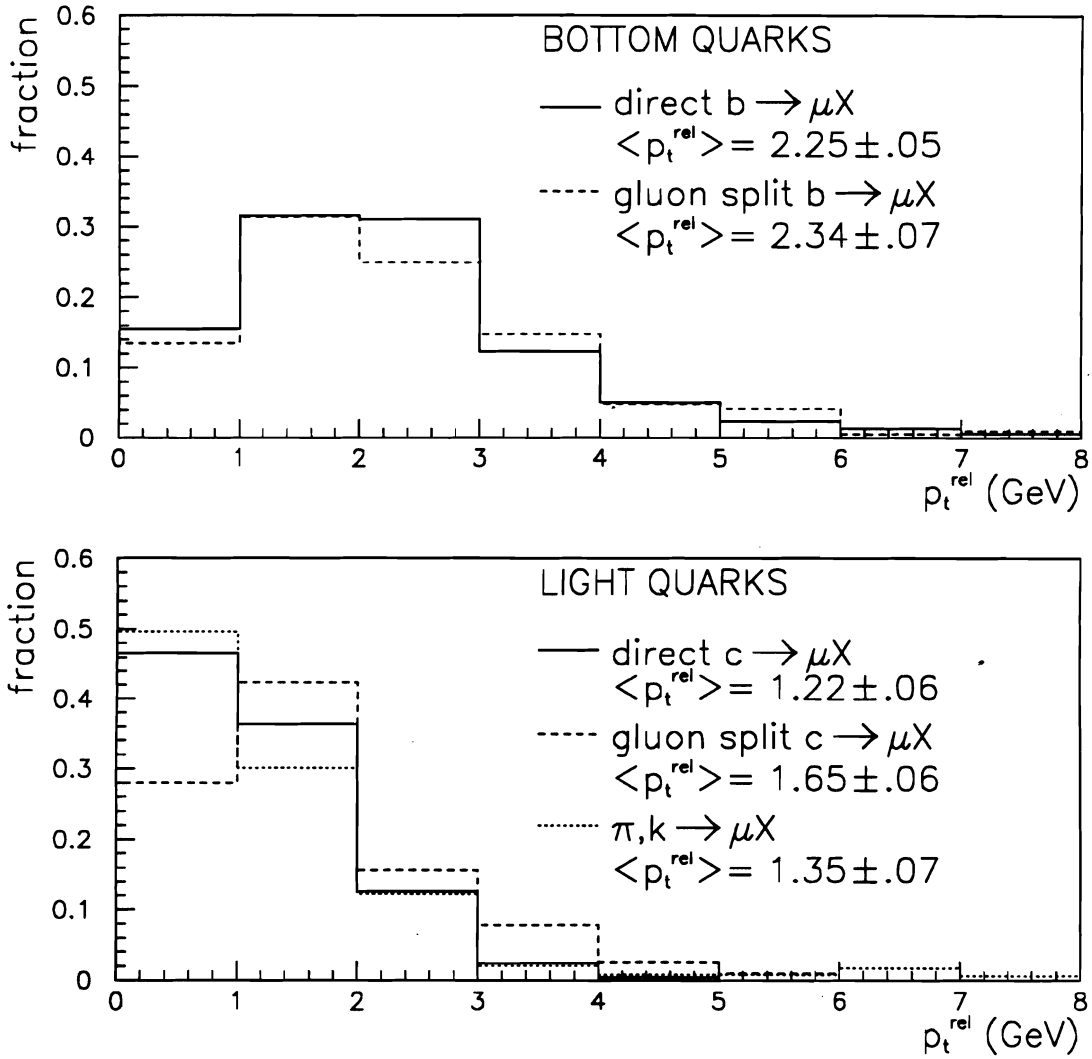

Figure 6.1: ***Distributions of p_t^{rel} normalized to unit area for the different processes which contribute to the muons in jets data sample. Notice that bottom quark processes have a different shape than light quark processes.***

	$p_t^{rel} < 2$ GeV	$p_t^{rel} > 2$ GeV	Total
signal processes:	$S^<$	$S^>$	
direct b	$(46.9 \pm 1.7)\%$	$(53.1 \pm 1.7)\%$	
gluon split b	$(44.1 \pm 2.6)\%$	$(55.9 \pm 2.6)\%$	
background processes:	$B^<$	$B^>$	
direct c	$(83.0 \pm 2.6)\%$	$(17.0 \pm 2.6)\%$	
gluon split c	$(70.4 \pm 2.6)\%$	$(29.6 \pm 2.6)\%$	
decay-in-flight	$(79.7 \pm 3.2)\%$	$(20.3 \pm 3.2)\%$	
data	$D^<$=173 events	$D^>$=153 events	326 events
	$(53.1 \pm 2.8)\%$	$(46.9 \pm 2.8)\%$	

Table 6.2: *The p_t^{rel} fractions for the simulations and data.*

signal process	background process	signal events β	background events α
direct b	direct c	(270 ± 32)	(56 ± 29)
direct b	gluon split c	(241 ± 45)	(85 ± 44)
gluon split b	direct c	(251 ± 32)	(75 ± 29)
gluon split b	gluon split c	(215 ± 43)	(111 ± 42)

Table 6.3: *The fit results for various simulated signal and background shapes.*

cuts on the opposite jet which are sensitive to differences in calorimeter modelling of quark and gluon jets.

To turn the measured number of signal events from various fits into bottom quark cross sections, it is necessary to account for the efficiency and acceptance of the detector using the simulation. The number of simulated events, N^{sim}, and simulated luminosity $\int_{sim} Ldt$ were listed in Table 6.1. The number of events which survived all the simulated effects is given by:

$$N^{sim} = \int_{sim} Ldt \times \sigma_{th}(P\bar{P} \longrightarrow bX) \times B(b \longrightarrow \mu) \times A \times \epsilon_{sim} \qquad (6.6)$$

where $\sigma_{th}(P\bar{P} \longrightarrow bX)$ is the theoretical cross section from ISAJET in the acceptance region $1.9 < |\eta^b| < 2.5$ and $p_t^b > 20$ GeV for the direct simulation and $1.8 < |\eta^b| < 2.5$ and $p_t^b > 14$ GeV for the gluon splitting simulation, $B(b \longrightarrow \mu) = .11$ is the branching ratio for bottom quarks to decay to muons, and $A \times \epsilon_{sim}$ is the simulated acceptance and efficiency. The detector, trigger and analysis cut acceptance is all contained in the simulation. The efficiency, ϵ_{sim}, is not equal to the true efficiency because not all effects are included in the simulation. The simulation used a 95% chamber efficiency to throw out both hits from the muon track and extra hits, resulting in a six-hit efficiency of $(.95)^6$. For the true efficiency this is replaced by the overall trigger efficiency which includes a factor, $(.92)^6$, reflecting the measured chamber efficiency as well as other effects. This trigger efficiency was found to be $\epsilon_{trig} = .395 \pm .014$ in chapter 3. The total

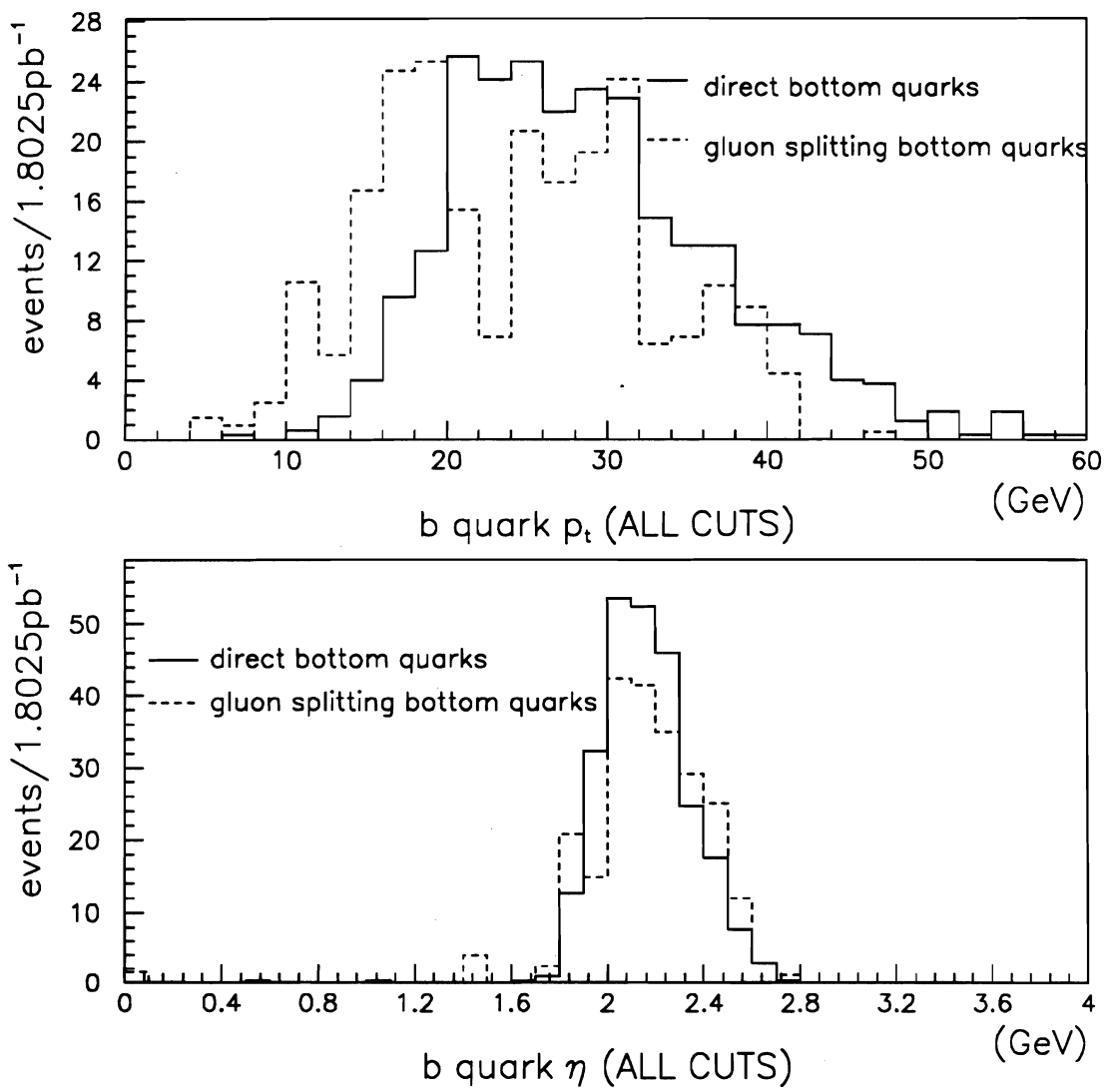

Figure 6.2: ***Simulated bottom quark p_t and η distributions for events which passed all analysis cuts.***

efficiency is therefore:

$$\epsilon = \epsilon_{trig} \times \frac{\epsilon_{sim}}{(.95)^6} \tag{6.7}$$

Thus, we may determine the simulated acceptance and efficiency:

$$A \times \epsilon_{sim} = \frac{N^{sim}}{\int_{sim} Ldt \times \sigma_{th}(P\bar{P} \longrightarrow bX) \times B(b \longrightarrow \mu)} \tag{6.8}$$

The simulated efficiency and acceptance can be used to relate the measured cross section, $\sigma_{meas}(P\bar{P} \longrightarrow bX)$, and measured event yield, N^{meas}:

$$N^{meas} = \int_{FMU} Ldt \times \sigma_{meas}(P\bar{P} \longrightarrow bX) \times B(b \longrightarrow \mu) \times A \times \epsilon \tag{6.9}$$

where $\int_{FMU} Ldt$ is the FMU luminosity, $(1.80 \pm .14)$ pb^{-1}. The measured number of events attributed to bottom decay were listed in Table 6.3. The fit parameter β is equal to the measured event yield, N^{meas}.

The bottom quark distributions generated by ISAJET were adjusted to match the next-to-leading order QCD calculations as discussed in Appendix C. Therefore, the next-to-leading order predicted cross sections are equal to the bottom quark cross sections produced by ISAJET.

The predicted cross sections were determined using the NLO code of Mangano, Nason, and Ridolfi (MNR). To confirm that the ISAJET input spectrum predicted the same cross sections, the yield and shape corrections were applied to match the NLO calculation (Appendix C). The MNR predicted cross sections were calculated using MRSD0 structure functions, a bottom quark mass of 4.75 GeV and $\mu_0 = \sqrt{m_b^2 + p_t^{b2}}$. The predicted cross section is:

$$\sigma(P\bar{P} \longrightarrow bX : p_t^b > 20 \text{ GeV}, 1.9 < |\eta^b| < 2.5) = (21.3 \pm .4^{+10.2}_{-5.9}) \text{ nb} \tag{6.10}$$

and with the lower p_t^b threshold:

$$\sigma(P\bar{P} \longrightarrow bX : p_t^b > 14 \text{ GeV}, 1.8 < |\eta^b| < 2.5) = (115. \pm 2.^{+47.}_{-28.}) \text{ nb.} \quad (6.11)$$

where the first uncertainty is statistical and the second is systematic. The range of systematic uncertainty comes from letting the bottom quark mass vary from 4.5 GeV to 5.0 GeV, the μ scale vary from $\mu_0/2 < \mu < 2\mu_0$, and using CTEQ structure functions. Clearly the measured cross sections are larger than the predictions regardless of background composition.

Using the information collected above, it is now possible to actually solve for the simulated acceptance and efficiency. For direct bottom quark production, $A \times \epsilon_{sim}$ is $.0127 \pm .0005$ and for gluon splitting bottom quark production it is $.00676 \pm .00035$.

The measured bottom quark cross sections for the different signal and background assumptions are given in Table 6.4. Figures 6.3 and 6.4 show the measured bottom quark cross sections in both p_t and η for the different signal assumptions.

To summarize the bottom quark cross section, it is necessary to condense the measurements with different assumed signals (direct and gluon splitting bottom quarks) and backgrounds (direct and gluon splitting charm) into a single number. Combining the results with a systematic uncertainty due to signal and background composition has substages which require separate interpretation. The topology and composition of direct and gluon splitting events differ sufficiently to signif-

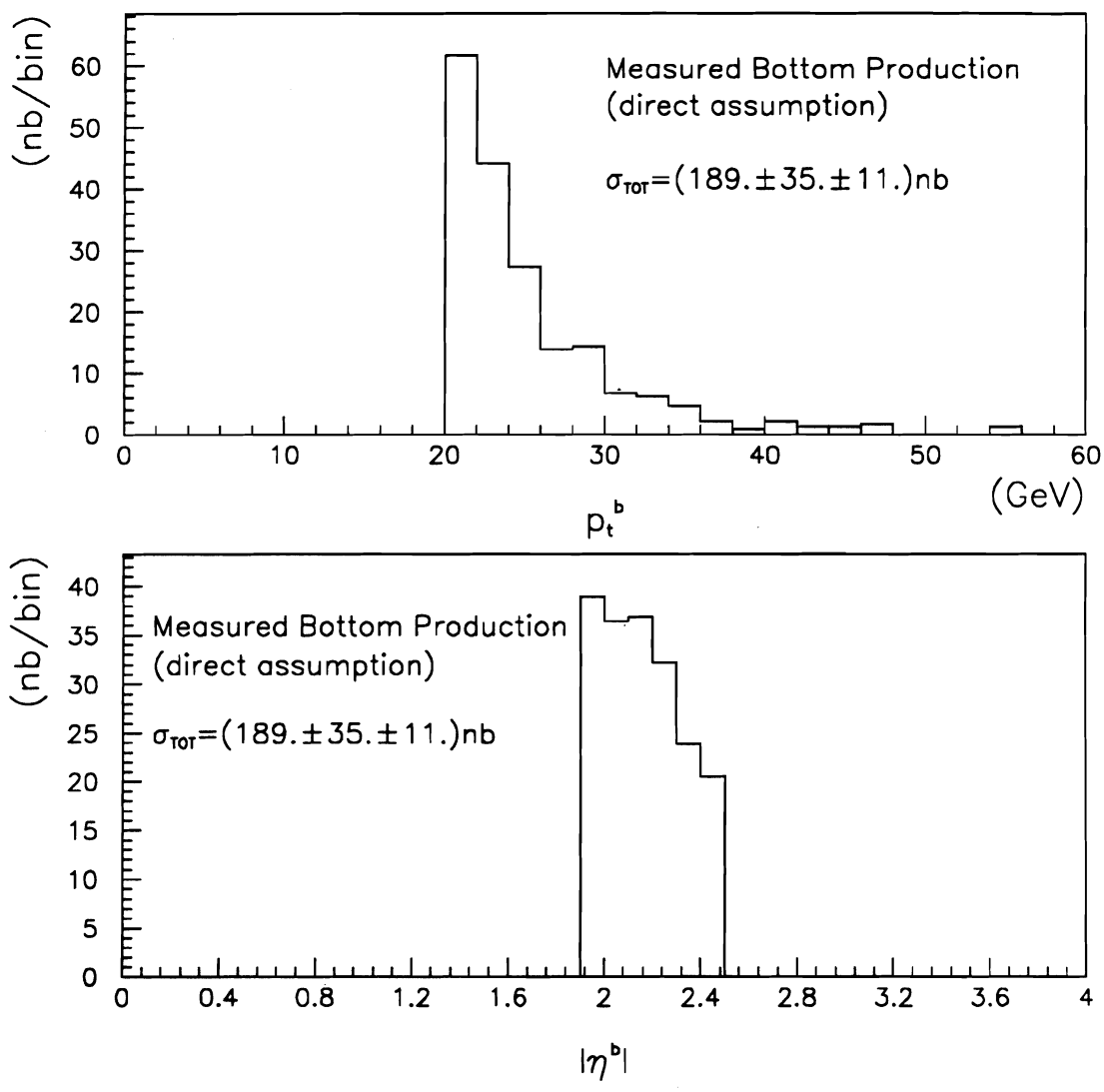

Figure 6.3: ***Measured bottom production with the assumption that direct b production represents the entire sample.***

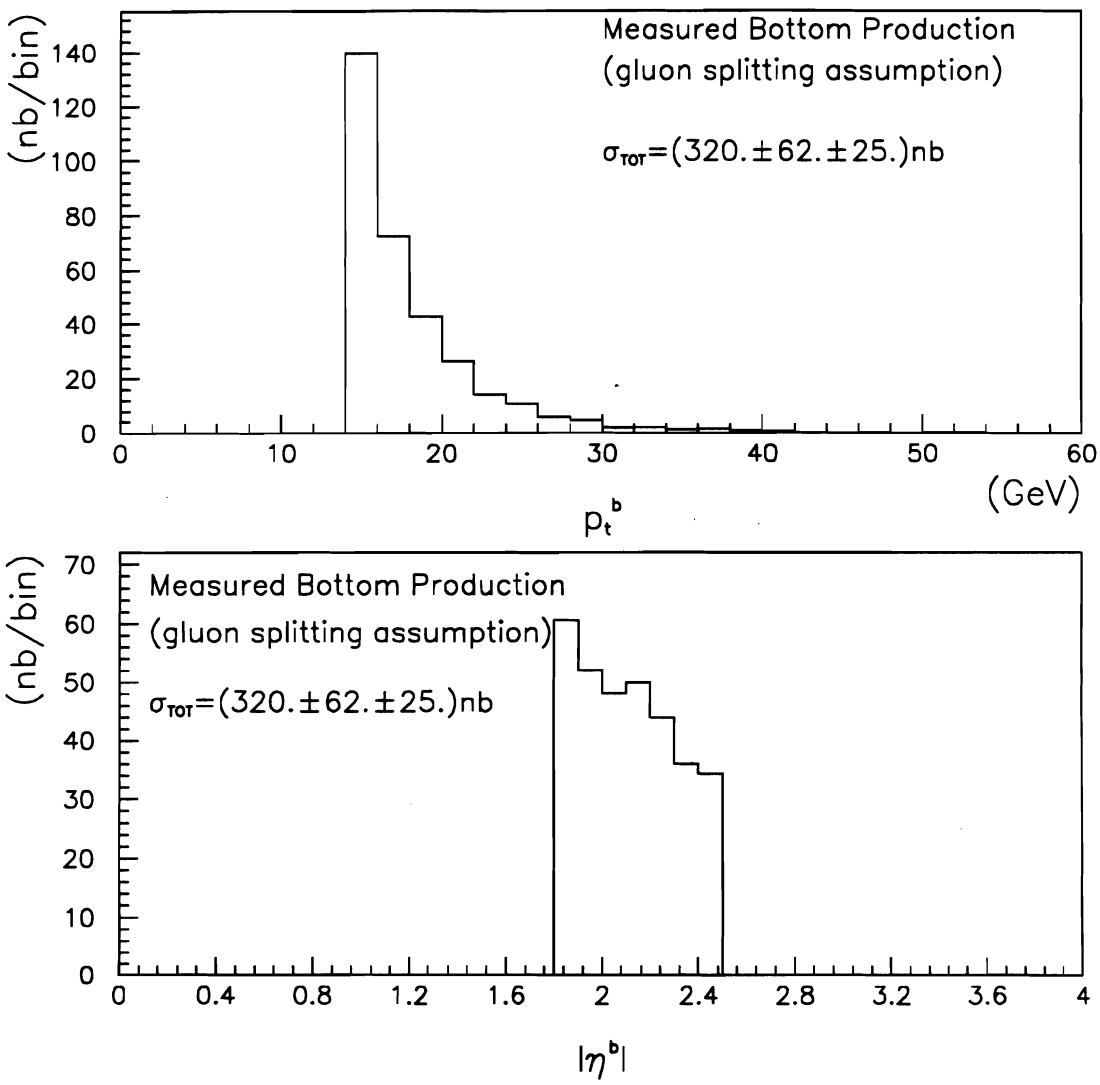

Figure 6.4: ***Measured bottom production with the assumption that gluon splitting b production represents the entire sample.***

signal	background	kinematic region	measured bottom quark cross section	predicted bottom quark cross section
			(nb)	(nb)
direct b	direct c	$p_t^b > 20$ GeV	200 ± 26	$21.3 \pm .4^{+10.2}_{-5.9}$
direct b	gluon split c	$1.9 < \|\eta_b\| < 2.5$	178 ± 35	
gluon split b	direct c	$p_t^b > 14$ GeV	344 ± 49	$115. \pm 2.^{+47.}_{-28.}$
gluon split b	gluon split c	$1.8 < \|\eta_b\| < 2.5$	295 ± 62	

Table 6.4: *The bottom quark cross sections for various signal and background assumptions. The uncertainty in the measured cross section is only statistical.*

icantly alter the measured cross sections. Real bottom events are never purely direct or gluon splitting, so the fits with one assumption or the other bound the true result which is due to some unknown mix of the two. Averaging over results with different background compositions gives:

$$\sigma(P\bar{P} \longrightarrow bX : p_t^b > 20 \text{ GeV}, 1.9 < |\eta^b| < 2.5) = (189. \pm 35. \pm 11.) \text{ nb} \quad (6.12)$$

for the direct b assumption and

$$\sigma(P\bar{P} \longrightarrow bX : p_t^b > 14 \text{ GeV}, 1.8 < |\eta^b| < 2.5) = (320. \pm 62. \pm 25.) \text{ nb} \quad (6.13)$$

for the gluon splitting b assumption. The first uncertainty is statistical and is chosen to be the larger of the two statistical uncertainties on the measured cross section from Table 6.3. The second uncertainty is systematic and is half

the difference between the measured cross sections in Table 6.3. The systematic uncertainty is only due to varying the background composition and does not include experimental systematics which are included later in section 6.5.. Figure 6.5 compares these results to the predicted results graphically. The gluon splitting and direct assumptions bound the result on the x-axis. The true result then falls somewhere in the measured polygon. Regardless of signal mix, the result is higher than predicted. Since the pure gluon splitting assumption is within 2.3σ of the predicted result, and the direct assumption is 3.5σ higher than the predicted result.

The systematic uncertainty in the cross section due to signal composition can be estimated if the cross sections pertain to the same kinematic acceptance region. Figure 6.5 shows that the cross sections have been measured with events from different kinematic regions. The uncertainty due to the different acceptance regions will now be turned into an uncertainty in nb for a single kinematic region. Remember that the number of events attributed to bottom decays found in the fits to data were similar for the two signal assumptions, so the systematic shifts in cross section are the result of different production processes and acceptance regions. The measured cross section for the higher $p_t > 20$ in the gluon splitting channel is

$$\sigma(P\bar{P} \longrightarrow bX : p_t^b > 20 \text{ GeV}, 1.9 < |\eta^b| < 2.5) = (59.5 \pm 11.6 \pm 4.6) \text{ nb.} \quad (6.14)$$

This comes from substituting the simulated acceptance and efficiency of the new

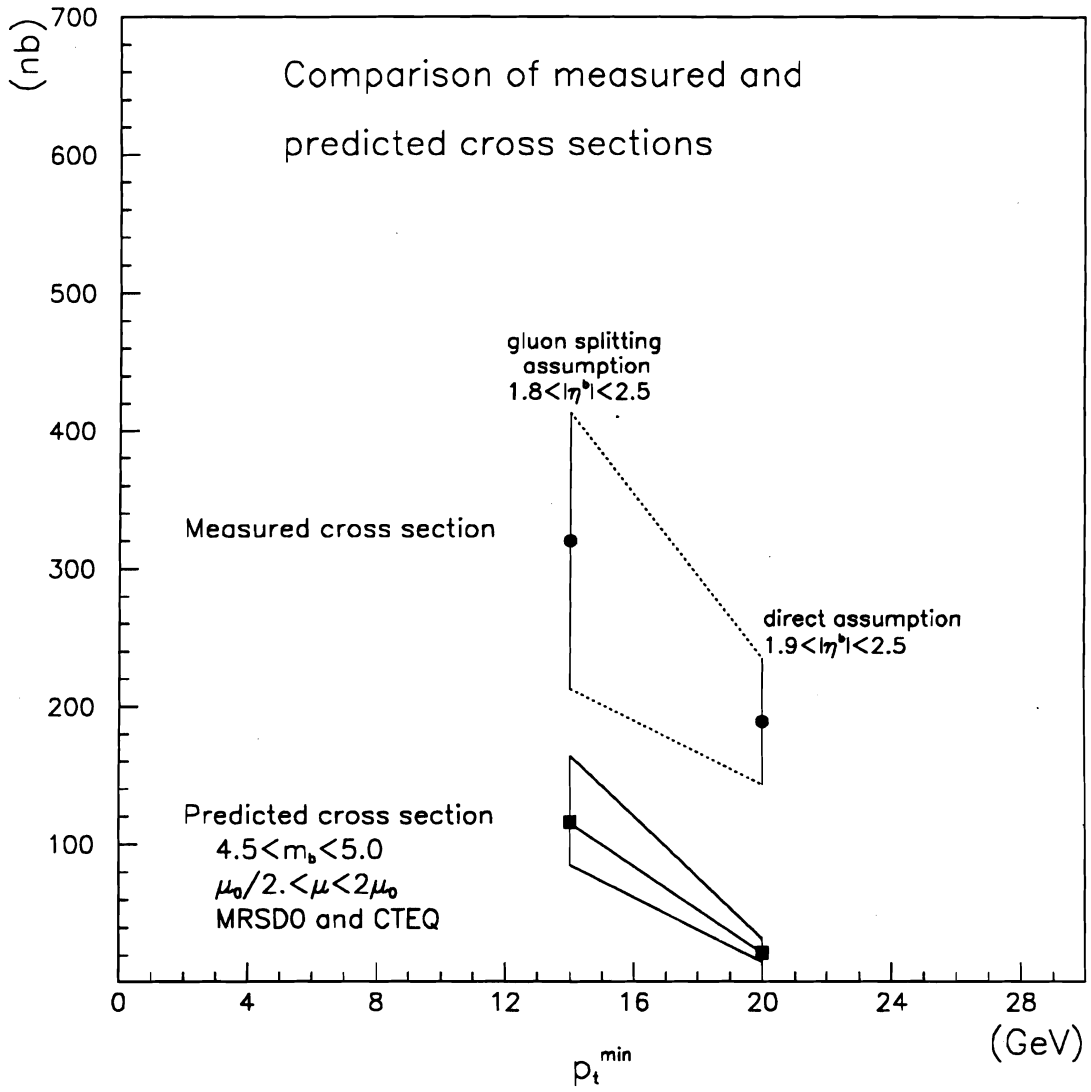

Figure 6.5: ***Comparison of the measured and predicted cross sections for bottom production. The extreme modelling assumptions bound the result on the horizontal axis. The real result lies somewhere between the two. The measured result is higher than predicted for all values of*** p_t^{min}.

p_t cut for the old while determining the measured cross section. The average of the measured direct and gluon splitting cross section for the same acceptance region is:

$$\sigma(P\bar{P} \longrightarrow bX : p_t^b > 20 \text{ GeV}, 1.9 < |\eta^b| < 2.5) = (124. \pm 35. \pm 66.) \text{ nb.} \quad (6.15)$$

This is the average of equations 6.12 and 6.14. The first uncertainty is statistical and is chosen to be the larger of the two statistical uncertainties. The second uncertainty is systematic and is half of the difference between the measured two cross sections added in quadrature with the systematic uncertainty due to background composition. Here the systematic error includes contributions from all signal and background compositions. This result is $5.82 \pm 1.60^{+4.16}_{-3.49}$ times higher than the predicted cross section which appears to be within 2σ of the prediction. The graphical presentation of Figure 6.5 is a more powerful presentation of the result.

6.3 Direct b quark cross section from fit using η_{opp}

Further information about bottom production can be obtained from the distribution of η_{opp}, defined as the pseudorapidity of the jet most opposite in azimuth from the muon. In those events where $\eta_\mu < 0$, it will be convenient in the following to reverse the sign of η_{opp} and η_μ. With this convention, all the forward

muon tagged jets are at positive η.

The kinematics of quark and gluon pair production are such that the shape of the η_{opp} distribution is different for these different sources of bottom quarks. The discriminating power of this variable can be seen in Figure 6.6 which shows the distributions normalized to unit area. The term "quark processes" will be used to refer to direct bottom and charm production, whereas "gluon processes" will refer to gluon splitting bottom and charm production as well as decay-in-flight background, all of which are dominated by gluon pair production. Decay-in-flight is not in general a gluon process, but because of the jet requirement in this data sample, the production process is that of jets rather than the inclusive particle spectrum. Since most jets at CDF come from gluon pair production, the decay-in-flight spectrum for this analysis is characterized as a "gluon process." For each process, the first jet is assumed to be in the range $2. < \eta < 2.5$. In the quark processes, the second jet is biased towards this same region, whereas in gluon processes, the second jet is spread more evenly between positive and negative pseudorapidity. Using the combination of p_t^{rel} and η_{opp} it is possible to extract the direct bottom content in the data sample.

Besides allowing a separate determination of the direct bottom contribution, the η_{opp} distribution can be used to rule out the possibility that the previous measurement resulted from poor simulations of p_t^{rel}. If for some reason, the tail of the p_t^{rel} distribution is not well understood, it is possible that the background jets could contribute more than the simulation indicates. Such an error would be

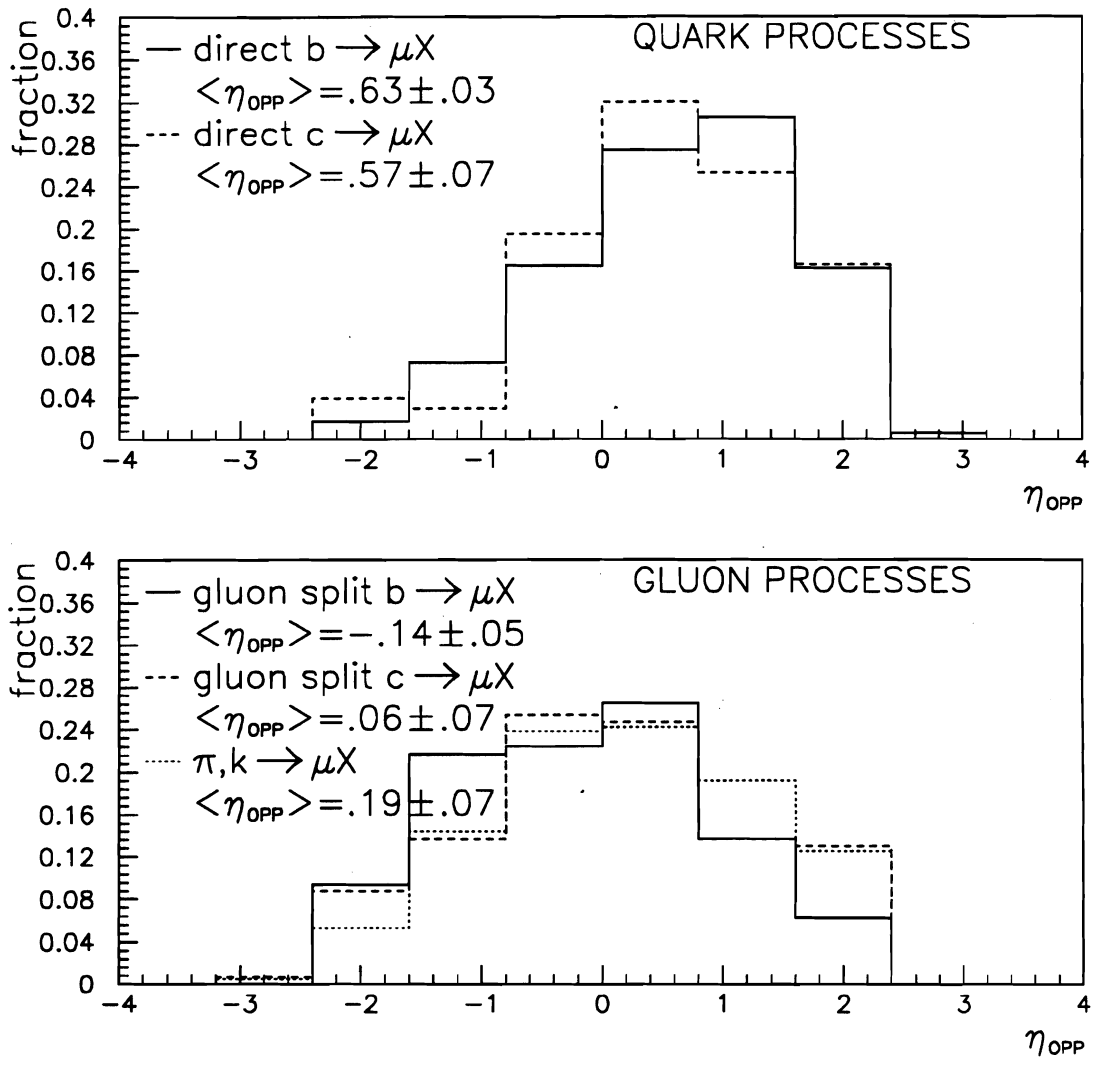

Figure 6.6: ***Distributions of η_{opp} normalized to unit area for the different processes which contribute to the muons in jets data sample. Notice that quark processes have a different shape than gluon processes.***

revealed by an η_{opp} distribution which looked too much like the gluon processes, expected to dominate the background jets. Conversely, if the η_{opp} distribution appears quark-like, this suggests that neither the gluon splitting charm nor decay-in-flight distributions were under represented in the previous fit. We may then argue that the direct charm is also simulated sufficiently. Since this accounts for all the background distributions, it is a powerful demonstration that the bottom content is being determined correctly.

In the following, a simple fit using a minimum of information will be used to place upper and lower bounds on the direct bottom production cross section. Then a global fit incorporating more information will be shown, and a number of distributions will be examined to verify agreement between the data and the simulations.

6.3.1 Simple fits

The simplest fitting procedure is that which analyzes η_{opp} in the region $p_t^{rel} > 2$ GeV where the light quark distribution is minimal. The data in this region should contain a higher percentage of bottom quark decays than that with low p_t^{rel}. Hence it will be referred to as the bottom enhanced region and the rest of the data will be called background enhanced. Only about 15% of the light quark distributions are in the bottom enhanced region compared to about 50% of the bottom quark distributions.

The distribution of η_{opp} is shown in Figure 6.7 for events with $p_t^{rel} > 2$ GeV.

	$\eta_{opp} < 0$	$\eta_{opp} > 0$	TOTAL
INPUT DIST:			
data	52 ± 7.2	101 ± 10.0	153 ± 12.4
direct b	$(26.3 \pm 2.1)\%$	$(73.7 \pm 2.1)\%$	100%
FIT RESULTS:			
direct b			$104. \pm 28.$
background			$50. \pm 27.$
percent b			$(68. \pm 13.)\%$
percent background			$(32. \pm 13.)\%$

Table 6.5: *The results of the fit to the η_{opp} distribution in the bottom enhanced region, $p_t^{rel} > 2$ GeV.*

Ignoring the direct charm contribution, the enhancement in the positive side of the η_{opp} plot is solely due to the direct bottom quark production. The fit divides the η_{opp} distribution into two bins, one greater and one less than zero. The gluon processes are assumed to contribute equally to both bins, which is within the statistical uncertainty of full simulations. The direct bottom signal contributes more in the positive bin. Table 6.5 lists the results of this fit. Notice that here the direct bottom contributes 67.6% of the bottom enhanced data.

The above fit actually determines the sum of direct bottom and direct charm for the region $p_t^{rel} > 2$ GeV, and it therefore gives an upper limit for direct bottom production in this region. The amount of charm contamination can be

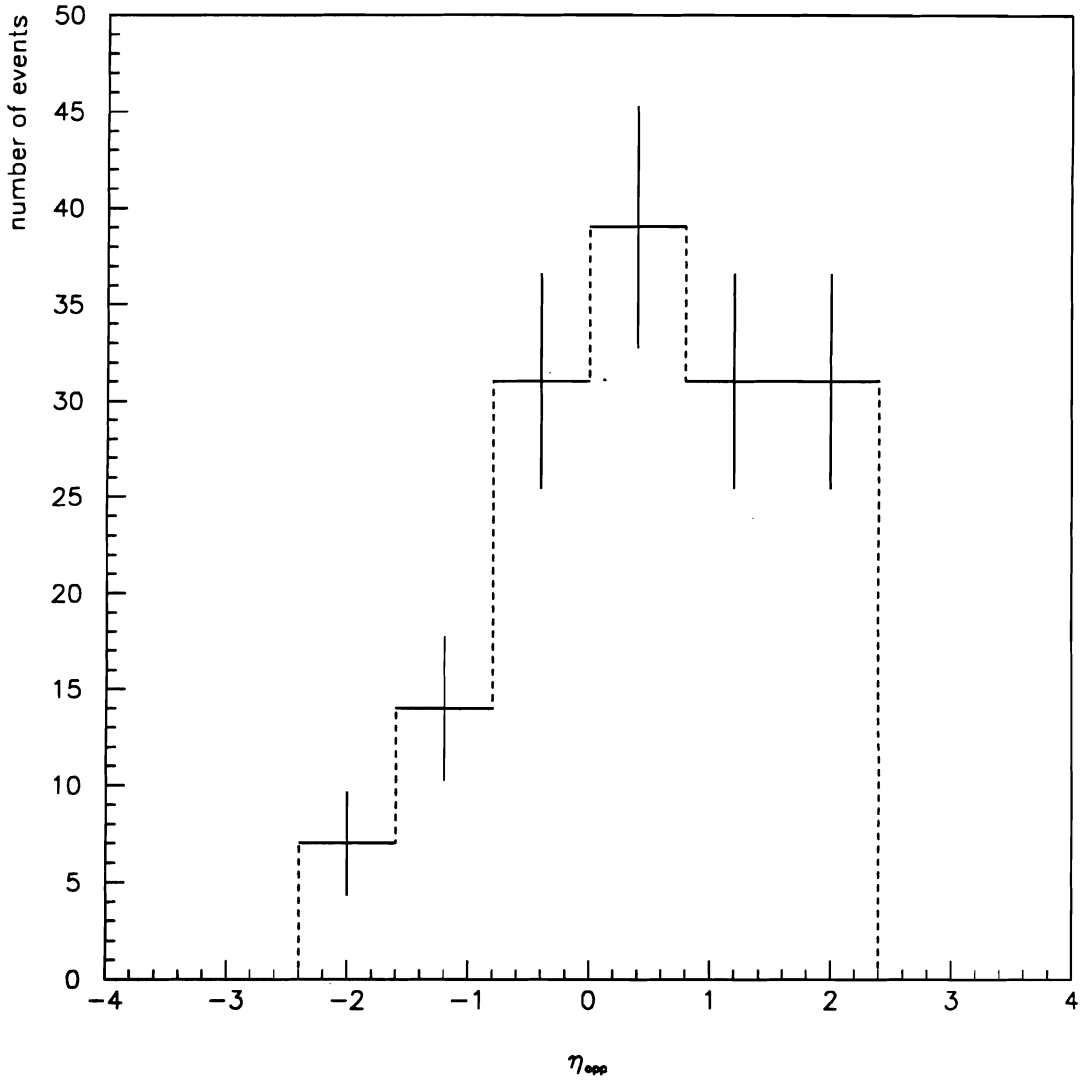

Figure 6.7: *The distribution of η_{opp} in the bottom enhanced region, $p_t^{rel} > 2$ GeV, for the muons in jets data sample.*

shown to be small, and a bound for it is derived, by considering the number of direct bottom and direct charm events with $p_t^{rel} < 2$ GeV, $N^{<}_{direct}$. The number, $N^{<}_{direct}$, is obtained from the total with $p_t^{rel} < 2$ GeV ($D^{<} = 173$ events - see Table 6.2) by subtracting off the contribution from background processes extrapolated from the $p_t^{rel} > 2$ GeV region:

$$N^{<}_{direct} = D^{<} + G^{<}. \tag{6.16}$$

Here, $G^{<}$ is the number of background events in the low p_t^{rel} bin, that is, events not from direct bottom or direct charm. The measured background contribution in the high p_t^{rel} bin, $G^{>}$, is $49. \pm 27.$ events. This can be extrapolated to the low p_t^{rel} bin using the fractions listed in Table 6.2,

$$G^{<} = G^{>} \times \frac{1 - F^{>}}{F^{>}} \tag{6.17}$$

where $F^{>}$ is the fraction of background events with $p_t^{rel} > 2$ GeV. In the current fit, all gluon processes, which includes gluon splitting bottom and charm as well as decay-in-flight simulations are background processes. The value of $F^{>}$ depends on background mix. The largest $F^{>}$ value, hence the largest value of $N^{<}_{direct}$, is obtained from a background composed solely of gluon splitting bottom events: $B^{<} > 39. \pm 22.$ events. Substituting this bound into equation 6.16 gives: $N^{<} < 134 \pm 25$ events. Now we know the number of direct events and the fractions of direct bottom and charm in two bins of p_t^{rel} and can therefore fit over these,

$$N^{>}_{direct} = \alpha C^{>}_{direct} + \beta B^{>}_{direct} \tag{6.18}$$

$$N^{<}_{direct} = \alpha C^{<}_{direct} + \beta B^{<}_{direct} \tag{6.19}$$

where C_{direct} and B_{direct} are the fraction of direct charm and bottom respectively in the two p_t^{rel} bins. Since the background was chosen to give the largest charm contamination, the result gives the lowest direct bottom contribution. The result is that 93 ± 35 events in the region $p_t^{rel} > 2$ GeV are attributed to direct bottom quark decays. This constitutes a lower limit on the direct bottom content in the sample which is statistically consistent with the upper bound and constitutes a conservative result.

Repeating this simple fit, but fitting for the mean of the η_{opp} distribution instead of the number of events on either side of zero, gives a result which is slightly more sensitive to the shape of the distribution. This fit uses the overall normalizations of the distributions and the means of the distributions to constrain the fit. The results are listed in Table 6.6. The simulated direct bottom spectrum fit by this method accounts for 80% of the bottom enhanced data, corresponding to 122 ± 26 events. Again, this overestimates the bottom content. The lower bound on the bottom content , determined using the maximum amount of charm leakage into the bottom enhanced region, is 89 ± 35 events. These results are consistent with the previous method, and the statistical errors are slightly reduced.

	$< \eta_{opp} >$	TOTAL
INPUT DIST:		
data	$.468 \pm .086$	153 ± 12.4
direct b	$.587 \pm .047$	1.00
FIT RESULTS:		
direct b		$122. \pm 26.$
background		$31. \pm 25.$
percent b		$(80. \pm 13.)\%$
percent background		$(20. \pm 13.)\%$

Table 6.6: *The results of the fit to the mean of the η_{opp} distribution in the bottom enhanced region, $p_t^{rel} > 2$ GeV.*

6.3.2 Global fits

As a caveat, it is observed that the statistical error in the η_{opp} distribution for gluon processes has not been accounted for in the above. This uncertainty is, however, included in the following global fits. Global fits to η_{opp} and p_t^{rel} distributions can be used to show that there is a fit which is consistent with the simple fits, but which includes all five possible physics contributions and sums to the observed number of events. The range of these fits also gives absolute bounds for the direct bottom contribution. Since there are five simulated physics processes and only two distributions to fit over, the basic idea is to vary the relative amounts of the four "background" processes in relation to each other and watch how the fits change.

The distinguishing shape factors in the p_t^{rel} distributions (Figure 6.1) are the first two bins and then the sum of those above 2GeV. Again, the bottom enhanced region, $p_t^{rel} > 2$ GeV, is split into two bins in η_{opp}; one greater and one less than zero. So the fit includes four bins; 0 GeV $< p_t^{rel} <$ 1 GeV, 1 GeV $< p_t^{rel} <$ 2 GeV, 2 GeV $< p_t^{rel}$ and $\eta_{opp} < 0$, and finally 2 GeV $< p_t^{rel}$ and $\eta_{opp} > 0$. Since there is a lot of similarity between the gluon splitting bottom and gluon splitting charm distributions, the relative amounts of these are not left free to be determined by the fit. Instead, their relative contribution is fixed by choice of coefficients C_b and C_c applied to each contribution. These coefficients are chosen such that $C_b + C_c = 1$, and then varied between 0 and 1 to obtain

	light quarks $C_{dc} = 0$ $C_{\pi/K} = 1$		$\longrightarrow$	light quarks $C_{dc} = 1$ $C_{\pi/K} = 0$	
gluon split C_b/C_c	direct b (events)	χ^2 of fit	$\longrightarrow$	direct b (events)	χ^2 of fit
1/0	168 ± 52	0.17		158 ± 54	0.97
.75/.25	183 ± 48	0.70		178 ± 48	1.71
.50/.50	200 ± 43	1.35		197 ± 43	2.42
.25/.75	215 ± 38	1.92		213 ± 38	3.03
0/1	226 ± 34	2.35		224 ± 34	3.51

Table 6.7: *The variation in the number of events in the data sample which are attributed to direct bottom decays for a range of global fits. The fits constrain the ratio of gluon splitting charm and bottom in the background simulations as well as the ratio of light quark contributions.*

a range of possible fit results. The relative amounts of direct charm and π/K decay-in-flight contributions are handled in the same way. The direct charm and π/K coefficients are C_{dc} and $C_{\pi/K}$ respectively. Table 6.7 lists the range of fit results for the direct bottom content of the sample which results from various choices of the relative background coefficients. There is one degree of freedom in the fit, and the χ^2 shows some preference for fits with a smaller charm content than that predicted by ISAJET.

The global fit uses only four bins, it is therefore a good idea to check that all features of the data are well described by the resultant fit. Table 6.8 gives a global fit which includes all known physics processes and still has a χ^2 consistent with one degree of freedom. The coefficients for this particular fit are: $C_b = .75$, $C_c = .25$, $C_{dc} = .25$, and $C_{\pi/K} = .75$. A slide show comparing the data to the corresponding sum of simulated processes is given in Figures 6.8 to 6.20. Of particular interest are the distributions where the different physics processes have different shapes. Other distributions just verify that the variable is well simulated. Since the fits include only the minimum amount of information (namely, four bins), the fact that the distributions are well described in detail by the mix which is found by the fit gives us more confidence in the method employed.

6.3.3 Connection between global fits and the simpler fits

The purpose of making global fits is to check consistency with the simple fits and to show that the data are well described by the simulated events. Table 6.7 shows that the bottom content stays reasonably consistent regardless of the mix of simulated backgrounds. The first measurement in this chapter found the total number of bottom decays in the data sample which ranged from 215 ± 43 to 270 ± 32 events (Table 6.3). Here we can see that of these events, somewhere between 158 ± 54 and 226 ± 34 of them are due to direct bottom decays. The simple fit shown in table 6.5 gives the number of direct bottom decays in the region $p_t^{rel} > 2$ GeV. Using the simulated fraction of events in each bin from

Physics process	Yield in data (events)	Percentage of total (%)
direct b	182 ± 48	$(55.9 \pm 20.2)\%$
direct c	8.3 ± 3.2	$(2.5 \pm 0.6)\%$
π decay	51 ± 20	$(15.7 \pm 3.8)\%$
gluon split b	56 ± 34	$(17.0 \pm 9.3)\%$
gluon split c	28 ± 17	$(8.7 \pm 4.7)\%$
data	326 ± 18	100.%

Table 6.8: *One of the global fits. The ratio of direct charm and π decay in flight are fixed. Also held fixed is the ratio of gluon splitting bottom and charm. The χ^2 of this fit over 4 bins with 5 distributions and 2 constraints is .81. There is one degree of freedom in the fit and the uncertainty in the fit values are the statistical uncertainties extracted from the diagonal covariance matrix elements.*

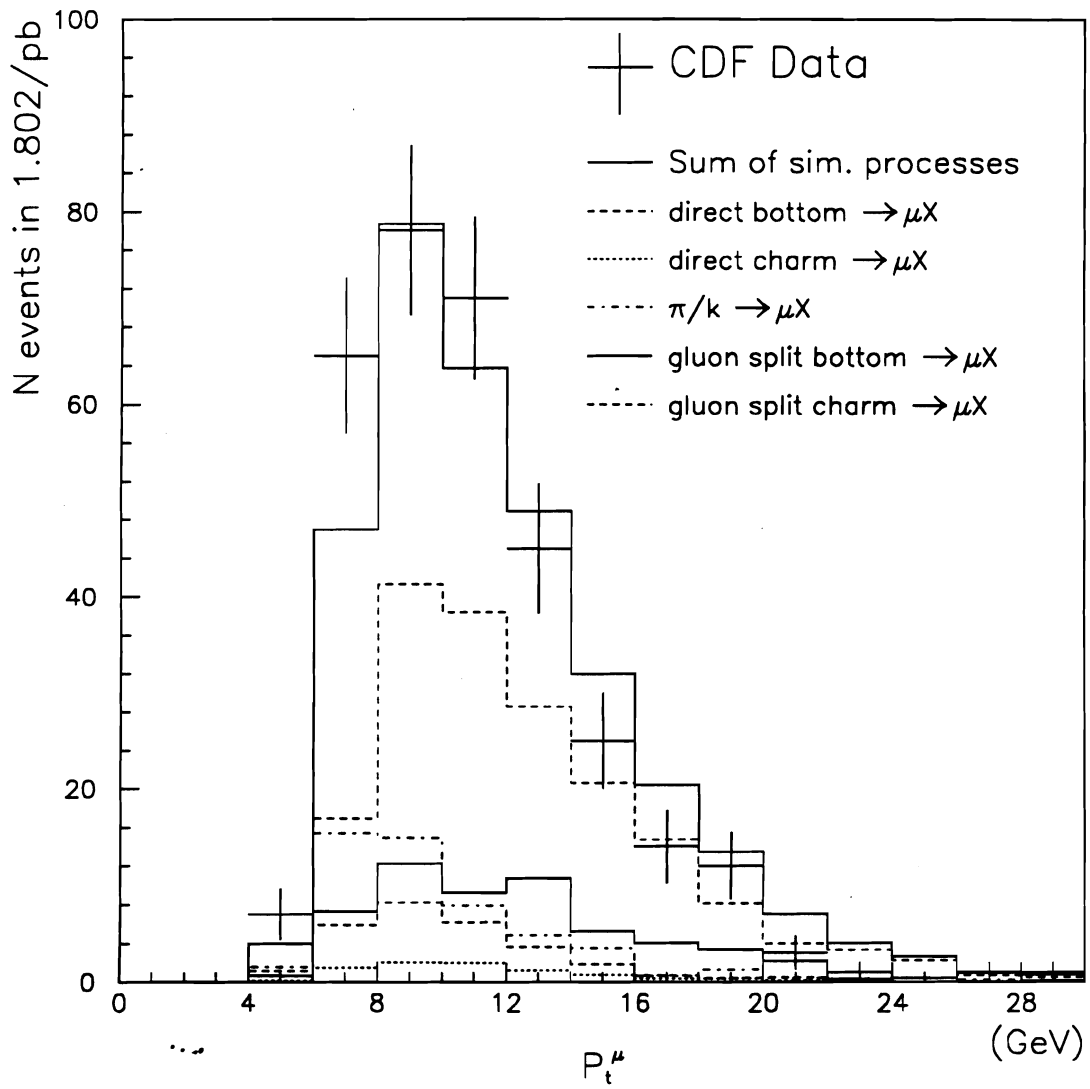

Figure 6.8: ***Momentum distribution for forward muons in CDF data displayed with the result of the global fit in Table 6.8.***

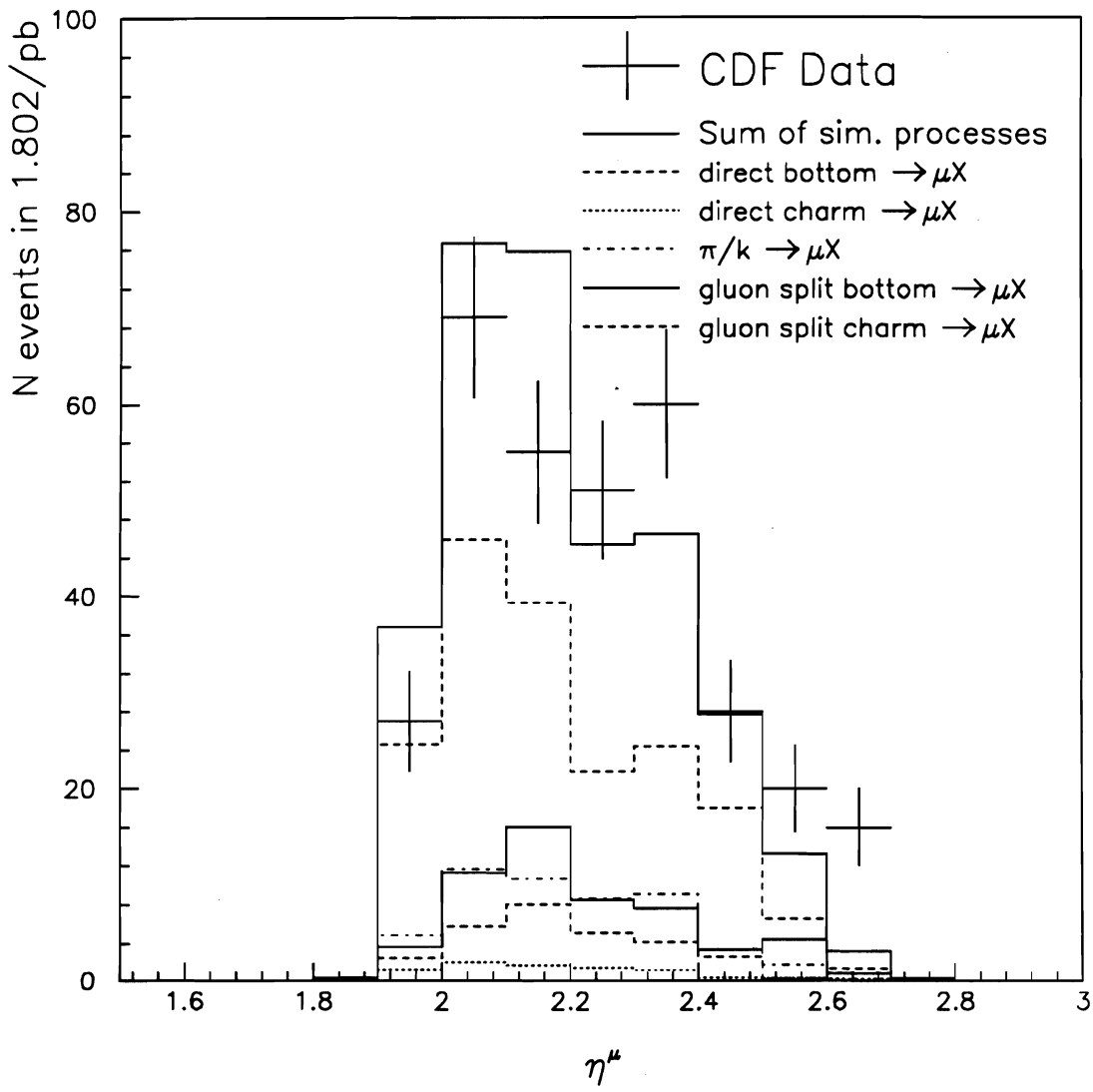

Figure 6.9: ***Pseudorapidity distribution for forward muons in CDF data displayed with the result of the global fit in Table 6.8.***

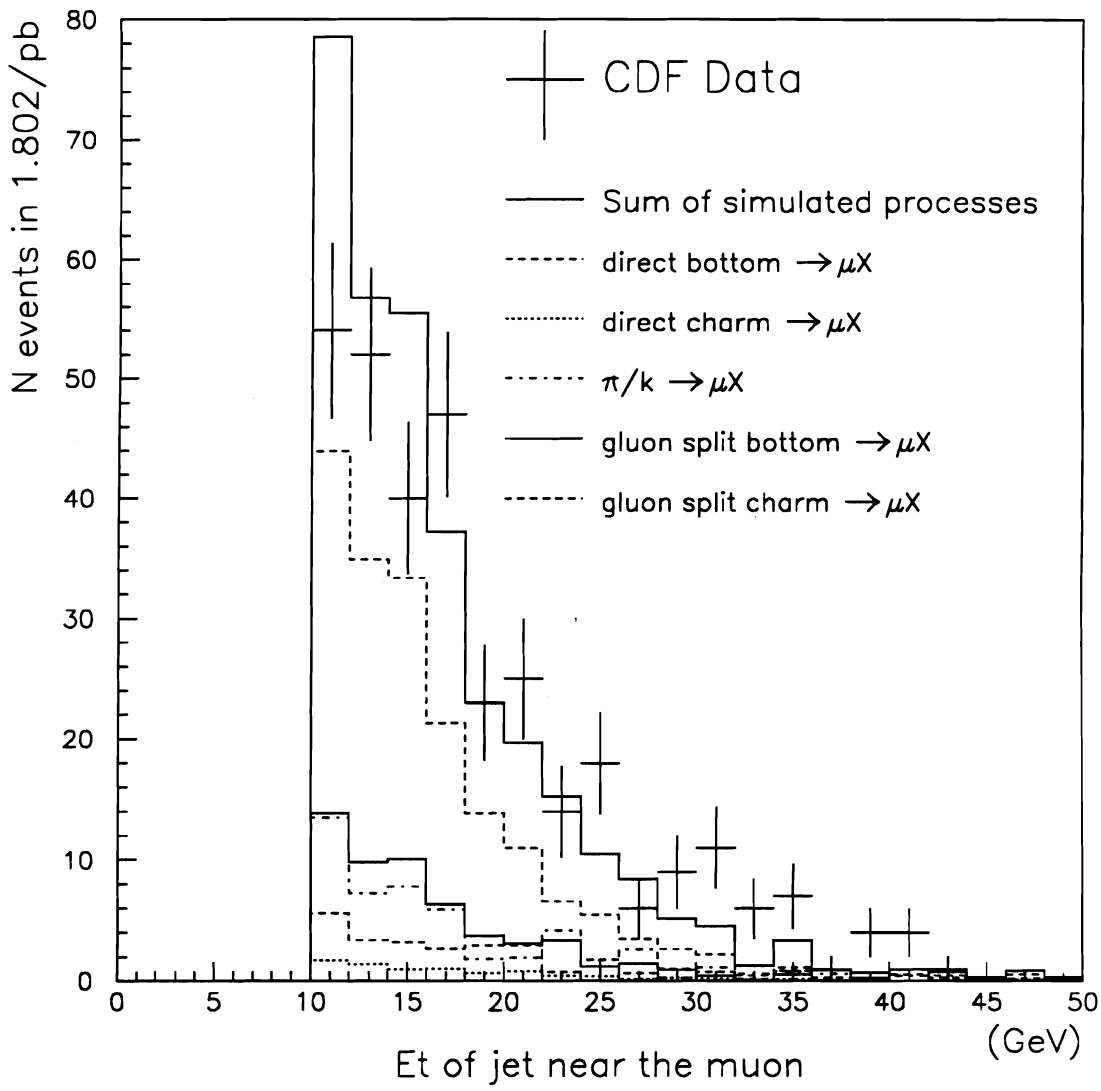

Figure 6.10: ***Corrected E_t distribution for the jet near the muon in CDF data displayed with the result of the global fit in Table 6.8.***

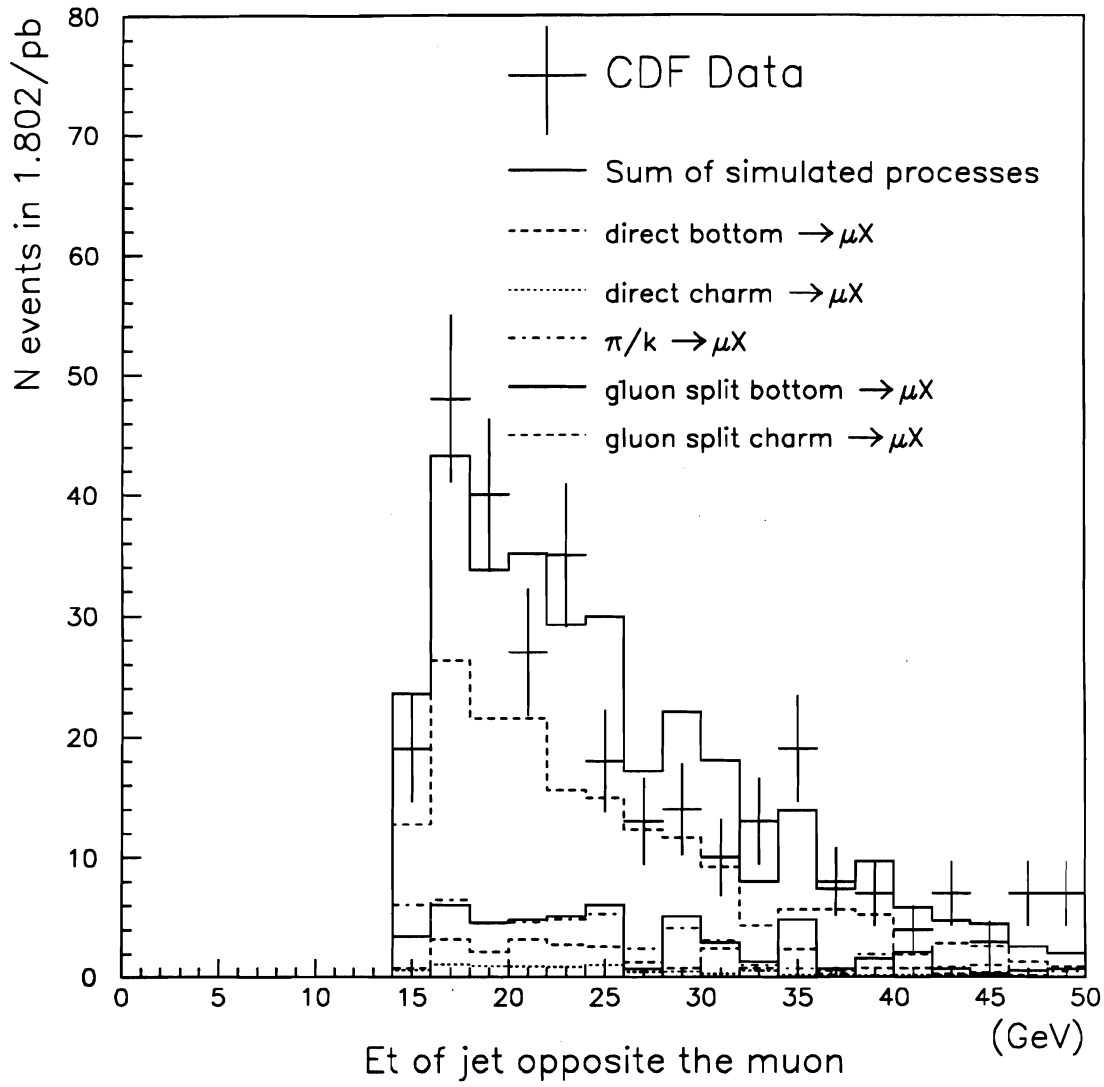

Figure 6.11: ***Corrected E_t distribution for the opposite jet in CDF data displayed with the result of the global fit in Table 6.8.***

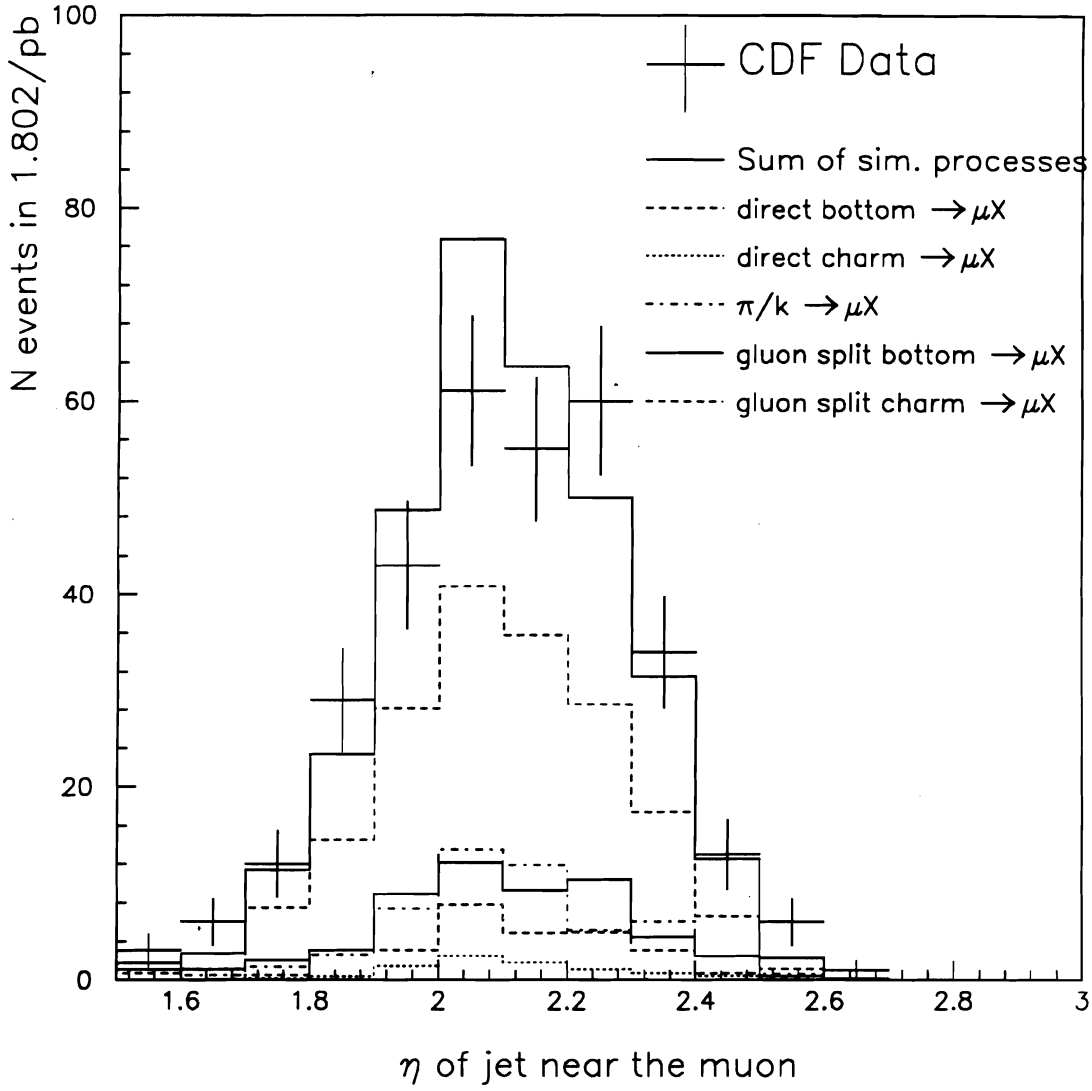

Figure 6.12: ***The pseudorapidity distribution for the jet near the muon in CDF data displayed with the result of the global fit in Table 6.8.***

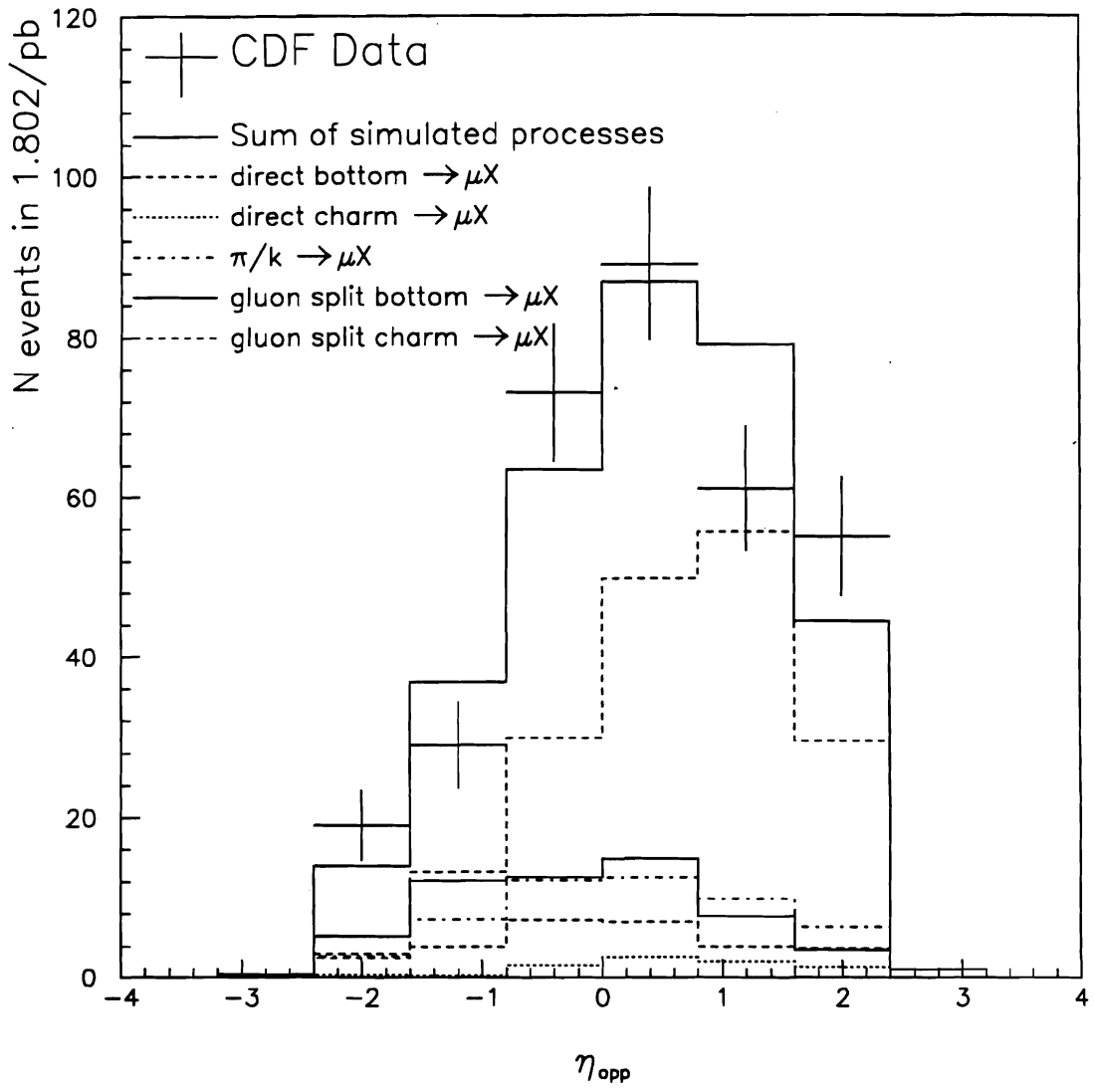

Figure 6.13: ***The pseudorapidity distribution for the opposite jet in CDF data displayed with the result of the global fit in Table 6.8.***

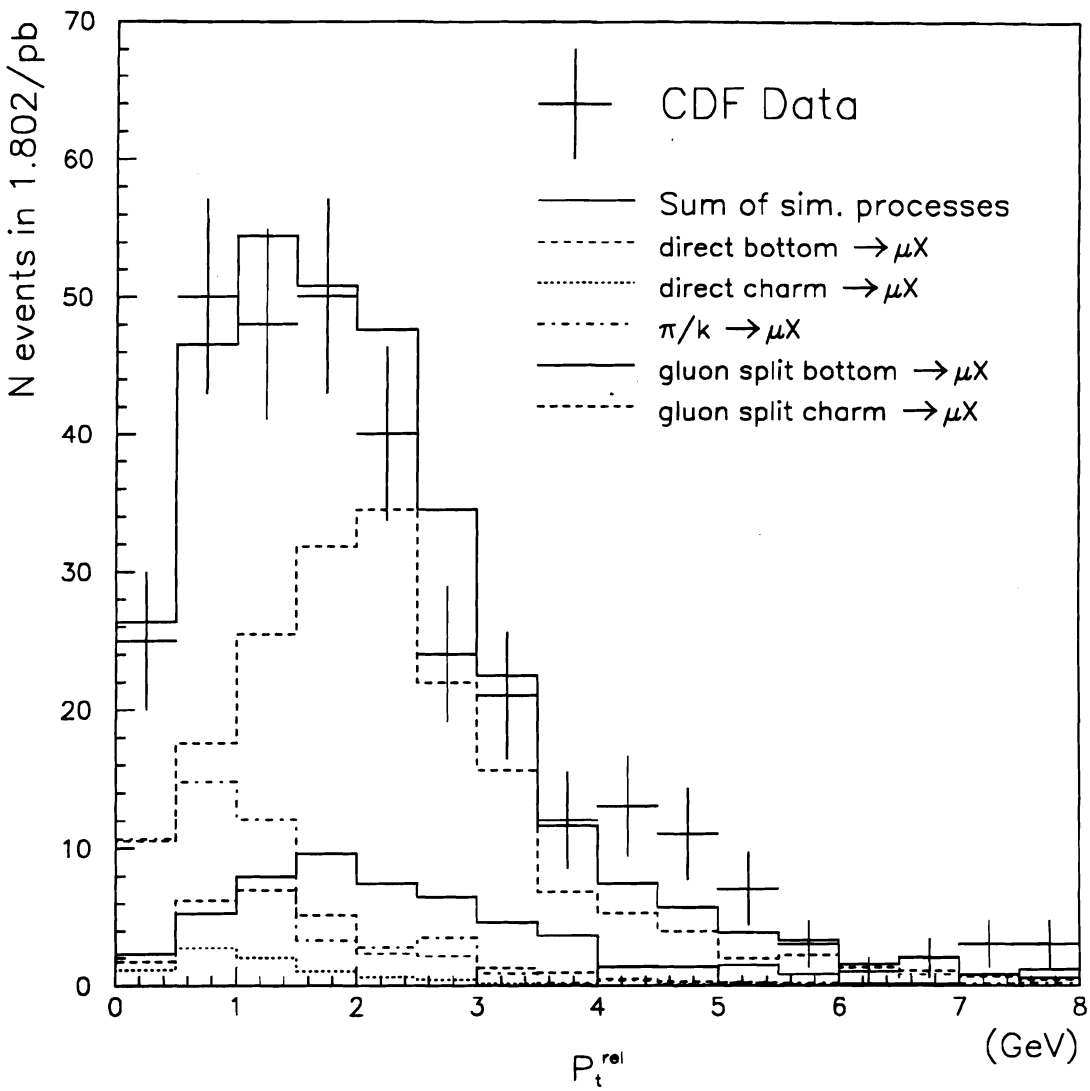

Figure 6.14: ***The p_t^{rel} distribution for CDF data displayed with the result of the global fit in Table 6.8.***

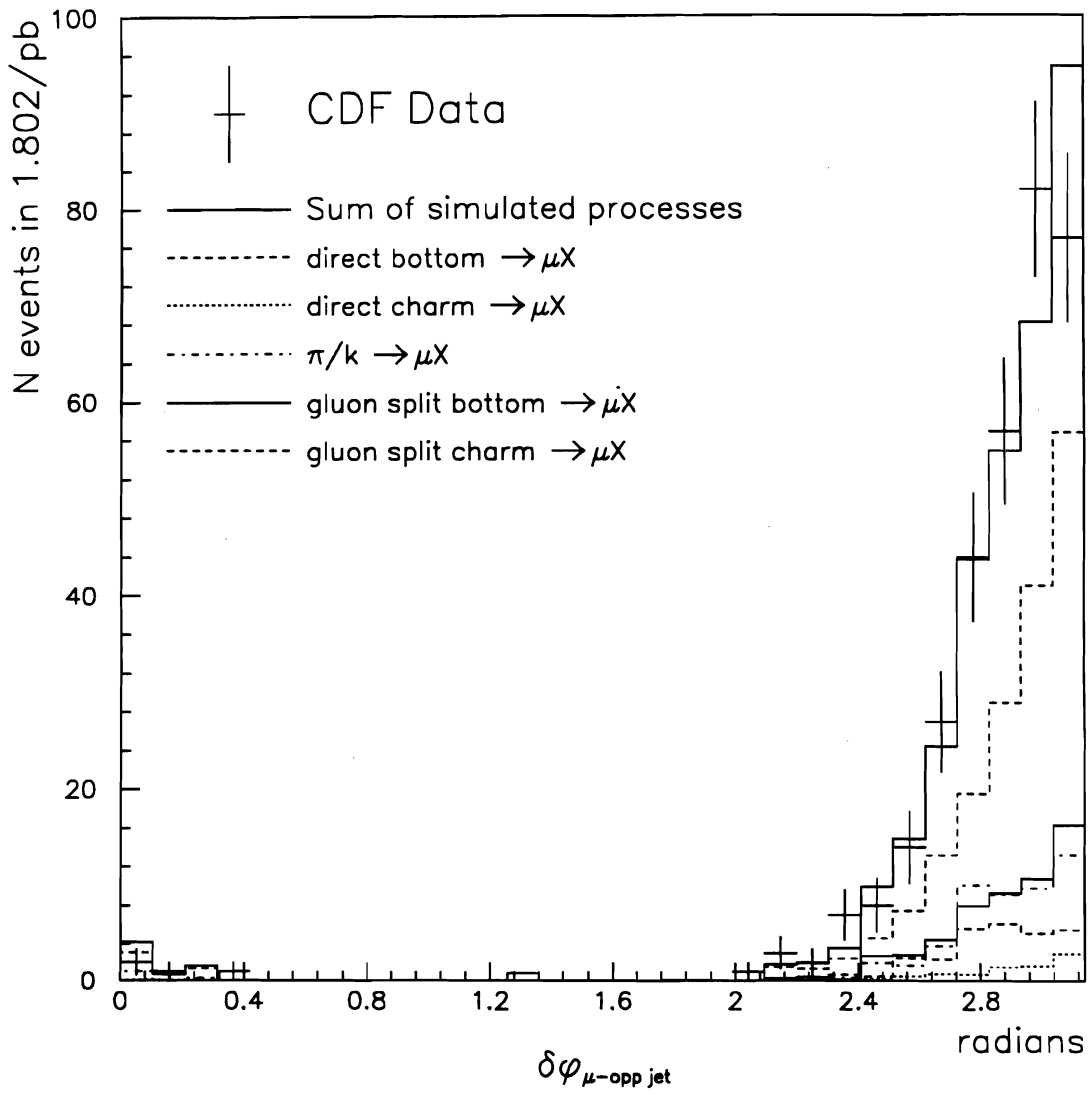

Figure 6.15: ***The azimuthal distance between the muon and the opposite jet for CDF data compared to the result of the global fit in Table 6.8.***

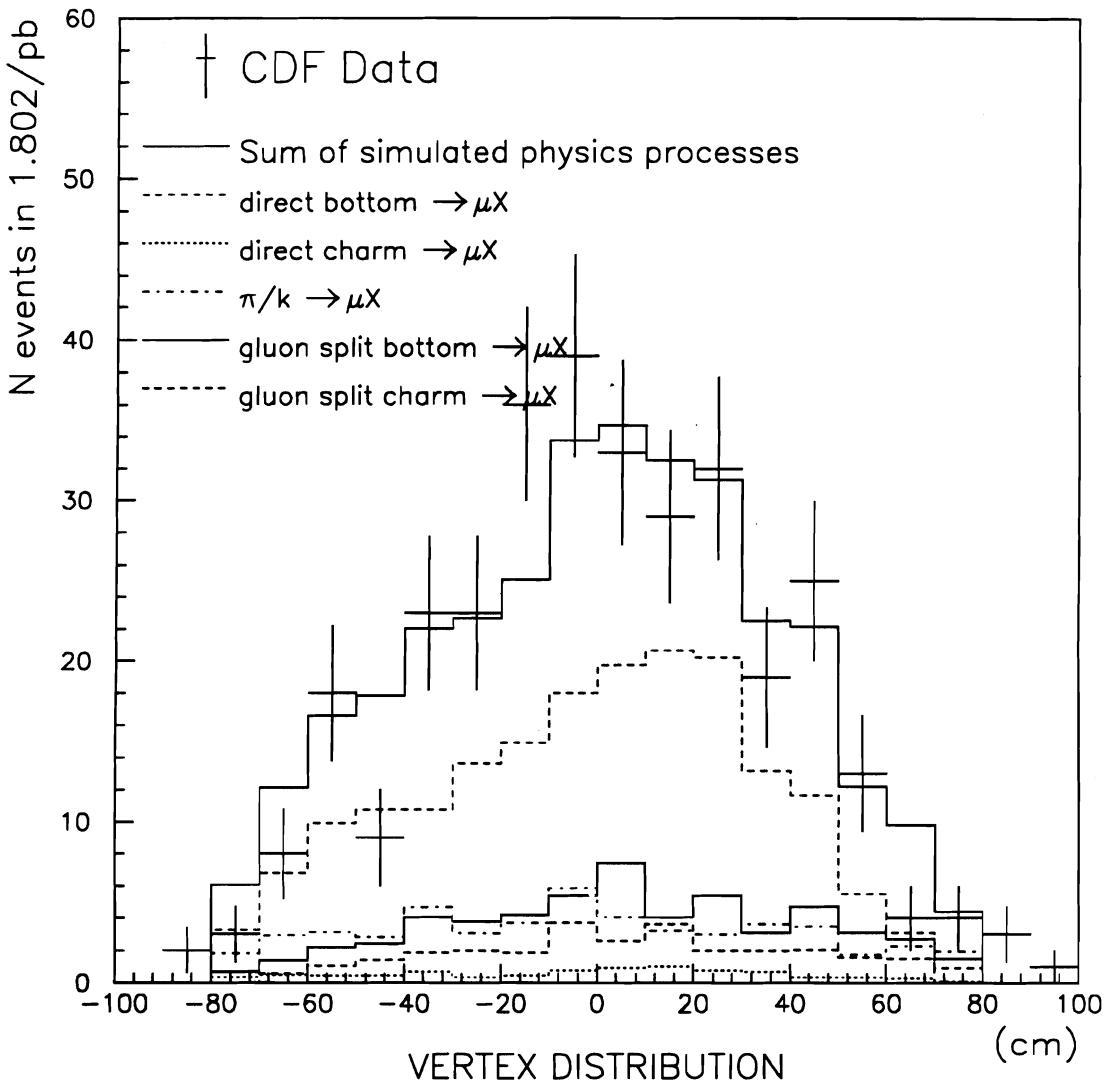

Figure 6.16: ***The vertex distribution for CDF data compared to the result of the global fit in Table 6.8.***

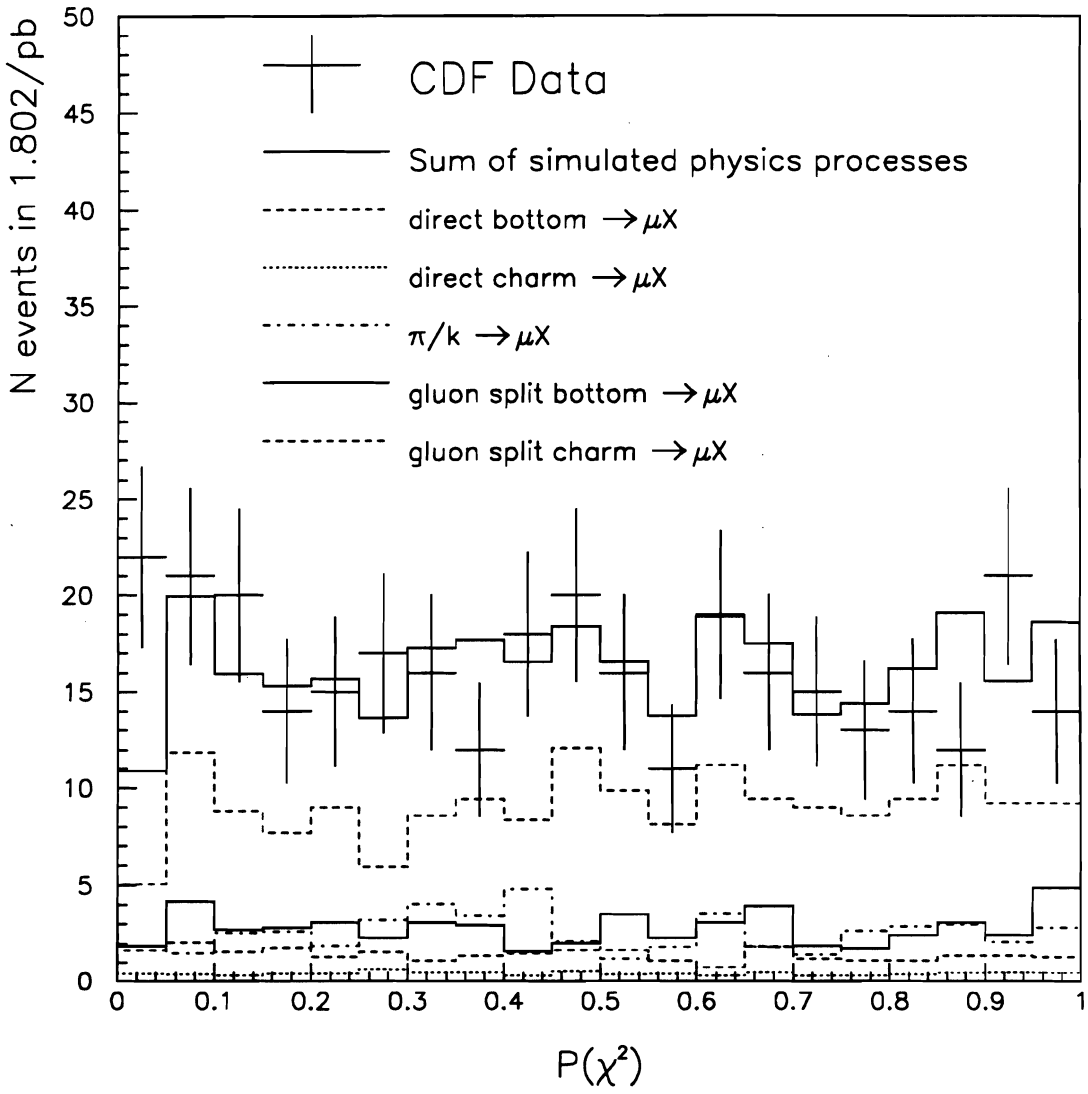

Figure 6.17: ***The probability of χ^2 distribution for CDF data compared to the result of the global fit in Table 6.8.***

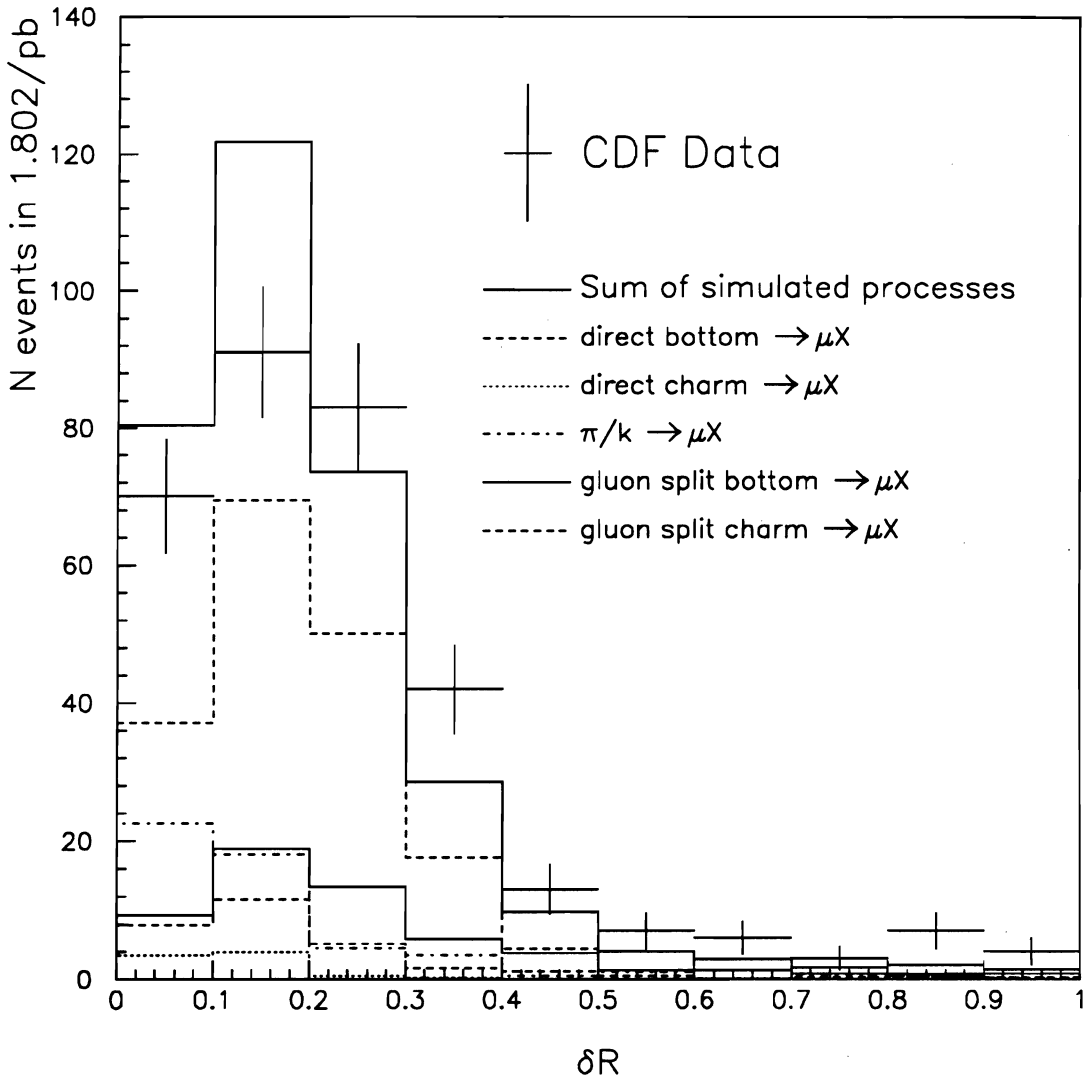

Figure 6.18: ***The distribution of δR between the forward muon and the nearby jet for CDF data displayed with the result of the global fit in Table 6.8.***

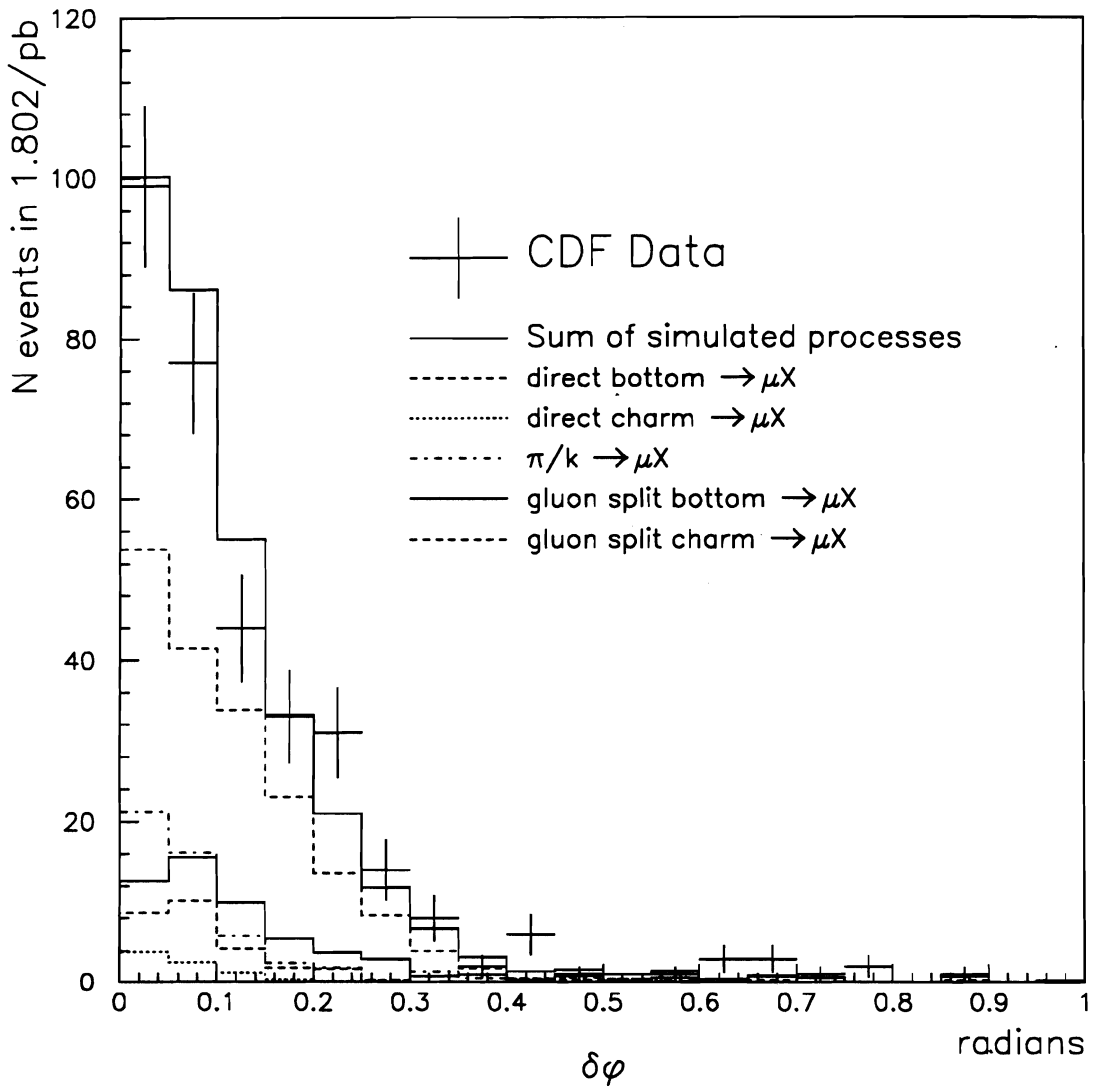

Figure 6.19: ***The distribution of $\delta\phi$ between the forward muon and the nearby jet for CDF data displayed with the result of the global fit in Table 6.8.***

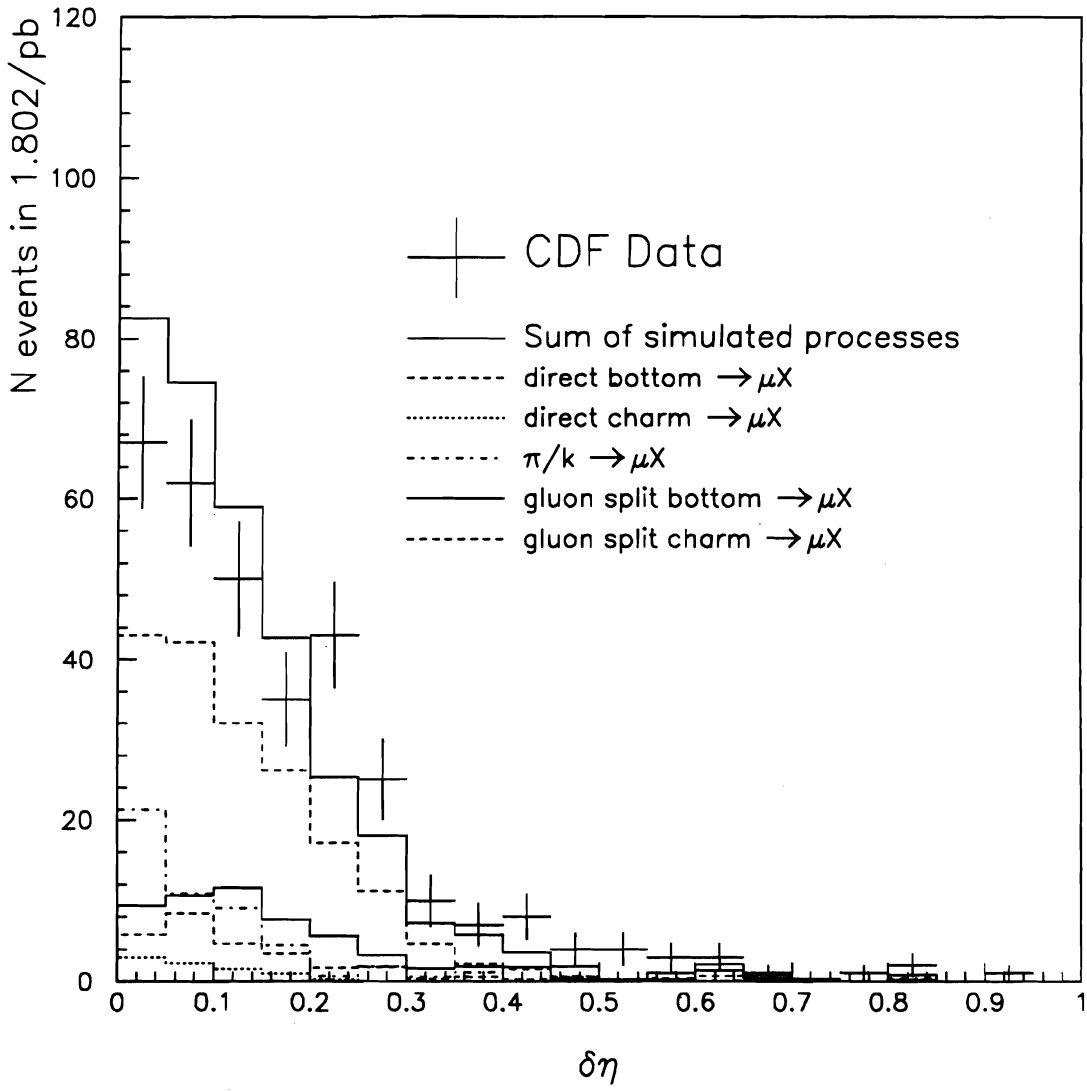

Figure 6.20: ***The distribution of $\delta\eta$ between the forward muon and the nearby jet for CDF data displayed with the result of the global fit in Table 6.8.***

Table 6.2, this indicates that the maximum direct bottom contribution to the data sample for all p_t^{rel} is 195 $\pm$ 53 events. The lower limit of the simple fit which assumes the maximum charm leakage into the high p_t^{rel} bin indicates that 93 $\pm$ 35 events in the data sample are attributed to bottom decays. These fits lend credence to the hypothesis that this data sample contains a large fraction of events which are the result of bottom decays. The direct bottom accounts for between 48% and 69% of the data sample and the contribution from both direct and gluon splitting bottom accounts for between 66% and 83% of data sample.

6.3.4 Extraction of direct bottom cross section

The p_t and η distributions for bottom quarks which contribute to the muons in jets sample were shown in Figure 6.2 In contrast to section 6.2, this time only the direct b quarks are to be considered. The acceptance region for the direct bottom quarks also includes the requirement on $p_t^{\bar{b}}$ which results from the central jet cut. The 90% point is determined from the momentum spectrum in Figure 6.21 and includes events with $p_t^{\bar{b}} > 15$ GeV. The global fit in Table 6.7 indicates that 182$\pm$48 events in the data sample emanate from direct bottom decays. This fit is consistent with the range of possible values in Table 6.6 and is in agreement with the simple fit performed earlier. On the basis of this agreement, it will now be used to calculate the direct bottom cross section. First, the simulated acceptance and efficiency is found using the theoretical cross section of MNR,

which is:

$$\sigma(P\bar{P} \longrightarrow bX : p_t^b > \ 20\text{GeV}, 1.9 < |\eta^b| < 2.5, p_t^{\bar{b}} > 15 \text{ GeV})$$
$$= (9.31 \pm .94 \pm 1.77) \text{ nb} \qquad (6.20)$$

The MNR calculation is discussed in Appendix E. Using this, the simulated acceptance and efficiency are, $A \times \epsilon_{sim} = .0171 \pm .0018$. After correcting for detector efficiency and acceptance, the integrated cross section for direct bottom production is:

$$\sigma(P\bar{P} \longrightarrow bX : p_t^b > 20 \text{ GeV}, 1.9 < |\eta^b| < 2.5, p_t^{\bar{b}} > 15 \text{ GeV})$$
$$= (100. \pm 30.) \text{ nb} \qquad (6.21)$$

where the uncertainty is only statistical. The predicted cross section is a factor of $10.7 \pm 3.4 \pm 2.0$ smaller than the measured direct bottom cross section.

6.4 Systematic effects

The measured cross sections quoted for both total bottom production and direct bottom production used central values for all contributions to the systematic uncertainty. The effect of the uncertainty in these factors on the cross section will now be addressed. Specifically, there are uncertainties in the jet energy scale and resolution, the muon momentum resolution and trigger efficiency, the angular resolution of muons and jets, and finally, the modelling of NLO bottom quark production with ISAJET.

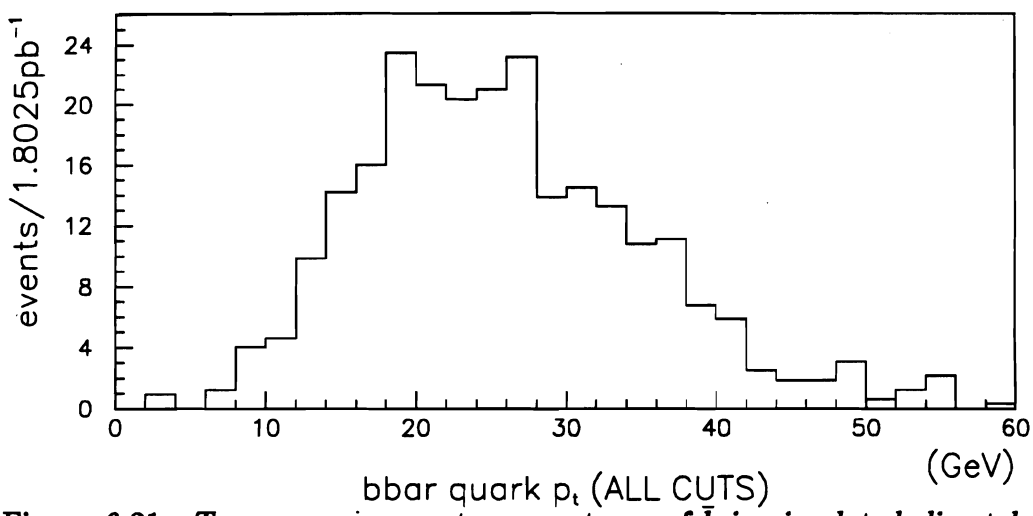

Figure 6.21: ***Transverse momentum spectrum of $\bar{b}$ in simulated direct bottom quark events which passed all analysis cuts.***

	uncertainty	resulting uncertainty in cross section
JET ENERGY SCALE:		
plug ($E_t > 10$ GeV)	$^{+9.7\%}_{-8.8\%}$	
central ($E_t > 15$ GeV)	$^{+7.5\%}_{-6.5\%}$	+16.6%
plug ($E_t > 15$ GeV)	$^{+7.6\%}_{-6.6\%}$	−30.5%
bottom fragmentation	+5%	
JET RESOLUTION:		
central	±10%	negligible
plug	±10%	

Table 6.9: *Systematic uncertainties for the jet energy measurement which affect the direct bottom quark measurement.*

6.4.1 Jet energy scale

Table 6.9 lists the size of the uncertainties in the jet energy scale and resolution. These come from the uncertainty in the calorimeter response to single particles, the underlying event and fragmentation as described in chapter 4.

A change in the energy scale is equivalent to a change in the jet E_t cut. To simulate this effect, the jet cut is both lowered and raised in the simulated samples by the uncertainty in the energy scale and then the fits are recalculated. The energy scale uncertainty due to bottom quark fragmentation is added in

quadrature to the calorimeter uncertainty for jets coming from bottom quarks in the simulated sample.

The bottom quark cross section changes as the modified cuts affect the efficiency of observing events. As the number simulated, N^{sim}, increases the cross section decreases as shown in equations 6.8 and 6.9. Lowering the jet cut allowed +30.5% more simulated events into the sample. Raising the jet cut reduced the number of simulated events by −16.6%. Since the number of simulated events comes into the denominator when calculating the cross section, the cross sections for this data sample have an uncertainty of $^{+16.6}_{-30.5}$%.

The fits for the number of bottom events in the data sample do not change significantly with the change in the number of simulated events since the shape of p_t^{rel} and η_{opp} remain approximately the same. To show that the measured bottom content in the sample remaines more or less constant as the jet cuts are varied, Table 6.10 lists the number of events in the data sample attributed to bottom decays for the nominal, lower, and higher jet cuts. The fit used is the first fit of the chapter, and the nominal values come from Table 6.3. The variation in the global fit is shown in Table 6.11. The fits fluctuate 5% to 10% which is well within the statistical uncertainty of the measurements. This is a secondary affect compared to the change in the acceptance with changes in the jet cuts.

signal	background	signal events nominal jet cut	signal events lower jet cut	signal events higher jet cut
direct b	direct c	(270 ± 36)	(286 ± 36)	(262 ± 36)
direct b	gluon split c	(241 ± 50)	(265 ± 50)	(232 ± 48)
gluon split b	direct c	(251 ± 35)	(258 ± 34)	(231 ± 33)
gluon split b	gluon split c	(215 ± 45)	(227 ± 43)	(194 ± 41)

Table 6.10: *Fluctuations in the bottom content of the data sample with systematic shifts in the jet energy scale.*

Physics process	Yield in data (events) nominal jet cut	Yield in data (events) lower jet cut	Yield in data (events) higher jet cut
direct b	182 ± 48	202 ± 59	172 ± 56
direct c	8.3 ± 3.2	7.5 ± 6.4	9.2 ± 6.6
π decay	51 ± 20	47 ± 23	56 ± 22
gluon split b	56 ± 34	45 ± 47	59 ± 45
gluon split c	28 ± 17	24 ± 44	33 ± 43

Table 6.11: *The global fit used to determine the cross section with the jet cuts adjusted according to the uncertainty in the jet energy scale. The ratio of the direct charm and π/K decay in flight are fixed. Also held fixed is the ratio of gluon splitting bottom and charm.*

6.4.2 Jet resolution

The jet resolution is known to within 10% of itself. Since the resolution of the calorimeters are on the order of 10%, the uncertainty in the resolution is on the order of 1% of the jet energy. Jets near the cut can slide into or out of the data sample with increased resolution. However, with a 10 GeV jet cut, the increased resolution is only 100 MeV. When this effect was simulated, only two events fell out of the simulated direct bottom simulation sample. Therefore the affect on the acceptance is negligible. Additionally, the jet energy is not used to determine the value of the fitted variables and so has no affect on the fits.

6.4.3 Forward muon momentum resolution

The forward muon momentum resolution described in chapter 3 included chamber resolution, multiple scattering and survey resolution. The nominal simulation neglected the survey resolution since it is not as well understood. The uncertainty of surveyed positions measured in the xy plane is 500 μm and in the z direction is 2000 μm. A conservative uncertainty in the number of chambers which were not exactly where expected is 10%. Doubling the survey resolution for these chambers overestimates the survey uncertainty. The survey resolution is:

$$\sigma(p)/p = .0012 \times p. \tag{6.22}$$

Muons with $p_t = 8$ GeV at $\theta = 15°$ have a momentum of 30 GeV and an additional survey resolution component of , $\sigma = 3.6\%$. The nominal resolution is greater

than 16.6%. The affect of the survey resolution when added in quadrature with the nominal resolution is barely noticeable.

Rather surprisingly, the affect of increasing the resolution on the p_t^{rel} distribution is to make all the spectrum slightly softer. Since at low momentum the muon spectrum is cut off by the trigger threshold, the resolution effect is to widen the bump in the low p_t spectrum. This tends to move a slightly larger fraction of events down in momentum than up. Thus, the p_t^{rel} spectrum becomes a tiny amount softer as it is the Fits using the increased resolution give higher bottom quark yields by 5% than those with the nominal resolution.

The number of simulated events which pass the acceptance requirements with the increased resolution also increases by +3.0%. The increase in N^{sim} drives the cross section down by the same percentage. The 5% increase in the cross section from the fits and the 3% decrease from the change in acceptance cancel each other leaving a net increase in the cross section of +2%.

6.4.4 Angular resolution

The angular resolution for jets is the size of tower. For the forward muon, the resolution in θ is .4° and in ϕ it is $5°/\sqrt{12}$. The uncertainty in the azimuthal resolution comes mainly from muons that scatter out of the pad road. This uncertainty was discussed in section 3.6 and does not contribute significantly. Figures 6.19 and 6.20 show the fit to the angular distributions. These distributions are consistent with the fit, however, the tail of the distribution in $\delta\eta$ is somewhat

signal	background	signal events fit over p_t^{rel}	signal events fit over $\delta\phi$
direct b	direct c	(270 ± 36)	(305 ± 45)
direct b	gluon split c	(241 ± 50)	(288 ± 75)
gluon split b	direct c	(251 ± 35)	(285 ± 45)
gluon split b	gluon split c	(215 ± 45)	(255 ± 72)

Table 6.12: *Fluctuations in the bottom content of the data sample with fits over $\delta\phi$ instead of p_t^{rel}.*

larger in the data. As a check, fits were performed substituting $\delta\phi$ distributions for those in p_t^{rel}. Table 6.12 shows that the cross section increases by up to 20% by fitting over $\delta\phi$ instead of p_t^{rel}.

6.4.5 Modelling

ISAJET has been used to generate direct bottom quark distributions. For the first measurement of the chapter, the momentum distribution in ISAJET was made to agree with the MNR prediction by including a weighting function, $f(p_t^b)$, for the gluon splitting simulation. The checks of the energy spectra and η_{opp} distribution for the three partons in the events for the direct bottom quark measurement are presented in Appendix D.2. It can be seen in figure D.3 that ISAJET predicts more asymmetry in the η_{opp} plot for the direct case and less for the gluon splitting case. A weighting function has been applied, $f(\eta_{opp})$, and the fits recalculated.

Physics process	Yield in data (events) η^{opp} from ISAJET	Yield in data (events) η_{opp} weighted
direct b	182 ± 48	175 ± 53
direct c	8.3 ± 3.2	8.1 ± 6.6
π decay	51 ± 20	50 ± 24
gluon split b	56 ± 34	59 ± 43
gluon split c	28 ± 17	34 ± 43

Table 6.13: *The global fit used to determine the cross section with the η_{opp} distribution weighted. The ratio of the direct charm and π/K decay in flight are fixed. Also held fixed is the ratio of gluon splitting bottom and charm.*

The new fits are within 4% of the fits without the weighting function. Table 6.13 compares the nominal fit to the fit with the weighting function applied. The systematic uncertainty in the cross section due to this affect is -4%.

6.5 Summary of the total and direct bottom quark cross section

The method of measuring the cross sections is described by equation 6.9. Factors contributing to the cross section measurement are listed in Table 6.14 along with the result.

The systematic error in the bottom quark cross section is dominated by the uncertainty in the jet energy scale. This contributes $^{+16.6\%}_{-30.5\%}$ from the acceptance calculation and $^{+10\%}_{-5\%}$ from the fits. The forward muon momentum resolution uncertainty contributes an additional +2% and the angular resolution contributes +20%. These systematic uncertainties were added in quadrature to find the total uncertainty of $^{+30\%}_{-31\%}$. This uncertainty applies to both the total and direct bottom quark cross sections quoted earlier. The direct bottom cross section has the additional uncertainty from modelling the η_{opp} distribution of −4%. The final results are listed in Table 6.14 with all systematic uncertainties added in quadrature including those from signal and background processes.

6.6 Dilepton check of the direct bottom content

As an additional check of the bottom quark production in this data sample of 326 events, the number of central muon candidates was determined. Muon candidates were defined by three simple cuts:

- $p_t^\mu > 3.0$ GeV
- dev x $< 3\sigma$
- dev y $< 3\sigma$

	Total		Direct
kinematic region	$p_t^b > 20$ GeV $1.9 < \|\eta^b\| < 2.5$		$p_t^{b(\bar{b})} > 20(15)$ GeV $1.9 < \|\eta^b\| < 2.5$
N^{meas} (events)	direct $256 \pm 32 \pm 15$	gluon split $233 \pm 33 \pm 18$	182 ± 48
$\int_{FMU} Ldt$	$(1.80 \pm .14)$ pb^{-1}		
$B(b \longrightarrow \mu)$	.11		
$A \times \epsilon_{sim}$	direct $.0127 \pm .0005$	gluon split $.0368 \pm .0019$	$.0171 \pm .0018$
$\epsilon_{trig}/(.95)^6$	$.537 \pm .019$		
predicted cross section (nb)	$21.3 \pm .4^{+10.2}_{-5.9}$		$9.31 \pm .94 \pm 1.77$
measured cross section (nb)	direct $189 \pm 35. \pm 11.$	gluon split $59.5 \pm 11.6 \pm 4.6$	$100. \pm 30.$
average measured cross section (nb)	$124. \pm 35. \pm 66$		$100. \pm 30.^{+0.}_{-4.}$
added sys. unc.	$^{+30}_{-31}\%$		
average measured cross section (nb)	$124. \pm 35. \pm 76$		$100. \pm 30.^{+30.}_{-31.}$

Table 6.14: *Summary of the total and direct measured bottom quark cross sections compared to theory. In all cases, the first uncertainty is statistical and the second is systematic. The cross sections are calculated using equations 6.6 to 6.9.*

where dev x and dev y are the deviation in x and y of the track from the muon stub. A multiple scattering model is used to project central tracks through the calorimeters to determine the uncertainty in the track position at the muon chambers. If the projected track and the muon stub are more than 3σ different, the event is rejected. This selection criteria produced 5 muon candidates.

To determine the predicted number of muons produced from bottom quark decays in the sample, simulated direct bottom events were selected with muons which pass the p_t cut and are within $|\eta| < .6$. Using the measured direct bottom cross section of $100 \pm 36^{+16.6}_{-30.6}$ nb, and an additional acceptance factor for the central muon chambers of .80, the predicted number of bottom quarks decaying to muons in the central detector was $4.8 \pm 1.8^{+1.2}_{-1.7}$ events. Gluon splitting events are not supposed to contribute many events because the opening angle between the two bottom quarks is expected to be small.

The fake muon rate for this sample is determined from the number of tracks in the minimum bias data which passed the muon cuts.[54] The fake rate, f_μ, is $(.27 \pm .10)\%$. In the 326 events in this data sample, there were 232 tracks with $p_t > 3.0GeV$ and $|\eta| < .6$. The number of fake muons, N_{fake} is given by:

$$N_{fake} = f_\mu \times 232\,\text{tracks} \times A \tag{6.23}$$

where A is the acceptance of the muon chambers (.80). The background events is therefore predicted to be $.50 \pm .18$ events. Clearly the dilepton yield in this data sample is best understood in terms of the direct bottom decays.

6.7 Interpretation

The interpretation of the present result is limited by the statistical and systematic uncertainties of the measurement. Future measurements are necessary to make more quantitative tests of quantum chromodynamics. Until a more statistically significant measurement is made, however, this measurement is indicative of bottom quark production at forward pseudorapidity.

The present result can be compared to both theoretical predictions and other b quark cross section measurements at CDF. Measurements of the b quark production cross section in the central region ($|\eta| < 1.0$) are shown in Figure 2.4, along with theoretical predictions for that region. The correlation between separate measurements of the cross section and the disagreement between experimental measurements and theoretical predictions have cast doubt on the theoretical predictions. There are three hypotheses for the difference between the theory and experiment: (1) uncertainty in the choice of the μ scale for the predicted cross section, (2) uncertainties in the gluon structure functions for the x values relevant to b quark production at CDF energies and (3) contributions from higher order Feynman diagrams.

As noted in section 6.4.6, the measured forward b quark cross section differs from the theoretical prediction. The measurement in the forward region is sensitive to the same theoretical uncertainties as the measurement in the central region. We can compare the η dependence of the cross section from experiment

to theory if the assumption is made that the theory reproduces the shape of the distribution correctly independent of the magnitude. In Figure 6.22 the η dependence of the total bottom quark cross section is shown, where the theoretical prediction has been normalized to measured values for $|\eta| < 1.0$. The change from the central value to the forward value is consistent (within the large experimental uncertainties) with the expected drop off with rapidity.

The direct bottom quark measurement has smaller uncertainties than the total bottom quark measurement, but again only weakly tests the theoretical prediction. The systematic uncertainty of the predicted direct bottom quark cross section is relatively smaller than the that of the predicted total bottom cross section. The main difference comes from the μ scale dependence of the cross section shown in Figure 6.23. Here it can be seen that the theoretical prediction for direct bottom quark production is stable with respect to variation in μ scale, while the prediction for gluon splitting production is highly dependent upon the choice of μ. Measuring the direct bottom cross section therefore removes one of the significant uncertainties in the theoretical prediction.

Attempts have been made to see if the discrepancy between theory and experiment in the central region can be accounted for by variations in the gluon structure functions[8]. The x region where this measurement probes is an extrapolation from regions where other measurements exist. The discrepancy can fit within the context of the global structure function fits[8], but requires an enhancement in the gluon structure function solely in the x range sampled by the

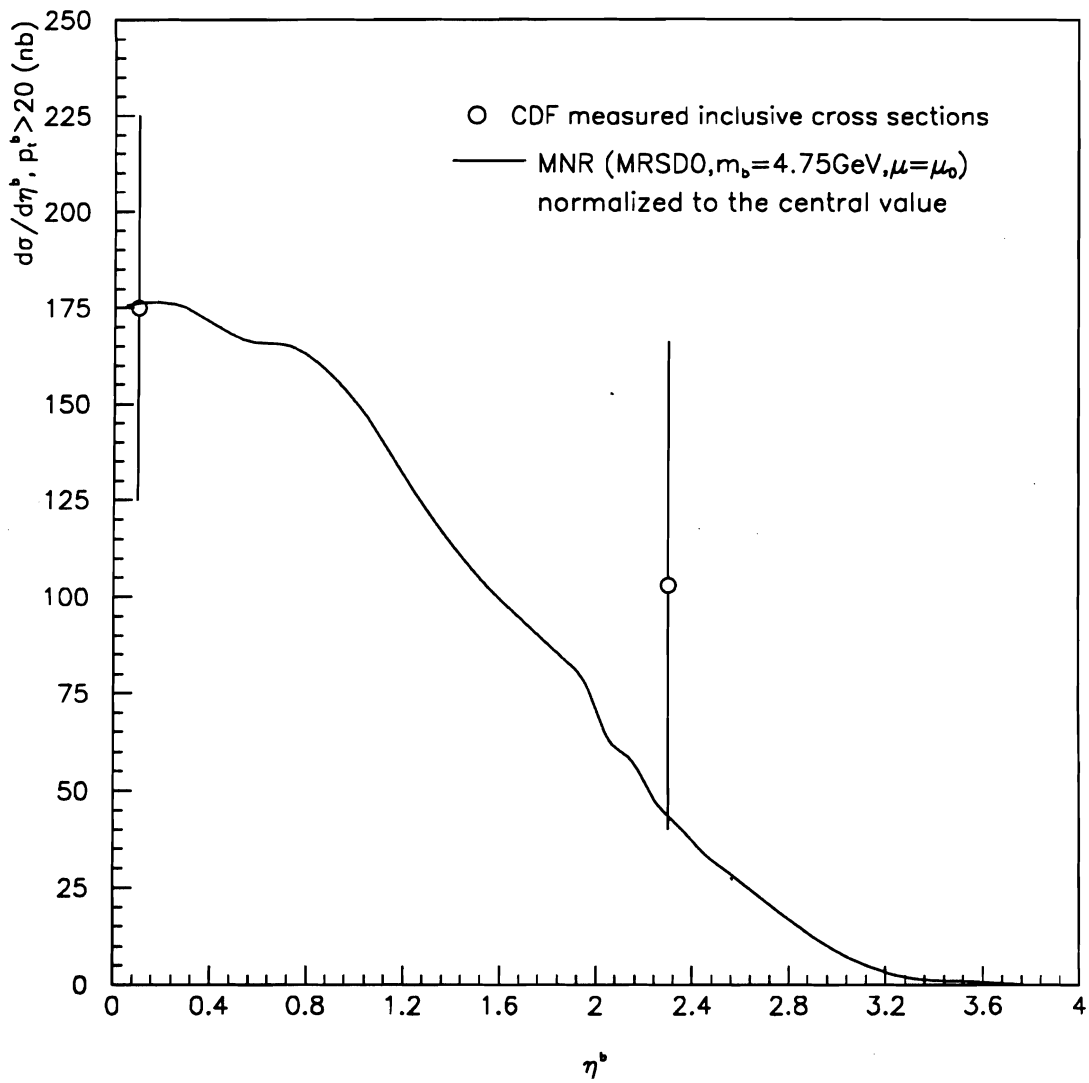

Figure 6.22: ***The measured η dependence of the cross section compared to the theoretical prediction normalized to the central measurement.***

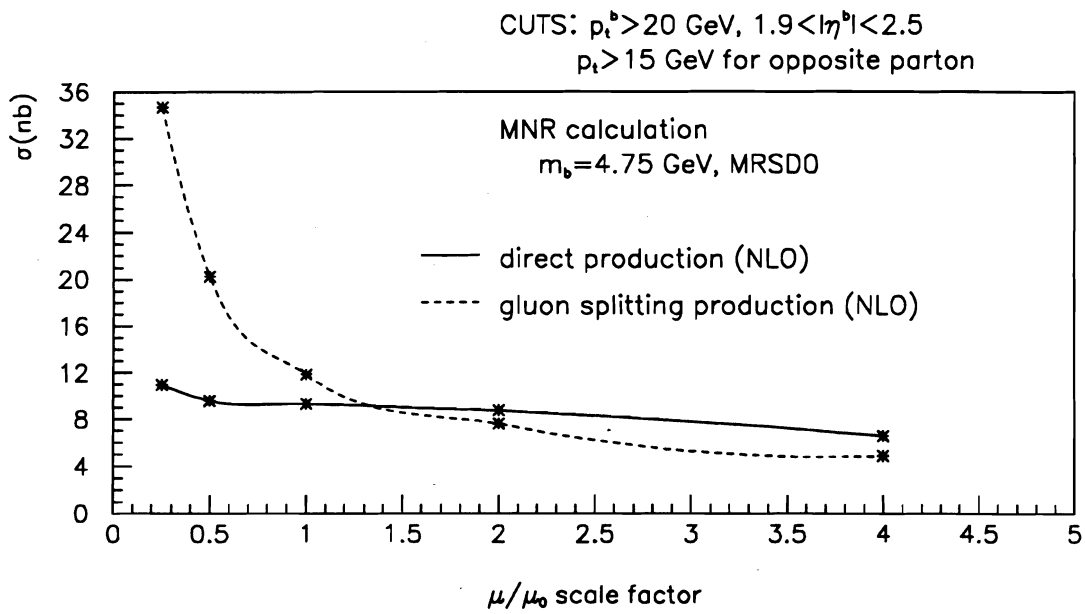

Figure 6.23: ***The μ scale dependence of the predicted cross section.***

central cross section measurements.

B production in the forward regions samples a lower x value (for one of the two partons) than an equivalent interaction with the same $\hat{S}$ in the central region. For instance, at $\eta^b = \eta^{\bar{b}} = 0$ and $p_t^b = p_t^{\bar{b}} = 20\ GeV$, $x_1 = x_2 = 0.02$. At the same momentum and $\eta^b = 2$ and $\eta^{\bar{b}} = 0$, $x_1 = 0.09$ and $x_2 = 0.01$. In the central region, the lowest x values which affect the current measurements correspond to the $p_t^{min} > 10$ GeV case. For these interactions, $x_1 = x_2 = 0.01$. In the forward region, the lowest x values correspond to $\eta^b = \eta^{\bar{b}} = 2.5$, where $x_1 = 0.271$ and $x_2 = 0.001$. The average x values for events in the direct forward bottom quark simulation are $x_1 = 0.13$ and $x_2 = 0.005$. This range implies that the forward measurements on average go a factor of two lower in x than the central measurements. Changes to the gluon structure function at low x, therefore, affect the production mechanism in this analysis.

The forward bottom cross section is a measure of the understanding of QCD heavy quark production and is sensitive to the gluon structure function. The discrepancy between the current measurement and theoretical predictions is intriguing, but quantitative statements on this discrepancy await more precise measurements. This thesis has shown that the measured forward bottom cross section is consistent within experimental uncertainties with other measurements made at $\sqrt{s} = 1.8$ TeV and theoretical predictions.

Appendix A

FMU 88/89 Detector Efficiency

The forward muon yields depend on the efficiency of the detector and trigger. The detector design efficiency and geometric acceptance are easily calculated and are not the concern of this appendix. Here, the focus is the contribution from detector components which did not perform at the design efficiency. Disabled or broken components, while relatively rare, contributed visibly to the efficiency. What follows is the tabulation of the individual failure modes and the overall effect on the data yield. The final result is then compared to track distributions to show consistency.

A.1 Single channel contribution to the trigger efficiency

The FMU detector consists of 3 planes of drift chambers and 2 planes of scintillators located in both the forward and backward directions. Each drift chamber has 56 coordinate cells and 40 ambiguity cells. In all, there are 13,824 drift cells, and 96 scintillators in the system. The gain of the drift chambers was sufficiently high to maintain sensitivity to minimum ionizing particles with an efficiency of $(99.6 \pm .5)\%$. However, breakage in the system affects our ability to collect chamber hits. We now calculate the efficiency of the drift chambers and scintillators. To calibrate the trigger, we use events which were collected independently of the FMU trigger. These volunteer events were triggered by one or more of the other detector triggers within CDF. The volunteer data for this piece of analysis were collected using the following triggers:

- L2 BBC_INTIME_PREREQ*
- L2 DIELECTRON*
- L2 DIMUON*
- L2 ELECTRON_5*
- L2 ELECTRON_EMC_5*
- L3 MISSING_ET_15*

- L3 MISSING_ET_10_V4
- L3 MISSING_ET_KDIJET_TALK
- L3 MISSING_ET_PHO_V*
- L3 JET_60_CLEANUP
- L3 JET_40_CLEANUP
- L3 JET_20_CLEANUP
- L3 TRIJET_20_CLEANUP
- L3 MULTIJET*
- L3 TOTAL_ET_120*
- L3 TOTAL_EM_ET_60_V2
- L3 CMU_FILT_V2
- L3 CMU_FILT_V3
- L3 CMU_FILT_V4
- L3 CMU_FILT_V6
- L3 ELECTRON_CENTRAL_12_V6
- L3 ELECTRON_CENTRAL_7_V8

- L3 PHOTON_CENTRAL*
- L3 PHOTON_GAS*
- L3 DIPHOTON_*
- L3 TAU_20
- L3 TAU_30
- L2 MISSING_ET* Runs$\leq$16593
- L2 TOTAL_EM_ET_* Runs$\leq$16801
- L2 CENTRAL* Runs$\leq$16801
- L2 DIPHOTON* Runs$\leq$16801
- L2 PHOTON* Runs$\leq$17808
- L2 ELECTRON* Runs$\leq$17808
- L2 JET* Runs$\leq$18900
- L2 TRIJET_20 Runs$\leq$18900
- L2 TOTAL_ET_* Runs$\leq$18900
- L2 PHOTON_GAS_EMC_23 Runs$\leq$18900
- L3 MISSING_ET_PHO_KDIJET Runs$\geq$18911

- L3 TAU_10* Runs$\geq$18911

In addition, loose quality cuts are placed on the muons to insure that erroneous backgrounds don't affect the result. The cuts are:

- Volunteer Trigger
- $Pt > 5$ GeV
- Calorimetry:

  PEM> .1 GeV and PHA> .9 GeV

  Or

  FEM> .2 GeV and FHA> 1.5 GeV
- Prob(χ^2) > .02
- 1st wire $\geq$ 33
- Splash$\leq$ 17 hits in the octant with the track
- Existence of a vertex

A discussion of these cuts and their efficiency can be found elsewhere.[13]

A.1.1 Drift chamber

Since the FMU trigger requires all six hits out of a possible six, it is crucial to know the single wire hit efficiency. Included here are the efficiencies for both a

working chamber and any isolated single channel failures. The chamber efficiency was measured by comparing the number of 5 hit tracks to the number of 6 hit tracks. The probability or efficiency of finding a 5 or 6 hit track where ϵ_{ce} is the single chamber efficiency and there are 6 possible chamber hits is:

$$\epsilon_{ce}(6) = \epsilon_{ce}^{6} \tag{A.1}$$

$$\epsilon_{ce}(5) = 6 \times (1 - \epsilon_{ce}) \times \epsilon_{ce}^{5} \tag{A.2}$$

Dividing $\epsilon_{ce}(5)$ by $\epsilon_{ce}(6)$ it is easy to solve for the single chamber efficiency. The ratio, $\epsilon_{ce}(5)/\epsilon_{ce}(6)$, may be multiplied top and bottom by the total data yield to produce the measured quantity in terms of the number of tracks with 5 and 6 hits, N_5 and N_6.

$$\epsilon_{ce} = \frac{6}{6 + N_5/N_6} \tag{A.3}$$

The distribution of 5 and 6 hit volunteer tracks are given in Table A.1 for each octant in the detector. Notice that there are more 5 hit tracks on the east than the west. Since the efficiency of the two ends of the detector vary significantly, they are calculated separately. Statistics are sufficiently poor for each octant, however, that the sum of hits in all octants are used. The efficiency results are shown in Table A.2.

A.1.2 Scintillator

From the beginning of the run until February 1989, front and rear planes of scintillators were required to show signals with a match in ϕ to the wire trigger

octants:	0	1	2	3	4	5	6	7	sum
$R < 18200$									
West 5 hit	17	13	8	11	7	12	18	10	96
West 6 hit	31	12	11	17	21	38	27	36	193
East 5 hit	16	8	7	11	16	6	23	20	107
East 6 hit	28	18	4	11	19	2	20	13	115
$R \geq 18685$									
West 5 hit	25	5	24	11	14	20	31	17	147
West 6 hit	47	27	25	50	48	36	27	47	307
East 5 hit	21	16	29	18	32	7	25	12	160
East 6 hit	38	47	27	44	44	16	31	45	292

Table A.1: *Number of volunteer tracks with 5 and 6 hits available for the fit.*

	ϵ_{ce}	$\epsilon_{ce}(5)$	$\epsilon_{ce}(6)$
$R < 18200$			
West	$.923 \pm .009$	$.308 \pm .021$	$.620 \pm .036$
East	$.866 \pm .016$	$.392 \pm .010$	$.421 \pm .046$
$R \geq 18685$			
West	$.926 \pm .007$	$.302 \pm .017$	$.631 \pm .028$
East	$.916 \pm .008$	$.324 \pm .016$	$.592 \pm .029$

Table A.2: *The chamber efficiency and probability for finding 5 and 6 hit tracks.*

ϵ_{scint}	R15880-R16566	R16567-R18199	R18865-R18847	R18848-end
West	$.751 \pm .024$	$.751 \pm .024$	$.751 \pm .024$	$.978 \pm .014$
East	$.733 \pm .028$	$.733 \pm .028$	$.733 \pm .028$	$.976 \pm .014$

Table A.3: *The scintillator contribution to the trigger efficiency.*

octant. The scintillator requirement was removed from the trigger between runs R19101 and R19179. Using the data selection described above for the data before R19101, there are 253 events on the west with a scintillator match and 84 without. Similarly, there are 181 events on the east with a match and 66 without. Since scintillators are required in pairs, this can be converted into a trigger efficiency of $.751 \pm .024$ on the west and $.733 \pm .028$ on the east. The scintillator efficiency is just the square root of the trigger efficiency. The scintillator efficiency is $.867 \pm .014$ on the west and $.856 \pm .016$ on the east.

Once the scintillator requirement was removed from the trigger, we assign a value of 1.00 to the scintillator efficiency. There were (92.9 ± 42.3) nb^{-1} of data collected with the FMU detector using the NUPU and scintillator trigger, and (944.2 ± 42.3) nb^{-1} collected using just the NUPU trigger. Thus for runs greater than R18848, the trigger efficiency contribution from the scintillators is $.978 \pm .014$ on the west and $.976 \pm .014$ on the east. Table A.3 lists the scintillator contribution to the trigger efficiency.

A.2 Group failures

Failures of groups of wires or entire wire chambers occurred due to broken HV connections or gas impurities (for example leaks in the wire chambers). A similar effect occasionally resulted from TDCs which were temporarily disabled to mask "hot" trigger octants. A group failure removes two hits from a 6-hit track since each chamber contains two wire planes. Group failures are therefore not counted by the single hit efficiency calculation which uses the ratio of 5-hit to 6-hit tracks. Also, since the chamber readout is an OR of the 3 chambers in an octant, the failure of a single chamber is not necessarily detected in the group failure. The single chamber failures are addressed in the next section. Here we concentrate on the intermittent failure of three chambers forming an octant.

For this analysis, a large number of events were scanned for FMU chamber hits in the trigger region. Coordinate and ambiguity hits in the trigger region were counted. Figures A.1a,b and c show the wire hit distributions in each plane. It should be noted that the rate is always highest at $\phi = 90°$ due to the main ring splash. Also, the middle chambers on both sides see lower overall rates because they are shielded from beam splash in both the frontward and backward directions by the toroid steel. The somewhat surprising result that the east and west chambers see the same rate modulo dead detector components was the inspiration for measuring the rate for each octant on both the west and the east during each run and comparing it to the rate for each octant averaged over west

and east and all runs for a long period of time. The measured fraction can be written:

$$R_{oct-end} = \frac{N_{oct-end} / \int_{CDF}^{run} Ldt}{\frac{1}{2} \sum_{end,run} N_{oct-end} / \int_{CDF}^{run} Ldt} \tag{A.4}$$

where $N_{oct-end}$ is the number of hits on wires used in the trigger in each octant on each end of the detector for each run and $\int_{CDF}^{run} Ldt$ is the integrated luminosity that CDF collected during each run. There are 8 octants and 2 ends of the detector. Therefore, for each run there are 16 ratios, $R_{oct-end}$.

The spread of $R_{oct-end}$ about its nominal value of 1.0 is shown in Figure A.2 for the first 420 nb^{-1} of the 1988/89 run. Collapsing this distribution on the y axis, we show the histogram of $R_{oct-end}$ in Figures A.3A,B,C and D for the different sections of the run. Octants with extremely low rates are, for all practical purposes, unplugged and do not contribute to the 5 or 6 hit distributions since a chamber takes out 2 hits on a track and 4 hit tracks are not recovered. Dead octants are determined from these plots to be any octant with a rate below a threshold of .4. This threshold is somewhat arbitrary, and the error in the number of dead octants is determined by varying it between .2 and .6. Similarly, runs with oscillating chambers can have enormous hit rates which overflow the allocated computer memory, so that tracks can not be recovered. Runs where the mean,

$$\bar{R} = \frac{1}{16} \sum_{oct,end} R_{oct-end}, \tag{A.5}$$

is above a threshold of 1.75 are deemed bad. Again, this threshold is chosen by

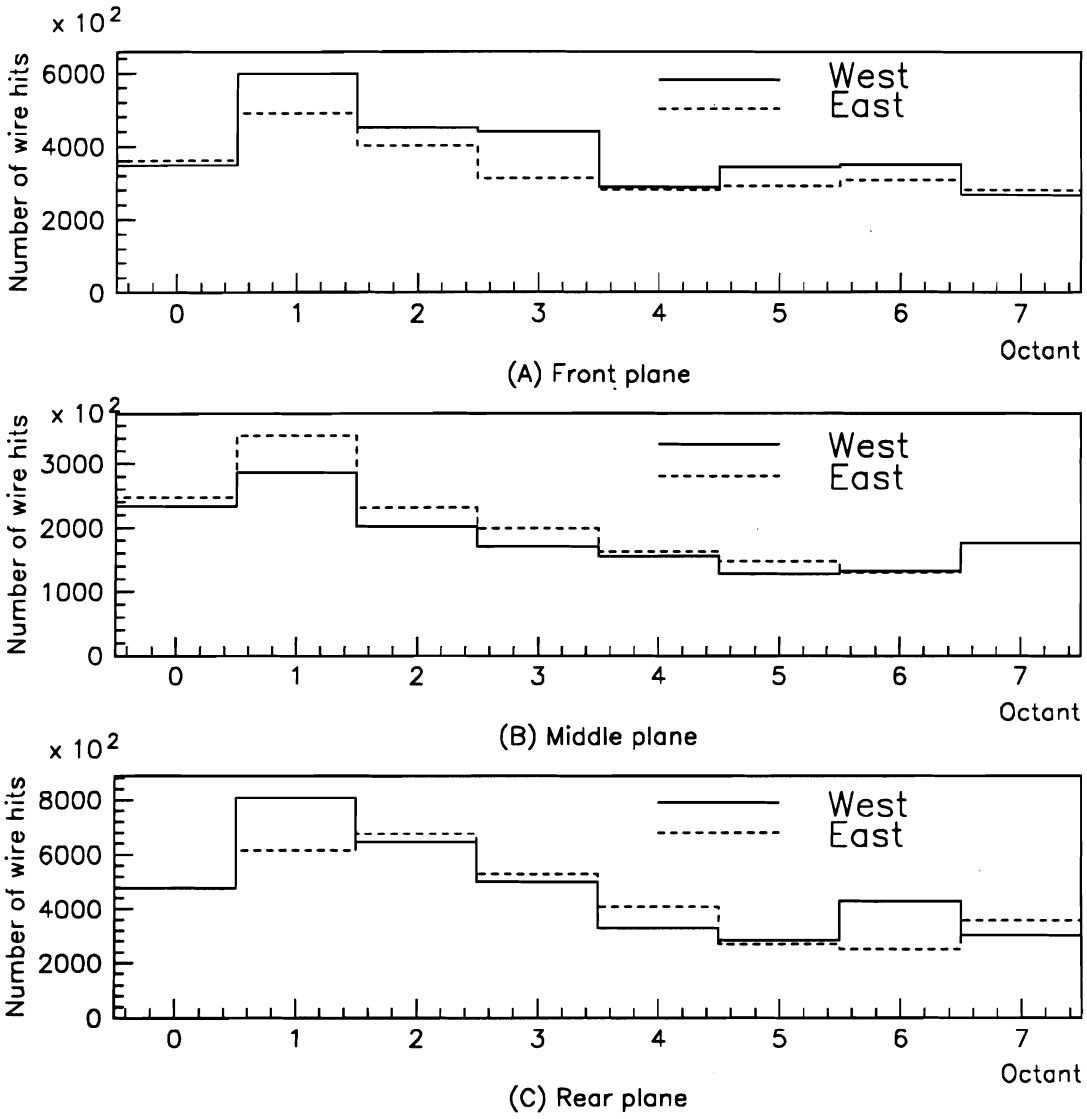

Figure A.1: ***Front, middle and rear plane chamber hit rates.***

looking at the distribution of $\bar{R}$ and the uncertainty in this number was determined by letting the threshold vary from 1.5 to 2.0. Plots of $\bar{R}$ are shown in Figures 4A,B,C and D for the different periods of the run. Exemplary chamber performance can be seen for all the plots in the last portion of the run.

To determine the group efficiency, first the amount of luminosity lost due to poor chamber performance or oscillations is summed. The luminosity, $\int_{CDF}^{bad} Ldt$ is the sum of two contributions. For those cases when $R_{oct-end}$ is below threshold, a sixteenth of the luminosity was lost. When the chambers oscillated, then the entire end was malfunctioning and half of the luminosity was lost. Therefore,

$$\int_{CDF}^{bad} Ldt = \sum_{run}(\frac{1}{16}\int_{CDF}^{run} Ldt \times N(\text{below } R_{oct-end} \text{ thresh.}) + \tag{A.6}$$

$$\frac{1}{2}\int_{CDF}^{run} Ldt \times N(\text{above } \bar{R} \text{ thresh.})) \tag{A.7}$$

where N(below $R_{oct-end}$ thresh.) is the number of octants on each end of the detector with rates below the threshold and N(above $\bar{R}$ thresh.) is the number of ends of the detector with rates above the threshold. The group efficiency is:

$$\epsilon_{group} = 1 - \frac{\int_{CDF}^{bad} Ldt}{\sum_{runs}\int_{CDF}^{run} Ldt} \tag{A.8}$$

Table A.4 lists the group efficiency attached to each period of the run. Variations of efficiency between HV groups of wires within a single octant were observed to be less than 1% although in the period before Christmas there were two octants which showed a slightly larger efficiency variation between HV cells in a single octant. In general, however, the efficiency is well determined by the average over HV groups.

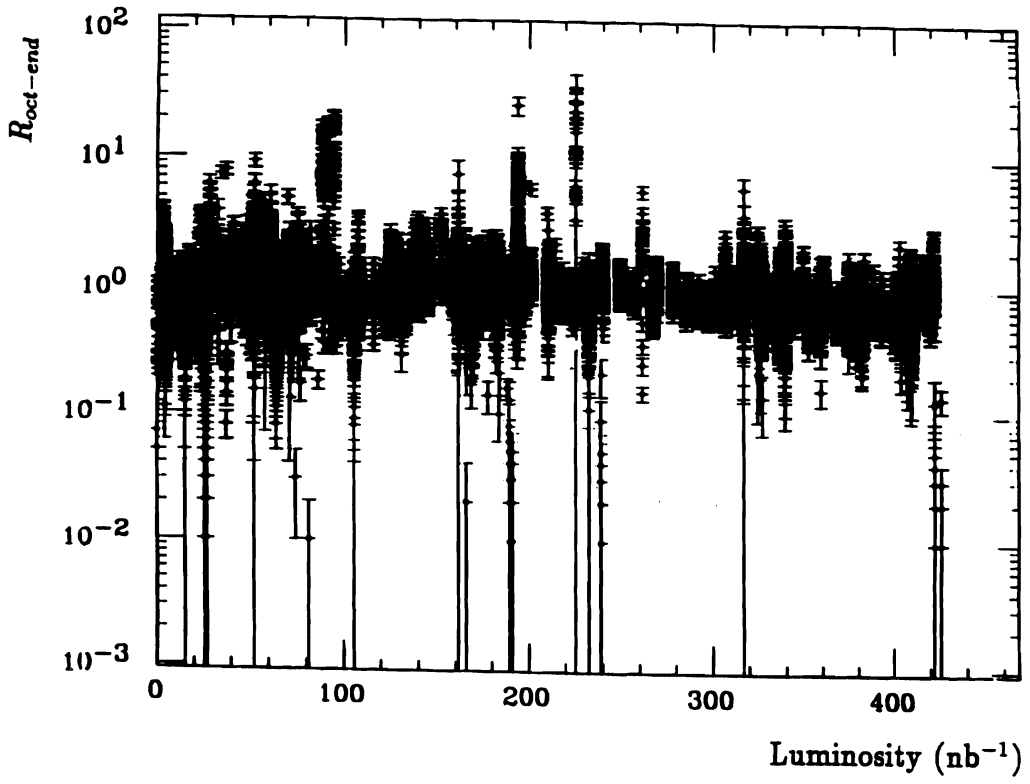

Figure A.2: *The rates for the first 420 nb^{-1} of the run compared to the average rate.*

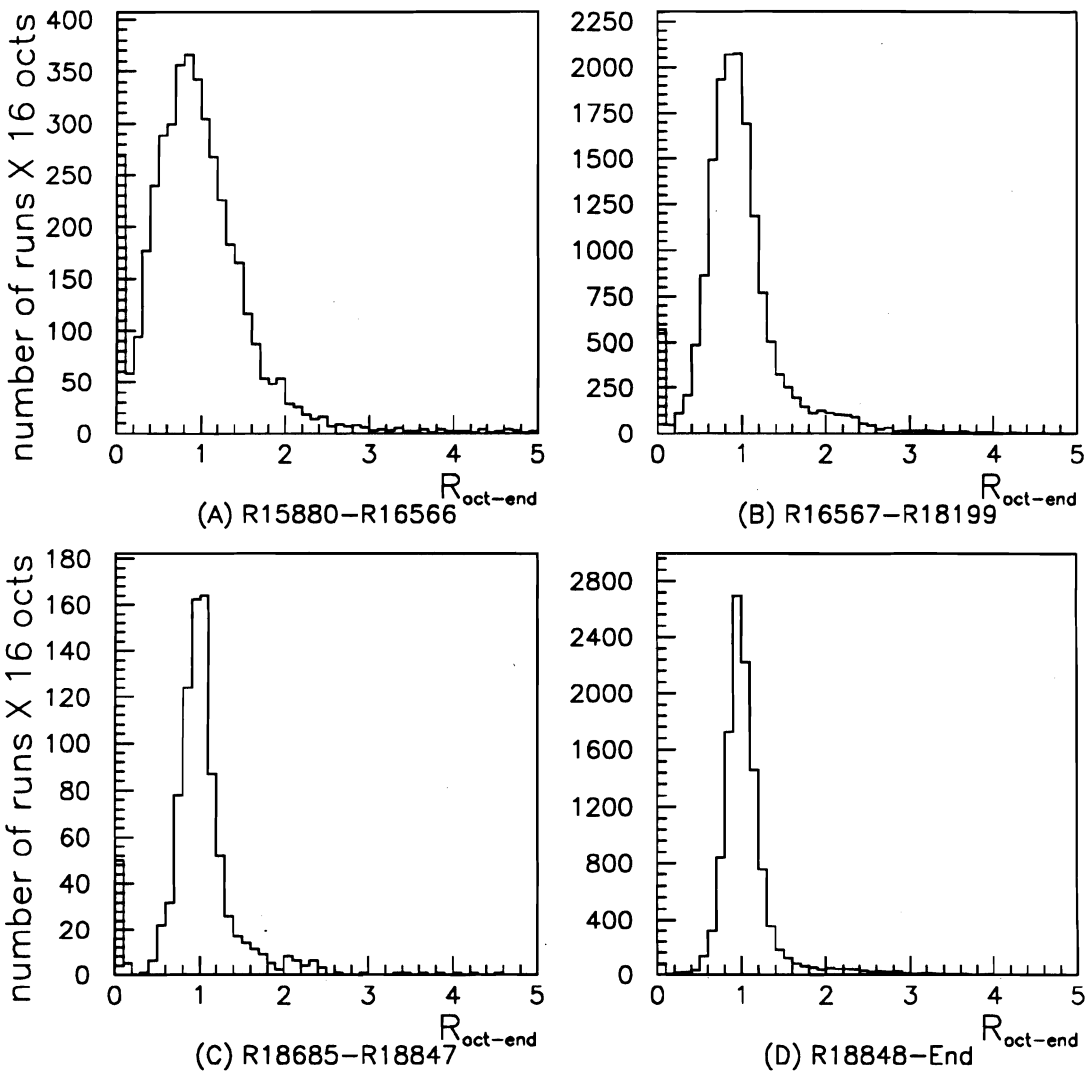

Figure A.3: ***Average wire hit rates for each run and octant.***

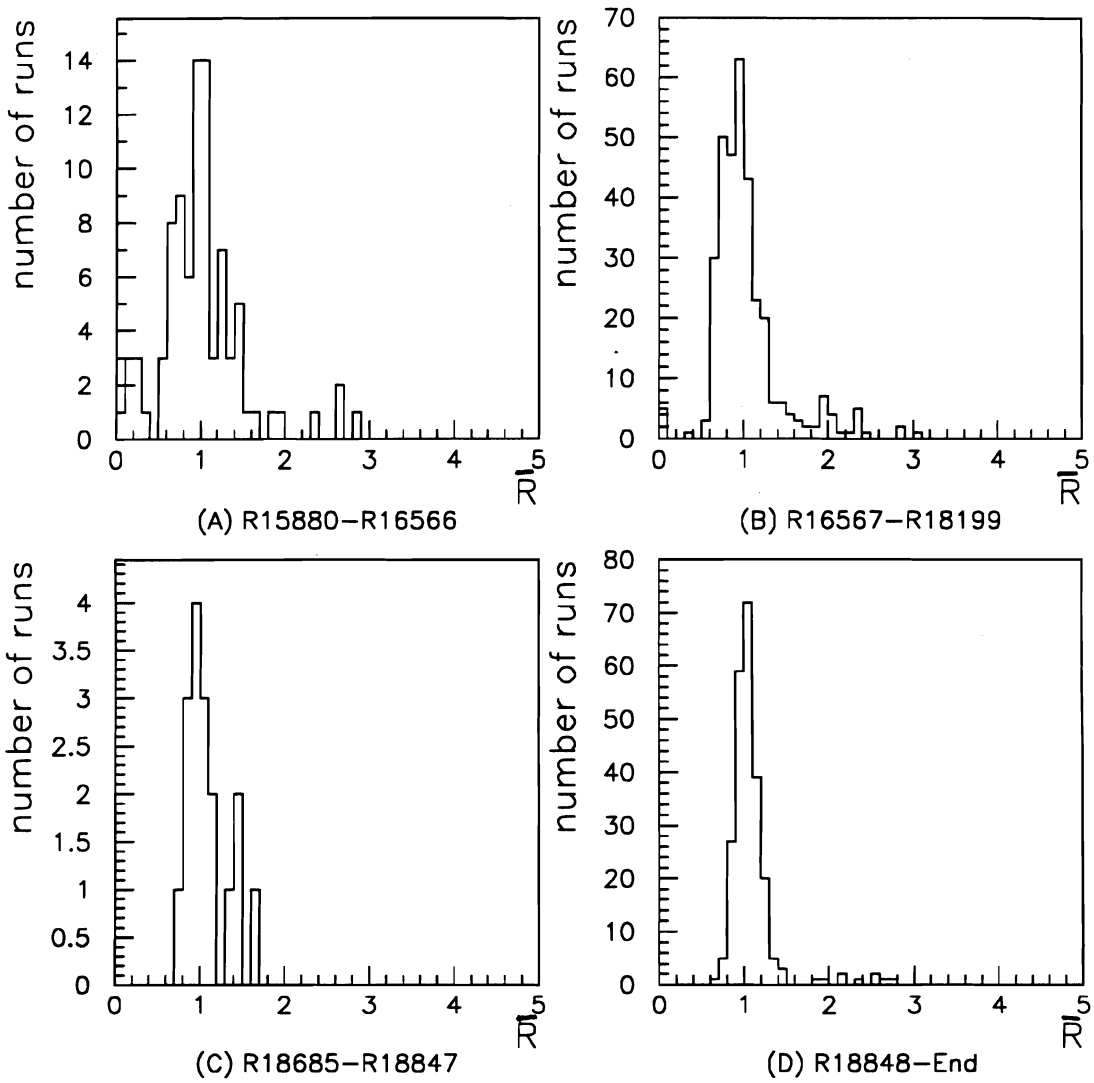

Figure A.4: ***Average wire hit rates for each run and octant.***

ϵ_{group}	R15880-R16566	R16567-R18199	R18865-R18847	R18848-end
West	$.787 \pm .060$	$.870 \pm .086$	$.895 \pm .014$	$.937 \pm .011$
East	$.774 \pm .087$	$.846 \pm .071$	$.621 \pm .009$	$.957 \pm .009$

Table A.4: *The group fraction for four sections of the 1988/89 run.*

A.3 Single chamber losses

There are three chambers which failed to produce any hits or tracks for parts of the CDF 1988/89 run. These chambers are not detected in the group failures because the other two chambers in the octant were sufficient to produce enough hits to pass the cut thresholds. Therefore, the chamber efficiency is adjusted here to reflect these dead chambers. There are 24 chambers in ϕ on each end of the detector. For the runs before Christmas, east chamber $\phi = 15$ and 17 contain no tracks. After Christmas, only east chamber $\phi = 17$ was observed to have no tracks. Table A.5 contains the single chamber efficiency, ϵ_{sc}, computed as

$$\epsilon_{sc} = \frac{\text{working chambers}}{24} \tag{A.9}$$

A 1% error bar is assigned to the efficiency since we believe that the system was not randomly affected by this problem.

ϵ_{sc}	R15880-R16566	R16567-R18199	R18865-R18847	R18848-end
West	$1.00 \pm .01$	$1.00 \pm .01$	$1.00 \pm .01$	$1.00 \pm .01$
East	$.917 \pm .009$	$.917 \pm .009$	$.958 \pm .010$	$.958 \pm .010$

Table A.5: *The single chamber failures for four sections of the CDF 1988/89 run.*

A.4 Level 1 trigger electronics efficiency

The largest portion of the forward muon data was collected using the NUPU 50% trigger. This trigger was installed for all runs greater than 18848, excluding special runs. The efficiency of this trigger was determined using the volunteer data selection described in section A.2. Events recorded by an assortment of non-FMU triggers were searched for chamber hits recorded by the TDCs which should have satisfied the Level 1 trigger. These "software triggers" were then divided up into two categories: those which succeeded and those which failed to produce a Level 1 trigger in the FMU hardware. The efficiency was then calculated to be:

$$\epsilon_{DIHOPU/NUPU} = 1 - \frac{\text{failures}}{\text{software triggers}} \tag{A.10}$$

The NUPU trigger has a choice of three p_t thresholds. In order to increase the selection of a high p_t prompt muon signal, the highest p_t threshold, the 50% threshold, was chosen to collect data during the run. This threshold required a track to traverse the FMU toroids without bending more than a few centimeters in the radial direction. The maximum allowed displacement in the rear plane of drift chambers was half the size of a drift cell. The 300% trigger threshold

was also monitored during the run. It allowed for a maximum displacement in the rear plane of drift chambers of up to three drift cells, thus allowing lower p_t tracks to satisfy the trigger.

There were 352 software triggers in this volunteer data, 34 of which failed to produce a level 1 trigger. Similarly, for the lowest pt threshold, the 300% threshold, there were 1107 software triggers and 71 hardware failures. Thus we find that the NUPU 50% trigger efficiency, ϵ_{NUPU}, is $.903 \pm .016$ and the NUPU 300% trigger efficiency is $.936 \pm .007$.

The difference between the 300% trigger and 50% trigger efficiency is explained by the larger number of possible drift cells which are allowed in the 300% trigger road. When more than one wire hit is allowed in a chamber plane, extra hits can satisfy the trigger even when one hit is missing. The trigger components which contribute to this efficiency include the fastbus back plane connectors between the TDCs and the NUPU boards, the NUPU and PUCKER trigger boards, and the "input" Struck latch which recorded the trigger information. The NUPU and PUCKER boards with associated connecting cables were tested periodically during the run and were found to have less than .5% failure rate for all possible trigger patterns. The "input" Struck latch was occasionally tested and had no known failures. A small sampling of the TDC-NUPU back plane connectors, however, showed a failure rate of $(2.9 \pm 1.1)\%$. For the 6 wire pattern required by the 50% NUPU trigger, the single wire efficiency is calculated to be $(98.3 \pm 0.3)\%$ which is consistent with the TDC-NUPU back plane failure rate.

The same method was used to determine the DIHOPU trigger efficiency. For this trigger, a coincidence of two 100% HOPU triggers was required. In the volunteer data, there are 143 software triggers and 32 hardware failures. Thus the DIHOPU trigger efficiency is, $\epsilon_{DIHOPU} = .776 \pm .035$.

The HOPU trigger was only responsible for collecting 4.9 nb^{-1} of data and required just three wire hits, making it more efficient than the six hit triggers. Since this trigger accounted for such a small part (.25%) of the data sample, we assign it an arbitrary efficiency of $\epsilon_{HOPU} = 100\%$.

A.5 Combined results

The efficiency for each section of the run is just the product the wire efficiency, the scintillator efficiency, of the group efficiency, the single chamber efficiency, and the trigger electronics efficiency. For the volunteer 5 and 6 hit tracks, however, the efficiency of the trigger components is neglected.

$$\epsilon_{trigger} = \epsilon_{ce}(6) \times \epsilon_{scint} \times \epsilon_{group} \times \epsilon_{sc} \times \epsilon_{DIHOPU/NUPU} \tag{A.11}$$

$$\epsilon_{vol5} = \epsilon_{ce}(5) \times \epsilon_{group} \times \epsilon_{sc} \tag{A.12}$$

$$\epsilon_{vol6} = \epsilon_{ce}(6) \times \epsilon_{group} \times \epsilon_{sc} \tag{A.13}$$

To combine all the above efficiencies for the different periods of the run, a weighted average is used:

$$\epsilon_{overall} = \frac{luminosity^{FMU}_{early} \times \epsilon_{early} + luminosity^{FMU}_{later} \times \epsilon_{later} + \ldots}{\sum luminosity^{FMU}} \tag{A.14}$$

For the four portions of the run, the FMU luminosity is given in Table 3.1.

The efficiencies and their weighted average are recorded in Table A.6. The right most column is the weighted average over the different sections of the run. The overall trigger efficiency averaged over east and west is thus $.395 \pm .014$ and the overall volunteer efficiency for combined 5 and 6 hit tracks averaged over east and west is $.796 \pm .021$.

A.6 Comparisons to track distributions

For consistency, the efficiency calculation will now be checked against the raw data yields. Our first comparison shows the difference in the data yields on the east and west ends of the detector and how that is reflected in the efficiency calculation. Table A.7 compares the efficiency calculation to the data. Within statistics, the efficiency ratio matches the ratio found in the data sample.

It should be noted here that due to limited statistics, the NUPU trigger efficiency was not calculated separately for each end of the detector. Hence the $E/W_{trigger}$ ratio is missing one piece of the asymmetry which turns out to be smaller than the error bar of the calculation. To complete the record, the efficiency for NUPU trigger with the 50% threshold is $.939 \pm .021$ on the west and $.882 \pm .022$ on the east. The DIHOPU trigger efficiency is $.691 \pm .051$ on the west and $.887 \pm .040$ on the east. This yields an $E/W_{trigger}$ efficiency ratio of $.833 \pm .063$ which is still consistent with the data ratio.

	R15880-16566	R16567-18199	R18685-18847	R18848-end
West $\epsilon_{trigger}$	$.366 \pm .037$	$.314 \pm .040$	$.329 \pm .024$	$.522 \pm .027$
West ϵ_{vol5}	$.242 \pm .025$	$.268 \pm .032$	$.270 \pm .016$	$.283 \pm .016$
West ϵ_{vol6}	$.488 \pm .047$	$.539 \pm .062$	$.565 \pm .027$	$.591 \pm .028$
East $\epsilon_{trigger}$	$.219 \pm .035$	$.186 \pm .028$	$.200 \pm .016$	$.478 \pm .027$
East ϵ_{vol5}	$.278 \pm .032$	$.304 \pm .027$	$.193 \pm .010$	$.297 \pm .015$
East ϵ_{vol6}	$.299 \pm .047$	$.327 \pm .045$	$.352 \pm .018$	$.543 \pm .028$
	weighted average $\epsilon_{overall}$			
West $\epsilon_{trigger}$	$.435 \pm .022$			
West ϵ_{vol5}	$.277 \pm .015$			
West ϵ_{vol6}	$.570 \pm .028$			
East $\epsilon_{trigger}$	$.355 \pm .018$			
East ϵ_{vol5}	$.294 \pm .013$			
East ϵ_{vol6}	$.452 \pm .023$			

Table A.6: *Efficiencies of triggers and volunteer tracks.*

	efficiency ratio	data ratio
$E/W_{trigger}$	$.816 \pm .058$	$.804 \pm .027$
E/W_{vol5}	1.06 ± 0.07	1.10 ± 0.10
E/W_{vol6}	$.793 \pm .056$	$.814 \pm .054$

Table A.7: *The prediction of data yields on the east compared to the west.*

Secondly, the distribution of tracks in ϕ is not particularly flat. The efficiency calculated by octants has larger error bars than the one averaged over octants, but is indicative of the same basic structure that the data shows. Figure A.5a shows the triggered data normalized to the the efficiency as a function of octant - west(0-7) and east(8-15). Due to limited statistics, an average NUPU efficiency was used for all octants and fluctuations in the plot are attributed to this. The remaining plots in Figure A.5 compare the volunteer 5 and 6 hit data to the efficiency calculation. Again, the data are normalized to the efficiency calculation. Thus we demonstrate that the FMU detector efficiency accounts for the fluctuations in the data yield within the uncertainty of the calculation in most cases.

The overall efficiency of $.395 \pm .014$ is found for triggered events, and $.796 \pm .021$ for combined 5 and 6 hit volunteer tracks. The resulting efficiencies when compared by end and octant show agreement with the distribution of tracks observed during the run and thus lend confidence to our result.

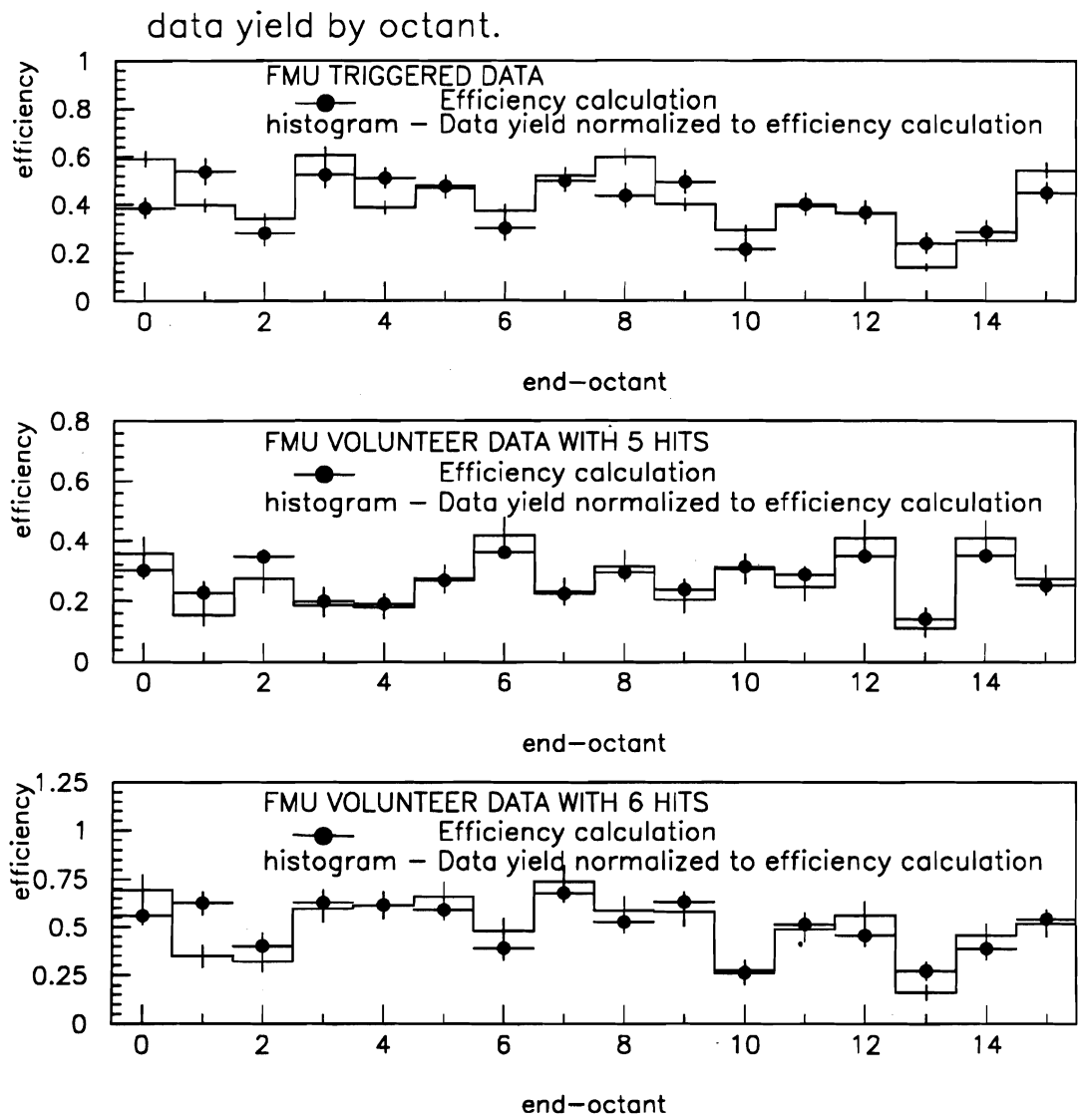

Figure A.5: ***The efficiency calculation compared to data yield as a function of octant.***

Appendix B

Simulating Decay-in-Flight Muons

The majority of all particles in jets are pions and kaons. Since pions and kaons often decay to muons this is a significant background to the muons in jets sample. To simulate this contribution, ISAJET is used generate jets following a to calculation including LO dijet diagrams, and to decay the short lived particles into long lived particles which include photons, leptons, pions and kaons. Partons with 8 GeV $< p_t <$ 100 GeV are generated.

Mesons reaching the calorimeter face are generally absorbed and do not contribute to the muon spectrum. Pions decaying before the calorimeter face produce a muon almost always.

$$B(\pi^{\pm} \longrightarrow \mu^{\pm} + X) = 99.99\% \tag{B.1}$$

Kaons decaying before reaching the calorimeter face produce a muon about 63% of the time.

$$B(K^{\pm} \longrightarrow \mu^{\pm} + X) = 63.51\% \tag{B.2}$$

The probability that the pion or kaon decays, is given by the standard exponential decay formula:

$$P(decay) = 1 - e^{-x/\lambda} \tag{B.3}$$

where the characteristic decay length is λ, ($\lambda = \beta\gamma c\tau$) and x is the distance to the calorimeter face. In particular,

$$\lambda = \frac{p^{meson}\tau}{M} \tag{B.4}$$

where p^{meson} is the momentum of the meson and M is its mass. Since x/λ is much smaller than one, the decay probability can be written:

$$P(decay) = \frac{p^{meson}\tau}{M} \tag{B.5}$$

For the purposes of simulation, all pions and kaons are decayed to muons uniformly distributed within the kinematic limits,

$$0.57p_t^{\pi} \leq p_t^{\mu} \leq p_t^{\pi} \tag{B.6}$$

$$0.05p_t^{K} \leq p_t^{\mu} \leq p_t^{K}. \tag{B.7}$$

Then if the muon survives the tracking and trigger cuts, the parent pion or kaon is removed from the final particle list and the muon is added. The probability

of the decay is recorded as a weight factor to keep track of the simulated cross section.

Appendix C

Single Heavy Quark Differential Distributions

Single particle differential distributions have been published at next-to-leading order (NLO) by Nason, Dawson and Ellis (NDE).[4] Since the published results all constrain η to a specific value, they are not sufficient for this analysis. Therefore, the NLO code of Mangano, Nason and Ridolfi (MNR) [5] is used to obtain predictions for the rapidity region of interest. The MNR program calculates double differential cross sections for up to three final state partons. In this analysis, ISAJET[39] has been used as an event generator. Verifying that MNR and ISAJET can be used to reproduce the published distributions in the central region is the topic of the next section. This will be followed by the extension of these predictions to the forward region, $1.9 < |\eta| < 2.5$.

Since ISAJET uses only the lowest order cross sections, differences in the p_t and η distributions will be corrected to represent the true NLO distributions. In most cases, a simple correction factor, K can be found, but in other cases, simple functions are used to reproduce the NLO distributions.

C.1 Comparison of NDE, MNR and ISAJET heavy quark production

The NDE published cross section is a full $O(\alpha_s^3)$ calculation. It uses the $\bar{M}S$ regularization scheme, DFLM structure functions which are consistent with this scheme, and a heavy quark mass of 4.75 GeV. For comparison, the MNR code was used with the same choices of mass and structure functions. The comparison of NDE and MNR then is expected to give the same result within statistical fluctuations. ISAJET has been used extensively as an event generator. Since it calculates only the lowest order diagrams and then uses the method of initial and final state radiation to produce events which are topologically similar to NLO, it is not expected to reproduce the cross section perfectly, only the shapes of the distributions. Hence, the ISAJET events can not be used to calculate cross sections without first being corrected for overall event yield. Figure C.1 shows the distribution $d\sigma/d\eta dp_t^2$ at $\eta = 0$. This distribution shows that the MNR calculation does reproduce the NDE result. Also, the shape of the ISAJET distribution is the same as the NDE curve, only low by a K factor of 1.5. The

very low end of the p_t^b distribution is irrelevant to the current measurement so discrepancies there will be ignored.

The ISAJET distribution shown in Figure C.1 is for direct bottom production. Since real data is composed of a mix of direct and gluon splitting events, any systematic effects between the two distributions must be simulated separately. The exact mix is unknown, therefore we use the two simulated samples separately to bound the result on all possible mixes by first letting one and then the other represent the total distribution. In section 6.1 the possibility that the entire b quark signal is due to gluon splitting is considered. Thus it must be normalized to represent the entire NLO bottom quark production. The distribution for gluon splitting events is compared at high p_t^b in Figure C.2. The efficiency of the bottom quark production was checked and the shape discrepancy for the gluon splitting case is not due to generation cuts, but features in the ISAJET production. To correct the gluon splitting p_t distribution so that it may be used to represent the total bottom cross section, a function has been applied to the events with $p_t^b < 24$ GeV in addition to a K factor of 1.5. The correction function, $f(p_t)$, is shown in figure C.3

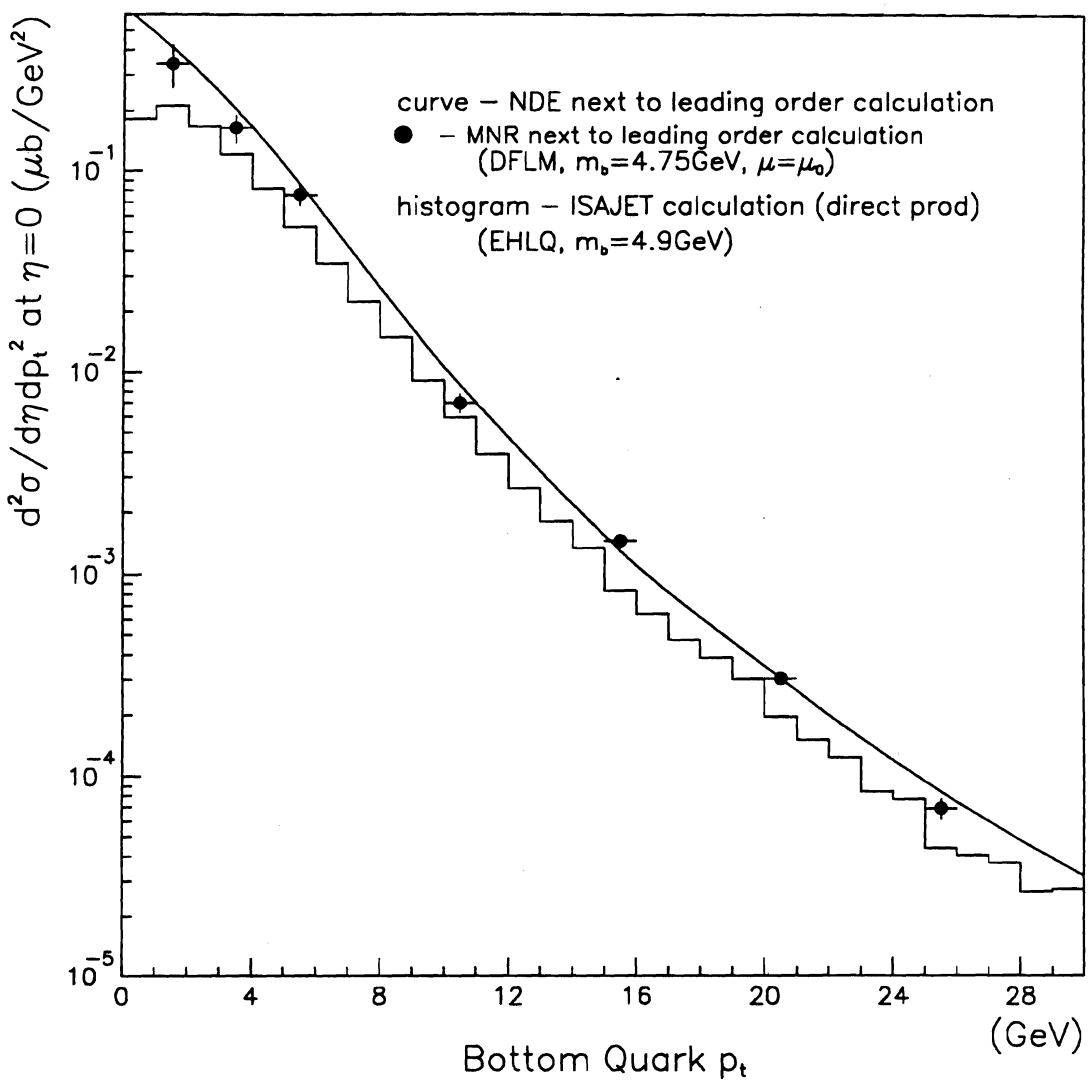

Figure C.1: ***Comparison of the MNR and ISAJET cross section calculations to the published NDE cross section.***

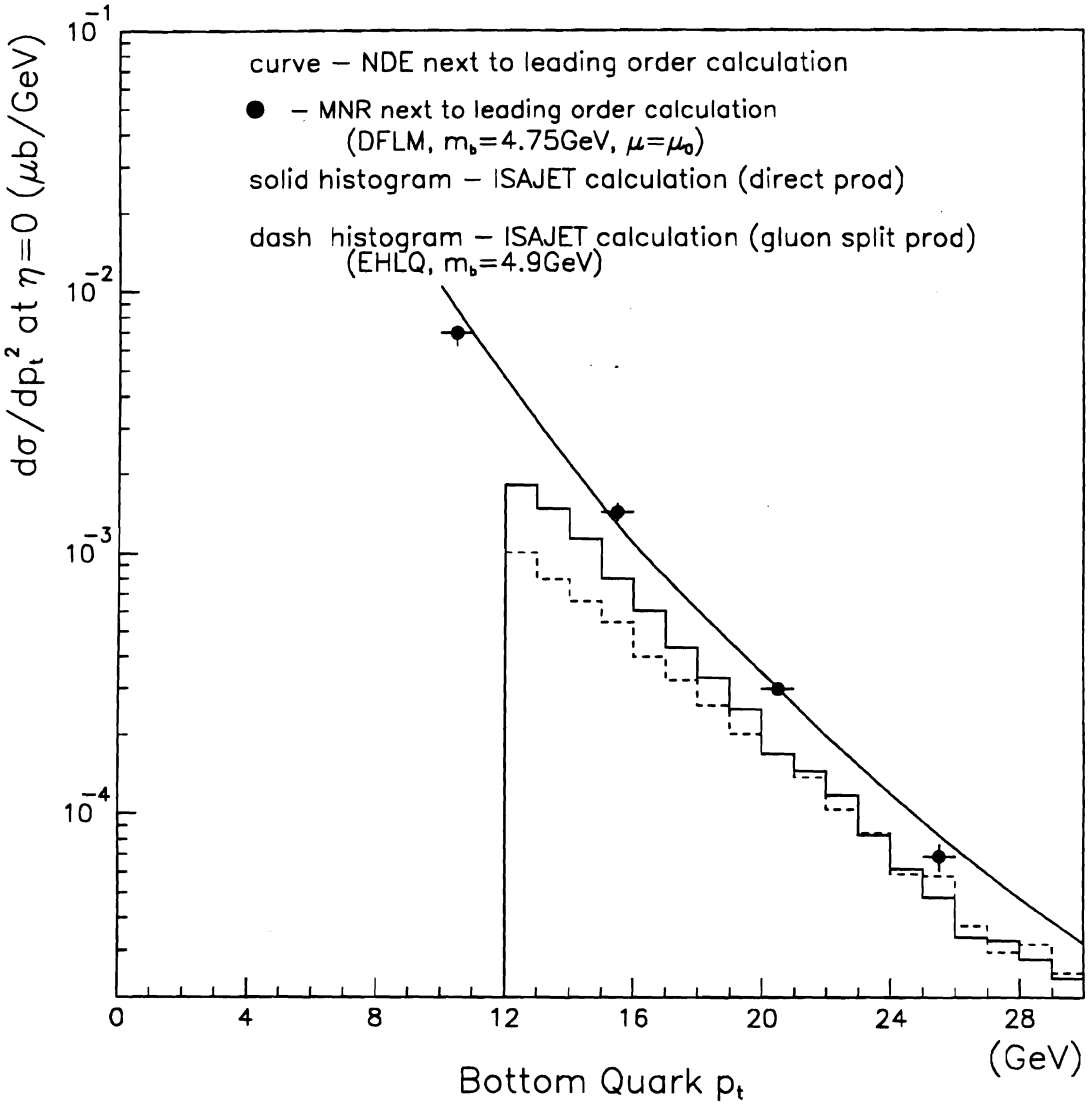

Figure C.2: ***Transverse momentum distribution for central bottom quarks.***

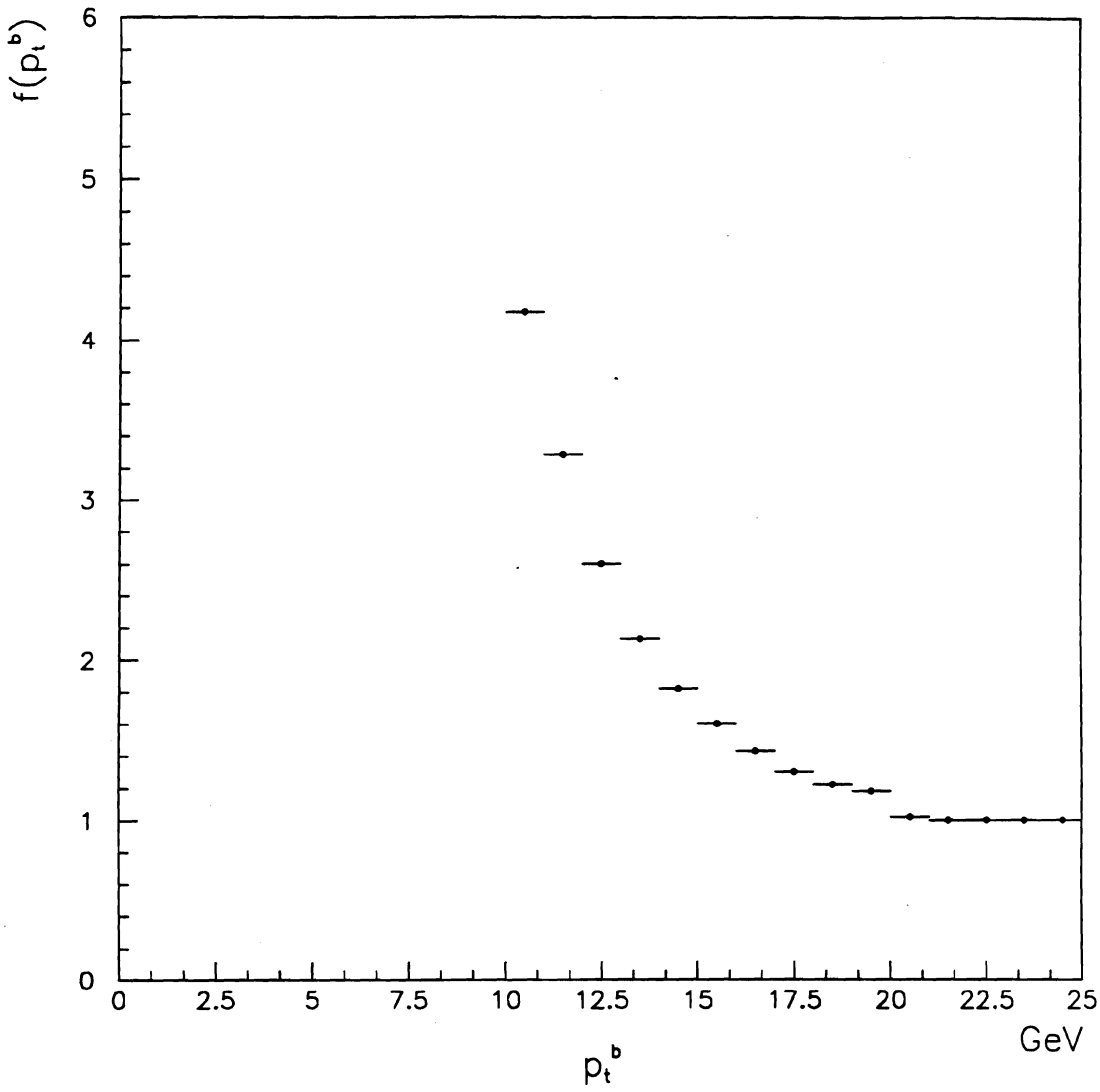

Figure C.3: ***Gluon splitting production bottom quark momentum correction function.***

C.2 Comparison of MNR and ISAJET at forward η

The bottom quarks which contribute to the data sample have $p_t^b > 20$ GeV and $1.9 < |\eta^b| < 2.5$. For these cuts, then, it is desirable to establish a similar K factor relationship between ISAJET and MNR as above. The new K factor is different from that found in the central. The most current structure functions of choice are the MRSD0 and CTEQ sets. For this analysis, therefore, MNR has been used with these structure functions and a bottom mass of 4.75GeV. The η^b distribution is shown in Figure C.3 with the momentum limited to the region, $p_t^b > 20$ GeV. Both the direct and gluon splitting bottom quark distribution from ISAJET are similar, but the shape is distinctly different from that of MNR. In the η^b region of interest, it can be seen that ISAJET and MNR give approximately the same event yield, therefore a K factor of 1.0 is used. Notice that near η^b of zero, the MNR calculation using DFLM structure functions yields a larger K factor as discussed in the previous section.

The p_t^b spectrum for events with $1.9 < |\eta^b| < 2.5$ is shown in Figure C.4. This shows that the direct bottom calculation from ISAJET reproduces the NLO result well and that the gluon splitting bottom calculation still requires a function to adjust it for $p_t < 24$ GeV.

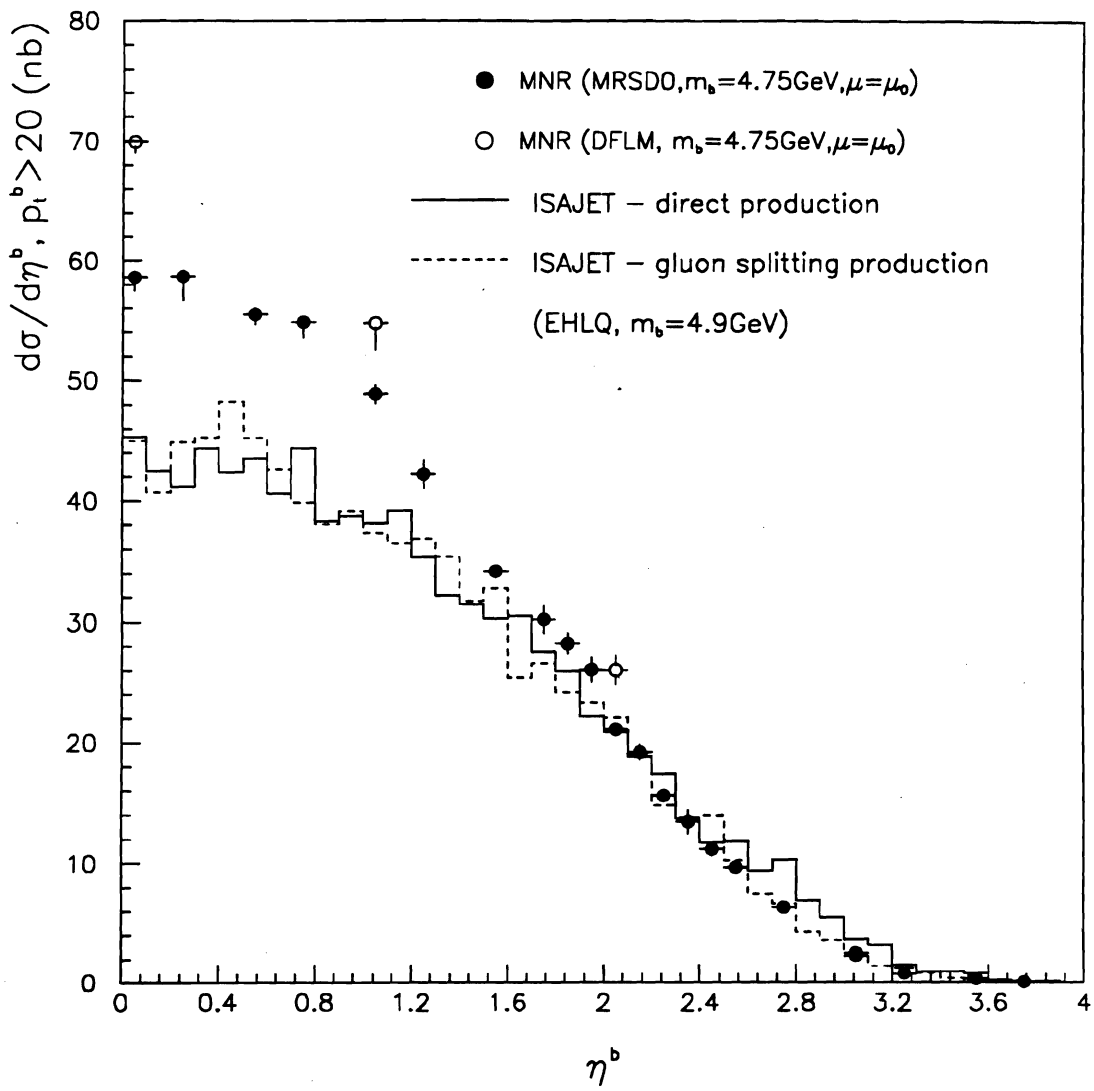

Figure C.4: ***Comparison of the MNR and ISAJET cross section calculations for $p_t^b > 20$ GeV.***

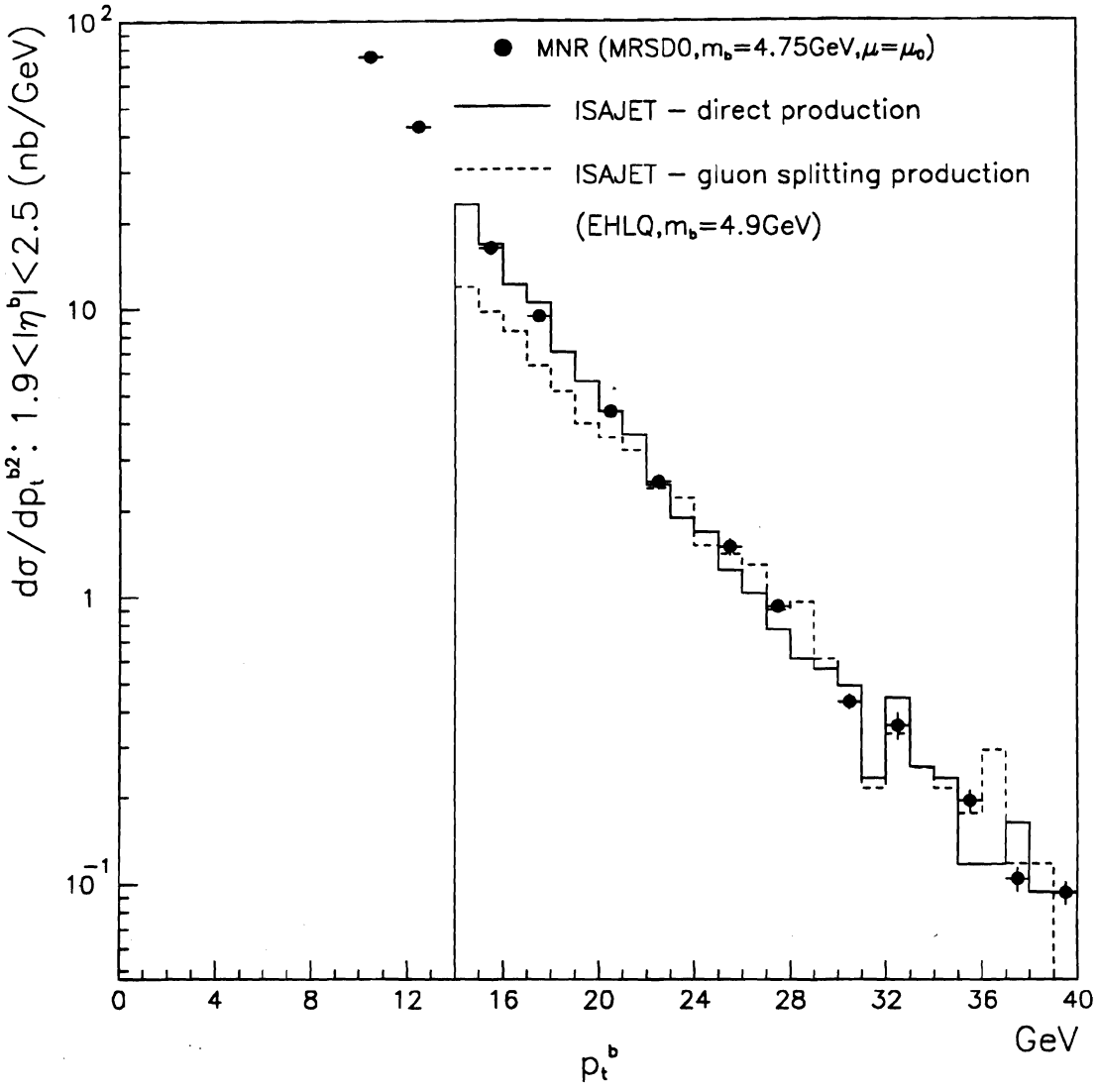

Figure C.5: ***Comparison of the MNR and ISAJET transverse momentum distributions for*** $1.9 < |\eta^b| < 2.4$.

Appendix D

Heavy Quark Double Differential Distributions

The previous appendix verified the NLO code of Mangano, Nason and Ridolfi (MNR) with published cross sections. Here, this code is used to study the kinematics of bottom events. The purpose is two fold. First, the definition of direct and gluon splitting production will be established. Then the kinematical distributions which affect the measurements will be compared to those produced by ISAJET verifying that the simulation models the NLO events sufficiently.

D.1 Energy distribution in bottom events

Direct bottom production differs from gluon splitting production in the topology of the final state. The first is characterized as a $2 \longrightarrow 2$ process and the latter as

a $2 \longrightarrow 3$ process. To study event correlations, two final state partons need to be selected. Therefore each event is required to have a bottom quark with $p_t > 20$ GeV and another parton with $p_t > 15$ GeV. The opposite parton is defined to be the gluon or antibottom quark which passes the lower p_t cut and is most opposite in azimuth from the bottom quark. In events generated by ISAJET, the opposite parton in direct production is an antibottom quark 94% of the time and in gluon splitting production the opposite parton is a gluon 99% of the time. Therefore, it is reasonable to compare direct production with NLO events where the opposite parton is an antibottom quark and gluon splitting production with NLO events where the opposite parton is a gluon.

The azimuthal difference between the b and both the $\bar{b}$ and gluon is shown in Figure E.1 for both direct and gluon splitting production. The opposite parton is usually mostly back to back with the bottom quark and the parton without any cuts tends to be uncorrelated. This distribution shows that the two partons with p_t cuts tend to balance the energy in the event and the third parton is more or less irrelevant to the energy balance. Figure E.2 shows the transverse momentum spectra for the three partons in the events. This shows that the third parton almost always fails the 15 GeV p_t cut and therefore contributes only minimally to the energy balance. The third parton only rarely contends for the status of opposite parton. Events selected in this way are similar kinematically to dijet events.

Very little confusion is found between gluons and antibottom quarks when

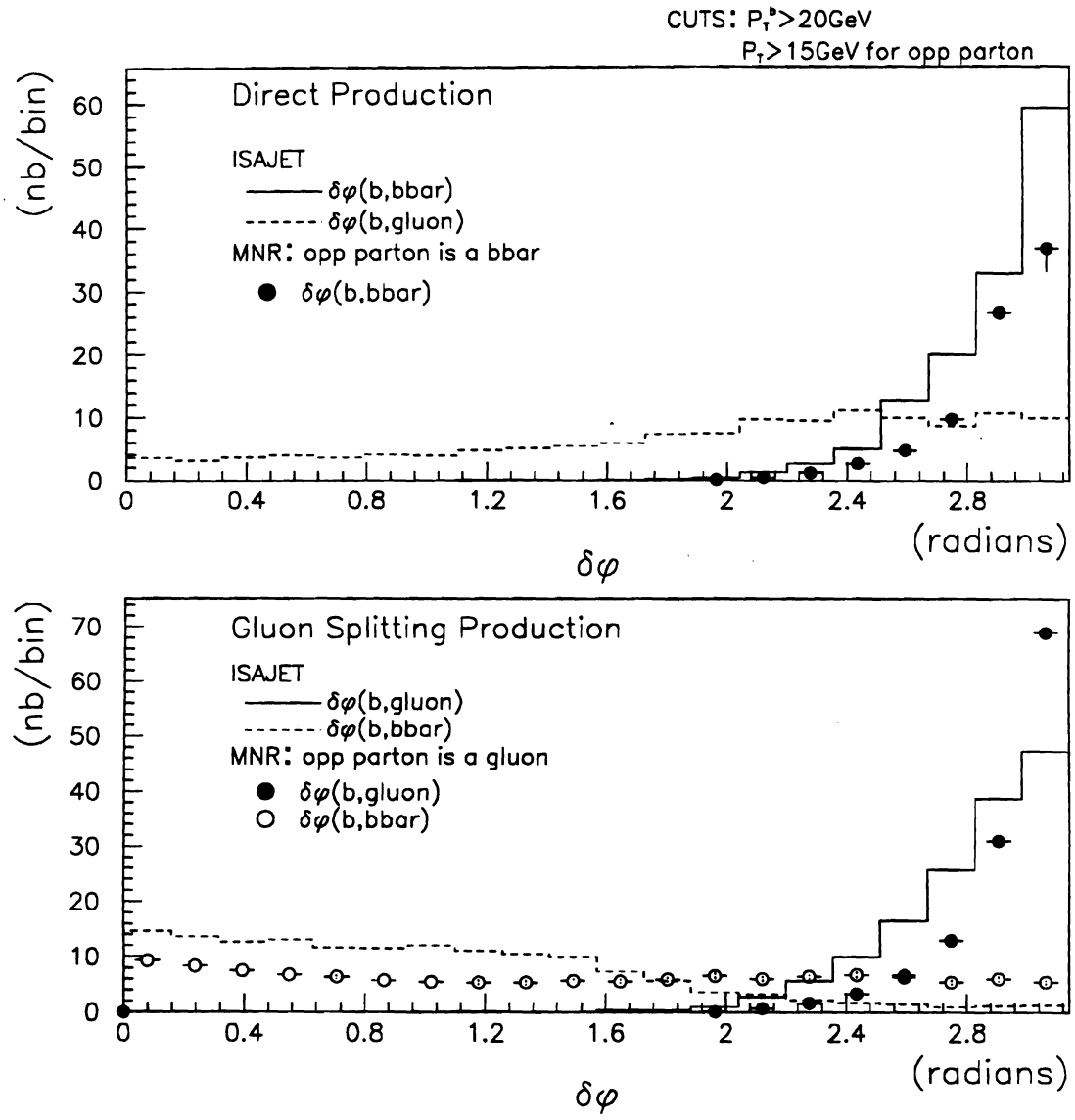

Figure D.1: ***The azimuthal difference between the b quark and both the $\bar{b}$ quark and the gluon.***

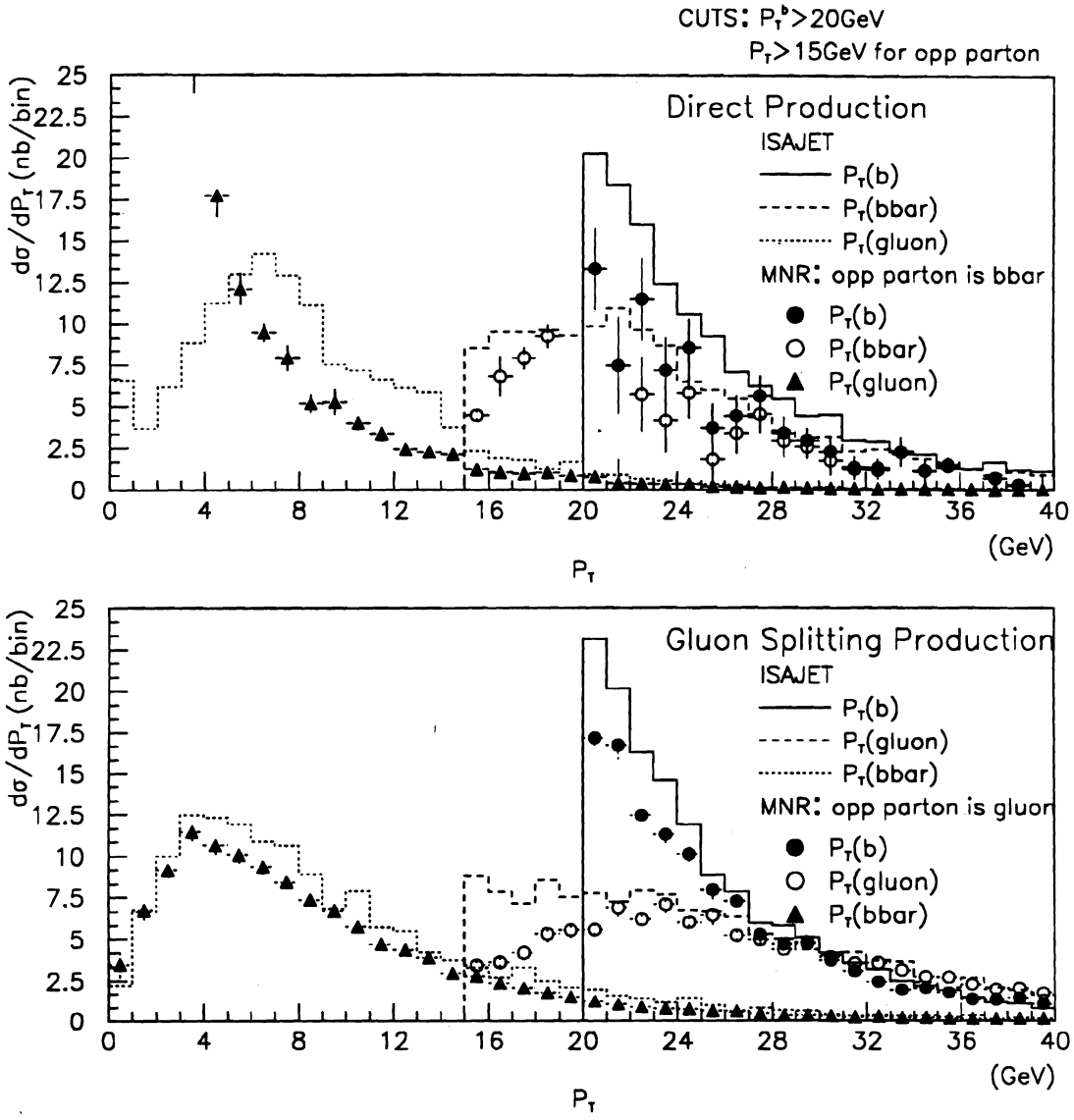

Figure D.2: ***The transverse momentum distribution for three partons in bottom events.***

choosing an opposite jet. This provides a natural separation of events into direct and gluon splitting contributions. Technically, the direct contribution contains the LO bottom production processes and the NLO processes with gluons of small momentum. The gluon splitting contribution contains all NLO processes with energetic gluons which includes flavor excitation processes also. Referring to these events as gluon splitting production stems from the method of generating the events with ISAJET. The gluon splitting generation method is used to represent all the NLO processes with a high momentum final state gluon.

D.2 Kinematics of bottom events

The η of the opposite parton, η_{opp}, is used to make a quantitative connection between ISAJET and MNR. The sign of η_{opp} is reversed if the b quark has a negative rapidity. Of course the distribution of η_{opp} is symmetric around zero if η_b is central, but a structure develops if the bottom quark is forward. The cut $1.9 < |\eta_b| < 2.5$ is made on all η_{opp} plots. The distribution of η_{opp} is shown in Figure E.3 for both direct and gluon splitting production. Here we see that the gluon and antibottom η distributions have different shapes. The ISAJET distributions have been renormalized to match the integrated MNR cross sections. Separate correction K factors were determined for direct and gluon splitting events.

$$K_{direct} = .59 \tag{D.1}$$

$$K_{splitting} = .69 \tag{D.2}$$

Now that we have established the definition of opposite parton and the absolute ISAJET normalization of the direct and gluon splitting contributions to the cross section for forward η^b, the emphasis will change to a more qualitative discussion. Distributions generated by ISAJET will be compared with those generated by MNR to see which may contribute acceptance uncertainties to the fully simulated sample. Where the partons generated by ISAJET are not similar to the NLO calculation the detector modelling of these partons will produce distributions with erroneous acceptance factors. For example, each analysis cut on the data retains quarks in a certain kinematic region. If the simulated spectrum of those quarks is skewed, then the acceptance corrections will be inaccurate.

The NLO calculation of MNR contains a singularity when a gluon with zero energy is produced. The gluon momentum spectrum shown in Figure E.2 for Direct Production is very large near zero. Because of the singularity at zero, all the distributions where the opposite jet is an antibottom quark have large fluctuations where these gluons contribute to the cross section. Since the real world does not contain singularities, the average ISAJET result will be used to smooth out these regions.

The azimuthal separation of the opposite parton and the bottom quarks at $1.9 < |\eta^b| < 2.5$ is shown in Figure E.4. In the current analysis there are no cuts which are affected by the azimuth of the opposite parton. The energy from partons which are near by the bottom quark, however, can leak energy into the cone

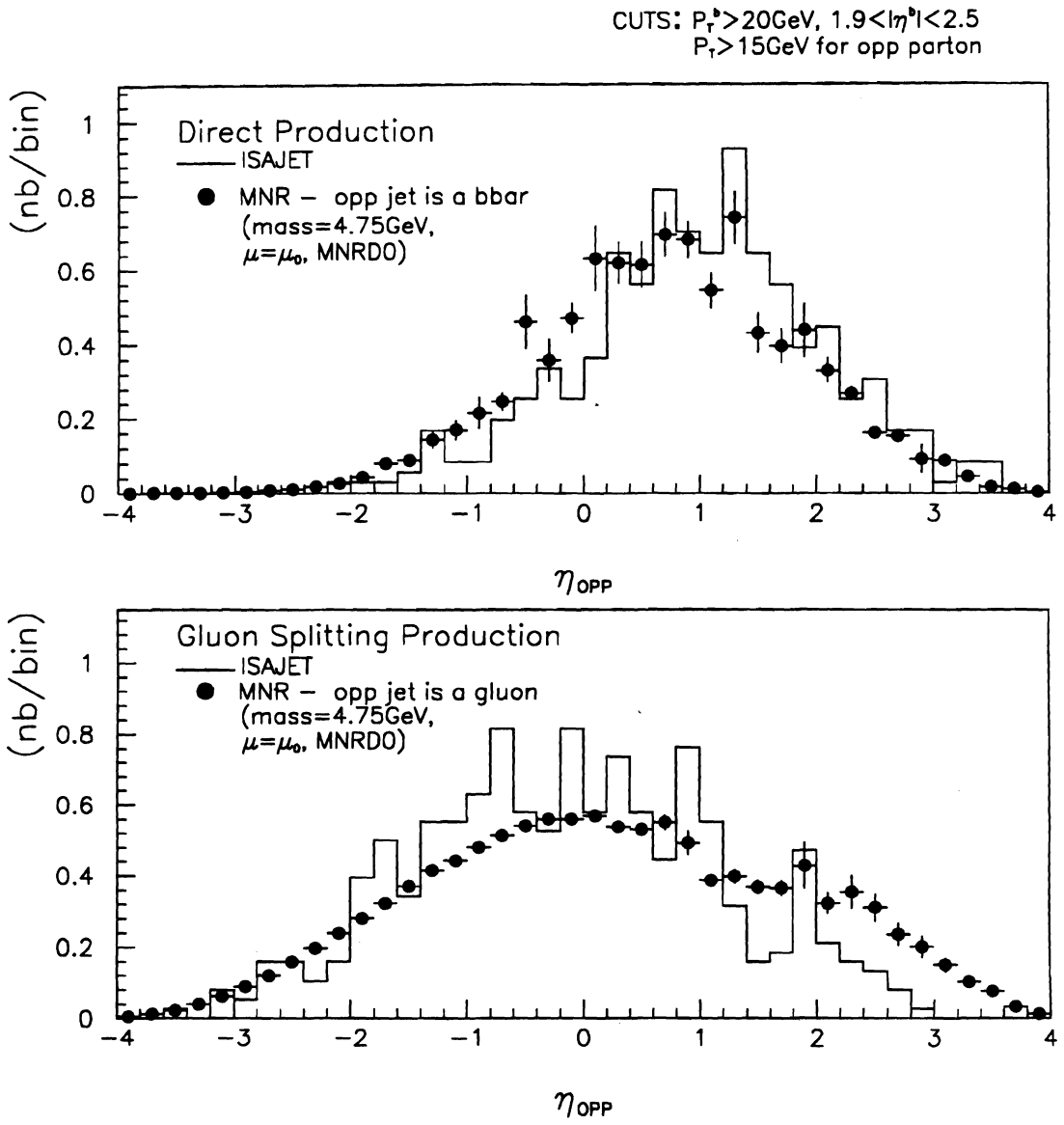

Figure D.3: *Distribution of η_{opp} for either the $\bar{b}$ or the gluon.*

of the jet which accompanies the muon. Since there is a singularity in the gluon energy, the NLO azimuthal separation can't be plotted for direct production. The leakage of small momentum gluons, however, is negligible anyway. These should be well modelled at CDF by the underlying event and its uncertainty. Gluon splitting events sometimes contain an antibottom near the bottom quark. These events may show some energy sharing in the jet cone. It is even possible that the muon may come from the bottom quark while the jet may result from the antibottom decay. Whatever the effect, it appears to be well modelled near zero by ISAJET.

The momentum distribution of all three partons are plotted in Figure E.5. Again, there is the singularity where the gluon has no energy. The ISAJET simulation does a good job of modelling the momentum spectra for both of the partons which are associated with jet cuts in the data analysis.

Finally, the distribution of η_{opp} was shown in Figure E.3. The direct production here is contaminated by the low energy gluons throughout the plot, but shows the same general shape as ISAJET. The gluon splitting production, differs where the rapidity of the gluon approaches that of the bottom quark. This fluctuation is also due to a singularity and will be ignored. However, the systematic shift in η_{opp} can be corrected for with a function, $f(\eta_{opp})$. The correction function is shown in figure D.6

As there are no more kinematical distributions which affect the measured bottom quark cross section, we conclude that ISAJET does a fairly precise cal-

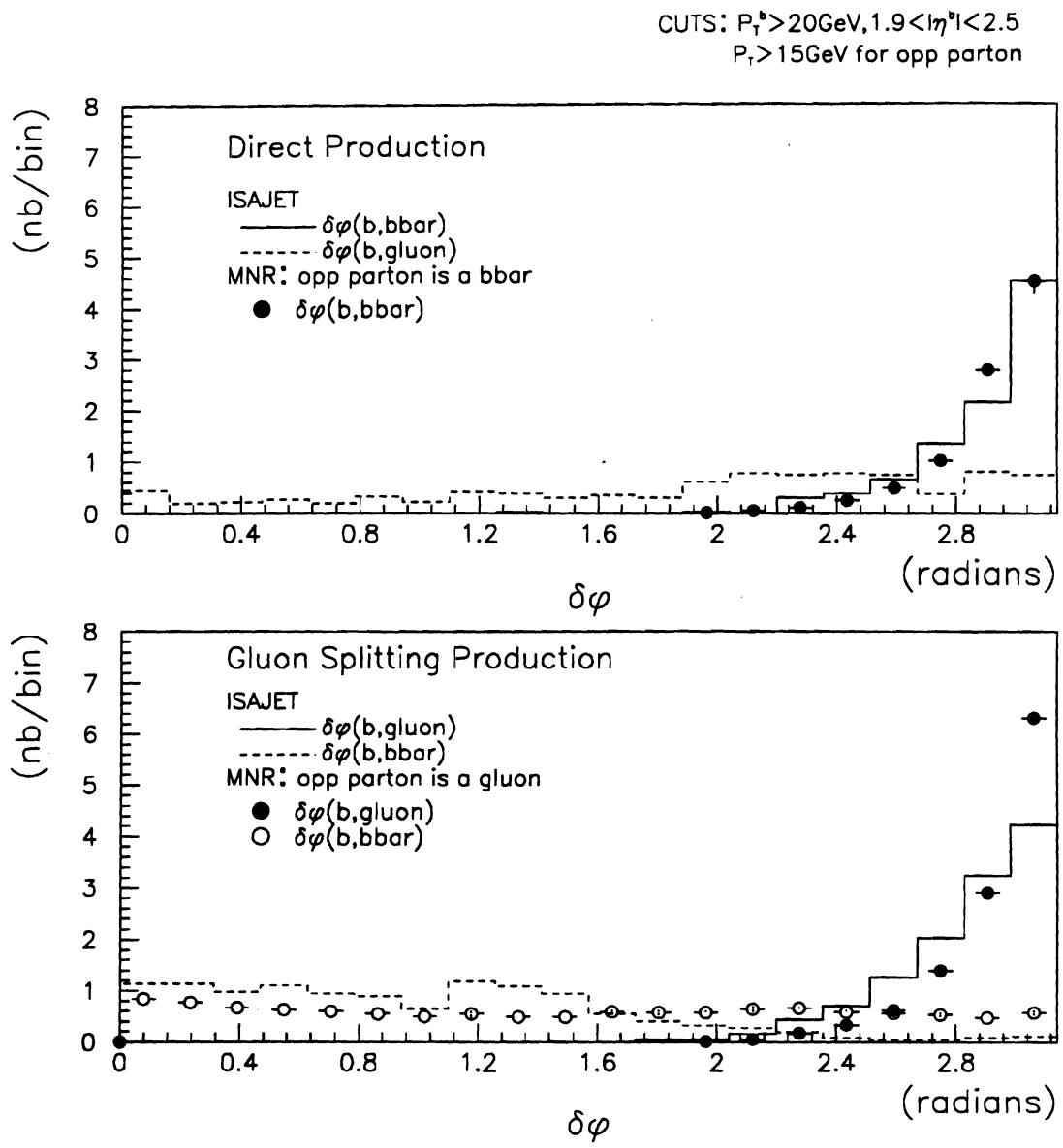

Figure D.4: ***The azimuthal difference between the b quark and both the $\bar{b}$ quark and the gluon for $1.9 < |\eta^b| < 2.5$.***

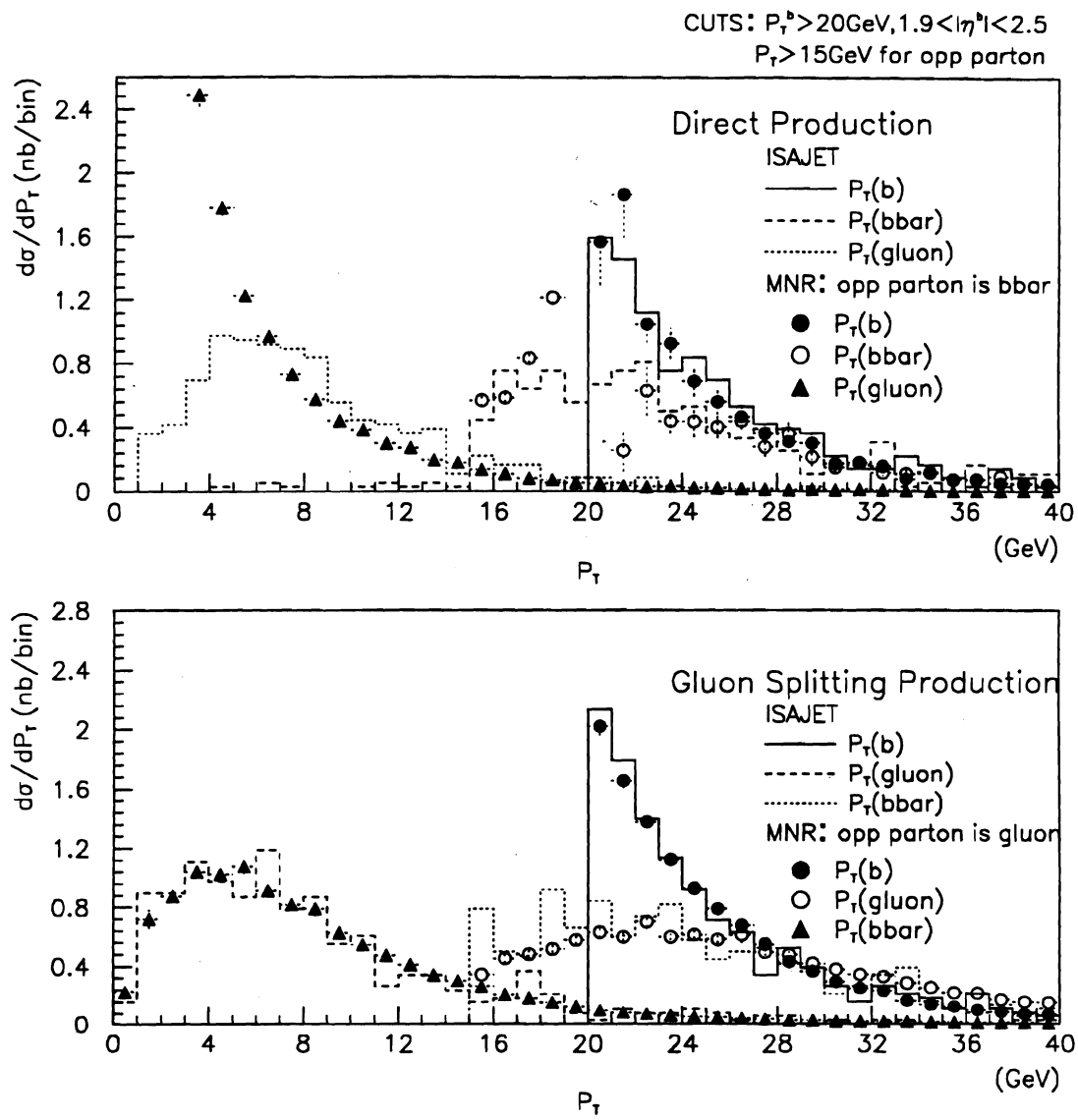

Figure D.5: ***The transverse momentum distribution for three partons in bottom events with*** $1.9 < |\eta^b| < 2.5$.

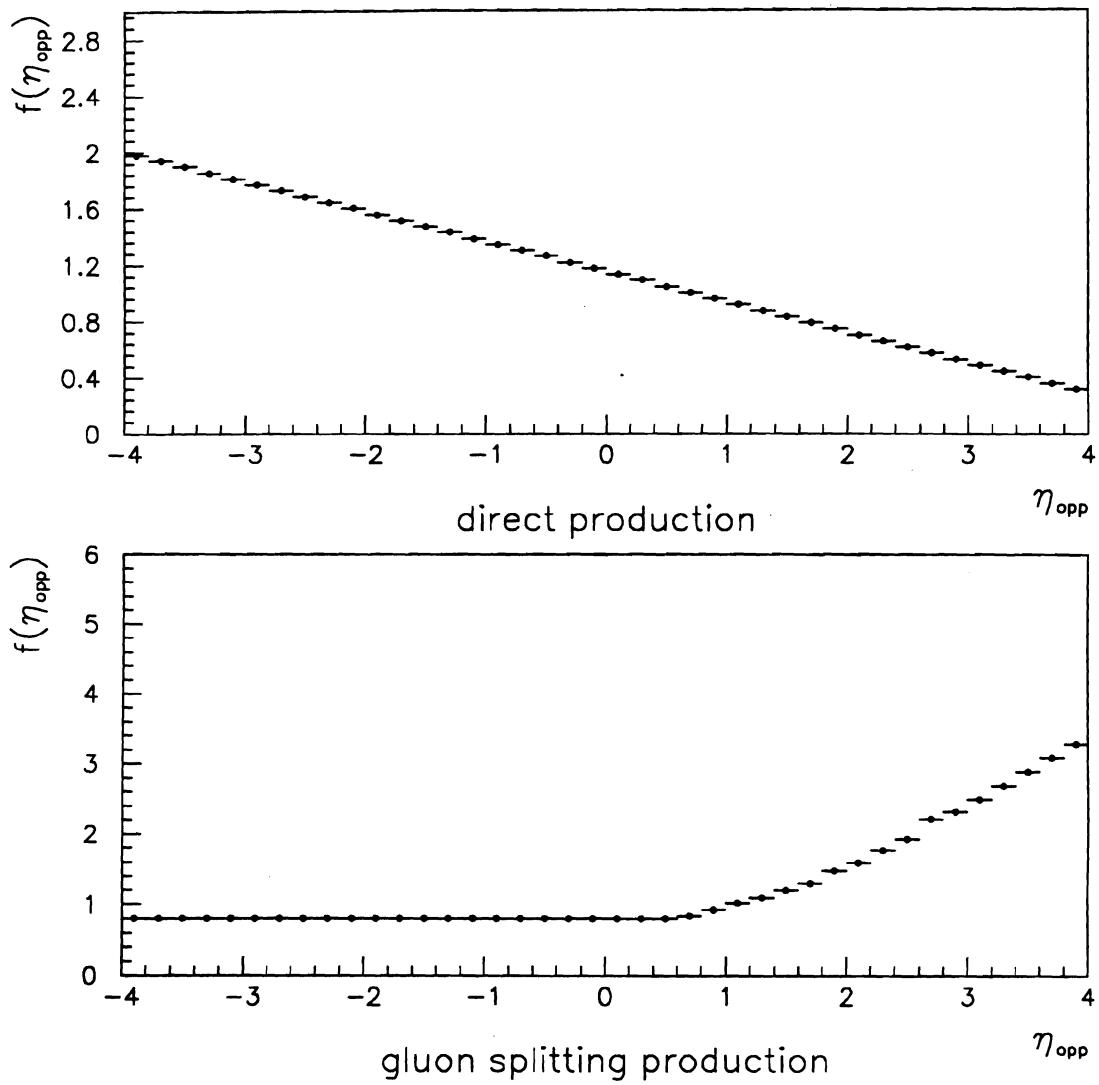

Figure D.6: ***The weighting function applied to the ISAJET simulation so it models the NLO calculation more closely.***

culation of bottom events with the cuts listed. The systematic uncertainty in the cross section due to modelling of η_{opp} will be calculated in chapter 6.

Appendix E

Glossary of Abreviations

- ADC - Analog to digital conversion.
- CDF - Collider Detector at Fermilab.
- CMU - A muon which was detected by the central muon detector.
- CTEQ - Structure functions produced by the Collaboration of Theorists and Experimentalists on QCD.
- DFLM - Structure functions with authors: Diemoz, Ferromi, Longo and Martinelli
- EHLQ - Structure functions with authors: Eichten Hinchliffe Lane Quigg
- EM - Electromagnetic.
- FEM - Energy detected in the forward electromagnetic calorimeter.

- FHA - Energy detected in the forward hadronic calorimeter
- FMU - A muon which was detected by the forward muon detector.
- FSIM - The fast simulation code for forward muons.
- HAD - Hadronic
- HOPU - Half-octant pattern unit which was a fastbus trigger module.
- HV - High voltage.
- LO - Leading order.
- MNR - Mangano, Nason, and Ridolfi; authors of the computer program which is used to calculate next-to-leading order bottom production.
- MPF - Missing projection fraction; it is mathematically defined in equation 4.7.
- MRSD0 - Structure functions with authors: Martin Roberts Stirling. D0 refers to a particular fit to the experimental data
- NDE - Nason, Dawson, and Ellis; authors of the first published next-to-leading order QCD calculation for heavy quark production.
- NLO - Next to leading order.
- NUPU - The new pattern unit which replaced the HOPU as the fastbus trigger module.

- PEM - Energy detected in the plug electromagnetic calorimeter.
- PHA - Energy detected in the plug hadronic calorimeter
- QCD - Quantom Chromo-Dynamics which is the mathematical model of the strong force.
- QDJSCO - The computer code which performs jet corrections.
- QFL - Computer code which simulates the CDF calorimeter response to particles.
- RMS - root mean square. The first moment of a distribution.
- TDC - The fastbus module which performed time to digital conversions.
- VTPC - vertex time projection chamber. The detector used to determine the vertex at CDF.

Bibliography

[1] F.Abe, et al., in proceedings of the International Symposium on Lepton and Photon Interactions (FERMILAB-CONF-93/199-E) August, 1993.

[2] V.D.Barger and R.J.N.Phillips, *Collider Physics* (Addison-Wesley Publishing Co.,Inc. Reading, Mass. 1987) pp.1-50.

[3] F.Halzen and A.D.Martin, *Quarks and Leptons,* (John Wiley and Sons, Inc.,New York, N.Y. 1984) pp.1-150.

[4] P.Nason, S.Dawson and R.K.Ellis, Nuclear Physics **B327**, 49(1989).

[5] M.Mangano, R.K.Ellis and Ridolfi, Nuclear Physics **B373**, 295(1992).

[6] R.K.Ellis, in proceedings of The Fermilab Meeting DPF92, Batavia, Il, ed. by C.H.Albright, P.H.Kasper, R.Raja and J.Yoh (World Scientific, River Edge, New Jersey, 1993) pp.173-174.

[7] A.Geiser, in the XXVIIth Rencontres de Moriond Conf. Proceedings (PITHA 92/19) June 1992.

[8] E.L.Berger and R.Meng, Physical Review D **46**, 1895(1992).

[9] S. Henderson, et al., Physical Review D **45**, 2212(1992).

[10] J.Skarha, Ph.D. Thesis, University of Wisconsin, 1989.

[11] L.Markosky, Ph.D. Thesis, University of Wisconsin, 1992.

[12] F.Abe, et al., Physical Review D **44** 29(1991).

[13] K.Byrum, Ph.D. Thesis, University of Wisconsin, 1992.

[14] C.Grosso-Pilcher and S.White (CDF-1202-unpublished).

[15] K.Byrum, et al. (CDF-1343-unpublished).

[16] D.Carlsmith and J.Skarha (CDF-925-unpublished).

[17] D.Coupal et al. (CDF-2036-unpublished).

[18] J.C.Yun and M.Binkley (CDF-884-unpublished).

[19] F.Abe, et al., Physical Review Letters, **62**, 613(1989).

[20] F.Abe, et al., Physical Review Letters, **68**, 104(1992).

[21] F.Abe, et al., Physical Review Letters, **62**, 3020(1989).

[22] F.Abe, et al., Physical Review Letters, **64**, 157(1990).

[23] F.Abe, et al., Physical Review D, **41** 1722(1990).

[24] F.Abe, et al., Physical Review Letters, **65**, 968(1990).

[25] F.Abe, et al., Physical Review D, **45** 1448(1992).

[26] F.Abe, et al., Physical Review D, **43** 2070(1991).

[27] F.Abe, et al., Physical Review Letters, **66**, 2951(1991).

[28] F.Abe, et al., Physical Review Letters, **67**, 2937(1991).

[29] F.Abe, et al., Physical Review Letters, **68**, 2734(1992).

[30] F.Abe et al., Nuclear Instruments and Methods, **A271** 387(1988).

[31] L.Keeble, Ph.D. Thesis, Texas A and M University, 1992.

[32] F.Abe, et al., Physical Review D, **47**, 4857(1993).

[33] A.Roodman, S.Behrends and M.Shapiro (CDF-1344-unpublished).

[34] S.Behrends (CDF-1286-unpublished).

[35] S.Behrends, M.D.Shapiro and E.Pare (CDF-1066-unpublished).

[36] R.D.Field and R.P.Feynman, Nuclear Physics **B136** 1(1978).

[37] T.Hessing, S.Behrends, P.Tipton and B.Winer (CDF-1131-unpublished).

[38] S.Behrends and A.F.Garfinkel (CDF-1650-unpublished).

[39] F.Paige and S.D.Protoposescu, "ISAJET Monte Carlo program Version 6.36", BNL Report No. BNL38034, 1986 (unpublished).

[40] C.Peterson, D.Schlatter, I.Schmitt and P.Zerwas, Physical Review D **27** 109(1983).

[41] B.Flaugher and S.Kuhlmann (CDF-685-unpublished).

[42] S.Behrends, in Proceedings of the International Symposium on Lepton and Photon Interactions (FERMILAB-CONF-93/207-E) August, 1993.

[43] T.Hessing and B.Winer (CDF-1347-unpublished).

[44] S.Kuhlmann and L.Nakae (CDF-1431-unpublished).

[45] L.Keeble and B.Flaugher (CDF-1513-unpublished).

[46] F.Abe, et al., Physical Review Letters **67**, 2937(1991).

[47] M.Banner, et al. Physics Letters **B118** 203(1982).

[48] T.Rodrigo, in Proceedings of The Fermilab Meeting DPF92, Batavia, Il, ed. by C.H.Albright, P.H.Kasper, R.Raja and J.Yoh (World Scientific, River Edge, New Jerssey, 1993) pp.1097-1099.

[49] K.Byrum (CDF-1417-unpublished).

[50] K.Byrum (CDF-1418-unpublished).

[51] K.Byrum and J.Lamoureux (CDF-1594-unpublished).

[52] F.Ukegawa, Ph.D. Thesis, University of Tsukuba, 1991.

[53] F.Abe, et al., submitted to Physical Review Letters (FERMILAB-PUB-93/091-E) April 1993.

[54] R.Hollebeek, L.Song, G.P.Yeh, and J.Yoh (CDF-1355-unpublished).